Iron(oxide) ferrofluids: synthesis, structure and catalysis

Iron(oxide) ferrofluids: synthesis, structure and catalysis

IJzer(oxide) 'ferrofluids': synthese, structuur en katalyse

(met een samenvatting in het Nederlands)

Proefschrift

ter verkrijging van de graad van doctor aan de
Universiteit Utrecht op gezag van de Rector Magnificus,
Prof. dr. W.H. Gispen, ingevolge het besluit van het
College voor Promoties in het openbaar te verdedigen
op maandag 20 oktober 2003 des middags te 14.30 uur

door

Karen Butter

geboren op 13 juni 1975, te Heemskerk

Promotor: Prof. dr. A.P. Philipse

Co-promotor: Dr. G.J. Vroege

Beiden verbonden aan de Faculteit Scheikunde van de Universiteit Utrecht.

ISBN: 90-393-3501-X

Voor mijn ouders

This work is part of the research program of the Dutch Technology Foundation (STW) with financial support from the Dutch Organisation for Scientific Research (NWO).

Cover: cryogenic electron micrographs of dispersions of iron colloids with different particle sizes.

Contents

1 General Introduction

Introduction

1.1. What are ferrofluids ?

Liquid magnets do not exist, since all magnetic substances lose their ferromagnetic properties above a certain temperature, the Curie temperature, which is always lower than the melting temperature[1]. However, magnetic liquids do exist in the form of so-called ferrofluids; they are black liquids that can be manipulated by an external magnetic field gradient which attracts the liquid (fig 1). Ferrofluids consist of small magnetic colloids (which are particles of the order of 1 nm-1 μm) in a non-magnetic solvent [1]. Colloidal particles are much larger than molecules and sediment under the influence of gravity. However, they are small enough to perform Brownian motion (due to the random thermal motion of the solvent molecules of the suspending fluid), which counteracts the sedimentation. Colloids usually attract each other due to Van der Waals forces, that have to be compensated by repulsive forces (e.g. charge or steric repulsion by surfactant layers) to obtain a stable colloidal dispersion, in which particles freely translate and rotate. In ferrofluids, as a special kind of colloidal dispersions, additional dipolar interaction forces between particles are present, that are direction dependent but attractive on average [1].

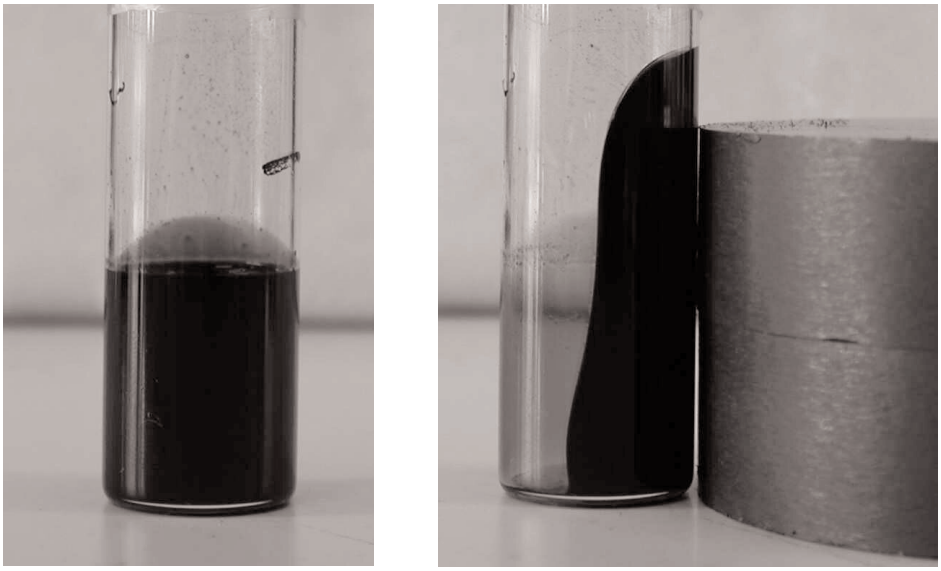

Figure 1. Example of an ironoxide dispersion in zero-field (left) and exhibiting the equilibrium shape in a field gradient typical for ferrofluids (right).

[1]A very few exceptions are known, such as liquid ^{3}He [3] and undercooled, metastable melts of $Co_{80}Pd_{20}$ [4].

1.2. The origin of magnetism

Magnetic fields are generated by electric currents. The motion of electrons around the nuclei of atoms thus causes the presence of magnetic fields on the atomic level [2]. Many atoms have a non-zero magnetic moment of the order of 10^{-23} Am^2 [2]. However, for most substances, the net magnetic moment is zero due to random orientation of all atomic moments within the assembly. A non-zero magnetic moment can be induced by application of a magnetic field, which causes the atomic moments to align with the field. Since the atoms rotate in a Brownian way, the degree of alignment depends on the temperature and field strength and the susceptibility of the material (a measure for the strength of response to a magnetic field).

1.3. Permanently magnetic materials

In some materials a strong dipole-dipole interaction of quantum-mechanical origin causes long-range orientational correlations of the permanent atomic dipoles, resulting in permanently magnetic substances (i.e. also in zero field). Examples are iron, ironoxides, nickel, cobalt, their alloys and some rare earth elements. Macroscopic objects made of magnetic materials do not have a permanent magnetic moment however, because the long-range correlation is limited; the material is divided into so-called domains, which contain different directions of the magnetization. For iron and ironoxide the size of such a domain is roughly 20 nm. In ferrofluids, particles are usually smaller than the domain size, resulting in permanently magnetic colloids, which however are free to rotate independently from each other (for dilute dispersions), but can be aligned by a magnetic field. The degree of alignment depends on the dipole moments of the particles and first increases linearly as a function of the field strength after which a plateau (fully aligned system) is reached at high fields (a so-called Langevin shape). After turning off the field, the dipole moments can relax in two ways: via Brownian rotation of the whole particle (depending on the particle volume V and viscosity of the solvent η) or via so-called Néel rotation of the magnetization with respect to the crystal lattice of the particle. The corresponding Brownian and Néel relaxation times t_B and t_N are given by

$$\tau_B = 3V\eta / kT \qquad (1)$$

$$\tau_N = f_0^{-1} \exp(KV / kT) \qquad (2)$$

where f_0^{-1} is of the order 10^9 s^{-1} [1,5] and K is the anisotropy constant, which depends on the composition, shape and surface of the particle.

1.4. Synthesis of ferrofluids

Ferrofluids do not exist in nature and are artificially prepared. The earliest method to produce ferrofluids was by grinding micro-sized magnetic particles for several weeks in ball mills in the presence of surfactants [6,7], producing a very broad particle size distribution. A more convenient method, which also results in better-defined particles with a much narrower size distribution is the preparation by precipitation reactions. A well-known example is the synthesis of magnetite by the addition of a stoichiometric mixture of Fe(II) and Fe(III) salts to an alkali solution [5,6].

$$8OH^- + 2Fe^{3+} + Fe^{2+} \rightarrow Fe_3O_4 + 4H_2O \qquad (3)$$

Aqueous dispersions of ironoxide particles are stabilized by a hydrophilic double layer of surfactants or by charge (due to acid-base reactions at the surface or specific adsorption of ions). The first (water-based) ferrofluid was synthesized already in 1938 by Elmore [8] (via the ball-mill procedure), but extensive research on ferrofluids started around 1960 by Rosensweig [9] and Papell [10]. They developed the synthesis of oil-based ferrofluids stabilized by surfactants that are still used today. Elaborate research on charged water-based magnetite was performed by Massart and Cabuil and others [11-13]. Later, also metallic magnetic particles were synthesized (Fe, Ni, Co) by metal vapor deposition [14,15], sonolysis [16], reduction of metal salts [17,18] or thermal decomposition of carbonyl compounds into metal and carbonmonoxide [19,20,21]. The first papers on the synthesis of cobalt by Thomas [22] and Hess and Parker [23] appeared in 1966. Important advantages of these ferrofluids compared to magnetite are their narrower size distribution and the better control of particle size by choosing the amounts of surfactants. However, metallic particles are chemically instable in air, which causes them to oxidize [19]. Later, a large variety of magnetic colloids was developed, e.g. composite particles consisting of magnetic cores in a silica shell [24,25], magnetic particles with attached functional groups like enzymes (mainly for medical or biological applications) [26,27], colloidal alloys [28,29] and magnetic rods [30]. Quite recently, a new synthesis method for very monodisperse magnetite dispersions was developed by Sun and Zeng [31], which seems to combine the advantages of metallic and oxidic particles (low polydispersity, size control, stability in air).

1.5. Applications of ferrofluids

Applications of magnetic fluids are numerous, and started around 1970. Many applications are based on the special property of ferrofluids, that they are attracted by magnetic field gradients while preserving their liquid character. They are used e.g. as liquid seals in rotary shafts, but also in computer hard disk drives, for prevention against contamination [6,7,32]. The same property is used in loudspeaker coils [32], that consist of a cylindrical voice coil fitted to a cylindrical permanent magnet with a small gap that allows

the coil to move. The heat developed in the voice coil can be dissipated more readily when the air in the gap is replaced by a liquid. An ordinary liquid would drip out, but a ferrofluid is retained by the magnetic field already present. Other applications of ferrofluids are the use as contrasting agent for MRI scans or as magnetic inks for jet printing [7], which are subjected to magnetic field gradients to deflect and position the ink droplets on the paper. Here, the magnetic properties of the dried ink are not relevant, but there are special constraints such as a quick drying time on the paper. For magnetic reading of letters and numbers, e.g. on cheques, the magnetic properties of the dried ink are of paramount importance; the paper is first subjected to a magnetic field, before it is fed into the magnetic reader, so the dried ink must have a suitably high remanence for the letters to be read. Nowadays, research is performed to influence the color of magnetic inks by building fluorescent dyes into the particles [33].

Magnetic fluids are also used in medical applications, for instance in magnetically controlled drug targeting, based on the binding of e.g. established anticancer drugs with ferrofluids that concentrate the drug in the area of interest (a tumor) by means of magnetic fields [27]. Other potential applications of ferrofluids are their use as optical devices (e.g. shutters), exploiting the change in transmittance of light upon alignment of the particles in a magnetic field. Here, small magnetic particles are needed to decrease the response time of the shutter [7]. A relatively new potential application is the use of a lattice of self-assembled monodisperse magnetic colloids in computers for data storage [34,35]. However, new methods for writing and reading of data have to be developed first, to be able to use this in practice. Another very interesting application would be the use of magnetic colloids attached to catalysts, which could be separated after their use by means of magnetic field gradients. This application would then combine the advantages of homogeneous catalysis (high efficiency due to the large available surface) and heterogeneous catalysis (easy recycling of the catalyst).

As is obvious, various applications of ferrofluids all require different properties and pose various constraints on the dispersions. To understand ferrofluid behaviour and to improve applications or develop new ones, careful study relating to fluid stability, control of surfactants, particle sizes, materials and physical behaviour are essential.

In addition, ferrofluids, consisting of permanent spherical dipoles freely rotating in a non-magnetic matrix can be regarded as a model for molecular dipoles, that are much more difficult to study.

1.6. Research on dipolar spheres

Since the 1970s and until this very day a lot of theoretical and simulation work has been devoted to dipolar sphere systems, showing interesting but often contradictory results on which a full consensus still has not been reached [36]. In a pioneering paper de Gennes and Pincus [37] found that the orientation-averaged dipolar attraction between particles had a similar form as Van der Waals interactions, and they predicted a Van der Waals like phase-

diagram of ferrofluids with vapour, liquid and solid phases and the presence of chainlike structures in zero field. Other theoretical work in this era ([36] and references therein) and one early simulation [38] confirmed this behaviour, although some theoreticians predicted a phase separation between a vapour and a ferroelectrically ordered liquid [39-41].

However, in 1993/1994 Weis and Levesque [42,43] performed extensive simulations on dipolar hard spheres, which surprisingly pointed to the absence of a phase separation. Instead, they found the aggregation of the spheres into linear chain-like structures, which grew, broke and recombined. Also in two dimensions, chaining was found, but here many closed rings of particles were seen [44,45]. The pioneering work of Weis and Levesque was extended by Tavares et al who determined several quantities such as mean chain length, number of free monomers, number of chains etc [36,46] from their simulations. Theoreticians treated the chains as a mixture of self-assembled chains of spheres in chemical equilibrium and also calculated their properties as a function of dipole moments, temperature and concentrations [46-48].

It has proven to be very difficult to obtain a suitable experimental system to verify many of the predictions described above, although there have been performed beautiful experiments showing chaining and crystallization for electrorheological fluids [49], magnetizable colloids [50,51] and inverse ferrofluids [52] (typically containing particles in the 100 nm - 5 μm range). However, all these studies involve induced (parallel) dipole moments and therefore only give information about structure in an externally applied field. In principle, ferrofluids (containing much smaller particles of about 10 nm) are a good candidate to study permanent spherical dipoles without external field. Many experiments were carried out indeed, most of which were performed in magnetic fields however, showing chaining of particles [53-58].

Experiments in zero field are much less numerous, but several studies were made using e.g. viscosity measurements [59], sedimentation [60], scattering [12,61,62], susceptibility measurements [63] or cryo-TEM [64,65]. However, these experiments were mainly performed on conventional magnetite particles, which are weakly magnetic, possess a large polydispersity, while their particle size control is limited, making them less suitable as a model system for dipolar spheres. In some cases phase separations [66-68] or aggregates were observed. These aggregates were mostly spherical [61,64,65], but often no clear information about the particle shape could be subtracted from the technique used [59,63]. It should also be noted that in experimental dispersions, ruling out isotropic interactions will always be difficult due to Van der Waals interactions, complicating comparison to theory or simulations (that often only include dipolar interactions). In addition, the presence of free surfactant molecules could induce isotropic depletion attractions. There is still an ongoing discussion whether or not the presence of some isotropic attraction (like Van der Waals) is required to induce phase separation. For example Van Leeuwen and Smit [69] only found L-V coexistence for a certain amount of isotropic attractions additional to the dipolar interactions. A theoretical study of van Roij [70] confirmed this aspect; dominant dipolar

attractions would lead to chain formation, while dominant isotropic attractions would cause the system to phase separate. Recently, the possibility of phase coexistence between branched and unbranched chains was considered [71]. Due to the presence of significant additional isotropic interactions, experimental studies could not really elucidate this point up to now. In this thesis, the subject described above is further investigated experimentally.

1.7. Overview of this thesis

This thesis describes the research on two topics concerning ferrofluids, i.e. the synthesis and use of catalytic magnetic colloids and the microstructural behaviour of ferrofluids in general. Here, we will briefly describe the content of both topics. As discussed in section 5 an interesting application of ferrofluids would be the use of magnetic colloids for catalysis (e.g. magnetic colloids with catalysts attached to the surface) and their separation for recycling the catalyst, which could be performed magnetically. The research described in this thesis is partly based on a research project on the synthesis of magnetic colloids and attachment of Pd-based NCN-pincer complexes (which are known to be catalytically active in aldol condensations and Michael additions [72-75]) and their magnetic separation (in cooperation with the department for metal-mediated synthesis and Stichting Toegepaste Wetenschappen (STW)) Magnetic iron particles in principle could form a suitable ferrofluid for this study, since they are well-defined and have a relatively large saturation magnetization. However, an impractical property of metallic particles is their sensitivity to air, which causes oxidation (especially for small particles). We attempted to protect metallic iron particles against oxidation by the application of a protecting surface layer like silica or noble metals (these experiments are described in the appendix at the end of this thesis). This was found to be very difficult and finally it was decided to employ conventional maghemite particles for the research on catalysis, which are insensitive in air, although less magnetic. A feasibility study of the synthesis of catalytic magnetic colloids and their separation was performed and is described in chapter 2.

However, the metallic iron particles we synthesized were found to be very interesting ferrofluids for a fundamental study of the properties of ferrofluids in general, which is not only important for scientific knowledge but of benefit for applications (e.g. magnetic separation) as well. Since they are fairly monodisperse, their particle size can be controlled well over a broad range and they can be stabilized by different surfactants, these ferrofluids turned out to be a good model system to study interparticle interactions and the resulting particle microstructure in ferrofluids as a function of size. Therefore, extensive research on iron ferrofluids was performed and is described in chapters 3 to 7 of this thesis.

In chapter 3 the synthesis and a detailed characterization of iron ferrofluids stabilized by different surfactants is presented. Subsequently, the composition of individual particles in one specific ferrofluid of oleic-acid-coated iron particles was elaborately studied by small angle neutron and X-ray scattering on dilute ferrofluids (described in chapter 4). More concentrated dispersions of the same system, employing interparticle interactions, were

examined by SAXS and are described in chapter 5. These measurements were also used to investigate the influence of magnetic fields on the particle-particle interactions and structure. Chapter 6 describes the direct study of particle structures in concentrated ferrofluids using cryo-TEM, which studies two-dimensional glassified liquid films of dispersions, enabling the direct photography of *in situ* structures in two dimensions. This research was performed for a series of ferrofluids as a function of particle size and type of surfactant layer, where interparticle structures were found to vary enormously depending on the exact properties. Since it would be interesting to also investigate structure formation in three dimensions, rotational diffusion was studied using frequency-dependent susceptibility measurements on the same dispersions (described in chapter 7) and compared to the results obtained from cryo-TEM (chapter 6).

References

[1] Rosensweig R E 1985 *Ferrohydrodynamics* (Cambridge: Cambridge University Press).

[2] Jiles D 1995 *Introduction to Magnetism and Magnetic Materials* (London: Chapman & Hall).

[3] Lang T, Moyland P L, Sergatskov D A, Adams E D and Takano Y 1996 *Phys. Rev. Lett.* **77** 322.

[4] Platzek D, Notthoff C, Herlach D M, Jacobs G, Herlach D and Maier K 1994 *Appl. Phys. Lett.* **65** 1723.

[5] Charles S W. 1992. in; Dormann J L, Fiorani, D., Ed.; Amsterdam: North-Holland; pp 267.

[6] Berkovski B, Bashtovoy, V. 1996 *Magnetic fluids and applications handbook* (New York: Begel House Inc.).

[7] Charles S W and Popplewell J 1982 *Endeavour, New Series* **6** 153.

[8] Elmore W C 1938 *Phys.Rev.* **54** 309.

[9] Rosensweig R E, Nestor J W and Timmins R S. 1965. in *Mater. Assoc. Direct Energy Convers. Proc. Symp. AIChE-I. Chem. Eng. Ser. 5*; pp 104.

[10] Papell S S. In *U.S. Patent*, 1965; Vol. 3; pp 215.

[11] Lefebure S, Dubois E, Cabuil V, Neveu S and Massart R 1998 *J. Mater. Res.* **13** 2975.

[12] Bacri J C, Perzynski R and Salin D 1990 *J. Magn. Magn. Mater.* **85** 27.

[13] Massart R 1981 *IEEE Trans. Magn.* **MAG-17** 1247.

[14] Gangopadhyay S, Hadjipanayis G C, Dale B, Sorensen C M, Klabunde K J, Papaefthymiou V and Kostikas A 1992 *Physical Review B* **45** 9778.

[15] Hahn H and Averback R S 1990 *J. Appl. Phys.* **67** 1113.

[16] Suslick K S, Mingming F and Hyeon T 1996 *J. Am. Chem. Soc.* **118** 11960.

[17] Tsai K L and Dye J L 1991 *J. Am. Chem. Soc.* **113** 1650.

[18] Bönnemann H, Brijoux W, Brinkmann R and Joussen T 1990 *Angew. Chem., Int. Ed. Engl.* **29** 273.

[19] Griffiths C H, O'Horo, M.P., Smith, T.W. 1979 *J. Appl. Phys.* **50** 7108.

[20] Smith T W and Wychick D 1980 *J. Phys. Chem.* **84** 1621.

[21] Papirer E, Horny P, Balard H, Anthore A, Petipas C and Martinet A 1983 *J. Colloid Interface Sci.* **94** 207.

[22] Thomas J R 1966 *J. Appl. Phys.* **37** 2014.

[23] Hess P H and Parker P H 1966 *J. Appl. Polym. Sci.* **10** 1915.

[24] Philipse A P, Bruggen van M P B and Pathmamanoharan C 1994 *Langmuir* **10** 92.

[25] Ewijk van G A, Vroege G J and Philipse A P 1999 *J. Magn. Magn. Mater.* **201** 31.

[26] Dyal A, Loos K, Noto M, Chang S W, Spagnoli C, Shafi K V P M, Ulman A, Cowman M and Gross R A 2003 *J. Am. Chem. Soc.* **125** 1684.

[27] Lubbe A S, Alexiou, C., Bergemann, C. 2001 *J. Surgical Research* **95** 200.

[28] Lambrick D B, Mason N, Hoon S R and Kilner M 1987 *J. Magn. Magn. Mater.* **65** 257.

[29] Regazzoni A E and Matijevic E 1983 *Colloids and Surfaces* **6** 189.

[30] Puntes V F, Krishnan K M and Alivisatos A P 2001 *Science* **291** 2115.

[31] Sun S and Zeng H 2002 *J. Am. Chem. Soc.* **124** 8204.

[32] Rosensweig R E 1982 *Scientific American* **247**(4), 136.

[33] Geraedts, Wieringa (Océ) *personal communication*

[34] Sun S, Murray C B, Weller D, Folks L and Moser A 2000 *Science* **287** 1989.

[35] Stamm C, Marty F, Vaterlaus A, Weich V, Egger S, Maier U, Ramsperger U, Fuhrmann H and Pescia D 1998 *Science* **282** 449.

[36] Teixeira P I C, Tavares, J.M., Telo da Gama, M.M. 2000 *J. Phys.: Condens. Matter* **12** R411.

[37] de Gennes P G, Pincus, P.A. 1970 *Phys. Kondens. Materie* **11** 189.

[38] Ng K-C, Valleau J P, Torrie G M and Patey G N 1979 *Mol. Phys.* **38** 781.

[39] Tsebers A O 1982 *Magnetohydrodynamics* **18** 137.

[40] Sano K and Doi M 1983 *J. Phys. Soc. Japan* **52** 2810.

[41] Zhang H and Widom M 1993 *J. Magn. Magn. Mater.* **122** 119.

[42] Weis J J and Levesque D 1993 *Phys. Rev. Lett.* **71** 2729.

[43] Levesque D and Weis J J 1994 *Phys. Rev.* **49** 5131.

[44] Weis J J 1998 *Mol. Phys.* **93** 361.

[45] Tavares J M, Weis J J and Telo da Gama M M 2002 *Phys. Rev. E* **65** 061201.

[46] Tavares J M, Weis, J.J., Telo da Gama, M.M. 1999 *Phys. Rev. E.* **59** 4388.

[47] Sear R P 1996 *Phys. Rev. Lett.* **76** 2310.

[48] Osipov M A, Teixeira, P.I.C., Telo da Gama, M.M. 1996 *Phys. Rev. E.* **54** 2597.

[49] Gast A P, Zukoski, C.F. 1989 *Adv. Coll. Int. Sci.* **30** 153.

[50] Fermigier M, Gast, A.P. 1993 *J. Magn. Magn. Mater.* **122** 46.

[51] Promislow J H E and Gast A P 1994 *J. Chem. Phys.* **102** 5492.

[52] Skjeltorp A T 1983 *Phys. Rev. Lett.* **51** 2306.

[53] Rosman R, Janssen J J M and Rekveldt M T 1990 *J. Appl. Phys.* **67** 3072.

[54] Hayes C F 1975 *J. Colloid Interface Sci.* **52** 239.

[55] Socoliuc V 1999 *J. Magn. Magn. Mater.* **207** 146.

[56] Vogelgesang P J, Charap S H and Bortz A B 1985 *J. Appl. Phys.* **57** 4277.

[57] Wu K T, Yao Y D, Wang C R C, Chen P F and Yeh E T 1999 *J. Appl. Phys.* **85** 5959.

[58] Martinet A 1974 *Rheol. Acta* **13** 260.

[59] Popplewell J and Al-Qenaie A 1992 *J. Magn. Magn. Mater.* **104-107** 1555.

[60] Popplewell J, Charles S W and Hoon S R 1980 *IEEE Trans. Magn.* **MAG-16** 191.

[61] Eberbeck D and Bläsing J 1999 *J. Appl. Cryst.* **32** 273.

[62] Gazeau F, Dubois E, Bacri J C, Boue F, Cebers A and Perzynski R 2002 *Phys. Rev. E* **65** 031403.

[63] Fannin P C, Giannitsis A T and Charles S W 2000 *Eur. Phys. J. Appl. Phys.* **12** 93.

[64] Donselaar L N, Frederik, P.M., Bomans, P.H., Buining, P.A., Humbel, B.M., Philipse, A.P. 1999 *J. Magn. Magn. Mater.* **201** 58.

[65] Shen L, Stachowiak, A., Fateen, S.K., Laibinis, P.E., Hatton, T.A. 2001 *Langmuir* **17** 288.

[66] Cabuil V, Perzynski R and Bastide J 1994 *Progr. Colloid Polym. Sci.* **97** 75.

[67] Dubois E, Cabuil V, Boué F, Bacri J C and Perzynski R 1997 *Progr. Colloid Polym. Sci.* **104** 173.

[68] Dubois E, Perzynski R, Boué F and Cabuil V 2000 *Langmuir* **16** 5617.

[69] Leeuwen van M E and Smit B 1993 *Phys. Rev. Lett.* **71** 3991.

[70] Roij van R 1996 *Phys. Rev. Lett.* **76** 3348.

[71] Tlusty T, Safran, S.A. 2000 *Science* **290** 1328.

[72] Gorla F, Togni A and Venanzi L M 1994 *Organometallics* **13** 1607.

[73] Stark M A, Jones G and Richards C J 2000 *Organometallics* **19** 1282.

[74] Stark M A and Richards C J 1997 *Tetrahedron Letters* **38** 5881.

[75] Zhang X, Longmire J M and Shang M 1998 *Organometallics* **17** 4374.

2 Catalytic magnetic colloids: preparation, catalytic activity and separation

Abstract

This chapter describes a feasibility study on the synthesis of catalytic magnetic particles and their magnetic separation, which is needed for recycling after their application as a catalyst. Various kinds of catalytic magnetic colloids, coated with [2,6-bis(N,N-dimethylaminoethyl)phenyl] palladium(II) pincer-type complexes, were synthesized and shown to be active in aldol condensation reactions. The grafting density of catalytic groups was similar for different grafting methods, but seems to depend on the coating reaction time. Grafting of the particles yielded instable dispersions; further study is needed to obtain stable catalytic colloids, which will improve their efficiency in catalysis. Single magnetic colloidal particles (without catalyst) or small aggregates could be separated by High Gradient Magnetic Separation (HGMS), in case their dipole moments were sufficiently large.

1. Introduction

Colloidal particles, with catalysts attached to the particle surface, combine the advantages of homogeneous catalysis (high efficiency) and heterogeneous catalysis (easy recycling of the catalyst). Since the particles are small, a relatively large surface is available for grafting catalysts. In addition, separation of colloidal particles to reuse the catalyst is expected to be easier than for molecular catalysts. Using *magnetic* colloids creates the additional possibility of magnetic separation of the catalytic colloids. For the feasibility study in this chapter, we chose to use dispersions of magnetic maghemite (Fe_2O_3) particles, as well as silica particles containing maghemite cores. Because the synthesis of these magnetic silica particles is relatively time-consuming, the first experiments on coating with catalytic groups were performed with non-magnetic (Stöber) silica particles, which can be synthesized easily according to well-established procedures [1,2]. Advantages of (magnetic) silica particles are their well-known surface properties and grafting methods [3,4,5]. The catalysts used for grafting are [2,6-bis(N,N-dimethylaminoethyl)phenyl] palladium(II) pincer-type complexes (figures 1 and 2), further denoted as NCN-complexes, that are known to be active catalysts for aldol condensations and Michael additions [6,7,8,9]. For preliminary experiments, the same complexes with Pt instead of Pd were also used, since these complexes are more stable and the Pt-complex is known to show an orange colour upon treatment with SO_2 (g) [10,11]. For grafting (magnetic) silica particles, we used the catalyst with a triethoxysilane end-group (figure 1). For grafting maghemite particles, we chose the pincer complex with a carboxylic acid end-group (figure 2), since it is known that other acids (e.g. oleic acid or dodecanoic acid) can be covalently linked to the surface of maghemite particles [12].

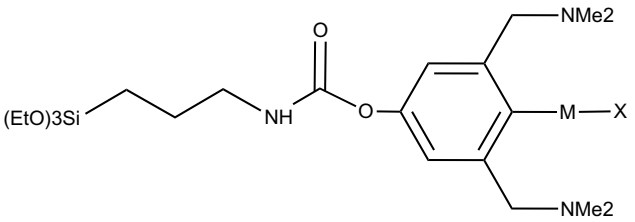

Figure 1. Pincer complex with silane endgroup, with M = Pd, X= Cl, or M=Pt, X=I.

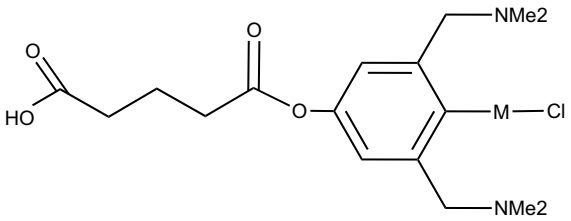

Figure 2. Acid-functionalized pincer complex, M= Pd, Pt.

In addition, we investigated the optimisation of the synthesis procedure of magnetic silica particles. To prevent aggregation, the synthesis of magnetic silica normally is performed in a very dilute solution of magnetic cores [12]. Since this method requires synthesis on an impractically large scale to achieve a considerable amount of particles, it was studied if magnetic silica could be synthesized in a solution with a higher concentration of maghemite cores. Because the magnetic separation is expected to be easier for magnetic particles with a thin silica shell, we also investigated whether the thickness of the silica layer could be reduced.

High Gradient Magnetic Separation (HGMS), a well-known technique [13,14] for separation of micrometer-sized magnetic particles, is based on the attraction of magnetic particles by a magnetic field gradient created in the neighbourhood of thin magnetizable wires along which a suspension of particles flows. The gradient exerts a force on the magnetic particles, which causes them to be trapped by the wires. Earlier, this technique has only been performed for large magnetic colloids (of the order of 0.1-1 μm) [15,16,17]. Here it is investigated whether HGMS can be used for ferrofluids (particle radii ~ 10 nm) as well.

2. Background

This section provides general information about the synthesis and coating of silica particles with silane coupling agents. In addition, Langevin behaviour of magnetic particles in a field, necessary for interpreting magnetization measurements will be described briefly. Finally, some approximate calculations on the capture of magnetic particles in a HGMS set-up are presented. For reasons of clarity, these will be directly applied to the specific set-up used in our experiments. More detailed literature about HGMS can be found in [13].

2.1. Synthesis and coating of Stöber silica particles

Silica particles can be synthesized in a mixture of ethanol and ammonia using the Stöber method [1]. The particles are prepared by the hydrolysis and subsequent polymerisation of tetraethoxysilane (TES). The net reaction is

$$n\,\mathrm{Si(OC_2H_5)_4} + 2n\,\mathrm{H_2O} \xrightarrow{C_2H_5OH,\,NH_3} n\,\mathrm{SiO_2} + 4n\,\mathrm{C_2H_5OH} \qquad (1)$$

Dissociation of surface silanol groups or adsorption of hydroxyl ions produce negative charges on the particle surfaces [5]. A silane coupling agent (i.e. $R_{(4-n)}SiX_n$ with X a hydrolysable group, for instance an alkoxy group, and R an organic chain) can form covalent bonds with an inorganic substrate. For this reason a silane coupling agent is often used to coat silica particles with organic chains (after which they can be dispersed in organic solvents). In presence of water, the alkoxy groups of the silane coupling agent hydrolyse under the influence of acid or base. Reactive silane triols are formed, which readily associate and condensate to oligomers. These oligomers adsorb on the silica particles and condense

on drying or distillation of water with surface silanol surface groups to form siloxane linkages (see figure 3) [5].

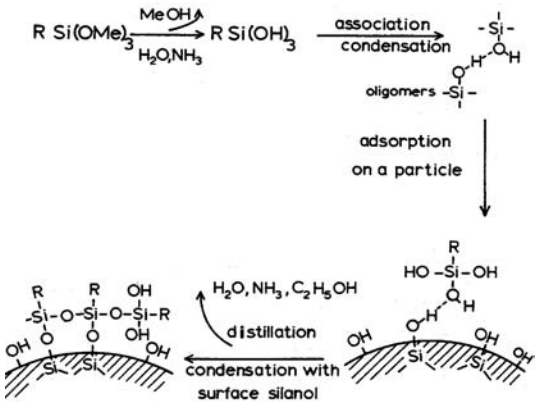

Figure 3. Grafting of silica particles with silane coupling agents [5].

2.2. Magnetization measurements

For single dipolar spheres, the magnetization M as a function of the magnetic field strength H is given by the Langevin equation [18]:

$$M(H) = M_s\left(\coth\left(\frac{\mu_0\mu H}{kT}\right) - \frac{kT}{\mu_0\mu H}\right) \tag{2}$$

Here, M_s is the saturation magnetization of the sample, reached upon complete alignment of all particles in the field direction and $\mu = 4\pi a_M^3 m_s/3$ is the dipole moment of the spheres with a_M the magnetic particle radius and m_s the bulk saturation magnetization per volume. For low fields, equation (2) can be approximated by [18]:

$$M(H) = \chi_i H \approx M_s\left(\frac{\mu_0\mu H}{3kT}\right) \qquad \left(\text{for } \mu_0\mu H << kT\right) \tag{3}$$

with χ_i the initial susceptibility. The particle radius can be determined from the magnetization curve (M as a function of H) from the ratio of χ_i (slope at small H) and M_s:

$$a_M^3 = \frac{\chi_i}{M_s}\left(\frac{9kT}{4\pi\mu_0 m_s}\right) \tag{4}$$

2.3. High Gradient Magnetic Separation

Our set-up consists of a reservoir, filled with magnetizable wires with their long axes in the direction of the flow velocity (schematically depicted in figure 4). The magnetic field is applied perpendicular to the long axes of the wires. To maximise the surface for capturing particles, the volume fraction of wires was chosen to be relatively high (13 %) in

comparison with conventional HGMS set-ups (~ 5 %).

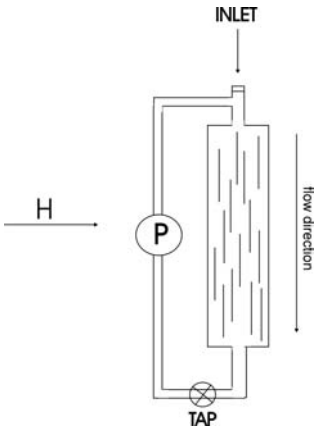

Figure 4. Schematic representation of the HGMS set-up (P = peristaltic pump).

The magnetic field due to a magnetizable wire with radius b in a homogeneous magnetic field H_0 as a function of the distance from the centre r in the direction perpendicular to its long axis and parallel to the field (for H_0 < the saturation magnetization H_s) is given by [14]:

$$H(b,r)_{//} = H_0(1 + b^2 / r^2) \tag{5}$$

The field gradient is given by its derivative:

$$\frac{dH}{dr} = -2H_0\left(\frac{b^2}{r^3}\right) \tag{6}$$

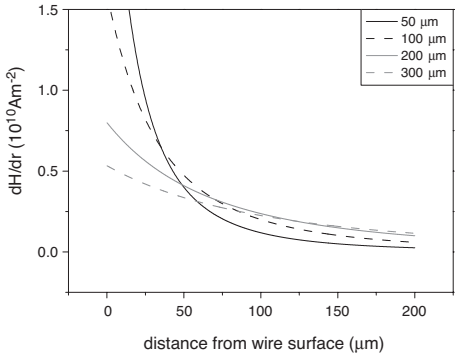

Figure 5. Field gradient as function of distance from the wire surface for wires with different radii (using equation (5)).

Figure 5 shows the calculated field gradient using equation 6 (in a field of 1 T, the saturation magnetization of our matrix material) as a function of the distance from the wire

surface r-b perpendicular to the long axis of a wire for different wire thickness. Although at small distance higher gradients can be achieved with thinner wires, a radius of 200 μm diameter was chosen, since this results in a high gradient (8 x 10^9 Am^{-2}) at r = b that is still considerable at larger distance (2.4 x 10^9 Am^{-2} at 100 μm).

In a separation experiment different forces act on a supposedly spherical magnetic particle, i.e. a magnetic force, a viscous drag force due to the solvent and a gravitational force [14]. The magnetic force F_m, proportional to the particle dipole moment μ and the field gradient dH/dr,

$$F_m = \mu_0 \mu \frac{dH}{dr} \tag{7}$$

(with μ_0 the magnetic permeability in vacuum of 4π x 10^{-7} Tm/A) attracts particles to the wire (in perpendicular direction), and is counteracted by the viscous drag force F_d in the opposite direction on the particle of radius a moving with a velocity v in a liquid with viscosity η [14]:

$$F_d = 6\pi\eta a v \tag{8}$$

For our small particles (radius ~ 5 nm), the gravitational force is about 2.5 x 10^{-20} N and can be neglected. The typical velocity v_{typ} of particles moving towards a wire is given by:

$$v_{typ} = \frac{\mu_0 \mu \frac{dH}{dr}}{6\pi\eta a} \tag{9}$$

The time t needed for a particle to travel from position r towards the surface of the wire (r = b), is given by:

$$t = \int_r^{r=b} \frac{1}{v_{typ}(r)} dr \tag{10}$$

with v_{typ} and dH/dr from equations (9) and (6). The maximum distance r_{max} from the wire centre value at which a particle can still be captured is given by the time t_{max} that the particle is at the same height as the wire (determined by the wire length l_{wire} divided by the flow velocity of the solvent $v_{solvent}$). In our case, where the average flow velocity is approximately 2.7 mms^{-1}, the length of the wires is 3 cm and b = 200 μm, t_{max} is about 11 seconds, resulting in a value for r_{max} of 300 μm.

When particles are trapped by the wires, another viscous drag force of the flowing solvent, acting on the particle at rest, competes with the magnetic force on the particle. The drag force on particles at rest due to flowing solvent, can be estimated by Faxén's theorem [19]:

$$\vec{F}(t) = 6\pi\eta a \overline{\overline{v_0}}^S(\vec{r},t) \tag{11}$$

where $\overline{\vec{v}_0(\vec{r},t)}^{s}$ is the flow velocity (in the absence of the particle), averaged over the particle surface. Here, the reservoir is considered as a porous matrix, where the distance between two wires forms the pores. In our case, where the volume fraction of wires in the reservoir is approximately 13 %, the average distance between two wires, assuming that they are all parallel to each other in an ordered array, is about 580 µm. In the pores a Poiseuille flow profile is assumed, with the average flow velocity $\bar{v}$ of the solvent equal to the flow velocity indicated by the peristaltic pump (2.7 mms^{-1}). The flow velocity as a function of the distance s from the centre of a pore with radius R can be calculated using [20]:

$$v(s)_{poiseuille} = v_{max} - \frac{v_{max}}{R^2}s^2 \qquad \text{with } v_{max} = 2\bar{v} \tag{12}$$

For our set-up, the velocity at a distance of a particle radius (5 nm) from the wire is approximately 0.19 μms^{-1} and can be considered as the average over the particle surface, since our particles are very small in comparison with the pore size. Accordingly, the drag force on a trapped particle is approximately 1.8 x 10^{-17} N. Since F_m is a factor of 140 larger (2.5 x 10^{-15} N) particles are indeed expected to be captured (even although strictly speaking these forces are perpendicular). It should be noted that these values are merely an estimate of the order of magnitude of the real values in view of the simplified Poiseuille flow in straight channels; obviously liquid flow in a fibre stacking is more complicated. In addition, it is assumed that the wires do not influence each other's field gradients, which will certainly not be the case for such high volume fractions.

3. Experimental

3.0. Characterization of dispersions

Transmission Electron Microscopy (TEM) photographs were made on a Philips CM10H transmission electron microscope from particles on grids coated with a Formvar film. Grids were dipped in a dilute dispersion and left to dry before bringing them in the microscope. Particle sizes were determined using the software AnalySIS Pro, an interactive computer program for analysing digital images.

Magnetization curves of the dispersions were measured at room temperature on an alternating gradient magnetometer (AGM) Micromag 2900 (Princeton Measurements Corporation) in small glass cups. Measurements were performed at the resonance frequency of the measuring probe (with sample attached), which was in the range 240-290 Hz. Curves were fitted by the Langevin equation (2), from which M_s was determined. For a more accurate determination of χ_i, it was determined from the slope of separate curves measured at low magnetic fields (< 1000 Am^{-1}) instead of from the whole Langevin curve. Assuming a spherical particle shape, magnetic particle radii were calculated via equation (4), using the bulk value for m_s of maghemite (0.48 x 10^6 Am^{-1} [21]). Particle concentrations were

determined from the weight after drying of a known volume of the dispersion. To determine the surface area, nitrogen physisorption on silica particles was measured. Textural analyses of the samples were performed on a Micromeritics ASAP 2400 apparatus. Measurements were carried out at -196 °C. Prior to analysis the samples were outgassed in vacuum at 120 °C. The isotherm was analysed according to the BET equation [22].

3.1. Synthesis of (magnetic) colloidal dispersions

Maghemite dispersions were synthesized following Massart's method [23,12]. $FeCl_2.4H_2O$ (3.29 g, 16.5 mmol) and $FeCl_3.6H_2O$ (8.68 g, 32.1 mmol) were dissolved together in 380 ml demineralised water. Magnetite was precipitated by adding 20 ml 25% NH_3 while stirring vigorously. After collection of the precipitate using a small permanent magnet, the supernatant was removed. The precipitate was washed with demineralised water, after which 40 ml 2 M HNO_3 was added, and the mixture was stirred for 5 minutes. The oxidation to maghemite was completed by adding 60 ml 0.35 M $Fe(NO_3)_3$ to the mixture and stirring at its boiling point for one hour. Next, the reddish sediment was washed with 2 M HNO_3 to keep the pH at a low value, after which it was redispersed in demineralised water. The resulting dispersion was coded FFaq. To be able to disperse particles in organic solvents, they were coated with oleic acid, using the method of van Ewijk [12]. 2 ml of FFaq (see table 2, section 4) was flocculated by adding a few drops of 25 % NH_3. The sediment, collected by using a small magnet, was washed with demineralised water, after which approximately 10 ml water was added. Under mild stirring, 2 ml oleic acid was added, which caused the magnetic material to transfer to the oil phase. The black oil phase, separated from the water phase, was washed a few times with acetone and dried under nitrogen flow. The resulting maghemite particles, coated with an oleic acid layer, were redispersed in cyclohexane. The resulting dispersion was coded FFch.

Silica dispersions S1 and S2 (with average particle radii 45 and 70 nm respectively) were synthesized by the Stöber method [1]. A dispersion of magnetic silica particles was prepared from FFaq following the method of van Ewijk [12], where maghemite particles were used as nuclei for the formation of silica particles. 11.5 ml of FFaq (22 gl^{-1}) was diluted 4 times. To lower the iso-electric point of the maghemite particles (from 7 to approximately 3.5) they were coated with citric acid by adding approximately 10 ml of a solution of citric acid (0.01 M) till flocculation was visible (approximately 10 ml). A concentrated tetramethylammoniumhydroxide (TMAH) solution was added until the pH of the mixture was raised to 7. Of the resulting ferrofluid, 20 ml was added to a mixture of 1500 ml ethanol, 400 ml water and 100 ml 25 % NH_3. For coating with silica, 2 ml freshly distilled tetraethoxysilane (TES) was added to the mixture while stirring. The mixture was stirred for 5 days, while after 3 days, another 4 ml TES was added. The resulting yellow-brownish dispersion was coded MS.

For separation experiments only, a bidisperse magnetite (Fe_3O_4) dispersion coded FFbi was used, consisting of a mixture of particles with two different sharp size distributions. The

synthesis was performed following a recently published method of Sun and Zeng [24]. First, magnetite seeds were synthesized by mixing 20 ml of diphenyl ether with iron(III)acetylacetonate (1.98 mmol), followed by 1,2-hexadecanediol (10.14 mmol), oleic acid (6.15 mmol) and oleyl amine (5.90 mmol). The mixture was allowed to reflux for 30 minutes under nitrogen atmosphere. After cooling to room temperature particles were flocculated by use of ethanol and sedimented with a magnet. Particles were dispersed in decalin and washed a second time with ethanol. The particles were stored in decalin. Later, particles were grown further in three steps after flocculating them again with ethanol and redispersing them in phenyl ether. For every step extra iron(III)acetylacetonate (2.2 mmol), 1.2-hexadecanediol (9.7 mmol), oleic acid (2.27 mmol) and oleyl amine (2.18 mmol) were added to the mixture. The mixture was again refluxed for 30 minutes under nitrogen atmosphere. After cooling to room temperature the particles were isolated and washed with ethanol. In the last growing step a second nucleation occurred, resulting in the bidisperse ferrofluid used for the separation experiments.

3.2. Improvement of synthesis procedure for magnetic silica particles

To prevent aggregation, the synthesis of magnetic silica usually is performed in a very dilute solution of magnetic cores (see above). Since this method requires synthesis on an impractically large scale to achieve a considerable amount of particles, attempts were made to make magnetic silica in a solution where the concentration of maghemite cores was 5 or 20 times higher. To study also the effect of dialysis of the citric-acid-coated ferrofluid before addition to the ethanol/ammonia mixture, all experiments were performed both with and without dialysis for 2 days.

To investigate the possibility of decreasing the thickness of the silica layer around magnetic silica particles (normally of the order of 30-50 nm), a series of silica coating experiments was performed in a dilute solution of maghemite cores, following the same procedure as described above (on smaller scale), but with smaller amounts of TES added (up to 38 times less). Dispersions were studied visually and with TEM.

3.3. Synthesis of Catalysts

The NCN pincer complexes with triethoxy silane end-group (both with Pd and Pt as metal centre M, see figure 1) were synthesized from p-hydroxy NCN pincer complexes (figure 6) and are coded Pd-S and Pt-S respectively. Experimental details and characterization are given in [25]. The acid-functionalized NCN pincer complex (with Pt as metal centre, see figure 2) was synthesized by reacting the *p*-hydroxy NCN-Pt-Cl complex (figure 6) with glutaric anhydride using the method of Bergbreiter et al [26] and coded Pt-A. A mixture of *p*-OH-NCN-Pt-Cl (2.54 g, 5.84 mmol) (figure 6), glutaric anhydride (0.70 g, 6.13 mmol) and dry triethylamine (4.5 ml, 32.1 mmol) in 250 ml dichloromethane was refluxed for an hour, during which the mixture turned from a slightly brown suspension to a clear brown solution. While stirring, the solution was allowed to cool to room temperature. The mixture

was concentrated to 100 ml (under vacuum atmosphere), washed four times with 0.4 M HCl (aq) (4 x 100 ml), and dried over $MgSO_4$. After removal of all volatiles under vacuum atmosphere, a brownish solid was collected on a glass frit and washed with a little ethanol 3 times. The compound was characterized by ^{1}H-NMR, ^{13}C-NMR at room temperature (using a Bruker AC-200 instrument) and by XRD (using a Nonius Kappa CCD diffractometer with rotating anode (Mo-Kα, λ = 0.71073 Å) at a temperature of 150 K).

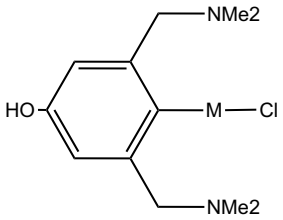

Figure 6. Pincer complex used for the synthesis of the catalysts in figures 1 and 2, M = Pd, Pt.

3.4. Synthesis and Characterization of Catalytic Colloids

This section describes the synthesis of catalytic magnetic colloids, using different methods. Characterization of the resulting colloids, coated with pincer complexes, was performed by the Diffuse Reflectance Infrared Fourier Technique (DRIFT) on a Mattson Instruments Galaxy Series FTIR 5000 spectrometer with SPECAC diffuse-reflectance assembly. Spectra were measured of the dried grinded samples in KBr. For comparison, uncoated particles were used as blank. In addition, the Pt and Pd content of the particles was determined by elemental analysis. Silica particles that were coated with Pt-S were exposed to SO_2 (g), since the NCN-Pt-pincer complexes are known to reversibly bind this gas [10,11]. The adduct thus formed has a bright orange colour whereas the SO_2-free complexes are colourless.

3.4.1. Use of colloidal maghemite support

Because surfactants with acidic end-groups (e.g. oleic acid or dodecanoic acid) were found to covalently link to maghemite [12], the acid-functionalized pincer complexes were also expected to attach to our maghemite particles. We always used (non-catalytic) Pt-A, because the corresponding Pd compound was not available. For our attempts to coat maghemite particles we used the following three different methods:

1. FFaq (0.5 ml) and Pt-A (0.075 g, 0.14 mmol) dissolved in a small amount of 1a. dimethylsulfoxide (DMSO) or 1b. dimethylformamide (DMF) were mixed thoroughly.
2. The same method as for coating maghemite with oleic acid (see paragraph 3.1) was used, but instead of oleic acid, a solution of Pt-A (0.18 g, 0.34 mmol) in a small amount of 2a. chloroform or 2b. dichloromethane was added to the aqueous ferrofluid.

3. FFch (coated with oleic acid, diluted) was mixed with Pt-A dissolved in a small amount of dichloromethane and stirred for a few days. We presumed that in this way the oleic acid might (partly) exchange for the catalyst. This experiment was repeated 4 times (experiments 3a-d). The amounts of reagents used are summarized in table 1.

Table 1. Coating of maghemite particles in dichloromethane.

Experiment number	Amount of FFch (ml)	Particle concentration of FFch (gl^{-1})	Amount of Pt-A		Ratio catalyst/colloids (mmol/g)
			(g)	(mmol)	
3a	1	3.4	0.1	0.187	55.0
3b	0.5	3.4	0.075	0.140	82.4
3c	1.5	5.0	0.17	0.317	42.3
3d	27	7.4	0.216	0.403	2.02

3.4.2. Use of colloidal (magnetic) silica support

For making catalytic magnetic silica particles, three different methods were studied. Dispersion S1 and S2 of *non-magnetic* silica particles that were available in large quantities were used for exploration. The experiments are summarized in table 5 (results section).

Method 1 was similar to that used for coating silica particles with another silane coupling agent (3-methacryloxypropyltrimethoxysilane, TPM) [5] as also described in the background section 2. Two samples were prepared, one by addition of solid Pd-S (89 mg, 0.149 mmol) to dispersion S1 (60 ml) and one by addition of solid Pt-S (86 mg, 0.126 mmol) to dispersion S2 (60 ml). Both samples were stirred for respectively 3 days and 1 day. Finally, Pd-S (61 mg, 0.102 mmol) dissolved in 20 ml ethanol was added to 20 ml *magnetic* silica (MS, 7.8 gl^{-1}) and stirred for 5 days.

Method 2 was another grafting method in dry toluene, used earlier for coating silica with silane coupling agents [25]. In this method, the catalyst was protected from moisture, because earlier it was found to polymerise on reaction with water (during storage for a few weeks). The experiment was performed as follows: dried silica particles from dispersion S1 (1 g) were pre-treated by heating at 100 ˚C under vacuum for 2 hours. After allowing it to cool to room temperature, a solution of Pd-S (0.2 mmol) in dry toluene (100 ml) was introduced. The resulting mixture was stirred to form a suspension and refluxed for 24 h, after which the silica was allowed to settle and the supernatant liquid was decanted. The silica was then subjected to Soxhlet extraction using dichloromethane for 16 h. Finally, it was dried under vacuum.

Method 3 is an attempt to build the catalytic groups directly into the silica particles, following ref [27] where this strategy is used for other silane coupling agents. The colloids synthesised in this way would probably (if porous enough for the reactants to reach the catalyst) contain more catalytic sites than particles that were only *grafted* with catalyst. In

addition, these so-called sol-gel materials [28,29] were earlier found to suffer less from leaching of functional groups [30,31]. The following procedure was used: Pd-S (95 mg, 0.16 mmol) was added to a mixture of ethanol (68 ml) and 25 % NH_3 (7.25 ml). While stirring, freshly distilled TES (3.34 ml, 15 mmol) was added. After 10 minutes, the solution became turbid due to formation of silica. Stirring continued for a few hours. The silica consisted of very large aggregates, since the silica settled down as soon as stirring was stopped.

3.5. Testing catalytic activity

The colloidal samples treated with Pd-catalyst were tested for catalytic activity using an aldol condensation reaction between methyl isocyanoacetate and benzaldehyde to form oxazolines [6,7] (figure 7) for which the catalyst is known to be active. The catalytic experiments were carried out using *i*Pr_2EtN (Hunig's base, 10 mol%) as a base, coated (magnetic) silica as catalyst, and methyl isocyanoacetate and benzaldehyde in dichloromethane at room temperature. For the used amounts is referred to table 6 (results section). The reaction progress was monitored by means of GC analysis of benzaldehyde using pentadecane as internal standard (using a Perkin Elmer Autosystem XL GC with a 30 m PE-17 capillary column and FID detector). After each run, the complete reaction mixture was centrifuged and the supernatant was separated. The remainders were washed with dichloromethane (2 x 20 ml) and dried under vacuum. The solid obtained was used for the next run.

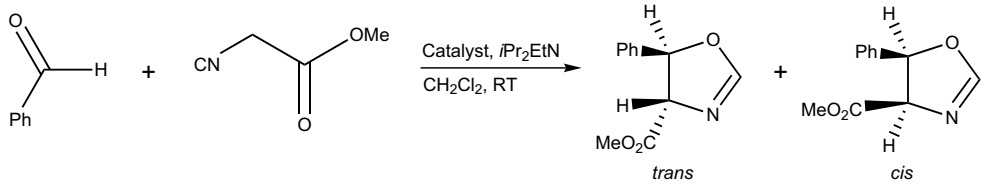

Figure 7. Aldol reaction between benzaldehyde and methyl isocyanoacetate, catalysed by Pd-pincer complexes.

3.6. High Gradient Magnetic Separation

A schematic presentation of the High Gradient Magnetic Separation set-up is shown in figure 4. The set-up consists of a glass reservoir, filled with magnetizable wires (Aluchrom I (74 % Fe, 20 % Cr, 5 % Al), ∅ 0.40 mm, Thyssen Krupp VDM, The Netherlands) cut into pieces with an approximate length of 3 cm. The reservoir is connected to a tube that is attached to a peristaltic pump. The wires are resistant against corrosion and have a high saturation magnetization (1.03 T) and low coercivity (15 A/cm), necessary to achieve a high field gradient and to avoid significant permanent magnetization after switching off the field. The tube (Omnilabo, Viton, inner/outer diameter 8/12 mm) is resistant against organic solvents, but still flexible enough for use in a peristaltic pump. The set-up was filled with ferrofluid from the top and placed between the poles of a strong electromagnet, which produced a homogeneous magnetic field (max. 2 T) over the complete area in which the set-

up was placed. When the field was on, and part of the particles were trapped by the magnetizable wires, the remaining solvent could be removed via the tap. After turning off the field and adding fresh solvent, the trapped particles were released from the wires and collected. Three separation experiments with different (non-catalytic) particles (FFaq, MS and FFbi) were performed.

In the first experiment 50 ml FFaq was added to the HGMS set-up and pumped around. Approximately 30 minutes after the field had been turned on (~ 2 Tesla), the circulating solvent had a less brownish colour than before (see figure 8), although it was certainly not colourless. A small sample of the solvent (containing non-trapped particles) was removed (fraction FFaq1) after which the field was turned off. The remaining ferrofluid was pumped around for 30 minutes to release the trapped particles and then collected via the tap (fraction FFaq2).

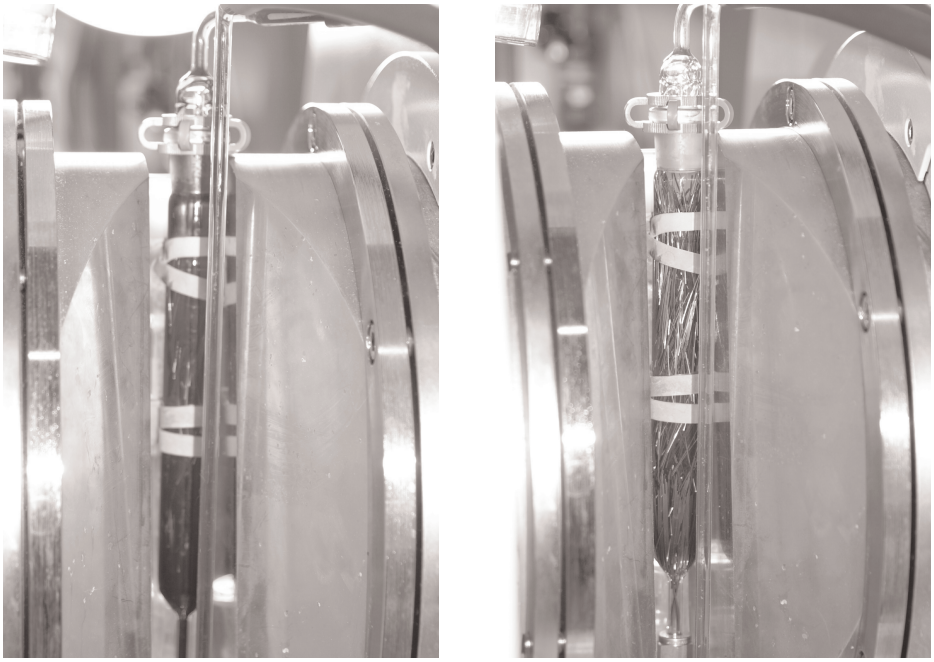

Figure 8. Colour change of maghemite ferrofluid in HGMS experiment 1. Photographs were taken before (left) and after (right) switching on the field. The length of the reservoir is about 11 cm.

In the second experiment 50 ml of dispersion MS was added to the HGMS set-up and the field was switched on (~ 2 T). After three hours, all circulating solvent (including non-trapped particles) was removed (fraction MS1). The set-up was thoroughly flushed with fresh solvent, which was collected as fraction MS2. After turning off the field, it was found that the trapped particles were aggregated and it was necessary to remove the wires and rinse them with fresh solvent to collect all particles in fraction MS3. The particles in this fraction

were redispersed by ultrasonification, the liquid was concentrated to 50 ml and added to the cleaned HGMS set-up for a second time. The field was switched on again (2 T) and this time the ferrofluid was pumped around for a shorter period (40 minutes). The almost colourless solvent was removed (fraction MS4), after which the field was turned off, fresh solvent was added and pumped around for another 30 minutes and finally collected as fraction MS5.

In the third experiment 50 ml of dispersion FFbi was added to the HGMS set-up, after which the field was switched on (2 T) and the ferrofluid was pumped around. All solvent was collected after 50 minutes as fraction FFbi1. After turning off the field, the wires were flushed two times by adding extra solvent and pumping for 20 minutes. These fractions were collected together as fraction FFbi2.

For all experiments, the amount of particles in the ferrofluids that were added to the set-up and in the different fractions, was determined by measuring the volume (by weighing) and concentration (from the weight after drying). In addition, samples were studied using TEM. Particle sizes were measured using analySIS Pro.

4. Results and Discussion

4.1. Synthesis and characterization of (magnetic) colloidal dispersions

Three dark brown ferrofluids FFaq, FFch and FFbi were obtained, as well as two white silica dispersions coded S2 and S1 and a yellowish magnetic silica dispersion MS containing one or more maghemite cores per silica particle. All dispersions were visually stable, and no permanent aggregates were observed on TEM micrographs. Magnetization measurements on dispersions FFaq and FFbi showed Langevin behaviour and resulted in a particle size corresponding to those of single particles (in case of FFbi an average of the two components), indicating that the colloids were superparamagnetic single dipoles. The concentration and particle sizes of all dispersions are presented in table 2.

Table 2. Properties of colloidal dispersions.

Dispersion code	Concentration (gl^{-1})	a_{TEM} (nm)	a_M (nm)
FFaq	22.04	5.3 ± 3.7	5.5
FFch	7.40	5.3 ± 3.7	5.5
S1	6.66	~ 45	-
S2	4.38	~ 70	-
MS	7.80	~ 40	-
FFbi	7.05	9.7 ±1.1 (fraction of large particles) 3.9 ± 0.7 (fraction of small particles)	4.39 (average)

4.2. Improvement of synthesis procedure for magnetic silica particles

It appeared that increasing the concentration of maghemite cores in the ethanol/ammonia mixture (5 times) for making magnetic silica resulted in dispersions that sedimented within a few hours, after which they could not be used for coating with silica. It was possible to immediately (before sedimentation) coat the non-dialyzed particles with silica, resulting in a visually stable magnetic silica dispersion. However, transmission electron microscopy showed the presence of many aggregates of magnetic silica particles. When dispersion FFaq was first dialyzed after coating with citric acid, visually stable dispersions of the maghemite cores in the ethanol/ammonia mixture were obtained. Probably, removal of free citric acid by dialysis increases the thickness of the electrical double layer, resulting in a more stable dispersion. Coating dialyzed maghemite particles with silica resulted in a stable dispersion, in which only a small amount of aggregates was observed with electron microscopy. Similar results were obtained for a concentration that was 20 times higher than in the original procedure. Thus, although optimisation of the procedure is necessary to obtain completely stable dispersions, dialyzing maghemite before coating with TES seems to be a suitable method for increasing the stability of magnetic silica dispersions.

Adding less TES for coating maghemite indeed resulted in magnetic silica particles with a thinner silica shell, but the particle shape was less well-defined. Whereas spherical particles with a thick shell (particle size approximately 40 nm) were formed when the original procedure was used, elongated worm-like clusters with much thinner silica shells were observed when adding less TES. Particles became increasingly less spherical upon decreasing the amount of added TES. It is not clear if this particle shape is formed immediately, or that smaller spherical silica particles grow together in a later stage. However, it appeared possible to grow the particles further by adding extra TES, resulting in a dispersion of spherical particles similar to that obtained by following the original method.

Because the procedures described above for improving the synthesis of magnetic silica particles are not yet optimal, we did not further use them for making catalytic magnetic particles at this stage.

4.3. Synthesis of Catalysts

The synthesis of the NCN-carbamate pincer complexes (Pd-S and Pt-S) from the compound as in figure 6 resulted in yellowish solids in more than 90% yield. The formation of the complex as in figure 1 was confirmed by X-ray and NMR analysis [25]. The yield of the synthesis of the acid-functionalized pincer complex was a white solid (2.57 g; 80 %). X-ray analysis and NMR spectra confirmed the formation of the acid-functionalized pincer complex as in figure 2 (see appendix 1). It must be noted that the Pd-centre is the catalytic active site and Pt-complexes are not catalytically active. Of the acid-functionalized compound only the platinum complex was prepared, but no major problems are foreseen in the preparation of the corresponding palladium complex.

4.4. Synthesis and Characterization of Catalytic Colloids

4.4.1. Using colloidal maghemite support

From coating reactions in aqueous ferrofluids using DMSO or DMF (method 1a and 1b) instable dispersions were obtained; one attempt using DMSO even resulted in gelation of the dispersion. A DRIFT spectrum of particles obtained via method 1b (using DMF) showed no significant difference between the particles before and after the coating procedure. The method of extraction by chloroform or dichloromethane (method 2) could not be used to coat maghemite particles with catalyst, since particles were not transferred to the organic phase on stirring, as usually happens when using oleic acid.

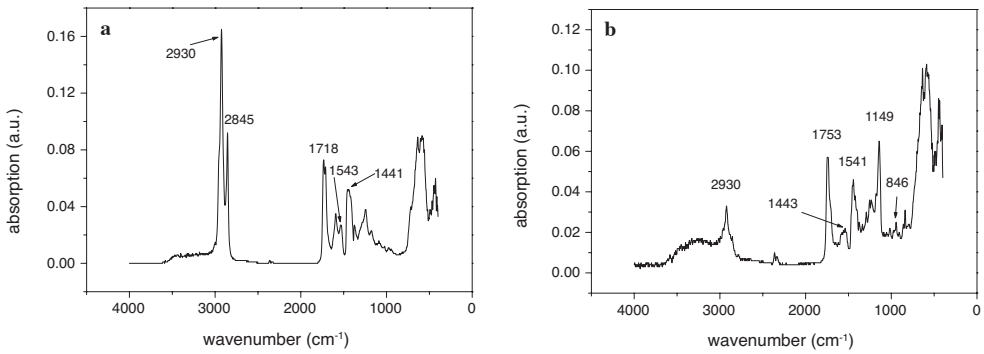

Figure 9. DRIFT spectra of oleic-acid-coated maghemite particles (**a**) and maghemite particles coated with Pt-A from experiment 3b (**b**).

The method of adding the catalyst in dichloromethane to FFch (method 3) gave irreproducible results. Whereas in most cases unstable dispersions were obtained (either immediately or after one day), a stable dispersion was obtained once (experiment 3b). In this case the DRIFT spectrum (figure 9b) of coated particles showed peaks corresponding to C=O and C-O stretch vibrations of esters (1753 and 1149 cm^{-1} respectively) present in the catalyst molecules, as well as a decrease of CH_2 (~ 2930 cm^{-1}) vibrations in comparison to the non-catalytic particles, since the catalyst is a shorter carbon chain than oleic acid. The spectrum of the particles before coating with catalyst (coated with oleic acid, figure 9a) showed the presence of peaks in the area 1300-1600 cm^{-1}, presumably corresponding to the symmetric and asymmetric stretching of carboxylate groups, indicating that a condensation reaction has occurred between the hydroxylated maghemite surface and oleic acid, like it was found by other authors [12].The exact positions of these peaks and the spacing between them, depends on the way the carboxylate molecules are bound to the maghemite substrate (e.g. mondentate (via one oxygen atom), bidentate (via both oxygen atoms to different iron atoms) or bidentate chelating (via both oxygen atoms to the same iron atom)) [32]. For our particles, the bonds with surfactant molecules presumably consist of a mixture of the cases

described above, resulting in several peaks in the 1300-1600 cm^{-1} area. Unlike in reference [12] in our case a significant peak at 1718 cm^{-1} corresponding to C=O stretching showed that part of the oleic acid was not bonded via carboxylate groups. The presence of free oleic acid is not very probable, since the washing procedures to remove free surfactant were very thorough. In addition, free oleic acid would also show characteristic vibrations of acid dimers connected via H-bonds at 3000-2500 cm^{-1} [33], which were indeed seen in our spectra of free oleic acid, but not in the spectrum of oleic-acid-coated particles. It is not clear what caused the appearance of C=O stretching in the spectrum of our particles, probably it is due to physical adsorption of oleic acid on the particle surface. Similar peaks as for oleic-acid –coated particles in the 1300-1600 cm^{-1} area, corresponding to symmetric and asymmetric stretching of carboxylate groups were found in the spectrum of particles coated with catalyst as well (figure 9b), suggesting that Pt-A was also linked to the particles via carboxylate groups. Assignment of the peaks is summarized in table 3, where also the assignment of peaks found in spectra of ungrafted catalyst and oleic acid are given. The result of experiment 3b suggests that oleic acid is exchanged for Pt-A. However, in another case (experiment 3d) no significant difference between the DRIFT spectra before and after treatment with catalyst was shown, although elemental analysis did show the presence of Pt after coating. The results are summarized in table 4.

Table 3. Assignments of DRIFT peaks for coating experiment 3b of maghemite particles.

	CH-stretch	Carboxylate ion (CO_2^-) asymmetric symmetric	C=O stretch (carboxylic acids)	C-H out of plane deformation (aromatic compounds)	C=O stretch C-O stretch (esters)
Maghemite particles after coating with catalyst	2930	1300-1600	-	846	1753 1149
Maghemite particles before coating with catalyst	2930, 2854	1300-1600	1718	-	-
Free catalyst	2921	-	1700	843	1762 1147
Free oleic acid	2925, 2855	-	1718	-	-
Literature value [38]	2845-2975	1574 1435 + shifts depending on bonds and substrate [32]	1725-1700	900-860	1800-1770 1200-1170

Table 4. Results of coating experiments of maghemite particles.

Experiment number	Stability	DRIFT	Amount of Pt (mg/kg)
3a	instable (immediately)	not measured	not measured
3b	stable	presence of catalyst	not measured
3c	instable (after 1 day)	not measured	not measured
3d	instable (immediately)	no difference	5449 mg/kg

From these experiments we can conclude that Pt-A presumably is present on our maghemite particles. However, it is not clear how the catalyst is attached on the surface (e.g. covalently bonded or physically adsorbed), since on this aspect the results were difficult to reproduce. It must be noted that the washing procedures were very thorough, which indicates that the catalyst was attached strongly. Presumably, the dispersion is only marginally stable since Pt-A has a shorter chain than oleic acid (C_{18}), and can be destabilized very easily, resulting in ambiguous results concerning stability. Since particles were not coated with Pd-A, no catalytic tests could be performed.

4.4.2. Using colloidal (magnetic) silica support

Grafting silica particles and magnetic silica particles with catalyst was successful, although also resulting in unstable dispersions. The experiments are summarized in table 5. Pt or Pd were always detected by elemental analysis (see table 5) for both grafting methods 1 and 2 (in ethanol and dry toluene respectively) and for the sol-gel method 3. The presence of the Pt-catalyst on non-magnetic silica particles (experiment 2) could also be demonstrated by orange colouring of the sample upon exposure to SO_2 (g), while after thoroughly washing, the supernatant did not colour, indicating that no free catalyst was present anymore. This experiment also shows the integrity of the Pt-pincer complex, since the coloration reaction only occurs for intact pincer complexes (with C-Pt bond, two N-Pt bonds and a Pt-halide bond) [10]. For magnetic silica, this experiment was not useful, since the particles themselves already had a brownish colour. The DRIFT spectra of coated and uncoated silica particles (experiment 1) were very similar, but after subtraction the difference spectrum clearly showed the presence of the carbonyl group at 1730 cm^{-1}. No clear presence of peaks corresponding to C-H stretching are present, probably because bare Stöber silica particles show a large contribution in this area already.

Unlike in coating reactions with other silane coupling agents [5], adding the catalyst always caused the silica particles to aggregate instantaneously. The particles were also not stable in toluene and other organic solvents like dichloromethane, chloroform and cyclohexane. Particles could not be redispersed by washing away free catalyst, indicating irreversible aggregation. Possibly, the attraction between particles was caused by depletion effects of the catalyst molecules, or by a preferable affinity of the catalyst tails for the silica surface (via hydrogen bonds to the halide atom, as found for other similar compounds

[34,35]) instead of the solvent. A test, in which some Pd-S was dissolved in an ethanol/water mixture and left undisturbed for a few weeks, did not show any sign of scattering that would point to the presence of large silicates, formed by polymerisation. This indicates that Pd-S is not very sensitive to moisture and protecting the catalyst against water, as in grafting method 2, presumably is not necessary.

Table 5. Summary of coating experiments of (magnetic) silica particles.

Experiment number	Short description	Concentration of Pd/Pt from elemental analysis (mg/kg)
1	S1, Pd-S, method 1	3730
2	S2, Pt-S, method 1	331
3	MS, Pd-S, method 1	8639
4	S1, Pd-S, method 2	4100
5	MS, Pd-S, method 2	unknown
6	Sol-gel, Pd-S, method 3	7800

Elemental analysis showed significantly different amounts of Pt or Pd per kg of silica for the various experiments. Although the difference in particle sizes can explain part of the discrepancy (for larger particles the surface-to-volume ratio is smaller) another reason presumably is the different stirring time. Whereas for experiment 1 and 3 the reaction proceeded for respectively 3 and 5 days, this was only 1 day for experiment 2. Probably, the reaction between the catalyst and silica particles is rather slow and the grafting density can be improved by running it for longer times. Grafting via method 2 results in a similar grafting density as with method 1 (experiment 1), but is faster (24 hours instead of a few days). However, method 1 is less laborious and there is no need to use high temperatures. Method 3, where the catalyst was incorporated in silica particles resulted in an instable dispersion, where very large silica aggregates were formed that sedimented within a few minutes. The amount of catalyst per gram of silica for the sol-gel dispersion is approximately equal to the particles grafted in 5 days in experiment 3.

4.5. Testing Catalytic Activity

The catalytic activity (percentage conversion) for the different catalytic particles in consecutive runs is indicated in table 6. The time in hours that the reaction was allowed to proceed for each run is indicated in brackets. For comparison, also the results from commercial silica particles (kindly provided by Engelhard de Meern BV, and coded CS1 and CS2) of different sizes (0.5-1.5 mm and 60 μm diameter respectively) and pore diameters (15 and 50 nm diameter respectively) are presented. The table shows the amounts of silica and reactants used in the catalytic tests, as well as the relative amount of Pd. For clarity, the amounts of Pd found from elemental analysis are also indicated. From these numbers is seen that all coated particles were active, which again proves that the catalyst is present on our

colloids; the aldol reaction in the presence of non-coated particles was found to proceed extremely slow. The catalyst was found to be stable under the reaction conditions and did not release from the particle surface [25]. In general, the absolute activity (in the first run) of the Stöber silica particles (experiments 1,3,4,6) is lower than for commercial silica (experiments CS1 and CS2), very likely because the amount of catalyst available per gram of silica is less (note here that the amount of reactants compared to the amount of colloids differ for the various experiments, see column 5).

Table 6. Results of catalytic runs.

Particles from experiment	Amount of coated silica (mg)	Amount of Pd per amount of silica from elemental analysis (mg/kg)	Amount of BA[1], MI[2] (mmol)	Mole % Pd (relative to BA, MI)	run 1[3]	run 2[3]	run 3	Decrease of catalytic activity (%) of run 2 compared to run 1
1	250	3730	0.175	5.0	47(5)	-	-	-
3	71	8639	1.6	0.4	31(20)	-	-	-
4	250	4100	1.6	0.6	30(21)	22(23)	-	27
6	260	7800	1.6	1.2	17(18)	13(21)	-	24
CS1	250	16300	1.6	2.4	55(5)	25(5)	20(5)	55
CS2	250	9400	1.6	1.4	45(5)	10(5)	10(5)	88

[1]Benzaldehyde (figure 7). [2]Methyl isocyanoacetate (figure 7). [3]% conversion of benzaldehyde as determined from GC, the number of hours that the reaction was allowed to proceed is indicated in brackets.

Although the size of Stöber silica particles is smaller than those of the commercial particles, in principle resulting in a much larger surface area per gram of silica, it was found from BET-measurements (nitrogen adsorption) that the commercial silica is very porous (215 m^2/g silica for CS1 particles, a much higher value than expected for compact spheres), while the Stöber silica is rather compact, as known from other BET-measurements [4] where the surface area was found to be of the order of the area assuming spheres of density 1.6 g/ml without pores. The grafting density of catalyst on our Stöber silica (0.5-1 molecules per nm^2), calculated from the amount of Pd or Pt found by elemental analysis, the average particle radius and the density of Stöber silica (1.6 g/ml) assuming compact spherical particles, is similar to that of CS1 particles (0.43 molecules/nm^2, using 16300 mg Pd/kg and the surface area of 215 m^2/g). These grafting densities are somewhat lower than the value of about 2.8 molecules per nm^2 found for coating Stöber silica particles by similar silane coupling agents containing nickel [36] and much lower than the value of 10 molecules/nm^2 found for Stöber silica coated with other silane coupling agents [5].

For all dispersions, the catalytic activity decreased gradually after each run. The reason for this decline is not yet clear and is discussed in reference [25]. Note that the decrease in catalytic activity for Stöber silica (experiment 4) seems to be much smaller than for commercial silica, although more experiments should be performed to investigate this further. The catalytic activity of the instable silica particles resulting from the sol-gel method (experiment 6) is rather low in comparison with the grafted particles, probably because the catalyst incorporated in the particles cannot be reached by the reactants due to a low porosity (the surface obtained from BET-measurements was only 24 m^2/g). However, also in this case the decrease in catalytic activity on recycling seems to be less than for commercial silica. For performing catalysis as efficient as possible, catalytic particles that are stable in the solvent would be recommendable, since the surface catalytic molecules at the particle surface will be more accessible for reactants. Of course, in this case more advanced separation methods (e.g. HGMS) will be needed to separate the particles for a next run (which for instable dispersions simply can be achieved by sedimentation).

4.6. High Gradient Magnetic Separation

For all separation experiments, 30 minutes after turning on the field, the flowing dispersion showed a less intense colour in comparison with the originally added dispersion (for an example see figure 8), indicating that part of the colloids were caught by the magnetizable wires in the HGMS set-up. The results are presented in table 7. For FFaq, about two thirds of the particles in the original dispersion (12.9 gl^{-1} ± 10%) could be trapped (particle concentration in fraction FFaq1 was 3.7 gl^{-1}). The average particle size of non-trapped particles (fraction FFaq1) was significantly smaller (3.7 ± 2.4 nm) than in the original dispersion (5.3 ± 3.7 nm). After turning off the field and pumping for about 30 minutes again, the original dispersion was recovered (FFaq2: concentration 14.0 gl^{-1} ± 10%, average particle size 5.2 ± 3.5 nm).

Table 7. Results from HGMS experiments.

Fraction	Amount of particles (mg)	a_{TEM} (nm)
FFaq (original)	Concentration: 12.9 gl^{-1}	5.3 ± 3.7
FFaq1 (small sample of non-trapped particles)	Concentration: 3.7 gl^{-1}	3.7 ± 2.4
FFaq2 (removed after experiment finished)	Concentration: 14.0 gl^{-1}	5.2 ± 3.5
MS (input first run)	342	–
MS1 (non-trapped particles first run)	221	–
MS2 (collected after flushing set-up)	6	–
MS3 (aggregated particles first run)	112	–
MS3 (input second experiment)	91	–
MS4 (non-trapped particles second run)	2.4	–
MS5 (trapped particles second run)	84	–

Also for dispersion MS, only part of the colloids were trapped by the wires (112 mg of the 342 mg (in 50 ml solvent) that was added, see table 7). However, when this part was again used for separation in a new experiment, 84.0 mg of the 90.8 mg added could be separated (fraction MS5), and only 2.4 mg was removed in fraction MS4 by flushing with the magnetic field on. It has to be noted that determination of the concentration by weighing is not so accurate; due to the small amounts the error is in the order of 10%.

Figure 10 shows TEM micrographs of different fractions of dispersion MS in a separate separation experiment. Here it is seen that in the original dispersion (left), the average amount of maghemite cores per silica particle is larger than in the sample of non-trapped particles (middle). After turning off the field without removal of the fraction of non-trapped particles, the original dispersion is again regained (right). Thus, it appears that the particles with a larger dipole moment (due to a larger amount of magnetic cores) are preferably separated by HGMS.

Dispersion FFbi was separated in two different fractions. Fraction FFbi1 (non-trapped particles) mainly contained small particles, although some large ones were also present. Fraction FFbi2 contained most of the large particles, but a significant amount of small particles was also present. From both fractions and the original dispersion a representative TEM-picture is shown in figure 11. It must be noted that the amount of small particles in fraction FFbi2 (where many empty areas are observed on the TEM grids) is much smaller than in fraction FFbi1, where the whole grid is full of small particles.

From our experiments it can be concluded that HGMS can indeed be used for magnetic separation of colloidal magnetic particles in ferrofluids. Separation can be achieved relatively quickly (30 minutes). Running a separation experiment for longer times (few hours) even seems to be undesirable, since this results in aggregation of the particles, which will presumably decrease the catalytic activity. However, from the results it is clear that particles must have a sufficiently large magnetic moment to be separated by HGMS. Both for FFaq and FFbi, the larger particles were preferentially trapped. Probably, the small particles that were trapped in fraction FFbi2 were located in between the large particles (as can e.g. also be seen in figure 11a), and were pulled to the wires and trapped along with the large particles. For dispersion MS it was found that especially the magnetic silica particles with a large amount of cores are trapped (figure 10). In addition, the particles that were trapped in the first experiment, could almost all be trapped again in the second experiment, despite the fact that the particle concentration was about three times as low as in the first run. This supports the conclusion that the magnetic moments of particles should be large enough (radius larger than ~ 3 nm for magnetite) to be trapped. We did not systematically investigate the effect of concentration on separation efficiency. From the measured amounts of trapped particles, it is clear that much more particles were captured than those needed to completely cover the wires by a monolayer. However, it is not clear if the capacity of the wires was a determining factor in our experiments.

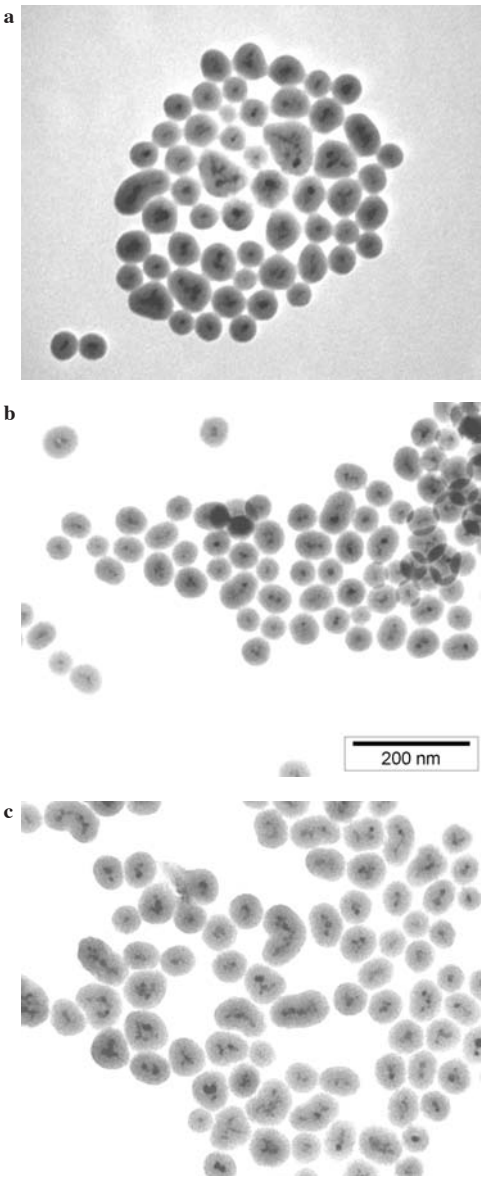

Figure 10. Dispersion MS **a** before separation, **b** non-trapped particles and **c** original dispersion after separation.

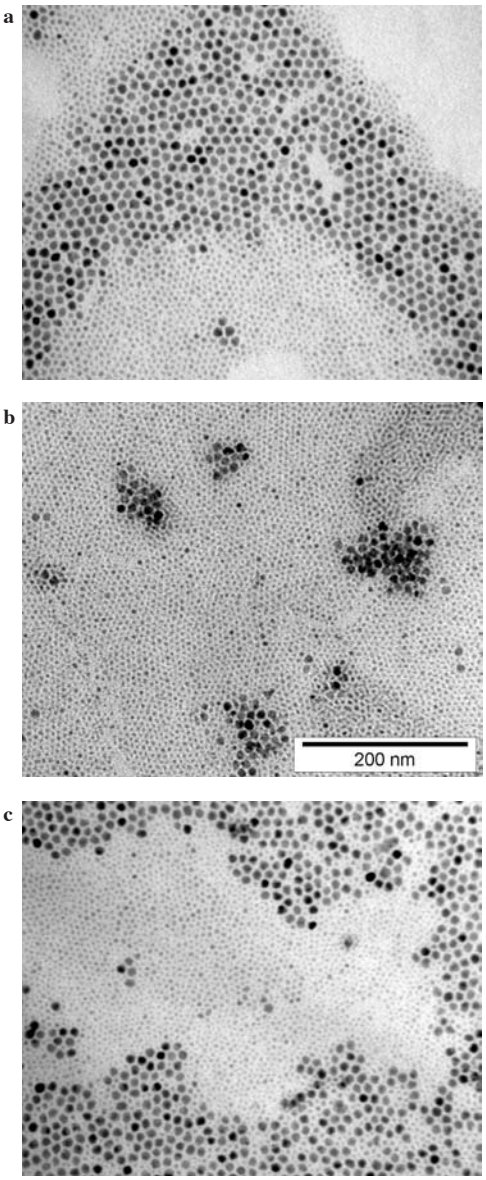

Figure 11. Dispersion Ffbi **a** original, **b** fraction FFbi1 and **c** fraction FFbi2.

It was found that almost no particles were lost in the separation procedure; the sum of the particles in different fractions was always similar (within the experimental error) to the amount of particles that was added. It seems that trapped particles are strongly attached to the wires, confirming our approximate calculation in section 2.3; flushing while the field is on only removed 3-5 % of the trapped particles.

This study shows that colloidal particles can indeed be separated by HGMS when their size is large enough. However, future experiments, varying the particle concentration of the ferrofluid, the field strength, the packing fraction and thickness of the wires are needed to optimise the separation procedure.

5. Conclusions

We synthesized magnetic silica colloids coated with NCN-pincer catalysts that were shown to be active in an aldol reaction between benzaldehyde and methyl isocyanoacetate. For both grafting methods used the presence of catalysts on the colloids was demonstrated by different techniques and the grafting density was similar (although it seems to depend on the reaction time). Both methods have their advantages; while method 1 is less laborious and is performed at room temperature, the reaction time is shorter in method 2. Unfortunately, the dispersions of coated particles were unstable in both ethanol and organic solvents, a feature that requires further study. Although the catalytic activity of our particles was lower than for commercial silica (due to the smaller available surface area per gram of silica), the decrease in catalytic activity on recycling seems to be less. The catalytic activity of the instable silica particles resulting from the sol-gel method is rather low in comparison with the grafted particles, probably because the catalyst incorporated in the particles cannot be reached by the reactants due to a low porosity. However, also in this case the loss of catalytic activity on recycling seems to be less than for commercial silica. Maghemite particles could also be coated with catalyst, but results were difficult to reproduce. The presence of catalyst on the particles was detected only once by DRIFT and the stability of particles varied for different samples.

Preliminary results showed that magnetic silica particles could be synthesized in higher concentrations when an extra dialyzing step of the maghemite dispersion was performed. In addition, magnetic particles with a thinner silica shell could be synthesized, at the expense of a well-defined shape. It was shown that different types of colloidal magnetic particles could be separated by HGMS, if their particle dipole moments were large enough. The separation of polydisperse magnetic dispersions (i.e. regarding particle size or amount of magnetic cores per silica particle) always resulted in a fractionation in particles with larger and smaller magnetic moments. However, it was shown that almost all particles of the large fraction could be separated again in a second run. Separation times should be short (~ 30 minutes) to avoid aggregation of the particles. Future experiments, in which particle concentration, field strength, packing fraction and thickness of the magnetizable wires are varied, are required to optimise the separation procedure. For more efficient catalysis, it is important to synthesize catalytic magnetic particles that are stable in the reaction mixture, since aggregation presumably reduces the catalytic activity due to the particle surfaces being less accessible for the reactants. In this case, it would be advisable to first select the larger

(separable) magnetic particles using the HGMS set-up, before coating them with catalyst.

Acknowledgements

Nilesh Mehendale and Bert Klein-Gebbink of the department of metal-mediated synthesis are thanked for various experiments, valuable discussions and for carefully reading the manuscript. Chris Bezemer (metal-mediated synthesis) is thanked for preliminary experiments at the start of this work. Paul van Gerven (metal-mediated synthesis) synthesized the acid-functionalized NCN pincer complex. Chantal Vonk is thanked for the synthesis of dispersion FFbi and for making the TEM-pictures. Natalie Zuiverloon synthesized dispersions S1 and S2. Ad Mens of the department of inorganic chemistry and catalysis performed the nitrogen physisorption measurements and their analysis. Bonny Kuipers is thanked for his help with building the HGMS set-up. The photographs of the HGMS set-up were made by Jan den Boesterd of the audiovisual service.

Editing Note

Quite recently, a paper by Moeser et al [37] was published about the use of magnetic fluids as extractants for synthetic organic compounds from wastewater. Here, 7.5 nm diameter magnetite particles were coated with a bifunctional polymer layer that has a high capacity for organic solutes. The authors used High Gradient Magnetic Separation to recover the magnetic nanoparticles from the solvent and were able to achieve a capture efficiency of 90 % for the first run. Like in our experiments, they found an increase of capture efficiency for the next runs (up to 98 %, similar to our result) since the small particles were preferentially lost in earlier runs. The main difference with our experiments is that their HGMS set-up consisted of 50 μm diameter stainless steel wires, whereas in our experiments 400 μm wires of an Fe-Cr alloy were used. Probably, higher field gradients could be obtained at the surface of these thinner wires, resulting in a higher capture efficiency in the first run than in our case.

References

[1] Stöber W, Fink A and Bohn E 1968 *J. Colloid Interface Sci.* **26** 62.
[2] Blaaderen van A, Geest van J and Vrij A 1992 *J. Colloid Interface Sci.* **154** 481.
[3] De Hek B and Vrij A 1981 *J. Colloid Interface Sci.* **79** 289.
[4] Helden van A K, Jansen J W and Vrij A 1981 *J. Colloid Interface Sci.* **81** 354.
[5] Philipse A P and Vrij A 1989 *J. Colloid Interface Sci.* **128** 121.
[6] Gorla F, Togni A and Venanzi L M 1994 *Organometallics* **13** 1607.
[7] Zhang X, Longmire J M and Shang M 1998 *Organometallics* **17** 4374.
[8] Stark M A and Richards C J 1997 *Tetrahedron Letters* **38** 5881.
[9] Stark M A, Jones G and Richards C J 2000 *Organometallics* **19** 1282.
[10] Albrecht M, Gossage R A, Spek A L and Koten van G 1998 *Chem. Comm.* 1003.
[11] Albrecht M, Lutz M, Spek A L and Koten van G 2000 *Nature* **406** 970.
[12] Ewijk van G A, Vroege G J and Philipse A P 1999 *J. Magn. Magn. Mater.* **201** 31.
[13] Gerber R 1983 *High Gradient Magnetic Separation* (Chichester: Research Studies Press).

[14] Oberteuffer J A 1974 *IEEE Trans. Magn.* **MAG-10** 223.
[15] Okada H, Tada T, Chiba A, Mitsuhashi K, Ohara T and Wada H 2002 *IEEE T Appl Supercon* **12** 967.
[16] Worl L A, Devlin D, Hill D, Padilla D and Coyne Prenger F 2001 *Separation Science and Technology* **36** 1335.
[17] Hubbuch J J and Thomas R T 2002 *Biotechnology and bioengineering* **79** 301.
[18] Rosensweig R E 1985 *Ferrohydrodynamics* (Cambridge: Cambridge University Press).
[19] Batchelor G K and Green J T 1972 *J. Fluid. Mech.* **56** 375.
[20] Batchelor G K 1967 *An Introduction to Fluid Dynamics* (Cambridge: Cambridge University Press).
[21] Jiles D 1995 *Introduction to Magnetism and Magnetic Materials* (London: Chapman & Hall).
[22] Boer de J H, Linsen B G and Osinga T J 1965 *J. Catal.* **4** 643.
[23] Massart R 1981 *IEEE Trans. Magn.* **MAG-17** 1247.
[24] Sun S and Zeng H 2002 *J. Am. Chem. Soc.* **124** 8204.
[25] Mehendale N C, Bezemer C, Klein Gebbink R J M, Walree van C A, Lutz M, Spek A L and Koten van G *in preparation.*
[26] Bergbreiter D E, Osburn P L and Liu Y 1999 *J. Am. Chem. Soc.* **121** 9531.
[27] Blaaderen van A and Vrij A 1992 *Langmuir* **8** 2921.
[28] Blum J, Avnir D and Schumann H 1999 *Chemtech* **29** 32.
[29] Wieland S and Pantser P 1994 *Catal. Org. React.* **62** 383.
[30] Lindner E, Kemmler M, Mayer H A and Weger P J 1994 *J. Am. Chem. Soc.* **116** 348.
[31] Lindner E, Schneller T, Auer F and Mayer H A 1999 *Angew. Chem., Int. Ed.* **38** 2154.
[32] Weidlein V J, Muller U and Dehnicke K 1981 *Schwingungsfrequenzen I: Hauptgruppenelemente* (Stuttgart: Georg Thieme Verlag).
[33] Hesse M, Meier H and Zeeh B 1991 *Spektroskopische Methoden in der organischen Chemie* 4 ed.(Stuttgart: Georg Thieme Verlag).
[34] Davies P J, Veldman N, Grove D M, Spek A L, Lutz B T G and Koten van G 1996 *Angew. Chem., Int. Ed.* **35** 1959.
[35] Albrecht M, Gossage R A, Lutz M, Spek A L and Koten van G 2000 *Chem. Eur. J.* **6** 1431.
[36] Pathmamanoharan C, Wijkens P, Grove D M and Philipse A P 1996 *Langmuir* **18** 4372.
[37] Moeser G D, Roach K A, Green W H, Laibinis P E and Hatton T A 2002 *Industrial and Engineering Chemistry Research* **41** 4739.
[38] Grasselli J G 1973 *CRC Atlas of spectral data and physical constants for organic compounds* (Cleveland, Ohio: CRC Press).

Appendix 1

Characterization of the acid-functionalised pincer complex *p*-OH-NCN-Pt-Cl by ^{1}H NMR, ^{13}C NMR and elemental analysis.

^{1}H NMR ($CDCl_3$, 200.13 MHz): δ 2.04 (quintet, 2H, -$CH_2CH_2CH_2$-), 2.50 (t, 2H, -$CH_2CH_2CH_2$-), 2.61 (t, 2H, -$CH_2CH_2CH_2$-), 3.06 (s, 12H, -$N(CH_3)_2$, $^{3}J_{Pt\text{-}H}$ = 37.0 Hz), 3.99 (s, 4H, -$CH_2N(CH_3)_2$, $^{3}J_{Pt\text{-}H}$ = 47.3 Hz), 6.53 (s, 2H, Ar-H)
^{13}C NMR ($CDCl_3$, 75.46 MHz): δ 19.96 (-$CH_2CH_2CH_2$-), 33.00 and 33.37 (-$CH_2CH_2CH_2$-), 54.61 (-$N(CH_3)_2$), 77.66 (-$CH_2N(CH_3)_2$), 113.01 ($ArC^{3,5}$), 142.40 (ArC^{1}), 144.06 ($ArC^{2,6}$), 147.47 (ArC^{4}), 171.98 and 178.41 (C=O)
Elemental analysis calculated for $C_{17}H_{25}ClN_2O_2Pt$: C, 37.00; H, 4.57; N, 5.08; found: C, 36.96; H, 4.68; N, 4.97 weight %.

3 Preparation and properties of colloidal iron dispersions

Abstract

We systematically study the properties of dispersions of iron-based colloids synthesized in a broad size range by thermal decomposition of ironcarbonyl using different stabilizing surfactants. The synthesis results in stable dispersions of monodomain magnetic colloids. Our particles appear to consist of an amorphous $Fe_{0.75}C_{0.25}$ alloy. Sizes of particles coated with modified polyisobutene or oleic acid can be easily controlled in the 2-10 nanometer range by varying the amounts of reactants. Extensive characterization with various techniques gives particle sizes that agree well with each other. In contrast to dispersions of small particles, which consist of single colloids, dynamic aggregates are present in dispersions of larger particles. On exposure to air, an oxide layer forms on the particle surface, consisting of a disordered Fe(III) oxide.

1. Introduction

Ferrofluids (dispersions of magnetic colloids), which have been subject of research for a long time [1,2], are widely used in industrial applications (e.g. in copying machines and printers [3]), but are also important as a model system for dipolar fluids [2,4,5]. In scientific research, magnetite (Fe_3O_4) particles have been investigated extensively, because their synthesis is convenient and well-known [6]. However, their polydispersity is large (around 25%) and the variation of particle size is limited (although very recently a different synthesis method of magnetite colloids with very low polydispersity has been described where particle sizes can be controlled well [7]). In contrast, *metallic* magnetic particles can be made quite monodisperse and in various sizes, while having the additional advantage of a larger magnetic moment compared to iron oxides [8]. Metallic iron particles can be synthesized in different ways, for example by chemical vapour deposition [9] or sonolysis [10]. A more convenient and controlled method is the thermal decomposition of metal carbonyl compounds which yields fairly spherical particles under release of carbon monoxide. Colloidal iron particles were synthesized in 1979 by Griffiths et al [11], who studied iron particles in various solvents using different stabilizing polymers and investigated the oxidation behaviour of the particles. Smith and Wychick [12] reported on the kinetics and growth mechanism of the particles. Recently, Pathmananoharan et al [13] published preliminary results on the synthesis and characterization of iron particles stabilized with modified polyisobutene (PIB) and oleic acid in decalin. They found that the size of particles grafted with polyisobutene could be controlled well, whereas this was not possible for oleic-acid-coated particles. Because van der Waals and in particular dipolar interactions between particles strongly depend on the particle radius, we expect the microstructure of the fluid (e.g. possible chain formation) and the response to magnetic fields to be sensitive to particle size. To study these size effects properly, monodisperse particles with a large saturation magnetization are needed. Therefore, we present an extensive study on iron dispersions, synthesized by thermal decomposition of ironcarbonyl, in which we systematically varied the radius of particles and studied the effect of size on the physical behaviour of magnetic fluids in a broad size range. To stabilize the particles we used two different surfactants, i.e. PIB or oleic acid. The particles were elaborately characterized by a variety of techniques, e.g. magnetization measurements, susceptibility measurements and Transmission Electron Microscopy (TEM), to study the influence of particle size. Throughout these experiments, we especially took care to prevent the dispersions from oxidation by carefully storing and handling all dispersions under dried nitrogen atmosphere. In addition, we studied the oxidation behaviour of these systems, by monitoring magnetic properties and size effects on oxidation as a function of time and comparing properties of oxidized and non-oxidized particles. A detailed Small Angle X-Ray (SAXS) study was included of both oxidized and non-oxidized particles as a function of particle size.

2. Experimental

2.1. Materials and Methods

Ironpentacarbonyl (Fluka Chemika) was taken from new bottles. Decalin (Merck), oleic acid (Merck, extra pure) and modified polyisobutene (PIB) coded SAP 285, consisting of a mixture of 2 polymers (figure 1) in a mineral base oil, (Shell Research Ltd., England), were used as supplied. The modification of polyisobutene was reported elsewhere [14]. According to the supplier, the molecular weight of the PIB is 2400 $gmol^{-1}$ and the polyisobutene/polyamine ratio is 2.0-2.5. To protect the iron particles against oxidation, all dispersions were treated and stored under dried nitrogen atmosphere, using schlenks and a glovebox with oxygen pressure lower than 12 ppm (measured by a MBraun MB-OX-SE1 active oxygen probe).

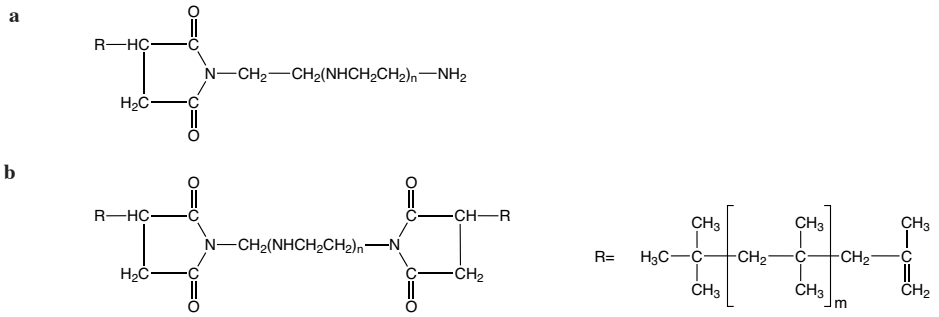

Figure 1. Structural formula of modified PIB (m = 41, n = 4). The used substance (SAP 285) is 40-50 % of a 1:1 mixture of the compounds **a** and **b** in a mineral oil.

2.2. Synthesis

Dispersions of monodisperse iron particles were synthesized by thermal decomposition of ironpentacarbonyl (a yellow liquid) in decalin in the presence of a stabilizing surfactant (PIB or oleic acid). Decalin is a good solvent for both surfactants and has a high boiling point (~190 °C), making it very suitable for the synthesis. The mechanically stirred solution was refluxed under nitrogen for 24 hours at 170˚C, using an oil bath.

The size of the colloidal particles was tuned by varying the $Fe(CO)_5$/surfactant ratio. The amounts of ironpentacarbonyl, decalin and surfactant used are presented in table 1. The final dispersions, ordered by increasing radius, are coded A to E (for PIB coated particles) and OA1 to OA3 (for oleic-acid-coated particles). Particles with a large radius (D and E) were prepared by a seeded growth method, adding additional ironpentacarbonyl in portions of approximately 15 ml to a dispersion of smaller particles (C). This method was employed, because earlier experiments where all $Fe(CO)_5$ was added at the start of the synthesis resulted in unstable dispersions. For this seeded growth the heating was stopped a few hours after the last portion had been added. Oleic-acid-coated particles could not be used for this 'seeded growth', since this resulted in instable dispersions.

Table 1. Amounts of reactants used for synthesis of iron dispersions.

Dispersion	$Fe(CO)_5$ (ml)	PIB (g)	Oleic acid (g)	decalin (ml)
A	5	17.5	-	420
B	41	17.5	-	420
C	70	17.5	-	420
D	70+56	17.5	-	420
E	70+134	17.5	-	420
OA1	7.8	-	5.6	10
OA2	44	-	4	20
OA3	50	-	2.5	60

2.3. Characterization

To check the stability of dispersions, susceptibility measurements at a low frequency (100 Hz) were performed on iron dispersions using a home-built susceptibility meter (chapter 6) that measures the local susceptibility at a certain height in a sample tube. The set-up consists of two concentric coils, one (the primary coil) connected to an alternating current (AC) supply and the other (the secondary coil) to a lock-in amplifier as AC voltmeter. The susceptibility is determined from the measured voltage change, induced by the ferrofluid, in the secondary electric coil. Samples were made in long glass tubes under nitrogen atmosphere. Details can be found in chapter 7. Transmission Electron Microscopy (TEM) photographs were made on a Philips CM10H transmission electron microscope (TEM) from particles on grids coated with a Formvar film. The grids were placed in the vacuum of the sample holder of the microscope within a few minutes after opening of a glovebox under nitrogen atmosphere, in which grids were made by dipping them in a dilute dispersion and leaving them to dry. Particle size distributions were measured using an interactive image analysis program.

Magnetization curves of the dispersions were measured at room temperature on an alternating gradient magnetometer (AGM) Micromag 2900 (Princeton Measurements Corporation) in small airtight glass cups, filled in a glovebox. Measurements were performed at the resonance frequency of the measuring probe (with attached sample), which was in the range 240-290 Hz.

For single non-interacting dipolar spheres, the magnetization M as a function of the magnetic field strength H is given by the Langevin equation [2]:

$$M(H) = M_s\left(\coth\left(\frac{\mu_0\mu H}{kT}\right) - \frac{kT}{\mu_0\mu H}\right) \qquad (1)$$

Here, M_s is the saturation magnetization of the sample, reached upon complete alignment of all particles in the field direction and $\mu = 4\pi a_M^3 m_s/3$ is the dipole moment of the spheres with a_M the magnetic particle radius and m_s the bulk saturation magnetization per volume. Further, $\mu_0 = 4\pi \times 10^{-7}$ Tm/A is the magnetic permeability in vacuum. For low fields,

equation (1) can be approximated by:

$$M(H) = \chi_i H \approx M_s \left(\frac{\mu_0 \mu H}{3kT} \right) \qquad \left(\text{for } \mu_0 \mu H << kT \right) \tag{2}$$

Curves were fitted by the Langevin equation (1), from which M_s was determined. The susceptibility χ_i was determined from the slope of separate curves measured at low magnetic fields (< 1000 Am^{-1}), since this allowed a more accurate determination of χ_i than via the whole Langevin curve (where the number of measuring points at low fields is small). Assuming a spherical particle shape, particle radii were calculated via equation (3), using the bulk value for m_s (see table 2).

$$a_M^3 = \frac{\chi_i}{M_s} \left(\frac{9kT}{4\pi\mu_0 m_s} \right) \tag{3}$$

The number of particles n in a sample was determined from $M_s = n\mu$. Knowing the sample volume and μ, the particle concentration could be determined. This small volume of samples for AGM-measurements (approximately 3 µl) was accurately determined by scaling of χ_i with the susceptibility measured on much larger, known volumes of the same dispersions, using a Kappabridge KLY-3 susceptibility meter (AGICO Corporation, Brno, Czech Republic, operating frequency of 875 Hz). For samples D and E it was known from separate measurements (see chapter 7) that the susceptibility is frequency-dependent in the range of the operating frequencies of the AGM and the Kappabridge susceptibility meter, so the volume could not be determined by calibration with the Kappabridge. In these cases, the value for n is not given here. The concentration of iron in all dispersions was determined by elemental analysis of a known amount of dispersion from which the iron particles were extracted (by flocculating them with pentanol) and dried. From both n and the iron concentration the volume fraction of iron cores was estimated, using the particle density (see table 3) and the particle TEM radius (table 2). The maximal theoretical volume fraction (table 3) was calculated from the particle mass density and the amount of ironcarbonyl used in the synthesis (table 1).

^{57}Fe-Mössbauer absorption spectroscopic measurements were performed for samples A, C and E at 4.2 K with a constant acceleration spectrometer in a triangular mode, using a ^{57}Co:Rh source (14.4 keV). Positive velocities corresponded to the source moving towards the absorber and the velocities are given relative to a calibration sample of sodium nitroprusside ($Na_2Fe(CN)_5NO.2H_2O$) at room temperature. Magnetic hyperfine fields were calibrated using α-Fe_2O_3. Measurements were carried out in a specially designed cell under nitrogen atmosphere on frozen liquid dispersions (A and E) and on a dispersion dried under nitrogen atmosphere (C) [15].

Table 2. Size of the iron particles.

Code	a_{TEM}[1](nm)	R_g[2] (nm)	a_G[3] (nm)	a_P[4] (nm)	$R_{g,OX}$[2]	$a_{P,OX}$[4] (nm)	a_M[5] (nm)	μ_{AGM}[6] (Am^2*10^{19})
A	2.1 ± 0.3	1.7 ± 0.03	2.2 ± 0.04	-	2.2 ± 0.04	2.7 ± 0.6	1.3	0.12
B	6.0 ± 0.7	4.1 ± 0.4	5.3 ± 0.5	4.6 ± 0.3	4.6 ± 0.4	5.5 ± 0.6	4.1	4.15
C	6.6 ± 1.1	4.7 ± 0.2	6.0 ± 0.3	5.4 ± 0.3	7.0 ± 1.8	6.4 ± 0.5	5.1	8.38
D	6.9 ± 1.0	6.8 ± 1.8	8.8 ± 2.4	5.4 ± 0.9	8.2 ± 2.9	6.5 ± 0.9	6.0	13.19
E	8.2 ± 1.5	7.4 ± 1.6	9.5 ± 2.1	5.9 ± 0.8	8.7 ± 3.1	7.6 ± 1.5	-	-
OA1	2.2 ± 0.3	1.5 ± 0.03	2.0 ± 0.04	2.1 ± 0.04	2.1 ± 0.04	2.8 ± 0.06	1.2	0.12
OA2	3.2 ± 0.3	2.3 ± 0.05	2.9 ± 0.06	2.9 ± 0.06	2.6 ± 0.05	3.6 ± 0.07	2.4	0.87
OA3	4.3 ± 0.3	3.0 ± 0.06	3.9 ± 0.08	3.8 ± 0.08	-	-	3.3	2.29

[1]Particle radius measured from TEM-micrographs. [2]Radius of gyration as determined from Guinier curves using equation (6). [3]Guinier radius as determined from radius of gyration using equation (7). [4]Porod radius as determined from maxima in Porod plot. [5]Magnetic radius determined from magnetization curves via equation (3). [6]Dipole moment $\mu = 4\pi a_M^3 m_s/3$ with bulk value for $Fe_{0.75}C_{0.25}$ ($m_s = 1.49*10^6$ Am^{-1} [29]). Note that the uncertainty in radii obtained from SAXS is due to the measurement method and does not reflect the polydispersity of the sample.

Table 3. Concentration of iron particles.

Code	Fe amount (Mass fraction)[1]	$Conc._{AGM}$ (particles/l)[2]	ϕ_{EA}[3]	ϕ_{AGM}[4]	$\phi_{theoretical}$[5]
A	0.004	$1.7 * 10^{19}$	0.00059	0.00066	0.00070
B	0.038	$8.0 * 10^{18}$	0.0049	0.0072	0.0057
C	0.061	$8.2 * 10^{18}$	0.0079	0.0099	0.0098
D	0.108	-	0.015	-	0.018
E	0.219	-	0.027	-	0.029
OA1	0.0824	$3.1 * 10^{20}$	0.0056	0.014	0.046
OA2	0.0587	$1.0 * 10^{21}$	0.064	0.14	0.13
OA3	0.257	$1.4 * 10^{20}$	0.045	0.047	0.049

[1]Amount of iron in dispersion from elemental analysis (g Fe/g dispersion). [2]Particle concentration determined from AGM measurements using the values for M_s, μ and sample volume. [3]Iron volume fractions using results from elemental analysis and a density for $Fe_{0.75}C_{0.25}$ of 7.58 g/cm^3 [29] . [4]Iron volume fractions using results from column 3 and the TEM-radius. [5]Maximum theoretical iron volume fraction using the amount of $Fe(CO)_5$ used in the synthesis and a density for $Fe_{0.75}C_{0.25}$ of 7.58 g/cm^3 [29].

2.4. SAXS measurements

Small-angle-X-ray scattering experiments were performed at the hard branch of the DUBBLE (Dutch-Belgian beamline) at the European Synchrotron Radiation Facility (ESRF) in Grenoble, France. The wavelength was fixed at 0.124 nm. The measured two-dimensional diffraction patterns were corrected for transmission, background radiation and detector response. All measured intensities are in arbitrary units and only have relative relevance. The measurements were performed on dilute dispersions A to E and OA1 to OA3 before and after oxidation. In this paper, the dilution factor is given in brackets directly behind the dispersion code, e.g. C(5) is dispersion C, diluted five times. Stock dispersion C

was also measured. The concentrations of the non-diluted samples are given in table 3. The suspensions were sealed in airtight glass capillaries.

The SAXS scattered intensity $I(\vec{q})$ of a suspension of N_p identical spherical colloidal particles with electron density difference $\Delta\rho^e$ relative to the solvent (also referred to as 'contrast') is given by [16]:

$$I(\vec{q}) = KN_p \left|F(\vec{q})\right|^2 S(\vec{q}) \tag{4}$$

Here, q is the momentum transfer vector, $F(\vec{q})$ the total scattering amplitude of a single particle and $S(\vec{q})$ the structure factor. K is a constant depending on the experimental set-up. For dilute suspensions of non-interacting colloidal particles the q-dependent part of the scattered intensity is only proportional to the scattering amplitude of single particles ($S(\vec{q}) = 1$). The total scattering amplitude of a homogeneous sphere with radius a is given by [16]:

$$F(\vec{q},a) = \frac{4\pi}{q^3} r_0 \Delta\rho^e \left(\sin(qa) - qa\cos(qa)\right) \tag{5}$$

with r_0 ($= e^2/mc^2 = 2.82 * 10^{-15}$ m) the Thomson radius of an electron. The radius of gyration R_g can be obtained from the scattering at low q-values ($q<2/R_g$) [16]:

$$I(q) = I(q=0)\exp(-q^2 R_g^2/3) \tag{6}$$

Plotting lnI(q) versus q^2 (Guinier plot) for small q should yield a straight line with slope $R_g^2/3$. For homogeneous spheres, the radius of gyration is related to the sphere radius a by:

$$R_g^2 = 3a^2/5 \tag{7}$$

In a so-called Porod plot the complete scattering curve is used. I(q) multiplied by q^4 is plotted versus q on a linear scale. The positions of the first maximum (q_{max}) and the first minimum (q_{min}) in this plot yield the particle radius a_P (here indicated as Porod radius) for homogeneous spheres via [17]:

$$a_P = 2.74/q_{max} = 4.49/q_{min} \tag{8}$$

Note that a_P is not equal to the radius obtained from the specific surface of the phase boundary using the Porod plot at high q-values [16]. The radius obtained from the Guinier plot and from the Porod plot should be the same for homogeneous monodisperse spheres. For polydisperse systems, the particle radius as determined from both the Guinier plot (which equals $(\langle r^8\rangle/\langle r^6\rangle)^{1/2}$ [18,19] for narrow size distributions) and the Porod plot ($= \langle r^7\rangle/\langle r^6\rangle$ [20]) should be corrected for polydispersity to obtain the number average particle radius [18,19]. Other factors, e.g. aggregation of particles could result in a difference between the Porod and Guinier radius; the Guinier plot is known to be influenced dramatically by clustering, which causes the scattering at low q-values to increase [16], while the Porod radius is not influenced significantly [16].

To obtain the experimental static structure factor over the measured q range for dispersions at a given volume fraction, the scattered intensities were divided by those of the lowest volume fraction and scaled to the concentration. The peak in the static structure factor for hard spheres corresponds roughly to the distance d_c of nearest approach between particles, given by Bragg's law [16]:

$$d_c q_{max} = 2\pi \tag{9}$$

Where q_{max} is the q value at the maximum intensity and d_c is the centre-to-centre distance at nearest approach. For a dispersion of monodisperse hard spheres, a fairly accurate description of S(q) was obtained from the Percus-Yevick [21] integral equation for the radial distribution function g(r) which could be solved analytically [22,23]. For this paper, calculations of structure factors for *polydisperse* hard spheres were performed using a computer program by van Beurten and Vrij [24] based on a closed expression for the scattering intensity of any number p of hard sphere components as derived by Vrij [25] using the Baxter [26] solution of the Percus-Yevick equation.

2.5. Oxidation behaviour

To study the oxidation behaviour of iron particles, the thickness was determined of a layer with decreased contrast visible on TEM micrographs made at different moments after exposing a TEM-grid with particles from dispersion C to air, using an interactive image analysis program. In addition, magnetic susceptibility measurements were performed with a Kappabridge KLY-3 susceptibility meter (Agico) at 875 Hz at several moments after exposing containers, filled with equal amounts of dispersion in a glovebox, to air. Because decalin has a very low vapour pressure, a correction for evaporation was not performed.

To characterize the oxide formed on the particles Mössbauer spectroscopy measurements were performed on liquid samples that had been exposed to air for one week. The formed oxide layer was also studied with transmission infrared spectroscopy on a Perkin Elmer 2000 infrared spectrofotometer (resolution 4 cm^{-1}). Spectra were measured by averaging 100 scans of a measuring cell, on which a droplet was spread of a dispersion that had been exposed to air for a few weeks. X-ray diffraction spectroscopy was performed with a Nonius Powder diffractometer on samples which were dried in air (wavelength 1.789 Å).

3. Results

3.1. Synthesis

Approximately 30 minutes after we started to heat the mixture the yellow ironpentacarbonyl solution turned either brown (dispersion A) or black (for larger particles), due to the formation of iron. Dispersions B to E, OA2 and OA3 could be manipulated by the field gradient of a small permanent magnet. Going from system A to E, the dispersion

viscosity appeared to increase as judged by the slower response to tilting of the vessel. Dispersions kept under nitrogen were stable for years (i.e. no flocs or sediment were observed). However, a few days after having been exposed to air, dispersions became unstable and the systems D and E formed a spacefilling gel, which could be turned upside down without flowing. This gel was also formed in closed containers, which had been exposed to air for a short time. When the gel was diluted, an unstable dispersion was formed, which sedimented within a few hours. The oxidation behaviour of the dispersions is further discussed in sections 3.4 and 4.4.

3.2. Characterization

For all dispersions, the susceptibility was independent of height in the sample tube, which indicates that our dispersions are stable and do not phase separate.

Figure 2 shows typical TEM-micrographs of all dispersions. The stabilizing polymer layer around the particles is invisible on these pictures. The particles do not touch each other, which is an important indication that they are not aggregated. The size of the iron cores and their standard deviation (7-18 %), measured from the micrographs, is given in table 2. It appears that oleic-acid-coated particles are less polydisperse and have a more spherical shape than PIB-coated particles, which sometimes show irregular surfaces (most clearly for dispersion C, figure 12a).

Magnetization curves (figure 3) of dispersions A to D and OA1 to OA3 did not show any hysteresis and could be properly fitted with the Langevin equation (1), indicating that the particles are monodomain and superparamagnetic. The magnetic particle radii and particle concentration determined from the measurements are given in table 2 and 3 respectively. For dispersion E the particle size could not be calculated from the magnetization curve because of its hysteresis. The maximum theoretical volume fractions and the volume fractions determined from elemental analysis are also given in table 3.

In figure 4 Mössbauer spectra are presented from dispersions A and E (measured as frozen liquids, under nitrogen atmosphere) and C (dried under nitrogen atmosphere) [15]. The spectra of particles C and E are dominated by a broadened sextuplet with H_{eff} = 262 kOe similar to that found by other authors [27,28] in sarcosyl-coated and oleic-acid-coated iron particles synthesized via similar methods. Note that here we use the unit kOe for magnetic field, which is common in the field of Mössbauer spectroscopy, instead of the SI-unit Am^{-1} (equal to $4\pi/10^3$ Oe). This hyperfine field characterizes an amorphous $Fe_{1-x}C_x$ alloy with $x \approx 0.25$ [29]. In addition, the spectrum of particles C shows a small contribution of a sextuplet with H_{eff} = 496 kOe characterizing a Fe(III) oxide [15]. This contribution is absent in the spectrum of particles E, while particles A turned out to be completely oxidic. From the spectra could be concluded that no significant amount of ironpentacarbonyl is present in the samples, because this would have caused the presence of a doublet (with isomer shift of 0.21 mm/s and quadrupole splitting of 2.49 mm/s) [30] as seen in a spectrum of a dispersion similar to OA3 (figure 5), synthesized via the same method [13].

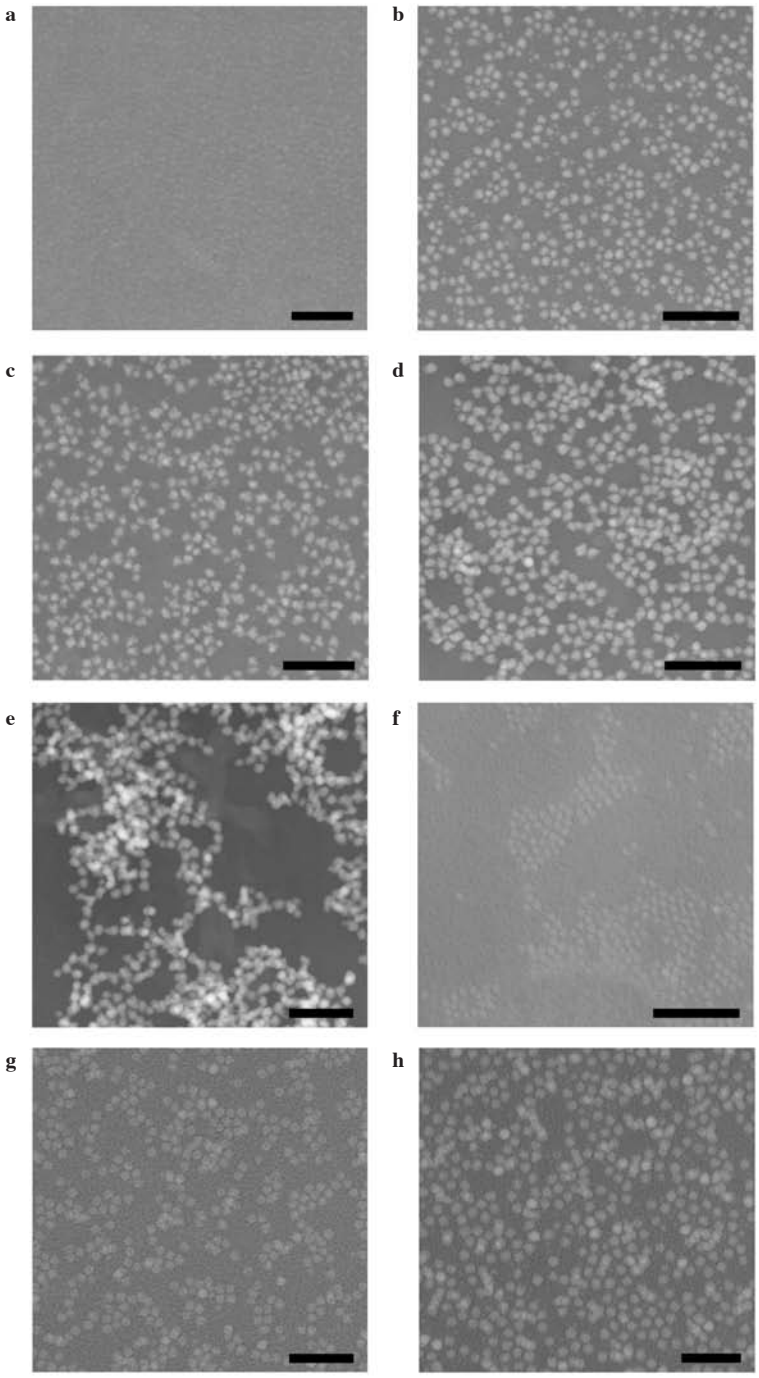

Figure 2. TEM-pictures of dispersions **a**) A, **b**) B, **c**) C, **d**) D, **e**) E, **f**) OA1, **g**) OA2, **h**) OA3. Scale bars are 50 nm (figures **a**, **f-h**) or 100 nm (figures **b-e**). Figures **a** and **f** illustrate that the sizes of the smallest particles are at the limit of the microscope resolution. However, the original micrographs are still clear enough to measure their size.

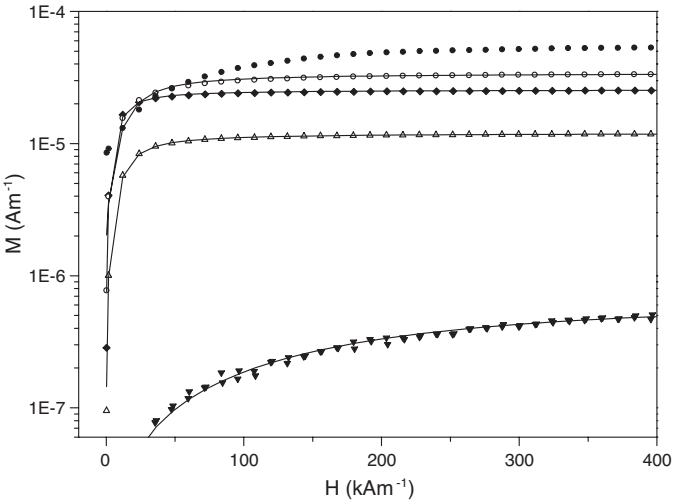

Figure 3. Magnetization curves of dispersion A (▼), B (△), C (◆), D (○), and E (●). The solid lines are Langevin fits. Dispersion E could not be fitted properly due to hysteresis at low fields. Values for χ_i were determined from separate curves measured at low magnetic fields (< 1000 Am^{-1}).

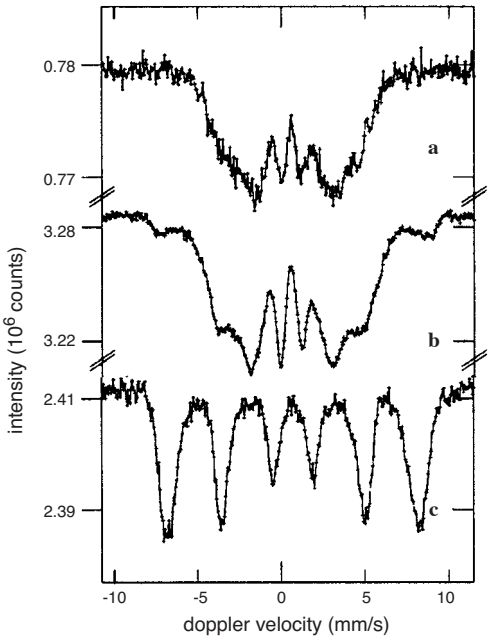

Figure 4. Mössbauer spectra measured under nitrogen atmosphere measured at 4.2 K of dispersions **a**) E, **b**) C, **c**) A.

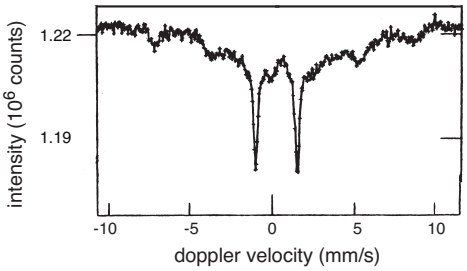

Figure 5. Mössbauer spectrum measured at 4.2 K of a dispersion similar to OA3 and synthesized via the same method. The doublet (25 % contribution to the spectrum) corresponds to the $Fe(CO)_5$, still present in the dispersion.

3.3. SAXS-measurements

As an illustrative example, figure 6 presents the scattered intensities from dispersion C for three different concentrations, divided by their concentration. Due to the large difference in electron density between the iron core of the colloidal particles and the solvent, contrary to the very small contrast of the grafted polymer layer, the scattering from the latter can be neglected. It can be observed that the two lower concentrations do not exhibit any interparticle structure, while the highest concentration shows clearly structure at low q.

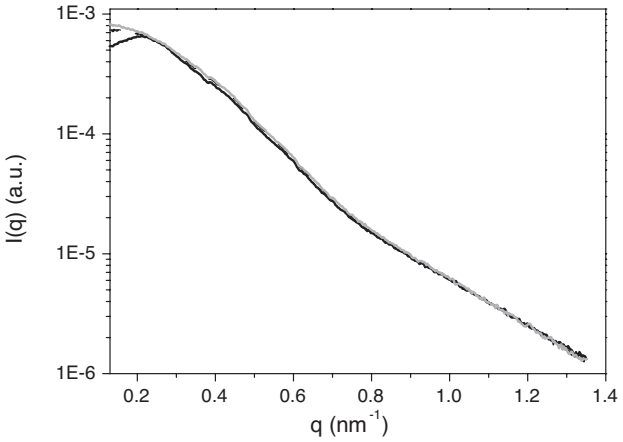

Figure 6. Scattered intensities normalized to concentration for samples C (black solid line), C(2) (black dashed line) and C(5) (grey solid line).

Figure 7 presents the Guinier plots of dispersions C(5) and D(10). The lines are the best least-square fit to the data. From the slope of this line the particle radius was calculated according to equations (6) and (7). The radii of gyration and Guinier radii for all dispersions are given in table 2. Since not all Guinier curves were perfectly linear, especially not for the larger particles (D and E), a considerable spread in the Guinier radii was found, depending on the exact part of the curve used for the Guinier fit. For particles B, although the Guinier curve was straight, resulting in a small error in the fit, a larger difference was found in the Guinier radii obtained in different measuring sessions, so that the final uncertainty in the value is significant. For the oxidized systems and dispersions D and E the Guinier plots showed a steep upturn at low q (see figure 7 for dispersion D), indicating aggregation. In these cases, the determination of the radius of gyration was even less accurate. The estimated uncertainty in the radii is indicated in table 2. Note that this uncertaintly is due to the measurement method and not due to polydispersity, the predominant cause of the spread in TEM-radii.

Figure 8 shows an example of the Porod plot of particles OA2(2) for the oxidized and the non-oxidized sample. The positions of the minima and the maxima in the Porod plots were

determined by differentiating the curves and equating the first derivative to zero. The particle radii obtained from the first maximum of the Porod plots (further indicated as Porod radii) for both the non-oxidized and oxidized particles of all dispersions are given in table 2. In some cases the peaks were rather broad, resulting in a considerable uncertainty in the radii, which is also indicated in the table.

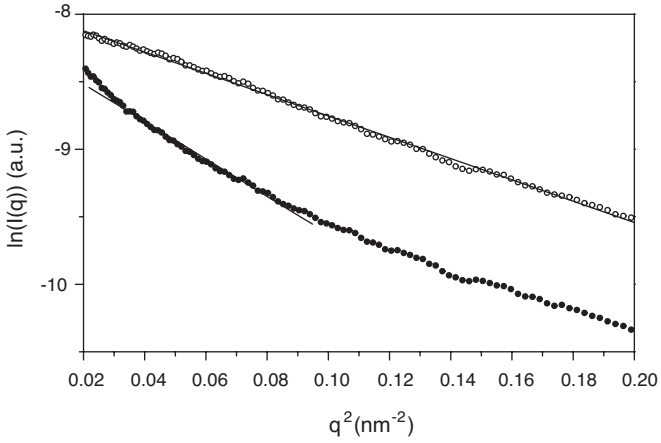

Figure 7. Guinier plot [lnI(q) vs q^2] of dispersion C(5) (○) and D(10) (●). The curve of D(10) shows a steep upturn at low q, indicating aggregation.

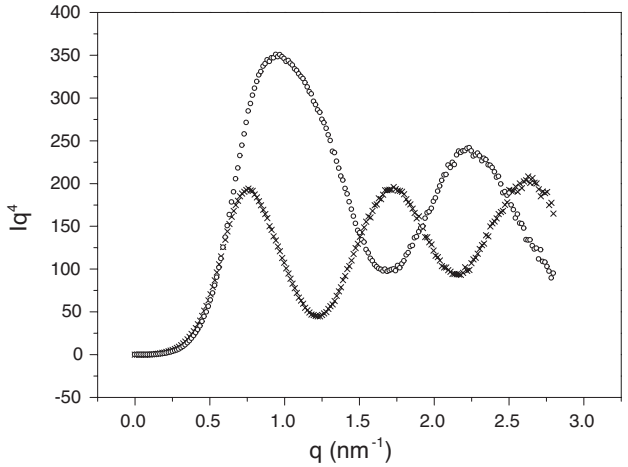

Figure 8. Porod plot [$I(q)q^4$] versus q for oxidized (x) and non-oxidized OA2(2) (○) samples. The increasing intensity with q for the oxidized sample probably is an artefact arising from problematic background correction.

Figure 9 shows the experimental static structure factor for non-oxidized particles C (samples C(2) and C, data from other samples not shown). From the position of the

maximum the closest particle distance could be estimated using equation (9). As mentioned above the grafted polymer chains are virtually matched. However, the closest interparticle distance is determined by the diameter of the whole core-shell particle. Therefore, the thickness of the polymer layer could be estimated from the position of the maximum in the structure factor as approximately 6 nm.

The curves could reasonably well be fitted with the structure factor for polydisperse hard spheres (with average core radius $<a_{core}>$ of 6.6 nm) with lognormal size distribution $P(a_{core})$ with standard deviation $\sigma = 0.35$:

$$P(a_{core}) = \frac{1}{\sqrt{2\pi\sigma^2}} \frac{1}{a_{core}} \exp\left[\frac{-\left(\ln \frac{a_{core}}{\langle a_{core} \rangle} \right)^2}{2\sigma^2} \right] \qquad (10)$$

and a surfactant layer (without scattering contrast) of 5.4 nm.

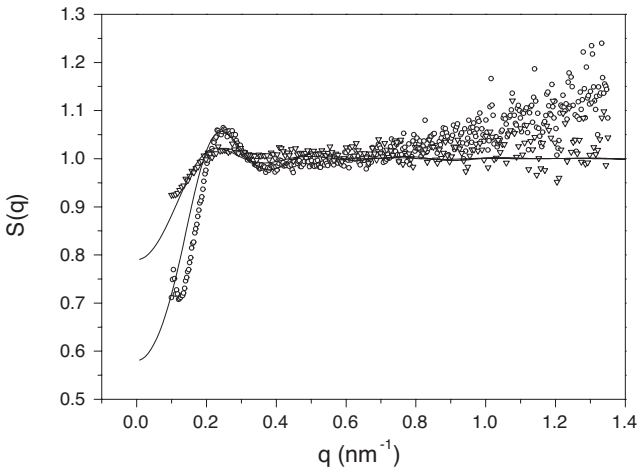

Figure 9. Static structure factor of particles C (non-oxidized) in decalin versus q for two different volume fractions (samples C(○) and C(2)(▽)). The scattered intensities have been divided by the scattered intensity of the sample with the lowest volume fraction (C(5)). Probably due to the use of cylindrical capillaries (where the path length depends on the exact position of the capillary with respect to the beam) or inaccuracies in the concentrations, the structure factors had to be corrected to achieve a value of 1 at higher q. The solid lines are the structure factors for hard spheres with a lognormal size distribution. The parameters used are a core radius a_{core} of 6.6 nm with standard deviation $\sigma = 0.35$ and a surfactant layer thickness (without contrast) of 5.4 nm. The volume fractions of the calculated curves are 0.07 and 0.03 for C and C(2) respectively.

3.4. Oxidation measurements

The decrease of susceptibility in time per gram iron after exposing the dispersions to air can be seen in figures 10 and 11. In the first few hours the susceptibility decreased fast, after

which it slowed down, though a decrease was still noticeable even after 700 hours. The curve for dispersion A is inaccurate because of the low positive values of the susceptibility (of the order of the negative susceptibility of the vessel), but the susceptibility was decreasing very fast. As expected the susceptibility was decreasing more slowly for larger particles, because their surface/volume ratio is smaller. While after 100 hours the susceptibility of dispersions A, B and C had decreased to below 10 % of the starting values, dispersions D and E still had a susceptibility of respectively 35% and 60% of the original value.

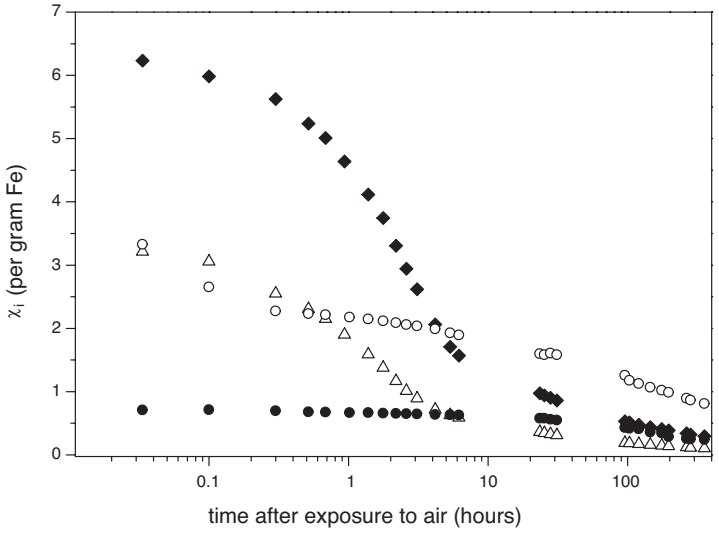

Figure 10. Decreasing susceptibility of dispersions B (△), C(◆), D (○) and E (●) in time during exposure to air.

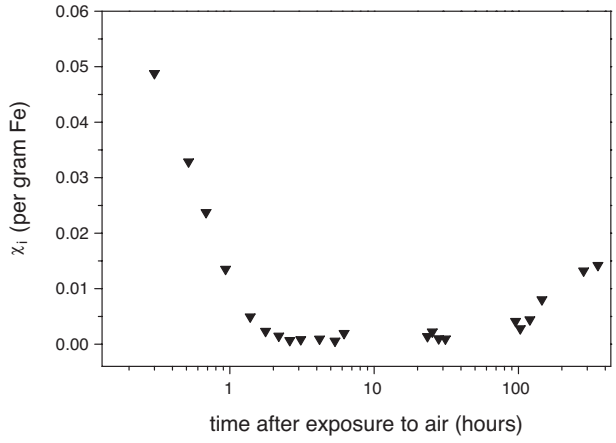

Figure 11. Decreasing susceptibility of dispersion A in time during exposure to air.

On TEM micrographs of oxidized particles a shell with a lower contrast could be observed around the iron cores, indicating an oxide layer at the surface of the particles (figure 12). It seems that this passivating oxide layer considerably slowed down the oxidation. TEM-micrographs of dispersion C, from which the grids were made under nitrogen atmosphere, showed that an oxidized layer of 2.4 nm developed in approximately 80 minutes when exposing the grid to air, while the radius of the particle had increased from 6.7 to 7.1 nm in this period. However, a non-oxidized iron core was visible even after a period of months, so the particles were not completely oxidized. From the dimensions of the iron core before and after oxidation, and the thickness of the oxidized layer after oxidation it was estimated that the volume of a certain amount of iron is becoming 1.3 times as large upon oxidation. Note that in this number, the error is rather large; an estimated error of 10 % in the sizes measured with TEM results in a standard deviation of 65 %.

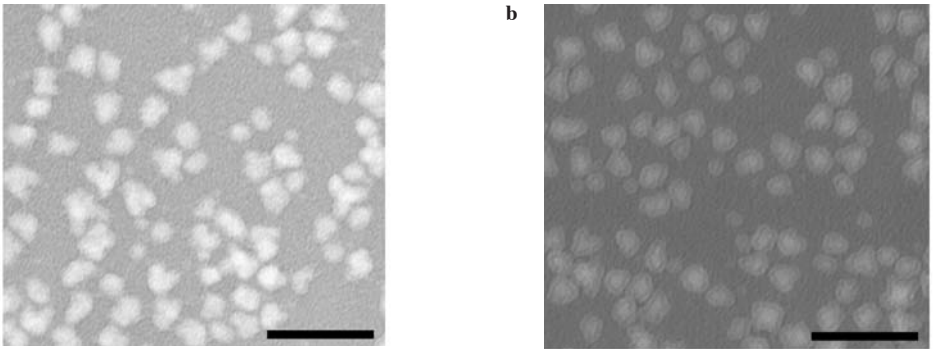

Figure 12. TEM-pictures of dispersion C. **a**) without exposure to air, **b**) after exposure of the grid to air for three weeks. Scale bars correspond to 50 nm.

The infrared spectra of oxidized particles did show several peaks, none of which were characteristic for bulk magnetite or hematite, however. Oleic-acid-coated particles exhibited peaks at 2800-3000 and 1400-1500, corresponding to alkane stretch and bending vibrations from oleic acid [31]. The peaks in the XRD-spectrum of oxidized particles C (figure 13) correspond well with a reference [32] of magnetite (table 4), although peaks are rather broad.

Table 4. XRD peaks for magnetite (Fe_3O_4) [32].

d (Å)	2θ	relative intensity	h	k	l
2.967	35.09	30	2	2	0
2.532	41.38	100	3	1	1
2.0993	50.44	20	4	0	0
1.6158	67.23	30	5	1	1
1.4845	74.11	40	4	4	0

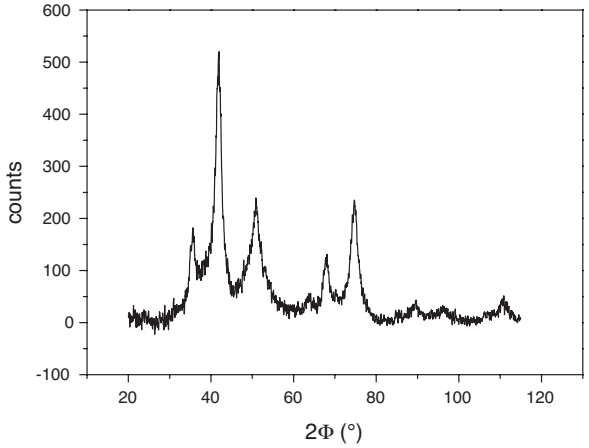

Figure 13. XRD spectrum of dispersion C after exposure to air for a few weeks.

On oxidation of particles E the Mössbauer spectra (figure 14) showed (in addition to the contribution of $Fe_{0.75}C_{0.25}$) a sextuplet with $H_{eff} \approx 470$ kOe, characterizing a disordered Fe(III) oxidic species [15]. For particles C the small contribution of Fe(III) oxide already present before exposure to air increased upon oxidation. In agreement with TEM pictures and susceptibility measurements, Mössbauer spectroscopy (figure 14) of particles E showed that they only oxidize partly. Although a significant contribution of the Fe(III) species could already be observed after exposure of the sample to air for one week (figure a), the spectrum had hardly changed after one year (figure b) and a significant part of the colloids was still present as $Fe_{0.75}C_{0.25}$ [15].

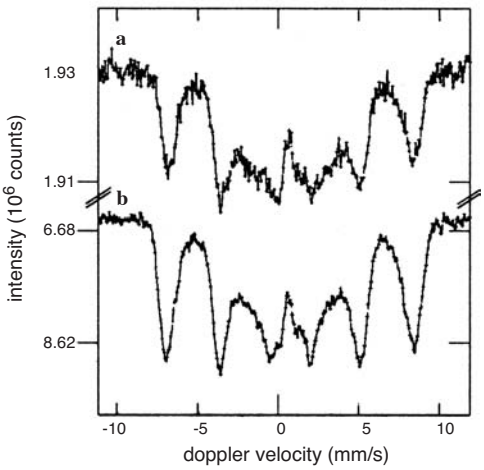

Figure 14. Mössbauer spectrum of dispersion E measured at 4.2 K after oxidation for **a**) 1week, **b**) 1 year.

4. Discussion

4.1. Synthesis

All dispersions in this study are stable, as judged by visual observations and susceptibility measurements (see chapter 7). This indicates that PIB and oleic acid are adsorbed on the iron surface, in accordance with earlier results for similar systems [33]. Large particles can be grown out of smaller PIB-coated particles without adding extra surfactant. Since dispersions D and E are still stabilized by the PIB surfactant layer, PIB molecules probably can move parallel to the surface of particles allowing newly formed iron to precipitate on the iron core. However, the surfactant density on particles D and E presumably will be lower than for dispersions synthesized without seeded growth.

4.2. Characterization

Particle radii measured with various techniques (table 2) correspond well with each other and show that the particle size increases with increasing $Fe(CO)_5$/surfactant ratio used for their synthesis. In contrast to what was found by Pathmamanoharan et al [13], not only sizes of particles coated with PIB but also oleic-acid-coated particle sizes could be controlled well. The reason presumably is that the authors of reference [13] did not take special care of excluding oxygen before measuring particle sizes with TEM. As discussed in sections 3.4 and 4.4, particle sizes increase considerably upon oxidation.

In general, the TEM radii for our dispersions are somewhat larger than the particle sizes from SAXS, certainly when the latter ones are corrected for polydispersity. This may be due to a slight oxidation (not yet visible by electron microscopy) of particles on the TEM-grids just before positioning them in the microscope. In addition, TEM radii for such small particles presumably contain a relatively large uncertainty, since we found that particle radii measured on various electron microscopes differed up to 20%. For most systems the radii determined from the magnetization measurements are significantly smaller than the TEM/SAXS radii. The difference can be ascribed to demagnetization of the near-surface region of the magnetic material, a general observation in ferrofluids [2]. Note that magnetic radii were calculated using the bulk value of $Fe_{0.75}C_{0.25}$ for m_s, which may not be completely correct. This point will be further discussed in chapter 4.

Volume fractions of iron (determined via different methods, see table 3), are in reasonable agreement with each other. For PIB-coated particles, the iron concentration is almost equal to the theoretical value, as calculated from the used amounts of reactants. This agrees with the absence of free $Fe(CO)_5$ in the dispersions, as found from Mössbauer spectroscopy on PIB-coated samples. However, for oleic-acid-coated particles OA1 and OA2 the experimental iron volume fractions are much lower than the maximum theoretical value. Presumably, in this case part of the ironpentacarbonyl was not converted, as is also found for a separate sample of oleic-acid-coated particles (figure 5). In some cases (B, OA2), the values for ϕ_{AGM} are somewhat larger than the maximum theoretical values. This is ascribed

to the fact that for calculation of ϕ_{AGM} the TEM radius was used, which may be somewhat too large.

From Mössbauer spectra it appears that a significant amount of carbon is present in the particles, which were determined to consist of $Fe_{0.75}C_{0.25}$ [15]. The composition was found by comparing our Mössbauer spectra with a series of spectra of amorphous $Fe_{1-x}C_x$ iron-carbon alloys with different values for x measured by Bauer-Grosse et al [29]. Presumably, the carbon originates from $Fe(CO)_5$ and is incorporated in the particles during synthesis. The same composition was also found by other authors [34] for oleic-acid-coated iron particles synthesized via the same method we used. Therefore, it is a plausible assumption that all iron dispersions described in this thesis consist of $Fe_{0.75}C_{0.25}$. The small contribution of Fe(III) oxide in the Mössbauer spectrum of particles C, which is not present for the particles E, could be explained by the presence of a small amount of oxygen during drying of the sample. To prevent the smallest particles (A) from oxidation is difficult; mössbauer spectroscopy revealed that despite careful precautions to exclude oxygen, particles A are almost completely oxidized. In view of this, it has to be considered that measurements on our dispersions were performed at various moments after their synthesis, which means that the particles A were at different stages of oxidation for the several experiments. Most likely, particles A were almost non-oxidized during the magnetization measurements and at the start of the susceptibility measurements in time (which both were measured at the day of their synthesis), since the dispersion showed Langevin behaviour and the susceptibility decreased by 99 % during one hour exposure to air. Probably, the TEM-radius is somewhat too large due to oxidation on the grid during a few minutes. SAXS-measurements showed that the Guinier radius increased in time from 2.2 nm (table 2, measured 3 months after the synthesis) to 2.7 nm (measured two years after the synthesis, in the same period as the Mössbauer measurements), very likely due to complete oxidation in time. This is consistent with the gyration and Porod radii of particles A that were oxidized deliberately, which two years after the synthesis were equal to those of particles kept under nitrogen atmosphere (R_g = 2.1 nm and a_p = 2.3 nm for both oxidized and 'non-oxidized' particles), while three months after the synthesis they still significantly differed from the radii of non-oxidized particles (see table 2). For the dispersions of larger PIB-coated particles (B-E), serious unintentional oxidation appeared to be absent, although a slight oxidation (maximum of 15 % decrease in susceptibility over 4 years) was measured. All measurements on our oleic-acid-coated particles were performed within 5 months after their synthesis, so that substantial oxidation during storage was avoided.

On TEM pictures one can see that the mutual positions of the particles depend on their size. Small particles are randomly distributed, while larger particles (E) show linear structures, but particles do not touch each other. Although these pictures are made from dried grids, which in principle do not provide information on particle arrangement in the fluid state, cryo-TEM on the same samples (see chapter 6) confirm the presence of anisotropic aggregates in vitrified thin films of samples D and E [35, 36]. These results are

supported by the hysteresis present in the magnetization curve of dispersion E. Because the Brownian relaxation time for single particles of this size is approximately $3 * 10^{-5}$ s, much smaller than the scanning speed of the AGM of 200 ms per measuring point, hysteresis behaviour is not expected for a system of separate particles. Therefore, much larger, slowly relaxing structures, must be present in the dispersion. The presence of larger aggregates is consistent with the increasing viscosity with particle size, which for single spherical particles is not expected to increase much for low volume fractions. Larger dynamic structures in both dispersions D and E are also found from frequency-resolved susceptibility measurements described in chapter 7. Probably, the magnetization curve of dispersion D does not show hysteresis, because the structures present here are much smaller [35] (see also chapter 6) and therefore have shorter relaxation times than in dispersion E.

4.3. SAXS-measurements

The data from SAXS show that the Porod radii generally are somewhat smaller than the Guinier radii but are in reasonable agreement for dispersions of relatively small particles (A, OA1-OA3). However, the discrepancy between the Porod and Guinier radius for dispersions D and E is rather large and presumably is the result of aggregation. The presence of aggregates was also found in the Guinier plots of these dispersions, showing a steep upturn at low q and preventing an accurate determination of the radius of gyration of single particles. Aggregate formation is not expected to influence the Porod radius significantly, since in the aggregates the iron cores are not expected to fuse. The discrepancy between the Porod and Guinier radii cannot be ascribed to polydispersity, since both values are influenced almost equally by a size distribution of the particles (see experimental section 2.4). For dispersions B and C, where no signs of aggregation were detected, the difference between the Guinier and Porod radius probably is the result of inhomogeneity of the particles (which consist of an amorphous iron-carbon alloy), causing the extrema in the Porod plot to shift to smaller q-values.

The radii of gyration of oxidized particles are about 1.2-1.5 times the radii of gyration of the non-oxidized particles, consistent with the other indications of particle volume increase upon oxidation. The same effect is found for the Porod radius, which is found to become up to 1.4 times larger upon oxidation. However, it is unlikely that the whole particle is transformed into iron oxide, as was also found from TEM, AGM and Mössbauer measurements (sections 3.4 and 4.4). Apparently, there is a layer of iron oxide covering a core of $Fe_{0.75}C_{0.25}$. Due to this partial oxidation, the modelling of the oxidized particles as spheres with a uniform electron density is not completely correct. However, since the exact thickness and electron density of the iron oxide layer is not known, no better approximation for the Porod radius could be made. On the other hand, the Guinier radii determined for the oxidized particles deviate significantly from the Porod radii. Moreover, the Guinier plot of most of the oxidized particles shows a steep upturn at very low q (data not shown), signifying that these particles also tend to aggregate. Therefore, the Guinier radii of these

particles could not be fitted properly and they certainly include contribution of the larger aggregates.

From the interparticle spacing derived from the positions of the maxima in the static structure factors of dispersions C (see figure 9) a thickness of a polymer layer of about 5-6 nm was determined. These structure factors could be reasonably well fitted with those for polydisperse hard spheres. The parameters for average particle radius (6.6 nm) and polydispersity (0.35 nm) are in reasonable agreement with results from other measurements (see table 2), although the polydispersity is lower than found with TEM. Also the values for the volume fractions used in the fits (of particles including the surfactant shell of about 6 nm) are consistent with what is expected from the volume fraction of the iron cores (see table 3).

4.4. Oxidation behaviour

TEM-micrographs show that upon oxidation of the particles an oxide layer is formed at their surface. This is consistent with the decrease of oxidation rate with time; a passivating oxide layer slows down the oxidation process. Upon oxidation, dispersions become unstable within a few days and particles sediment, probably because particle surface area increases (and surfactant density decreases) due to oxidation. Dispersions of larger particles (D and E) even form a space-filling gel, possibly because of the higher volume fractions involved. From the values of the saturation magnetization before and after oxidation and the thickness of the oxidized layer from TEM-micrographs, never exceeding 3 nm (after a few months of exposure to air), it can be argued that the formed oxide is not pure magnetite or maghemite, because the magnetic moment has decreased too much for that (the saturation magnetization m_s per volume for $Fe_{0.75}C_{0.25}$ is estimated to be $1.49 * 10^6$ Am^{-1} (using a density of 7.58 g/ml (table 4 in [29]) and $m_s = 1.59$ μ_B/Fe atom [29]), while for magnetite and maghemite this is approximately $0.48 * 10^6$ Am^{-1} [8]). Also from the infrared spectra it is clear that our oxidized particles do not consist of pure hematite or magnetite. However, XRD spectra show peaks that correspond to magnetite, although broader than for the perfectly crystalline oxide. From Mössbauer experiments, oxidized particles are found to partly consist of a disordered Fe^{3+} oxide. Possibly the structure of the oxide is an amorphous non-magnetic iron oxide, which does not contribute to the magnetic moment of the particle. The volume increase with a factor of 1.3 upon oxidation is somewhat lower than the value of 2.1 that is expected from bulk densities when metallic iron is transformed into magnetite, maghemite or hematite. However, since measurements of such thin oxide layers on TEM-micrographs are not very accurate the value of 1.3 seems reasonable.

From the susceptibility measurements as a function of time (figure 10), the low susceptibility of dispersions D and E in comparison with other samples seems remarkable, since the initial susceptibility scales with μM_s (see equation (2)), as is indeed experimentally found for dispersions B and C (at t = 0). Frequency dependent susceptibility measurements (chapter 6) of dispersion E show a decrease of the susceptibility with frequency, starting

from 1 Hz. This can explain the low susceptibility at 875 Hz, the measuring frequency of the kappabridge susceptibility meter. The same argument holds for dispersion D, but here the effect is less strong because the aggregates are smaller.

5. Conclusions

We synthesized stable dispersions of superparamagnetic monodomain iron-based particles in a broad size range with low polydispersity using different surfactants. Particle sizes can be controlled by varying the $Fe(CO)_5$/surfactant ratio; increasing this ratio increases the particle size for both surfactants. Both PIB and oleic acid appear to be good stabilizers for the particles in decalin. It was found that a significant amount of carbon was present in the particles, which were determined to consist of an amorphous $Fe_{0.75}C_{0.25}$ alloy. Particle sizes, measured with various techniques, correspond reasonably well with each other. Oleic-acid-coated particles are less polydisperse and have a more spherical shape than PIB-coated colloids. However, PIB-coated particles can be synthesized in a larger size range, due to the possibility to grow them from smaller particles. Iron concentrations are almost equal to the maximum theoretical value for the PIB-coated particles, whereas for dispersions of oleic-acid-coated particles free unconverted $Fe(CO)_5$ still seems to be present. Dispersions of smaller particles consist of single colloids, but dispersions of larger particles contain aggregates. Upon exposure to air, dispersions become unstable and a passivating oxide layer is formed on the particle surface, presumably consisting of a disordered non-magnetic iron oxide. Particle sizes increase due to oxidation; the density of the oxide is smaller than of iron. Smaller particles oxidize more rapidly than larger ones. Particles do not oxidize completely; even after several months an iron core is still present, as was found from various techniques (except for very small particles A). If handled under nitrogen atmosphere iron dispersions, containing relatively monodisperse colloids, of which the particle size and thickness of the surfactant layer can be controlled over a broad range, are promising ferrofluids for studying the physical behaviour of dipolar fluids. An interesting aspect to investigate further is the dipolar structure formation in dispersions of larger particles in comparison to sufficiently small particles, which are expected to remain dispersed as single colloids. This investigation is presented in chapters 6 and 7.

Acknowledgements

Igor Dolbnya, Wim Bras, Dirk Detollenaere and Ruud van Tol from the European Synchrotron Radiation Facility (ESRF) and Mohamed Ramzi from Rhodia Recherche (Aubervilliers, France) are thanked for their help with the SAXS measurements. Katarina Kassapidou from the General Chemical State Laboratory (Athens, Greece) is thanked for her help with the SAXS measurements and their

analysis. Andrei Petukhov is thanked for valuable discussions. Maarten Terlou is thanked for assistance with analysis of the TEM micrographs. The infrared measurements were performed by Joop van der Maas. The XRD spectra were measured by Marjan Versluijs-Helder. Anton Goossens, Adri van der Kraan, Menno Crajé, Peter Paulus and Kees Flipse are thanked for the Mössbauer measurements and valuable discussions. Financial support was granted by the Dutch Technology Foundation (STW) with financial aid from the Council for Chemical Science of the Netherlands Organization for Scientific Research (CW/NWO).

References

[1] Papell S S In *U.S. Patent*, 1965; Vol. 3; pp 215.
[2] Rosensweig R E 1985 *Ferrohydrodynamics* (Cambridge: Cambridge University Press).
[3] Berkovski B and Bashtovoy V 1996 *Magnetic fluids and applications handbook* (New York: Begel House Inc.).
[4] Ewijk van G A, Vroege G J and Kuipers B W M 2002 *Langmuir* **18** 382.
[5] Teixeira P I C, Tavares J M and Telo da Gama M M 2000 *J. Phys.: Condens. Matter* **12** R411.
[6] Massart R 1981 *IEEE Trans. Magn.* **MAG-17** 1247.
[7] Sun S and Zeng H 2002 *J. Am. Chem. Soc.* **124** 8204.
[8] Jiles D 1995 *Introduction to Magnetism and Magnetic Materials* (London: Chapman & Hall).
[9] Gangopadhyay S, Hadjipanayis G C, Dale B, Sorensen C M, Klabunde K J, Papaefthymiou V and Kostikas A 1992 *Physical Review B* **45** 9778.
[10] Suslick K S, Mingming F and Hyeon T 1996 *J. Am. Chem. Soc.* **118** 11960.
[11] Griffiths C H, O'Horo M P and Smith T W 1979 *J. Appl. Phys.* **50** 7108.
[12] Smith T W and Wychick D 1980 *J. Phys. Chem.* **84** 1621.
[13] Pathmamanoharan C, Zuiverloon N L and Philipse A P 2000 *Progr. Colloid Polym. Sci.* **115** 141.
[14] De Hek B and Vrij A 1981 *J. Colloid Interface Sci.* **79** 289.
[15] Goossens A, de Jongh L J, Butter K, Philipse A P, Crajé M W J and van der Kraan A M 2002 *Hyperfine Interactions* **141/142** 381.
[16] *Small Angle X-ray Scattering*; Glatter O and Kratky O, Eds.; Academic Press Inc.: London, 1982.
[17] Motte L, Billoudet F and Pileni, P 1995 *J. Phys. Chem.* **99** 16425.
[18] Dhont J K G 1996 *An introduction to dynamics of colloids* (Amsterdam: Elsevier).
[19] Kruif de C G, Briels W J, May R P and Vrij A 1988 *Langmuir* **4** 668.
[20] Petukhov A V *personal communication.*
[21] Percus J K and Yevick G J 1958 *Phys. Rev.* **110** 1.
[22] Thiele E 1963 *J. Chem. Phys.* **39** 474.
[23] Wertheim S 1963 *Phys. Rev. Lett.* **10** 321.
[24] van Beurten P and Vrij A 1981 *J. Chem. Phys.* **74** 2744.
[25] Vrij A 1979 *J. Chem. Phys.* **71** 3267.
[26] Baxter R J 1970 *J. Chem. Phys.* **52** 4559.
[27] Wonterghem van J, Morup S, Charles S W, Wells S and Villadsen J 1985 *Phys. Rev. Lett.* **55** 410.
[28] Wonterghem van J, Morup S, Charles S W and Wells S 1988 *J. Colloid Interface Sci.* **121** 558.
[29] Bauer-Grosse E and Le Caër, G 1987 *Philosophical Magazine B* **56** 485.
[30] Crajé M W J *personal communication.*
[31] Grasselli J G 1973 *CRC Atlas of spectral data and physical constants for organic compounds* (Cleveland, Ohio: CRC Press).

[32] Powder diffraction file 2000. Joint Committee on Powder Diffraction Standards. Swarthmore, Pennsylvania, card 190629.
[33] Pathmamanoharan C and Philipse A P 1998 *J. Colloid Interface Sci.* **205** 340.
[34] Hanson M, Johansson C, Pedersen M S and Mørup S 1995 *J. Phys.: Condens. Matter* **7** 9269.
[35] Butter K, Bomans P H, Frederik P M, Vroege G J and Philipse A P 2003 *Nature Materials* **2** 88.
[36] Butter K, Bomans P H, Frederik P M, Vroege G J and Philipse A P 2003 *J. Phys.: Condens. Matter* **15** S1451.

4 Small angle neutron and X-ray scattering of dispersions of oleic-acid-coated iron particles

Abstract

This chapter describes the characterization of dispersions of oleic-acid-coated magnetic iron particles by SANS and SAXS. Both oxidized and non-oxidized dilute samples were studied by SANS at different contrasts. The non-oxidized samples are found to consist of non-interacting superparamagnetic single dipolar particles, with a lognormal distribution of iron cores, surrounded by a surfactant shell, which is partially penetrated by solvent. This model is supported by SAXS-measurements on the same dispersion. On oxidation, a non-magnetic oxide layer is formed around the iron cores, which causes an increase of particle size. In addition, particles are found to aggregate upon oxidation, presumably because the surfactant density on the particle surfaces is decreased.

1. Introduction

Dispersions of iron particles appear to be very suitable for studying the physical behaviour of ferrofluids. Their synthesis from ironcarbonyl compounds results in particles with low polydispersity of which the particle size can be varied in a controlled way [1] (as is also shown in chapter 3). Variation of the iron core size, as well as the thickness of the surfactant layer (by using different types of surfactant) allows control of both the dipolar and isotropic interparticle interaction [2] (see also chapter 6). In this chapter, the characterization of dispersions of iron particles coated with oleic acid using small angle scattering is described. Dispersions kept under nitrogen atmosphere (to prevent oxidation of the particles), as well as oxidized dispersions were studied. Since the ferrofluids are black, the use of light scattering is difficult due to strong absorbance of visible light. This problem is avoided using Small Angle Neutron- and X-ray Scattering (SANS and SAXS). An additional advantage of SANS is the possibility to study the *magnetic* properties of ferrofluids, since neutron scattering consists of both a nuclear and a magnetic part (see theory). In addition, contrast variation can be used to study different parts of a composite particle by controlled deuteration of the solvent. The theoretical section 2 summarizes the most important background concerning scattering, required to understand the experiments; for a more extensive description of SANS and SAXS see references [3,4,5,6]. Sections 3 and 4 describe the scattering experiments and two models that were used to fit the scattering data. In section 5, the results are discussed and compared with other experiments on the same dispersions.

2. Theory

2.1. Scattering

From the scattering of electromagnetic radiation (X-rays) or matter waves (neutrons) by colloidal particles as a function of the scattering angle θ, information can be subtracted about particle size, shape and interparticle correlation. The scattering from a dilute dispersion of monodisperse spherical colloids (where particle interactions are assumed to be negligible) as a function of the scattering direction is given by

$$I(\vec{q}) = KN_p \left|F(\vec{q})\right|^2 \tag{1}$$

with N_p the number of scattering particles and K a constant, depending on the experimental set-up. $F(\vec{q})$ is the total scattering amplitude of a single particle

$$F(\vec{q}) = \int_{V_p} \Delta\eta(\vec{r}) e^{i\vec{q}\cdot\vec{r}} d\vec{r} \tag{2}$$

which integrates all coherent scattering contributions within the particle of volume V_p weighted by their phase shifts $e^{i\vec{q}\cdot\vec{r}}$ with $\vec{r}$ the position vector within the particle and $\vec{q}$ the

scattering vector with magnitude:

$$q = \frac{4\pi}{\lambda}\sin(\theta/2) \tag{3}$$

Here, λ is the wavelength of the scattered radiation (equal to that of the incoming beam) and θ the scattering angle between the incident and scattered waves. The local scattering amplitude is quantified as the local scattering length density difference $\Delta\eta(\vec{r})$ with respect to the (homogeneous) solvent scattering length density η_s ($\Delta\eta$ is also referred to as 'contrast').

For spherically symmetric core-shell particles with core radius a_1 with $\Delta\eta=\Delta\eta_1$ and a shell with thickness (a_2-a_1) and $\Delta\eta=\Delta\eta_2$ the total scattering amplitude of a single particle is given by:

$$\begin{aligned} F(\vec{q}) &= \int_0^{a_1} \Delta\eta_1 \frac{\sin(qr)}{qr} 4\pi r^2 dr + \int_{a_1}^{a_2} \Delta\eta_2 \frac{\sin(qr)}{qr} 4\pi r^2 dr \\ &= \frac{4\pi}{q^3}\left[\Delta\eta_1 g(qa_1) + \Delta\eta_2 (g(qa_2) - g(qa_1))\right] \end{aligned} \tag{4}$$

with $g(x) = \sin x - x \cos x$

Note that for a homogeneous spherical particle $F(\vec{q})$ is given by only the first term in equation (4). For particles with more than one shell, equation (4) can be easily extended with terms corresponding to the different shells. Whereas till now only the scattering of monodisperse particles was treated, in case of polydisperse particles, the square of the total scattering amplitude $|F(q)|^2$ in equation (1) has to be averaged with the weight given by their size distribution.

For small values of q, the Guinier approximation is valid, by which the radius of gyration R_g can be derived from the slope of a plot of the logarithm of the intensity against q^2:

$$I(q) = I(0)\exp(-\frac{1}{3}R_g^2 q^2) \tag{5}$$

For a spherical particle, the radius of gyration is defined as follows:

$$R_g^2 = \frac{\int_0^r 4\pi r^4 \Delta\eta(r)\, dr}{\int_0^r 4\pi r^2 \Delta\eta(r)\, dr} \tag{6}$$

which is equal to $\frac{3}{5}a^2$ for a homogeneous sphere of radius a. For polydisperse systems the particle radius as determined from the Guinier plot overestimates the average particles radius, since the larger particles have a higher weight in the scattering intensity $I(q) \propto a^6$. The effective value of the radius of gyration is then given by $R_g^2 = (\langle a^8\rangle/\langle a^6\rangle)$ [3], where the angular brackets denote the averaging over the particle size distribution P(a). For a

narrow width of the size distribution, the apparent radius derived from the scattering at low q can be corrected for the relative polydispersity σ, according to [7]:

$$a_G = \langle a_G \rangle \left[1 + \frac{13}{2}\sigma^2 \right] \qquad \text{with} \quad \sigma^2 = \frac{\langle a_G{}^2 \rangle - \langle a_G \rangle^2}{\langle a_G \rangle^2} \tag{7}$$

where a_G is the measured and $\langle a_G \rangle$ is the number average Guinier radius:

$$\langle a \rangle = \int P(a) a da \tag{8}$$

Equation (7) is derived from the more general equation valid for narrow size distributions [8]:

$$\langle a^n \rangle = \langle a \rangle^n \left(1 + \frac{n(n-1)}{2}\sigma^2\right) \tag{9}$$

For X-rays and neutrons, with small wavelengths (< 1 nm), the information from scattering of colloidal particles will be found at small angles, which is why these techniques are called Small Angle X-ray Scattering (SAXS) and Small Angle Neutron Scattering (SANS) respectively. X-rays are scattered by the electrons in a material. For SAXS, η is determined by the electron density ρ^e of the scattering atoms within the particles; atoms of heavier elements scatter more strongly:

$$\eta(\vec{r}) = r_0 \rho^e(\vec{r}) \tag{10}$$

Here, r_0 (= e^2/mc^2 = 2.82 x 10^{-15} m) is the Thomson radius of an electron.

Neutrons are scattered by the atomic nuclei in the sample. Here, η depends on the kind of scattering nucleus and is even different for isotopes. Especially the hydrogen (^{1}H) and deuterium (^{2}D) atom have a very different scattering length (-0.374 x 10^{-12} cm and 0.667 x 10^{-12} cm, respectively [5]). This property can be used to perform so-called contrast variation: by varying the ratio of hydrogenated and deuterated solvent the contrast of the particle can be changed, which is e.g. interesting for core-shell particles, where the core and shell have different scattering length densities. For conventional SAXS, contrast variation is more difficult, since in this case the chemical structure has to be varied, which often will also influence the particle interactions. A disadvantage of SANS is the presence of incoherent scattering. Part of the scattered neutrons loses its phase, resulting in a uniform incoherent background. Especially hydrogen atoms lead to a large contribution of incoherent scattering.

Neutron scattering from *magnetic* nanoparticles is caused both by direct interactions of neutrons with the nuclei of atoms within the particles and by interactions between the spins of the neutrons and those of the unpaired electrons in the magnetic particles. This results in two types of scattering: magnetic and nuclear. The nuclear (N) and magnetic (M) scattering length densities are given by the sums over all atomic species i:

$$\eta_N = \sum_i c_i b_i / \Omega_i \tag{11}$$

$$\eta_M = \sum_i c_i p_i / \Omega_i \tag{12}$$

with b_i and p_i respectively the nuclear and magnetic scattering lengths, c_i the molar fraction of atoms i, and Ω_i the atomic volume of constituent i. p_i is proportional to the Thomson electron radius $r_0 = e^2/mc^2 = 2.82 \times 10^{-15}$ m, the magnetic moment of the neutron $\gamma = -1.913$ nuclear magnetons, and the magnetic moment of the atom $\vec{M}_i$ in Bohr magnetons [5]:

$$p_i = \gamma r_0 \left|\vec{M}_i^{\perp}\right| f(\vec{q}) / 2 \tag{13}$$

with $f(\vec{q})$ the electronic form factor, which is 1 at the small q-values involved. The scattering amplitude b_i for the nuclear (N) scattering varies apparently arbitrarily for different isotopes. The corresponding scattering amplitudes F_N and F_M for nuclear and magnetic scattering are given by equation (2) with respectively $\Delta\eta = \eta_N - \eta_s$ and $\Delta\eta = \eta_M$.

Note that the $\perp$ sign in equation (13) is the consequence of an important selection rule in neutron scattering namely that only those components of the magnetization $\vec{M}$ perpendicular to $\vec{q}$ are effective in magnetic neutron scattering [5,9]. This leads to a scattering intensity which depends on the angle α between $\vec{q}$ and $\vec{M}$. When the particles are completely aligned in an external field H, the intensity in the case of unpolarized neutrons is [10]:

$$I(\vec{q}, \alpha) \propto F_N^2 + F_M^2 \sin^2 \alpha \tag{14}$$

giving an anisotropic scattering pattern.

The so-called SANSPOL technique makes use of polarized neutrons by sending them through a polarizer. With a spin-flipper the polarization direction of the incoming beam can be chosen to be up (+) or down (-). In this case four scattering processes have to be distinguished, two for conserving the polarization direction (non-spin-flip, ++ and --) and two where the polarization is reversed (spin-flip, +- and -+). With SANSPOL the polarization direction after scattering is not analysed; the intensity collected in the detector contains both spin-flip and non-spin-flip contributions and depends on the spin polarization of the incoming neutrons. The respective intensities at high field are given by [10]:

$$\begin{aligned} I^+(q,\alpha) &= \left|F^{++}\right|^2 + \left|F^{+-}\right|^2 = F_N^2 + (F_M^2 - 2F_N F_M)\sin^2\alpha \\ I^-(q,\alpha) &= \left|F^{--}\right|^2 + \left|F^{-+}\right|^2 = F_N^2 + (F_M^2 + 2F_N F_M)\sin^2\alpha \end{aligned} \tag{15}$$

Note that the average of I^+ and I^- (for non-polarized neutrons) results again in equation (14). At lower magnetic fields, the situation is more complicated since the magnetic moments are no longer completely aligned and their orientation distribution (for non-interacting superparamagnetic particles) follows Langevin statistics [6,9]. The net alignment of particles in the field direction L(x) is given by:

$$L(x) = \coth(x) - \frac{1}{x} \tag{16}$$

where x is proportional to the magnetic moment per particle $\mu=4\pi a^3 m_s/3$ (m_s is the saturation magnetization per volume) and the magnetic field H:

$$x = \frac{\mu_0 \mu H}{3kT} \tag{17}$$

with μ_0 the magnetic permeability in vacuum and kT the thermal energy. In this case, the intensities I^+ and I^- are given by [6]:

$$\begin{aligned} I^+(q,\alpha) &\propto F_N^2 + 2F_M^2 L(x)/x + \left\{F_M^2(1-3L(x)/x) - 2F_N F_M L(x)\right\}\sin^2\alpha \\ I^-(q,\alpha) &\propto F_N^2 + 2F_M^2 L(x)/x + \left\{F_M^2(1-3L(x)/x) + 2F_N F_M L(x)\right\}\sin^2\alpha \end{aligned} \tag{18}$$

For the case of complete alignment ($L(x \to \infty) = 1$), equation (15) is again obtained. In the limit of zero applied field ($x \to 0$), $L(x)/x \to 1/3$ and the scattering intensity $I^+ = I^- = F_N^2 + 2/3\ F_M^2$ does not depend on neutron spin polarization and α. As is clear from the above equations (18), L(x) can be derived by subtraction of I^- and I^+ for a certain field value [6]:

$$L(x) = \frac{I_x^- - I_x^+}{I_{x_\infty}^- - I_{x_\infty}^+} \tag{19}$$

Using SANS has the advantage that both information about the 'nuclear' and 'magnetic' behaviour of particles can be extracted. In this case it is of course necessary to apply a magnetic field to the sample, which might change the particle structure. For polarized neutrons, the two independent scattering patterns for both polarization states are fitted for all q-values to the $\sin^2\alpha$ dependency as in equation (15). From the resulting fits, the scattering intensity is calculated for $\alpha = \pi/2$ ($\vec{q} \perp \vec{H}$):

$$\begin{aligned} I^+(q,\frac{\pi}{2}) &\propto (F_N - F_M)^2 \\ I^-(q,\frac{\pi}{2}) &\propto (F_N + F_M)^2 \end{aligned} \tag{20}$$

Thus, SANSPOL provides an additional method of contrast variation (apart from contrast variation by deuterating the solvent) where the total scattering length density of the (magnetic) core for the different polarization states can be given by $\eta_N + \eta_M$ for (–) and $\eta_N - \eta_M$ for (+), as is employed in figure 4 (discussed later). Of course, no magnetic scattering contribution is present for the solvent and non-magnetic parts of the particles, resulting in equal scattering length densities for both the (–) and (+) polarization states. Another important advantage of polarized neutrons is that due to the presence of the mixing term of both nuclear and magnetic scattering in equation (15) the actual scattering of a composite particle (e.g. with a core-shell structure) is measured, whereas measurements with unpolarized neutrons only result in separate magnetic and nuclear size distributions.

2.2. SANS and SAXS instruments

A schematic set-up for measuring SANS is presented in figure 1 [11,12]. Neutrons produced in a nuclear reactor first are monochromised in a velocity selector, consisting of a rotating axis with helical lamellae, selecting only neutrons of a certain velocity (corresponding to a certain wavelength) [13,14]. For the SANS instrument V4 installed at the HMI reactor Ber II, the spread in wavelength is rather large ($\Delta\lambda/\lambda \approx 10$ %) [11]. For SANSPOL, the beam is polarized by a high-transmission supermirror polarizer [11], after which a collimation system aligns the neutrons. By changing the sample-detector distance, different q-ranges can be measured [12]. To preserve the polarization direction of the beam, guide fields are needed along the collimator system that are transverse to the neutron beam and generated by permanent magnets. In front of the sample a spin-flipper is placed to invert the polarization for measuring both spin-up and spin-down scattering. The detector is a two-dimensional array of detector cells, which transform the neutrons into electronic pulses.

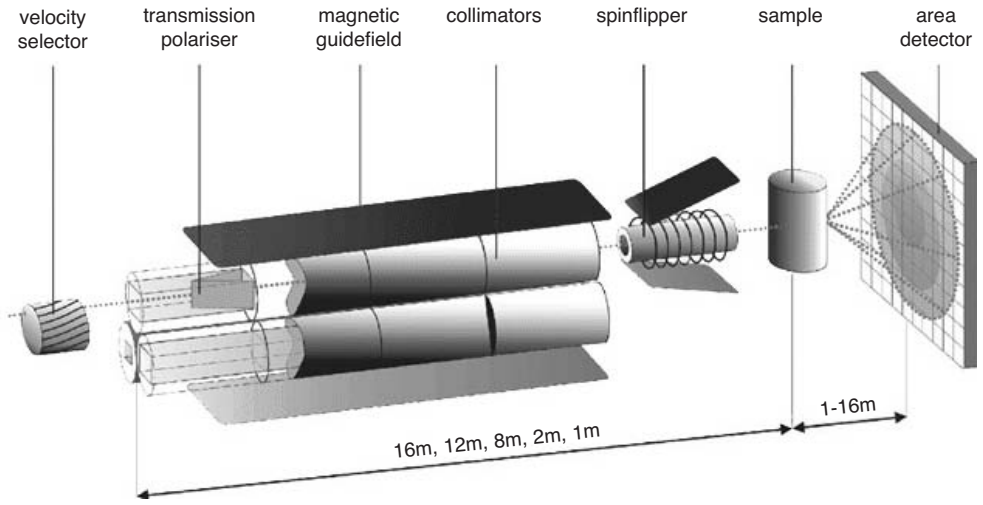

Figure 1. Set-up of SANSPOL instrument V4 at BENSC, Berlin.

For SAXS-measurements, one can use synchrotron radiation, which is emitted by electrons circulating in a storage ring [3]. The double crystal monochromator [15] used for SAXS has the advantage that the X-rays can be produced with a much more narrow spectral width than for SANS. Whereas SANS scattering has an intrinsic spread in wavelength of about 10%, resulting in an apparent polydispersity of the particles, this effect is less important using SAXS, where $\Delta q/q$ is typically a few percent.

3. Experimental

The iron dispersion OA3 was synthesized under nitrogen atmosphere by thermal decomposition (at 170 °C) of $Fe(CO)_5$ in decalin in the presence of oleic acid as described in chapter 3. The resulting black dispersion was always stored and handled under nitrogen atmosphere to prevent oxidation of the particles. Part of dispersion OA3 was exposed to air for two days and is further coded as dispersion OA3ox. For further details about the synthesis and characterization is referred to chapter 3 (system code OA3).

Samples for SANS measurements were prepared in a glovebox under nitrogen atmosphere in flat circular quartz cells (Hellma, thickness 0.1 cm). Diluted samples were prepared from the stock dispersion OA3 by adding decalin and/or deuterated decalin to vary the contrast of particles. Sample cells, closed with a cap, were tested to be airtight. Oxidized samples were also prepared in the glovebox (to keep the same level of oxidation for all samples) from the stock dispersion OA3ox.

Measurements were performed at the Berlin Neutron Scattering Center (BENSC) at the instrument V4 using polarized neutrons (SANSPOL) [11,12] at a wavelength of 0.605 nm with a beam diameter of 16 mm. Because neutrons at BENSC are produced in a cold source, a relatively high wavelength can be selected, which has the advantage that the scattering angles are not too small (and consequently the sample-detector distance not too large). Measurements were performed at three different sample-detector distances (1, 4 and 12 meter), resulting in a total accessible q-range of 0.04 to 3.3 nm^{-1}. The samples were placed between the poles of a strong magnet with the homogeneous magnetic field (up to 1.1 Tesla) in the horizontal direction perpendicular to the beam. Unless stated otherwise, all measurements were performed at maximum field intensity. The neutrons were collected by a ^3He detector of 64x64 elements of 10x10 mm^2. Measurements were performed on series of different contrasts of dilute samples, both for non-oxidized (~ 6.5 times dilution of OA3) and oxidized particles (~ 3.3 times dilution of OA3ox). In addition, the non-oxidized stock dispersion and a dilute dispersion were measured in different magnetic field strengths.

Two-dimensional data were corrected for transmission and for background and empty cell scattering. The sensitivity of individual detector pixels was normalized by comparison with the isotropic scattering of water. The scattering patterns for both polarization states were fitted separately to the $\sin^2\alpha$ fit (as in equation 15) for all q-values. Of the resulting fits, the scattering intensity was calculated for $\alpha = \pi/2$ (for $\vec{q} \perp \vec{H}$). The curves resulting for the three different sample-detector distances were merged to one curve. Scattering curves were fitted using least-square model fitting computer programs FISH [16] and SASFIT [17].

SAXS samples were prepared in a glovebox in flat glass capillaries (Vitrocom, internal thickness 1 mm) that were closed with epoxy glue. Measurements were performed at the Dutch-Belgian Beamline (DUBBLE) [15,18] at the European Synchotron Radiation Facility (ESRF) in Grenoble, France. The wavelength of the X-ray beam of 0.13 nm (9.5 keV, $\Delta\lambda/\lambda \sim 5 \times 10^{-4}$) and a sample-detector distance of 1.9 meter, resulted in a q-range of

0.15-3.2 nm^{-1}. The scattering was collected on a two-dimensional position-sensitive detector, with an area of 13x13 cm^2, containing 512 x 512 pixels.

Two-dimensional data were corrected for transmission, detector sensitivity and background scattering. The two-dimensional patterns were radially averaged.

4. Results

The synthesis resulted in a black dispersion that could be manipulated by the field gradient of a small permanent magnet. An Electron Microscopy picture of the particles is given in figure 2. The layer of oleic acid around the particles is invisible on the micrograph. From separate Mössbauer measurements (see chapter 3, [19]) it was found that the particle cores consist of $Fe_{0.75}C_{0.25}$. Upon exposure to air, the particles oxidize, as found by decrease of the magnetic susceptibility in time. On Electron Microscopy pictures of oxidized particles (not shown), a layer around a core with different intensity is observed, indicating that an iron oxide layer is formed at the surface of the particles. Characterization of the ferrofluid with various techniques is summarized in table 1.

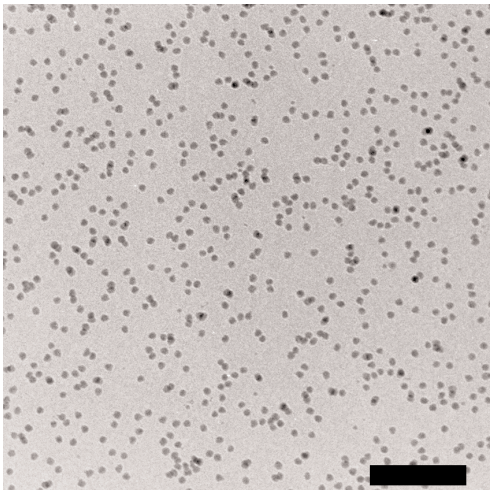

Figure 2. Cryogenic Transmission Electron Microscopy (cryo-TEM) picture of a glassified film of dispersion OA3 showing the iron-based cores. Surfactant layers are not visible with this technique. The scale bar is 100 nm.

Table 1. Characteristics of dispersion OA3.

a_{TEM}[1] (nm)	4.3 ± 0.3
a_M[2] (nm)	3.3
$\phi_{iron,EA}$[3]	0.045 (stock)
	0.0070 (non-ox, dilute)
	0.014 (ox, dilute)

[1]Average particle radius measured from TEM micrographs. [2]Magnetic particle radius, determined by magnetization measurements (see figure 9) using a literature value for m_s of Fe_3C (1.49 x 10^6 Am^2). [3]Estimated volume fraction of iron, from elemental analysis of stock dispersion OA3. The value for oxidized particles is calculated assuming that the volume fractions of OA3 and OA3ox are equal (increase of particle size upon oxidation is neglected).

SANS-curves for dilute samples with different contrasts are presented in figure 3. All (+) and (-) curves could be fitted fairly well with a core-shell model with lognormal distribution (with standard deviation σ) of the iron core radius a_{core}

$$P(a_{core}) = \frac{1}{\sqrt{2\pi\sigma^2}} \frac{1}{a_{core}} \exp\left(\frac{-\left(\ln \frac{a_{core}}{\langle a_{core} \rangle} \right)^2}{2\sigma^2} \right) \qquad \text{with} \langle a_{core} \rangle = \int P(a_{core}) a_{core} da_{core} \tag{21}$$

presented in figure 4 (for fitting parameters see table 2). For small values, σ is equal to the relative polydispersity of a_{core}:

$$\sigma^2 = \frac{\langle a_{core}^2 \rangle - \langle a_{core} \rangle^2}{\langle a_{core} \rangle^2} \tag{22}$$

Table 2. Fitting parameters for SANS-curves of dilute dispersions OA3 and OA3ox.

parameter	OA3		OA3ox	
$\langle a_{core} \rangle$[1] (nm)	3.48		2.74	
dR_{shellA}[2] (nm)	-		1.37	
dR_{shellB}[2] (nm)	2.08		2.08	
η_N (core)[3] (10^{10} cm^{-2})	7.92		7.92	
η_N (shellA)[3] (10^{10} cm^{-2})	-		7.29	
η_N (shellB)[3] (10^{10} cm^{-2})	0.08 (without solvent penetration)		0.08 (without solvent penetration)	
	0.01 (0 % D)[4]		0.02 (0 % D)[4]	
	1.27 (28 % D)[4]		1.05 (25 % D)[4]	
	2.61 (58 % D)[4]		2.02 (50 % D)[4]	
	3.88 (88 % D)[4]		3.05 (75 % D)[4]	
η_M[5] (10^{10} cm^{-2})	1.49		1.49	
η_s[3] (10^{10} cm^{-2})	0% D	-0.031	0% D	-0.031
	~28% D	1.99	~25% D	1.81
	~58% D	4.13	~50% D	3.54
	~88% D	6.16	~75% D	5.37
x[6]	0.625		0.562	
ϕ(core)[7]	7.0 x 10^{-3} (0 % and 28 %)		2.7 x 10^{-3}	
	7.4 x 10^{-3} (58% and 88%)			
σ[8]	0.170		0.147	

[1]Average radius of the iron core. [2]Thickness of the oxide layer (shell A) and the surfactant layer (shell B). [3]Nuclear scattering length density of the iron core (core), oxide layer (shell A), surfactant layer (shell B), and solvent (for different contrasts). [4]Calculated from x: $\eta_N(shellB) = 0.08 + x(\eta_s - 0.08)$. [5]Magnetic scattering length density of the iron core. [6]Fraction of the surfactant layer penetrated by solvent. [7]Volume fraction of iron cores from the absolute intensity of the scattering. [8]Relative polydispersity of iron cores.

The scattering length density variation shown in figure 4 clearly revealed a partial penetration of the solvent into the oleic acid shell. Without this feature the scattering curves could not be fitted consistently. The partial penetration resulted in an average scattering length density of the surfactant layer in between those of oleic acid and the solvent.

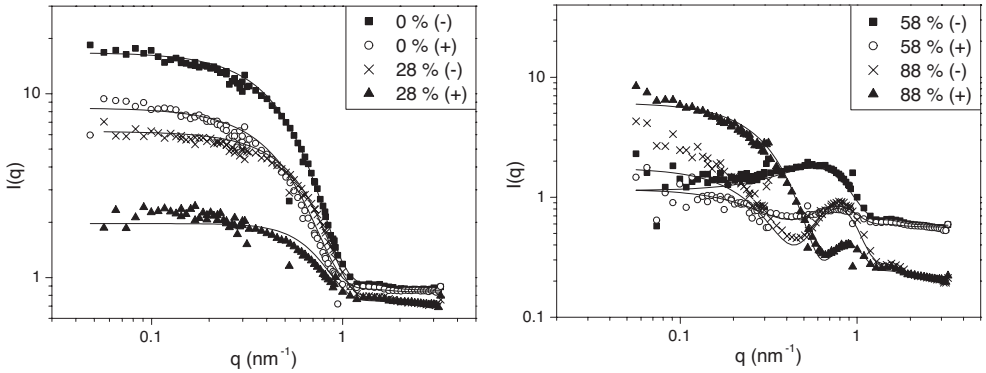

Figure 3. SANS scattering curves of dispersion OA3 for different compositions of the solvent (the volume percentage of deuterated decalin is indicated). Both the curves measured with spin up (+) and spin down (-) are shown. The solid curves are fits according to a core-shell model with partial penetration of solvent in the surfactant shell. The fitting parameters can be found in table 2.

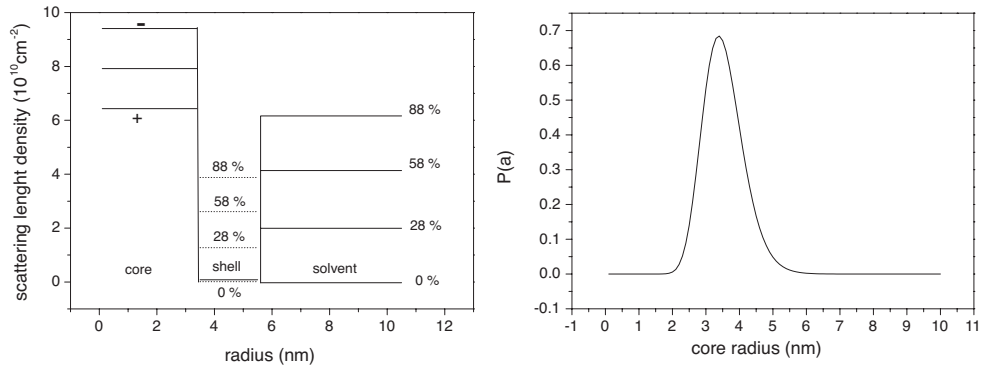

Figure 4. Left: model used to fit SANS curves for dispersion OA3. The dotted lines indicate the average scattering length densities of the surfactant layer (partially penetrated by solvent). The penetration fraction is given by the factor x (see table 2). For the (-) curves, the magnetic and nuclear scattering length densities were added, while for the (+) curves, the magnetic scattering length density was subtracted from the nuclear scattering length density. Right: distribution of the core radius as used in our model.

The curves of the *oxidized* particles could not be fitted with one distribution for the whole q-range, since the intensity strongly goes upwards at low q (figure 5). At higher q (> 0.25 nm^{-1}) curves could be reasonably well fitted with a core-2shell model with a lognormal distribution of the core size and again a partial penetration of solvent in the oleic acid shell. Here, we used the same contrasts as for the non-oxidized samples for the core and the oleic acid layer and a different contrast to account for an extra iron oxide layer around the core (figures 5 and 6). An additional contribution of aggregates was needed to fit the curves well at low scattering angles. However, this fit contribution very much depends on the exact parameters chosen and we have no information about the exact size, shape and distribution of the aggregates from other techniques. It appeared that the scattering intensity

at lower q-values could be properly fitted by an additional contribution of larger polydisperse particles (a = 8.3 nm, lognormal distribution with $\sigma = 0.52$), which practically does not influence the intensity at higher q-values. This point will be further discussed in section 5 (discussion). The fitting parameters are summarized in table 2.

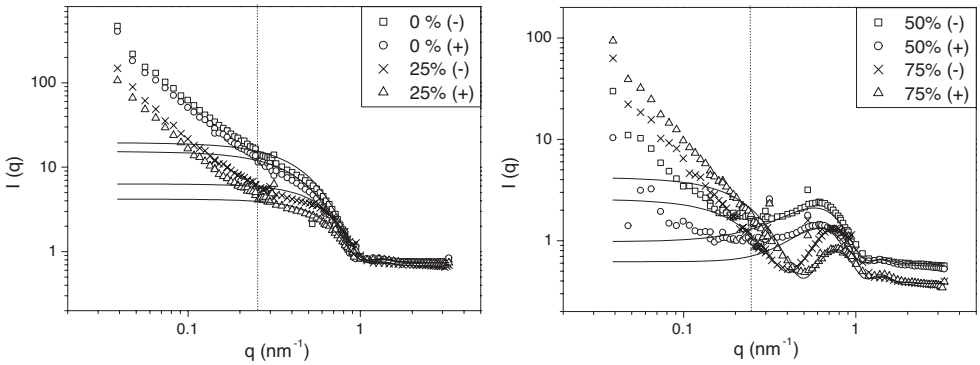

Figure 5. SANS scattering curves of dispersion OA3ox for different compositions of the solvent (the volume percentage of deuterated decalin is indicated). Both the curves measured with spin up (+) and spin down (-) are shown. The solid curves are fits according to a core-2shell model with partial penetration of solvent in the surfactant shell. The penetration fraction is given by the factor x (see table 2). The experimental data were only fitted for $q > 0.25$ nm^{-1} (on the right side of the dotted lines). The fitting parameters can be found in table 2.

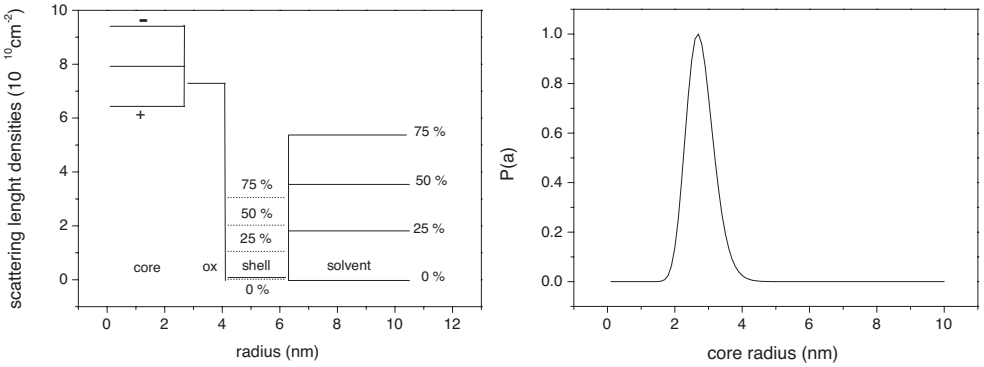

Figure 6. Left: model used to fit SANS curves for dispersion OA3ox. The dotted lines indicate the average scattering length densities of the surfactant layer (partially penetrated by solvent). The penetration fraction is given by the factor x (see table 2). For the (-) curves, the magnetic and nuclear scattering length densities were added, while for the (+) curves, the magnetic scattering length density was subtracted from the nuclear scattering length density. Right: the distribution of the core radius as used in our model.

Figure 7 shows that the SANS Guinier curve for a dilute sample of non-oxidized particles is nearly straight and from the slope a radius of gyration of 2.9 nm is calculated, corresponding to a particle core radius of 3.8 nm. The Guinier plot of oxidized particles

(figure 8) shows a much stronger steep upturn at low q, indicating the presence of aggregates. However, at slightly higher q-values, the dispersion displays clearly Guinier behaviour with a radius of gyration radius of 3.2 nm, while it is calculated to be 3.1 nm from equation (6), using the fitting parameters of the core-2shell model.

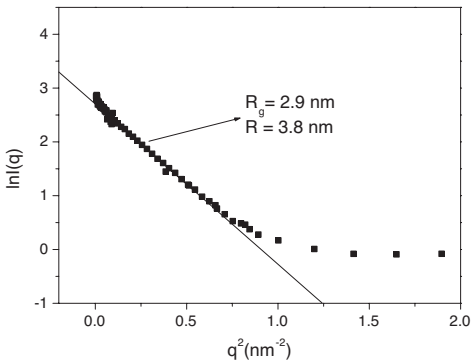

Figure 7. Guinier plot from SANS measurements on a dilute dispersion OA3 in 0 % deuterated decalin.

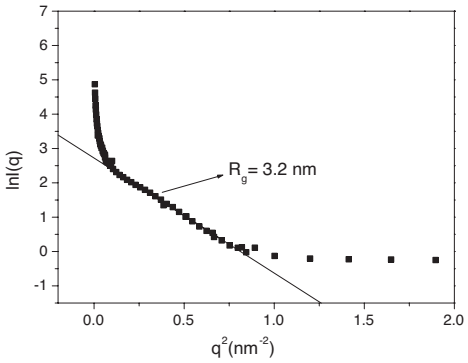

Figure 8. Guinier plot from SANS measurements on a dilute dispersion OA3ox in 0 % deuterated decalin.

The Langevin behaviour of the particles as a function of magnetic field is calculated using equation (19) (figure 9). Both curves (from the stock dispersion OA3 and a dilute dispersion (88 % deuterated)) are very similar to the normalised magnetization curve of the same stock dispersion, which can be fitted properly to the Langevin function, resulting in a particle dipole moment of 2.24 x 10^{-19} Am^2 corresponding to a particle radius of 3.3 nm (using a value of 1.49 x 10^6 Am^{-1} for the saturation magnetization of amorphous $Fe_{0.75}C_{0.25}$, see table 1). This point will be further discussed in section 5 (discussion). It must be noted that the magnetization curve is much more accurate than the results from SANS, and it consists of many more measuring points. The good agreement between SANSPOL and magnetization results for both the stock and dilute dispersion indicates again the absence of aggregates in the non-oxidized samples.

SAXS-curves of dilute samples of OA3 only show scattering from the iron cores, since the contrast of the oleic acid layer compared to the solvent can be neglected. Figure 10 shows a curve of a dilute dispersion (50 times compared to the stock dispersion) that can be fitted reasonably well with the same particle radius as for the SANS curves (table 2) and a slightly smaller polydispersity (σ = 0.14 instead of 0.17). Since for SAXS no absolute intensities are measured, the contrast and particle concentration cannot be compared to the values found for SANS. The radius of gyration found from the SAXS curve is 3.0 nm, corresponding to a Guinier particle radius of 3.9 nm.

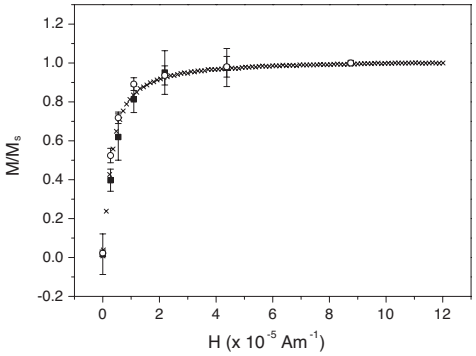

Figure 9. Langevin curves for dispersion OA3. ■ SANS measurements on stock dispersion, ○ SANS measurements on dilute dispersion (88 % deuterated decalin), x magnetization curve of stock dispersion.

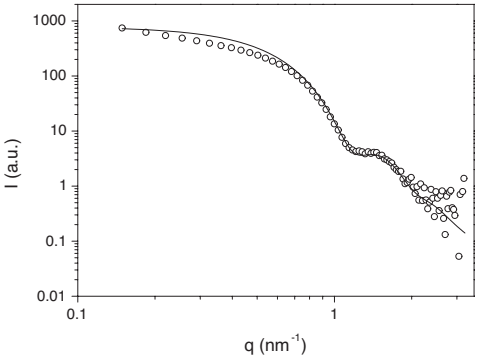

Figure 10. SAXS curve of a dilute dispersion OA3. The solid curve is a fit, using the same core radius and a slightly lower polydispersity (0.14) as for the model in figure 4.

5. Discussion

The parameters for the particle radius and volume fraction used for fitting the SANS curves of the non-oxidized samples agree well with information from other techniques (see tables 1 and 2). The polydispersity found from SANS (17 %, table 2) is significantly larger than is found from TEM measurements (7 %, table 1). The apparent polydispersity can be partly caused by smearing of the scattering pattern due to the large distribution in the wavelength of neutrons ($\Delta q/q \sim \Delta\lambda/\lambda \sim 10$ %). The SAXS-data suggest a somewhat smaller polydispersity (14 %), although still much larger than found from TEM. In spite of the much narrower spectral width ($\Delta\lambda/\lambda \sim 10^{-4}$) of X-rays, which does not limit the resolution $\Delta q/q$, other factors like the finite detector resolution and the finite transverse coherence length [20] restrict the actual resolution $\Delta q/q$ to a few percent. Thus, although the resolution in SAXS measurements is better than for SANS, it is also limited and SAXS may overestimate the polydispersity as well. On the other hand, TEM is probably less sensitive for smaller particles, that are sometimes neglected when determining the average particle radius, resulting in a slight underestimation of polydispersity.

The particle radii found from both Guinier plots (respectively 3.8 and 3.9 nm for SANS and SAXS) are somewhat larger than the average particle radius used in our model. However, these values should be corrected for polydispersity (0.14 from SAXS) using equation (7) to obtain the average radii. This results in particle radii of 3.4 nm and 3.5 nm for SANS and SAXS respectively, both very close to the value of 3.48 nm from the model. The thickness of the oleic acid layer (2.08 nm) used in our model is in agreement with the value that is normally used in literature for other oleic-acid coated ferrofluids [21,22]. In our model, the fraction of solvent penetration into the oleic acid shell x (taking the theoretical value of 0.08 x 10^{10} cm^{-2} for the scattering length density of pure oleic acid) was found to

be 0.62. From the fits it appeared that an equal fraction of solvent throughout the whole surfactant layer is a better model than a linear gradient of solvent penetration, where the fraction of solvent is larger at the outside of the surfactant layer. From the fraction of solvent penetration x in the surfactant shell, a rough estimation of the fraction of core surface coverage φ by oleic acid of 0.66 can be made, using the core radius a_{core} (3.48 nm) and thickness of the oleic acid layer L (2.08 nm) as found from the model, and assuming that the surfactant molecules are straight cylinders:

$$\varphi = (x-1)\frac{1-(1+\frac{L}{a_{core}})^3}{3\frac{L}{a_{core}}} \qquad (23)$$

With a cylinder radius equal to an aliphatic C-H bond length of about 1.5 Å, the value corresponds to a packing density of about 2.3 oleic acid molecules per nm^2 which is significantly lower than is found for oleic-acid-coated magnetite particles (~ 3.6/nm^2 [23]).

The nuclear scattering length density of the core found in the model (7.9 x 10^{10} cm^{-2}) lies slightly lower than the theoretical value for pure iron (8.1 x 10^{10} cm^{-2} [24]) and lower than the value for $Fe_{0.75}C_{0.25}$, estimated to be 8.9 x 10^{10} cm^{-2} using a density of 7.58 g/ml [25]. It should be noted that this last value may not be very accurate, since our particles consist of amorphous material, for which the carbon content and the density could only be estimated [19]. The magnetic scattering length density from our model (1.49 x 10^{10} cm^{-2}) is significantly lower than for α-iron (4.6 x 10^{10} cm^{-2} [24]), which is surprising. For our particles, where the nuclear scattering length density is 7.9/8.9 = 0.888 times lower than the theoretical value for Fe_3C and the magnetic scattering length is 1.49/4.6 times lower than for α-iron, the saturation magnetization per volume can be calculated to be 1.49/(0.888 x 4.6) = 0.36 times the value for α-iron (1.71 x 10^6 Am^2 [26]), resulting in a value of 0.62 x 10^6 Am^2. This value is much smaller than the literature value for Fe_3C (1.49 x 10^6 Am^2) that was used to calculate the magnetic particle radius a_M in table 1 from the average magnetic moment obtained from the Langevin curve. Using the calculated value of m_s = 0.62 x 10^6 Am^2 to determine a_M instead, a larger radius of 4.4 nm is obtained. For polydisperse particles, the value obtained for a_M from a Langevin curve is somewhat higher than the number average value $\langle a_M \rangle$, since it equals $(\langle a_M^6 \rangle / \langle a_M^3 \rangle)^{1/3}$ [27]. After correction for polydispersity (using equation (9) with σ = 0.14, from SAXS) a value for $\langle a_M \rangle$ of 4.0 nm is obtained. Unexpectedly, this radius is larger than the radius found from our fitting model (3.48 nm), while usually the magnetic radius is somewhat smaller than the physical radius due to the presence of a non-magnetic surface layer [28]. This result also influences the determination of magnetic particle radii for other iron dispersions (as described in chapter 3), since in these cases we also used the literature value for m_s. However, it has to be considered that the determination of m_s made here is only based on a measurement on one particular dispersion (OA3) with a single technique, which makes the exact value of m_s

somewhat uncertain.

Although the fits for non-interacting particles agree fairly well with our experimental data, some effect of the magnetic field on particle structure was observed in SAXS measurements on dilute samples of the same concentration as used for SANS, showing a different intensity in the horizontal and vertical direction at low q (< 0.45 nm^{-1}, up to about 25% difference at the lowest q-value of 0.15 nm^{-1}). However, this effect does not seem to be very strong, as the particles show Langevin behaviour of single-domain non-interacting dipoles (figure 9), from which a particle size was determined (4.0 nm) that still corresponds reasonably well with that of single particles.

When the same particles are exposed to air, an oxidized layer is formed at the surface of particles of approximately 1.4 nm. The total particle size (core + oxide shell= 4.1 nm) is significantly larger than for the non-oxidized core (3.5 nm), most probably because the density of the oxidized layer is lower than before oxidation. Increase of the particle size upon oxidation was also found from separate SAXS-measurements on a similar dispersion and from measurements of particle sizes on TEM-micrographs (chapter 3). From the fit parameters of the oxidized and non-oxidized particles it can be calculated that the volume of the oxidized layer has increased with a factor of 2.3 due to oxidation. This is in reasonable agreement with what is expected for conventional iron oxides (e.g. a factor 2.1 for transforming Fe into Fe_3O_4). As expected, the scattering contrast of the oxide layer is somewhat lower than for non-oxidized iron (see table 2). In addition, no magnetic scattering is present from the oxide layer, indicating that a non-ferromagnetic oxide has been formed. This is in agreement with measurements on similar dispersions of the magnetic susceptibility upon oxidation, showing such a large decrease in time, that formation of a magnetic oxide is not very plausible (chapter 3).

There are important indications that oxidation decreases the colloidal stability of the particles. As mentioned earlier, the scattering curves for oxidized dispersions could not be fitted properly at low q-values, since all curves showed a steep upturn in this region (figure 5, left side of dotted line), which is a clear sign of aggregates. Also the Guinier plot for the oxidized system is extremely steep at low q-values (figure 8), giving a radius of gyration of many times the single particle value. However, the radius of gyration of single particles can still be determined from a Guinier fit at slightly higher q-values (figure 8); this R_g (3.2 nm) corresponds well with the value that is expected from the fitting parameters for the oxidized particles (3.1 nm, using equation (6)). Presumably, the decrease in surfactant density (scaling with a^{-2}, in our case with a factor of 1.4) due to increase of the particle radius upon oxidation, destabilizes some particles, resulting in aggregation. Whereas the scattering curves (figure 5) at higher q-values (> 0.25 nm^{-1}) can be fitted with a model of single core-2shell particles (see results section), an additional contribution of small aggregates (a = 8.3 nm, lognormal distribution with $\sigma = 0.52$) is needed to fit the curves well at low scattering angles. Since the fitting values for ϕ and η of the aggregates are dependent on each other and are not known from other techniques, it is not possible to obtain information

about the composition and concentration of the aggregates. Concerning this it should be mentioned that the volume fraction of single particles in the model we used for oxidized particles (for $q > 0.25$ nm^{-1}) is significantly smaller than is expected from the value for elemental analysis (table 1). Note that this is partly due to the fact that in our model solely the size of the non-oxidized cores is incorporated in the value for ϕ. From the discrepancy left after correction of ϕ for the above effect (with approximately a factor of 2), one could theoretically derive the volume fraction of aggregates in the oxidized dispersion, assuming that the total volume fraction of aggregates and single particles is equal to the value derived from elemental analysis. However, for our fitting contribution of aggregates ($q < 0.25$ nm^{-1}), this then yields a value for η ($\sim 1.5 \times 10^{10}$ cm^{-2}) that is much lower than would be expected from aggregates of iron particles coated with oleic acid. Probably, also larger aggregates that have sedimented to the bottom of the container were present in the dispersion of oxidized particles, resulting in an apparently lower concentration from the SANS measurements. Despite the fact that the exact compostion, shape and concentration of clusters cannot be derived from our curves, it is clear that the contribution of aggregates does not influence the fits at higher q-values, indicating that the scattering curves can be treated as consisting of two separate parts; at high q the scattering results from single core-2shell particles, whereas the intensity at lower q arises from scattering of aggregates.

6. Conclusions

The internal structure of oleic-acid-coated iron particles in ferrofluids was derived by SANS and SAXS measurements. Our particles can be modelled by non-interacting core-shell particles with lognormal distribution of the iron cores and partial penetration of the surfactant shell by the solvent. The particle sizes, volume fraction of particles and scattering length densities correspond well with those expected from theory and other experimental techniques. On the basis of our model, the packing density of oleic acid on the particle surface was estimated to be 2.3 molecules/nm^2. Accurate fitting of the data with our model shows that the dilute ferrofluids consist of superparamagnetic dipoles, where interparticle interaction is negligible. This picture is confirmed by the Langevin behaviour of the particles, as found from both SANS and magnetization measurements. Unexpectedly, the value found from SANS for the saturation magnetization of our particles was found to be significantly lower than the literature value for Fe_3C. However, this finding should be considered with some reservation since it results in a magnetic particle size that is somewhat larger than the physical particle size found from scattering. Upon exposure to air, an oxidized layer is formed around the particles, which causes the total particle radius to increase due to decrease of the mass density. Oxidation also causes aggregation of the particles, presumably because of decrease of the surfactant density at the particle surface. Nevertheless, SANS curves of dispersions of oxidized particles could be treated as

consisting of two separate parts, which could be fitted by a contribution of aggregates ($q < 0.25$ nm^{-1}) and a core-2shell model of single particles ($q > 0.25$ nm^{-1}).

Acknowledgements

Armin Hoell, Martin Kammel and Albrecht Wiedenmann of BENSC are greatly thanked for their help with the SANS measurements, the analysis of the SANS data and carefully reading the manuscript. Andrei Petukhov is thanked for his help with the SAXS experiments and for helpful discussions. This work was supported by the European Union under Human Potential Program HPRI-CT-2001-00138. Financial support was also granted by the Dutch Technology Foundation (STW) with financial aid from the Council for Chemical Science of the Netherlands Organization for Scientific Research (CW/NWO).

References

[1] Butter K, Bomans P H, Frederik P M, Vroege G J and Philipse A P 2003 *Nature Materials* **2** 88.
[2] Butter K, Bomans P H, Frederik P M, Vroege G J and Philipse A P 2003 *J. Phys.: Condens. Matter* **15** S1451.
[3] *Small Angle X-ray Scattering*; Glatter O and Kratky O, Eds.; Academic Press Inc.: London, 1982.
[4] Feigin L A and Svergun D I 1987 *Structure Analysis by Small-Angle X-Ray and Neutron Scattering* (New York: Plenum Press).
[5] Hayter J B 1991 *J. Chem. Soc. Faraday Trans.* **87** 403.
[6] Wiedenmann A 2001 *Physica B* **297** 226.
[7] Dhont J K G 1996 *An introduction to dynamics of colloids* (Amsterdam: Elsevier).
[8] Kruif de C G, Briels W J, May R P and Vrij A 1988 *Langmuir* **4** 668.
[9] Pynn R 1992 in *Studies of Magnetic Properties of Fine Particles and their Relevance to Materials Science*; Dormann J L and Fiorani D Ed.; Amsterdam: Elsevier Science Publishers B.V.; pp 287.
[10] Wiedenmann A 2000 *J. Appl. Cryst.* **33** 428.
[11] Keller T, Krist T, Danzig A, Keiderling U, Mezei F and Wiedenmann A 2000 *Nuclear Instruments and Methods in Physics Research A* **451** 474.
[12] Keiderling U and Wiedenmann A 1995 *Physica B* **213&214** 895.
[13] Wagner V, Friedrich H and Wille P 1992 *Physica B* **180&181** 938.
[14] Friedrich H, Wagner V and Wille P 1989 *Physica B* **156&157** 547.
[15] Borsboom M, Bras W, Cerjak I, Detollenaere D, Glastra van Loon D, Goedtkindt P, Konijnenburg M, Lassing P, Levine Y K, Munneke B, Oversluizen M, van Tol R and Vlieg E 1998 *J. Synchotron Rad.* **5** 518.
[16] Heenan R K 1998 *Rutherford-Appleton Laboratory* **report 89-129**.
[17] Kohlbrecher J 2000 *Berlin Neutron Scattering Centre (BENSC)*.
[18] Bras W 1998 *J. Macromol. Sci.-Phys.* **B37(4)** 557.
[19] Goossens A, de Jongh L J, Butter K, Philipse A P, Crajé M W J and van der Kraan A M 2002 *Hyperfine Interactions* **141/142** 381.
[20] Petukhov A V, Aarts D G A L, Dolbnya I P, de Hoog E H A, Kassapidou K, Vroege G J, Bras W and Lekkerkerker H N W 2002 *Phys. Rev. Lett.* **88** 208301.
[21] Ewijk van G A, Vroege G J and Philipse A P 2002 *J. Phys.: Condens. Matter* **14** 4915.
[22] Wiedenmann A 2002 in *Lecture notes on Physics*; Odenbach S, Ed. Springer Verlag; pp 33.
[23] Ewijk van G A, Vroege G J and Philipse A P 1999 *J. Magn. Magn. Mater.* **201** 31.

[24] Shen L, Stachowiak A, Fateen S K, Laibinis P E and Hatton T A 2001 *Langmuir* **17** 288.

[25] Bauer-Grosse E and Le Caër G 1987 *Philosophical Magazine B* **56** 485.

[26] Jiles D 1995 *Introduction to Magnetism and Magnetic Materials* (London: Chapman & Hall).

[27] Berkovski B and Bashtovoy V 1996 *Magnetic fluids and applications handbook* (New York: Begel House Inc.).

[28] Rosensweig R E 1985 *Ferrohydrodynamics* (Cambridge: Cambridge University Press).

5 Small angle X-ray scattering of iron dispersions: influence of concentration and magnetic field

Abstract

A series of three dispersions of oleic-acid-coated iron particles with different average core sizes (2-4.5 nm) was studied using Small Angle X-Ray Scattering (SAXS). Dilute dispersions were found to consist of single non-interacting particles; their scattering patterns could be fitted with form factors of spheres with narrow lognormal size distributions, yielding fitting parameters that were consistent with other measurements. For higher concentrations, the smallest particles were found to interact like hard spheres, while the structure factors of only slightly larger particles contained a significant contribution of attractions; scattering curves could be fitted well using the structure factor for a relatively long-ranged shallow square-well potential. Only the largest particles were influenced by a magnetic field. Here, the scattering patterns differed in the directions parallel and perpendicular to the field, which could be explained by alignment of the slightly anisotropic particles and a tendency to chain formation between particles in the magnetic field.

1. Introduction

This chapter describes Small Angle X-ray Scattering measurements on a series of three dispersions of iron particles of different sizes (2-4.5 nm range) coated with an oleic acid surfactant layer. The synthesis and particle characterization of the same dispersions is already presented in chapter 3 where, among other things, SAXS measurements on dilute samples are presented, from which the radii of gyration (and the corresponding Guinier radii) and Porod radii of the particles were determined. In addition, chapter 4 describes (X-ray and neutron) scattering measurements on one of the (dilute) dispersions (both before and after oxidation), which allowed a precise determination of the composition of both non-oxidized and oxidized particles. It appeared that particle sizes could be controlled by variation of the ratio of reactants. Particles were found to consist of a $Fe_{0.75}C_{0.25}$ core and a stabilizing oleic acid layer of about 2 nm. Upon exposure to air, it was established that particle sizes increased due to formation of a layer of non-magnetic iron oxide on their surfaces. In this chapter, besides providing an extension of the SAXS study of dilute dispersions, we study the structural behavior of particles as a function of size and concentration and investigate the influence of a magnetic field. Since dipolar attractions between particles are very sensitive to size, the interparticle structure is expected to significantly change with the radius of magnetic colloids. For theoretical background of scattering measurements is referred to chapter 3 (SAXS) and 4 (SAXS and SANS). In addition, SAXS-measurements on a series of dispersions of PIB-coated iron particles with different particles sizes, are presented in the appendix of this chapter.

2. Experimental

SAXS measurements were performed on three dispersions of oleic-acid-coated iron particles differing in average core sizes. They were synthesized by thermal decomposition of ironpentacarbonyl in the presence of oleic acid as a surfactant. For detailed information is referred to chapter 3. Here, the core sizes determined from various techniques, as described and discussed in chapter 3, are given in table 1. This table includes the radii of gyration (and corresponding Guinier radii) as well as the Porod radii determined from the same series of SAXS measurements as will be described here. Dispersions OA1 and OA2 were also measured after oxidation and the corresponding particle radii are given in table 1 as well.

SAXS measurements were performed at the hard branch of the DUBBLE (Dutch-Belgian beamline) at the ESRF. The measurements were performed on stock dispersions OA1 to OA3 (concentrations are presented in table 2), as well as on samples obtained by dilution of these (concentrations are indicated by the reciprocal dilution factor right before the symbol C (indicating the stock concentration), e.g. a two-times-diluted sample is indicated as 0.5C).

All dispersions were always treated and stored under dry nitrogen atmosphere (using a glovebox) to avoid oxidation of the particles. Samples were prepared in the glovebox in airtight closed glass capillaries. The wavelength of the X-rays and the sample-detector distance were 0.103 nm and 7.8 m respectively (for dispersion OA1) and 0.13 nm and 1.9 m respectively (for dispersions OA2 and OA3) resulting in q-ranges of 0.076-1.65 nm^{-1} (for dispersion OA1) and 0.15-2.9 nm^{-1} (for dispersion OA2 and OA3). The measured two-dimensional scattering patterns were corrected for transmission and detector response, after which they were in general radially integrated to obtain 1-dimensional curves of the intensity versus q. All measured intensities are in arbitrary units and have only relative relevance. However, it appeared from the analysis that also the (total) relative intensity of the scattering patterns was not always trustworthy. In many cases the subtraction of the background signal (capillary with solvent) from these curves was not straightforward; the background signal had to be multiplied with a correction factor before subtraction in order to avoid negative intensity values and to obtain equally shaped curves (at high q-values) for different concentrations. The background subtraction was especially problematic for dispersion OA3, where correction factors down to 0.65 were used. Scattering curves were scaled to concentration. Often additional corrections had to be performed; curves were multiplied with a factor of the order of 0.9-1.1, but in some cases larger correction factors (between 0.65 and 1.8) were necessary. From the curves finally obtained, it was found that our correction procedure worked out well, as will be further discussed in section 3.

Table 1. Size of the oleic-acid-coated iron particles.

Code	a_{TEM}[1](nm)	R_g[2] (nm)	a_G[3] (nm)	a_P[4] (nm)	a_M[5] (nm)	$R_{g,OX}$[2] (nm)	$a_{P,OX}$[4] (nm)
OA1	2.2 ± 0.3	1.5 ± 0.03	2.0 ± 0.04	-	1.2	2.1 ± 0.04	2.8 ± 0.06
OA2	3.2 ± 0.3	2.3 ± 0.05	2.9 ± 0.06	2.9 ± 0.06	2.4	2.6 ± 0.05	3.6 ± 0.07
OA3	4.3 ± 0.3	3.0 ± 0.06	3.9 ± 0.08	3.8 ± 0.08	3.3	-	-

[1]Particle radius measured from TEM-micrographs. [2]Radius of gyration as determined from Guinier curves. [3]Guinier radius as determined from radius of gyration, not corrected for polydispersity. [4]Porod radius as determined from maxima in Porod plot. [5]Magnetic radius determined from magnetization curves. Note that the uncertainty in radii obtained from SAXS is due to the measurement method and does not reflect the polydispersity of the sample.

Table 2. Concentration in stock dispersions of oleic-acid-coated iron particles.

Code	Fe amount (Mass fraction)[1]	$Conc._{AGM}$ (particles/l)[2]	ϕ_{EA}[3]	ϕ_{AGM}[4]	$\phi_{theoretical}$[5]
OA1	0.0824	$3.1 * 10^{20}$	0.0056	0.014	0.046
OA2	0.0587	$1.0 * 10^{21}$	0.064	0.14	0.13
OA3	0.257	$1.4 * 10^{20}$	0.045	0.047	0.049

[1]Amount of iron in dispersion from elemental analysis (gFe/g dispersion). [2]Particle concentration determined from AGM measurements using the values for M_s, μ and sample volume. [3]Iron volume fractions using results from elemental analysis and a density for $Fe_{0.75}C_{0.25}$ of 7.58 g/cm^3 [13] . [4]Iron volume fractions using results from column 3 and the TEM-radius. [5]Theoretical iron volume fraction using the amount of $Fe(CO)_5$ used in the synthesis and a density for $Fe_{0.75}C_{0.25}$ of 7.58 g/cm^3 [13].

Curves of dilute dispersions were fitted by a (not-normalized) form factor of spheres with core radius a_{core}:

$$F^2(q) = \frac{4\pi}{q^3}\left[\Delta\eta(\sin(qa_{core}) - qa_{core}\cos(qa_{core}))\right]^2 \quad (1)$$

with q the scattering vector and $\Delta\eta$ the scattering contrast. A lognormal size distribution $P(a_{core})$ was employed with standard deviation σ and number average particle radius $\langle a_{core}\rangle$:

$$P(a_{core}) = \frac{1}{\sqrt{2\pi\sigma^2}}\frac{1}{a_{core}}\exp\left[\frac{-\left(\ln\frac{a_{core}}{\langle a_{core}\rangle}\right)^2}{2\sigma^2}\right] \quad (2)$$

using the software program SASFIT [1]. For these fits, the scattering of the surfactant layer was neglected, since its contrast with the solvent is very low.

Effective structure factors of concentrated dispersions were obtained by division of their scattering curves by those of the most dilute ones after scaling with concentration. The obtained experimental structure factors were fitted by the structure factor for polydisperse hard spheres as described in [2] using a computer program developed by van Beurten and Vrij [3]. We also calculated structure factors for attractive spheres, where the hard sphere repulsion was supplemented by a simple square-well potential, with depth ε over a range λd with d the particle diameter (figure 1):

$$U(r) = \begin{cases} \infty & r < d \\ -\varepsilon & d < r < (\lambda+1)d \\ 0 & r > (\lambda+1)d \end{cases} \quad (3)$$

Here, r is the centre-centre distance between two particles. The Fourier transform of the direct correlation function, within the mean spherical approximation, is a relatively simple expression obtained by Sharma and Sharma [4], and used here to fit our experimental data of S(q).

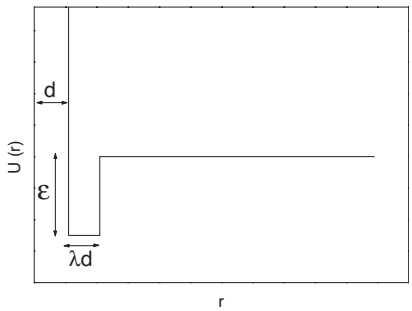

Figure 1. Square-well potential with depth ε and range λd.

To study the effect of magnetic fields on our dispersions, they were also measured in fields up to 100 mT (OA1) or 1.5 T (OA2 and OA3). In these cases the two-dimensional patterns were integrated separately in the direction parallel and perpendicular to the field over an angle of 10 degrees. For comparison, scattering patterns were also radially averaged.

3. Results and Discussion

3.1. Dilute dispersions

Figure 2 presents the scattering curves of our three dispersions for different concentrations after all corrections as described in the experimental section. As can be seen, all curves of one dispersion have equal shapes and intensities at high q-values, showing that our correction procedure worked out well. At lower q-values, the more concentrated dispersions clearly show structure as caused by interparticle interactions. The concentration of the most dilute systems is such that no interparticle interaction is expected and observed. All curves can be reasonably well fitted by the form factor of spheres with a lognormal size distribution

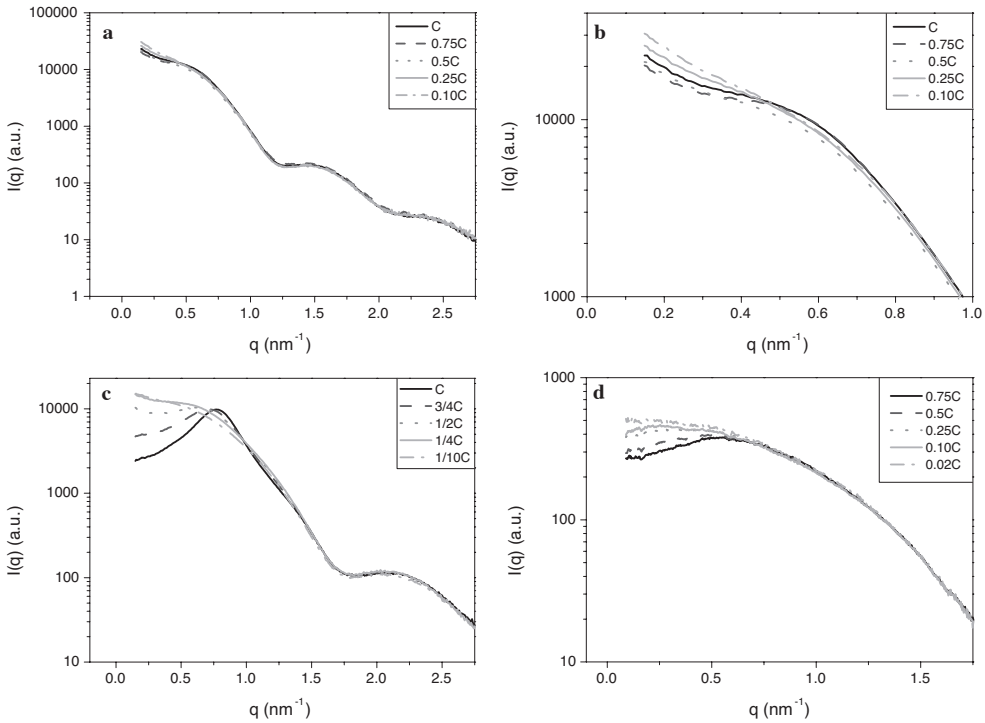

Figure 2. Scattering intensities in zero field for different particle concentrations. **a.** dispersion OA3 **b.** Zoom of figure a **c.** dispersion OA2 **d.** dispersion OA1. Background and blank (capillary with solvent) scattering were subtracted and curves were corrected for concentration.

(equations 1 and 2, figure 3). The contrast of the surfactant shell is negligible compared to that of the core and is not included in the form factor. Parameters used in our fits are indicated in the figure caption and agree reasonably well with results from other techniques (see table 1). In general, the particle radii obtained from our fits are slightly lower than the Guinier and Porod radii, which are given by $(\langle a_{core}^8\rangle/\langle a_{core}^6\rangle)^{1/2}$ [5,6] and $\langle a_{core}^7\rangle/\langle a_{core}^6\rangle$ [7] respectively. This is presumably due to polydispersity, which will increase the above moments of the distribution. The TEM-radius is also somewhat larger than the radii obtained from the fits, probably because this technique is less sensitive to small particles. This could also explain the somewhat higher polydispersity found from our fits in comparison with TEM.

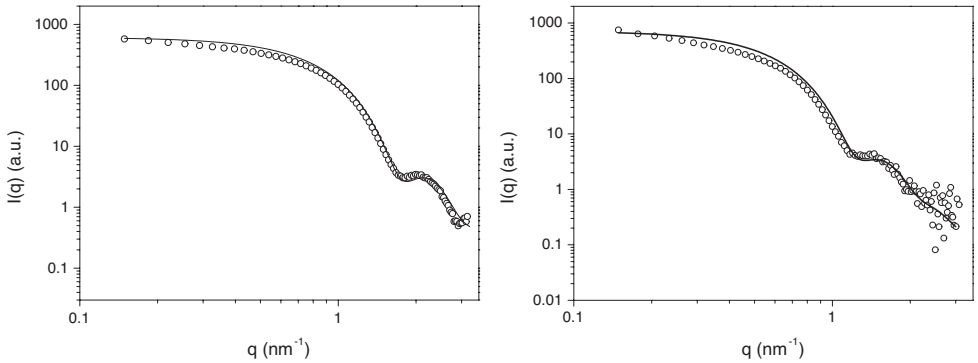

Figure 3. Scattering curves of dispersions OA2 (0.02C, left) and OA3 (0.02C, right). The solid lines are the calculated form factors of spheres with lognormal size distribution. Parameters: OA2: a_{core}= 2.5 nm, σ = 0.13, OA3: a_{core}= 3.5, σ = 0.14 Dispersion OA1 (not shown) could be fitted reasonably well with parameters a_{core}= 2.0 nm, σ = 0.10

Figure 4 shows an illustrative example of the clear increase of particle size upon oxidation of dispersion OA2, which was found for all dispersions; for the oxidized sample the minima in the form factor are shifted to lower q-values in comparison with the particles before oxidation. This is also reflected in the larger radii of gyration and Porod radii for oxidized particles (table 1).

3.2. Concentrated dispersions

The structure factors obtained from the scattering curves of dispersion OA1 (figure 5) can be fitted reasonably well with structure factors for polydisperse hard spheres (a_{core} = 2.2 nm, σ = 0.2) including a surfactant layer without contrast of 1.2 nm. The fitting parameters correspond well with values from other techniques (see table 1). It has to be noted that a small polydispersity does not influence the structure factors significantly; curves could equally well be fitted with structure factors for monodisperse particles. Also the volume fractions (including a surfactant layer) as used in the fits are in the range of the values

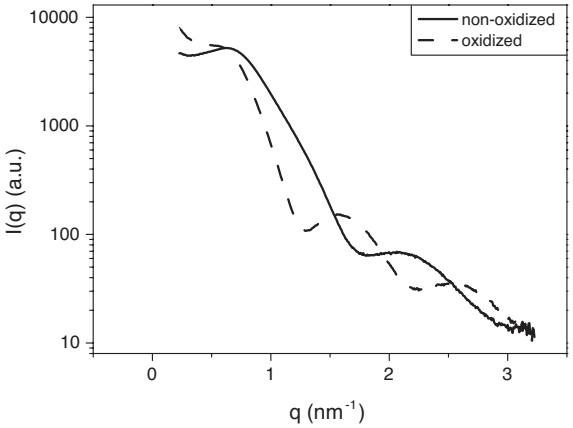

Figure 4. Scattering intensities of dispersion OA2 (0.5C) before and after exposure to air. The minima in the form factor are clearly shifted to lower q-values upon oxidation.

calculated (by including the volume of a layer of oleic acid of 1.2 nm) from those of the iron cores in table 2 (except for small errors in the concentration upon dilution). However, note that the values for the volume fraction obtained from elemental analysis and magnetization measurements (table 2) differ significantly, pointing to a considerable uncertainty in the concentration.

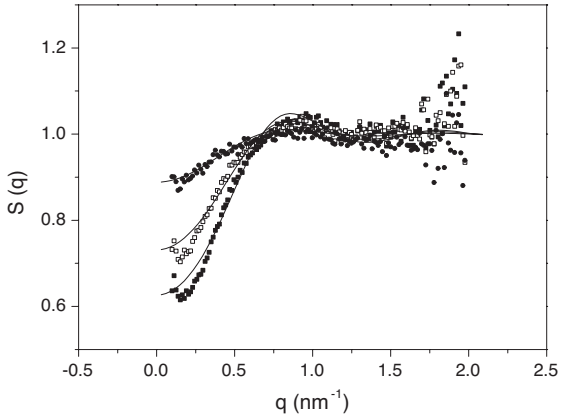

Figure 5. Experimental structure factors of dispersion OA1 for concentrations 0.75C (■), 0.5C (□) and 0.25C (●). The solid lines are fits of structure factors for hard spheres with lognormal size distribution and a surfactant layer (without contrast) of 1.2 nm (a_{core} = 2.2 nm, σ = 0.2). The volume fractions used in the fits are 0.06, 0.04 and 0.0015.

The thickness of the oleic acid layer used in our fit (1.2 nm), is smaller than the value found from SANS measurements (2.1 nm) on dispersion OA3 (using contrast variation, described in chapter 4). Probably this is due to the fact that from SANS measurements the solvent was found to penetrate the surfactant layer partly, which was not taken into account

in our fit here. In addition, the value of 1.2 nm, obtained via the spacing between particles as determined from the structure factors, is the thickness of the steric repulsion layer, which is not necessarily the same as the thickness of the surfactant layer having contrast in dilute dispersions.

The interparticle structure of dispersion OA2 significantly deviates from that of monodisperse hard spheres. Polydispersity cannot account for this discrepancy, as is seen in figure 6, showing the experimental curves together with the optimised fits with a structure factor of polydisperse hard spheres with lognormal size distribution (parameters can be found in the figure caption). Although the first peak positions agree well, the scattering at low q-values is much higher than expected for hard spheres. In addition, the peak positions of the second peak of the fit for hard spheres are shifted compared to those of the experimental data. Especially the scattering at low q-values (the value at S (q = 0) is a measure for the compressibility) suggests that an attraction is present between the particles. It appeared that the scattering curves could be surprisingly well fitted (figure 7) with the structure factor of the square-well potential for monodisperse attractive spheres (equation (3)), although at the expense of the agreement between the ratios of the volume fractions of the different samples involved (see fit parameters in captions of figures 6 and 7). The absolute volume fractions (including surfactant layer) used in the fits including attraction are in the range of the values calculated from the volume fractions of iron cores (table 2) including a surfactant layer of 1.2 nm, although a significant difference is present between the numbers in table 2 for different measuring techniques. The quality of the fits turned out to be rather sensitive to the chosen parameters, accurate fits were only obtained using a well depth ε of 0.35 kT with a range of $\lambda d = 0.4d$ ($d = 7.7$ nm, including a surfactant layer). The value for the minimal centre-to-centre distance d between two particles enables one to estimate the thickness of the oleic acid layer by subtraction of the core diameter (5.0 nm) as 1.35 nm, in good agreement with the value found for dispersion OA1. The relatively long range of the attraction, characteristic for dipolar attractions, seems to be realistic. The depth of the well ε can be estimated by calculation of the attraction potential for our particles. The dipolar interaction $U_{dipolar}$ between two dipoles depends on the size and orientation of their dipole moments $\vec{\mu}$ and the centre-to-centre distance $\vec{r}$ [8]

$$U_{dipolar} = \frac{\mu_0}{4\pi}\left(\frac{\vec{\mu}\cdot\vec{\mu}}{r^3} - \frac{3\left(\vec{\mu}\cdot\vec{r}\right)^2}{r^5}\right) \qquad (4)$$

The maximal dipolar attraction $U_{max,dipolar}$ (oriented head-to-tail at distance $r = d = 7.7$ nm) between two particles is given by [8]

$$U_{max,dipolar} = -\frac{\mu_0}{2\pi}\frac{\mu^2}{r^3} \qquad (5)$$

and is of the order of 0.8 kT for particles from dispersion OA2 (with $\mu = 8.7 \times 10^{-20}$ Am^2,

value from chapter 3, table 2). The dipolar interaction averaged over all orientations of the dipoles, will be somewhat lower than this value. The maximal van der Waals attraction [9] (at closest distance, using a value for the Hamaker constant of iron in organic solvents $A = 10^{-19}$ J [8]) is approximately only 0.2 kT and has a much shorter range (at r = 2d, the van der Waals attraction is only 0.001 kT, while the dipolar attraction is still 0.1 kT), so it does not influence the total interaction potential strongly. Here we approximate the anisotropic dipolar attraction, decreasing with interparticle distance, by an isotropic square well potential with a constant (average) depth of the attraction potential of 0.35 kT, which seem to be a reasonable value. Presumably, this approximation is possible due to the small values of attractions involved. For the relatively small concentration of our dispersions, a pair potential neglecting many-body interactions appears to be a good approximation.

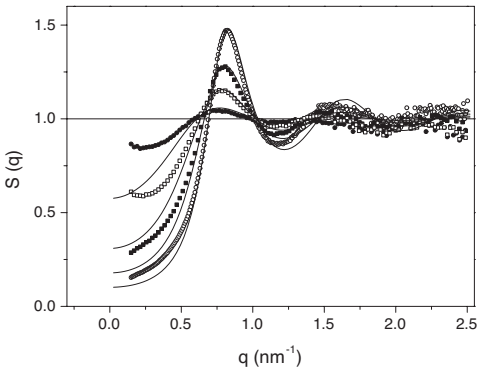

Figure 6. Experimental structure factors of dispersion OA2 for concentrations C (○), 0.75C (■), 0.5C (□), 0.25C (●). The solid lines are fits of structure factors for hard spheres with lognormal size distribution and a surfactant layer (without contrast) of 1.05 nm (a_{core} = 2.8 nm, σ = 0.1). The volume fractions used in the fits are 0.29, 0.22, 0.15 and 0.07.

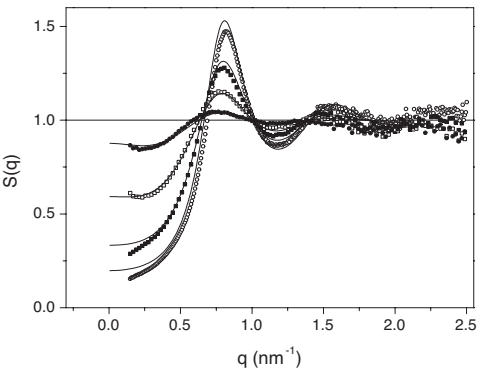

Figure 7. Experimental structure factors of dispersion OA2 for concentrations C (○), 0.75C (■), 0.5C (□), 0.25C (●). The solid lines are fits of structure factors for monodisperse attractive spheres with a square-well potential (equation (3)) of ε = 0.35 kT and λ = 0.4d, d = 7.7 nm. The volume fractions used in the fits are 0.24, 0.17, 0.099 and 0.033.

Calculation of the second virial coefficient B_2 [10]

$$B_2 = B_2^{HS} + 2\pi\int_d^\infty (1 - e^{-U(r)/kT})r^2 dr \qquad \text{with } B_2^{HS} = \frac{2}{3}\pi d^3 \tag{6}$$

for this square-well potential (equation (3)) gives a value that is significantly smaller (0.27 times) than the coefficient for hard spheres B_2^{HS}, but is still positive, showing that the interactions in this dispersion are still predominantly repulsive due to the hard sphere contribution. Summarizing, we see that small magnetic particles (dispersion OA1) behave like hard spheres; presumably dipolar interactions are so small that they do not influence the particle structure. However, for somewhat larger particles (OA2), the particle structure is

certainly influenced by dipolar attractions, but these are small enough to be approximated by a relatively long-ranged shallow square-well potential. Indeed, cryo-TEM pictures (not shown) of both dispersions OA1 and OA2 do not show signs of large interparticle attraction (e.g. chain formation or the presence of isotropic clusters).

Since for dispersion OA3 the background subtraction and correction for concentration were problematic, we felt that fitting of these data to theoretical structure factors would not be meaningful. However, it was certainly possible to compare the different structure factors obtained via identical data reduction procedures (e.g. from measurements on the same sample with or without magnetic field) with each other. This will be discussed in the next paragraph.

3.3. Influence of Magnetic Field

For dispersions OA1 and OA2 no influence of a magnetic field (up to 100 mT for dispersion OA1 or 1.5 T for dispersion OA2) was detected. Scattering patterns that were integrated parallel or perpendicular to the field did not show any difference and the same holds for radially averaged curves of measurements with or without field on the same sample (figure 8). This was valid for all concentrations. Presumably, the dipole moments of particles OA1 and OA2 are too small for the particle structure to be influenced, even when particles are completely aligned (which is expected for dispersion OA2 in a field of 1.5 T).

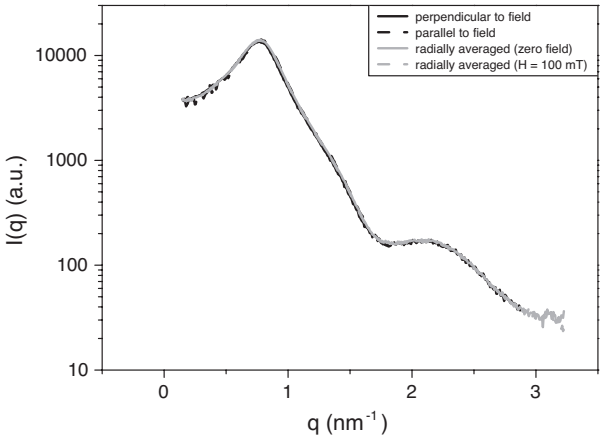

Figure 8. Scattering intensities of dispersion OA2 (C) in a magnetic field of 100 mT integrated parallel and perpendicular to the field. The q-range perpendicular to the field is larger than parallel to the field because the beamstop was not positioned in the center of the two-dimensional detector. The radially integrated scattering intensity (in zero field and in a field of 100 mT) is also presented. No significant difference between the curves was observed for dispersions OA1 and OA2 for all fields and concentrations.

However, dispersion OA3 is clearly influenced by a magnetic field. Figure 9 shows the scattering curves of the most concentrated sample in a field of 1.5 Tesla integrated parallel

and perpendicular to the field. First, a rather subtle effect is seen at a q-value of about 1.3 nm^{-1}, where the minimum in the form factor is positioned at a slightly lower q-value for the curve parallel to the field. The difference between the positions of the minima is estimated as 5-10 % (for the highest field and largest concentration). This can be explained by the fact that our particles are not perfectly spherical (as seen on TEM pictures); it is known that dipole moments in magnetic particles are preferably oriented in the longer particle direction due to shape anisotropy. This causes particles to align their long axes parallel to a magnetic field, which results in effectively larger particles (with the minima in the form factor at lower q-values) in the direction parallel than perpendicular to the field.

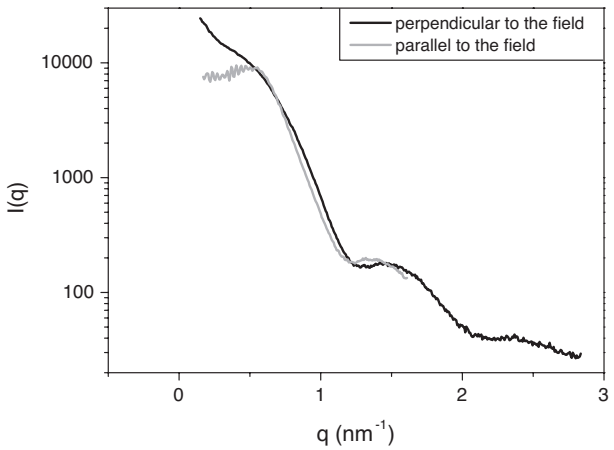

Figure 9. Scattering intensities of dispersion OA3 (C) in a magnetic field of 1.5 T integrated parallel and perpendicular to the field. The q-range perpendicular to the field is larger than parallel to the field, because the beamstop was not positioned in the center of the two-dimensional detector. Differences are discussed in the text.

A very obvious effect of the field is observed in figure 10, where the peak in the structure factor parallel to the field of dispersions OA3 (figure 10) is much more pronounced than perpendicular to the field; particles are more structured in the field direction. The peak position in the parallel direction is at approximately 0.61 nm^{-1}, corresponding to a characteristic particle distance of 10.3 nm, which is of the order of a particle diameter including surfactant layer. This structure peak presumably is due to a tendency to chain formation in the field direction, which is induced by the magnetic field due to the increase of the dipolar interactions on alignment of the particles. Note that these chains are expected to only consist of a few particles, and most likely a considerable part of the colloids is still present as single particles since dipole-dipole interactions are less than 1 kT. In the perpendicular direction, some structural ordering at approximately the same interparticle distances is present, but is much less important due to smaller dipole-dipole interactions, resulting in the presence of a less pronounced first peak at a similar q-value as for the parallel direction.

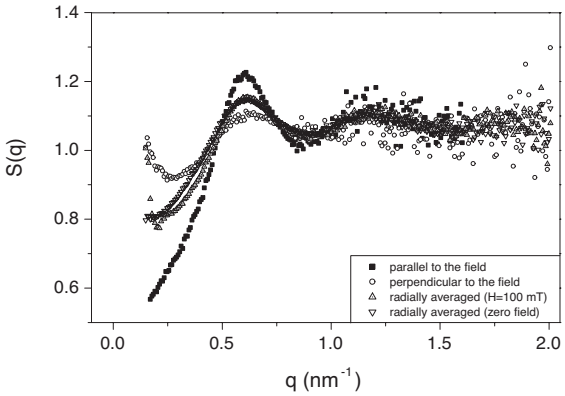

Figure 10. Structure factors of dispersion OA3 (C) in a magnetic field of 100 mT parallel and perpendicular to the field. Differences are discussed in the text.

Another important effect of the field is the scattering intensity at small q-values (down to 0.17 nm^{-1}, see figures 9 and 10), corresponding to a length scale of a few particle diameters, which is distinctly lower in the direction parallel to the field. On this intermediate length scale, the particle-particle position correlation is enhanced in the direction of the field as was seen from the structure factor peaks. Looking at a single chain with its long axis in the field direction, the scattering of the individual particles within the chain will be coherent in the lateral direction adding up to n^2 times the scattering of a single particle (for a perfectly aligned chain consisting of n particles). However, in the field direction, due to the different positions of all particles in the chain, the scattering will be out of phase and partly cancel, resulting in a lower scattering intensity at these q-values. In our case, the dispersion still consists of many single particles, and the effect at low q-values (> 0.17 nm^{-1}) seen in figures 9 and 10, is caused by the presence of part of the colloids in chains. Note that chain-chain interactions would be reflected at much smaller q-values (which we could not measure), but are expected to be small due to the weak dipolar interactions. For lower fields the same effects as described above were found, but they were less pronounced. The same holds for dispersions with lower concentrations.

The structure factors obtained by radial integration of the scattering patterns in the field and in zero field are in between those in the horizontal and vertical direction, because of averaging of the field effects in all directions. Perhaps, one would naively expect both scattering patterns to be equal. However, the slight difference between those two (around q = 0.3 nm^{-1}, as seen in figure 10) might be qualitatively understood using the Porod invariant [11], which tells that the total scattering intensity integrated over all q-values in three dimensions should be a constant independent of the arrangement of particles. In our case, the particle arrangement in a field is expected to be cylindrically symmetric; in the three-dimensional reciprocal space, the decrease of the scattering intensity in the field direction is compensated by a weaker increase in each of the two orthogonal directions, from which only one is probed in the scattering experiment (although for the Porod invariant

one should in principle take into account the complete q-range, including wave vectors beyond the experimentally accessible range).

Note that our results are somewhat different from what was found by Gazeau [12] et al from SANS measurements in magnetic fields of aqueous ferrofluids of charged cobalt ferrite colloids (whereas our particles are sterically stabilized). Although they also found a lower scattering intensity in the parallel compared to the perpendicular direction at small q-values, the opposite effect was found concerning the structure factor, which was more pronounced in the direction perpendicular to the field. From this they concluded that no particle chains were formed in their dispersions and repulsion due to charge was the dominant interaction. They explained their results by a Brownian motion of the particles favoured in the direction parallel to the field (resulting in a less structured dispersion in this direction) due to the presence of anisotropic dipolar attractions.

4. Conclusions

Dilute dispersions of oleic-acid-coated iron particles of different average particle sizes (2-4.5 nm) were found to consist of single non-interacting spheres of low polydispersity. The Small Angle X-Ray Scattering data of these dispersions could all be fitted reasonably well with a form factor of spheres with a lognormal size distribution, using fitting parameters that agree well with values found from other techniques and measurements (see tables 1 and 2 and chapter 4). Upon exposure of a dispersion to air, the minima of the form factor seen in the scattering patterns of dilute samples shifted to lower q-values, confirming the increase of particle size upon oxidation found earlier (e.g. chapter 3).

For more concentrated dispersions, the effective thickness of the oleic acid layer (approximately 1-1.5 nm) could be estimated from the structure factor peaks, after subtraction of the core radius, and was in reasonable agreement with results from SANS-measurements (chapter 3) and literature values. Pronounced size effects on the particle structure were found from the SAXS structure factors. Small oleic-acid-coated iron particles (radius ~ 2 nm) were found to behave like hard spheres; apparently dipolar and van der Waals interactions are negligible for these particle sizes. Slightly larger particles (radius ~ 3 nm) are influenced by small (predominantly dipolar) attractions, and their structure factors could be modelled by a shallow, relatively long-ranged square-well potential. Only the largest particles (radius ~ 4 nm) were influenced by a magnetic field. Dispersion OA3 was more structured and at small q showed a lower scattering intensity in the direction parallel than perpendicular to the magnetic field, pointing to a larger particle-particle position correlation in the field direction, which is explained as a tendency to chain formation. In addition, also single particles were found to align with their (slightly) longer axis in the field direction due to shape anisotropy.

Acknowledgements

Andrei Petukhov and Igor Dolbnya are thanked for their help with the SAXS measurements. Andrei Petukhov, Prof. A. Vrij and Stephen Williams are thanked for valuable discussions.

References

[1] SASFIT, Kohlbrecher J BENSC, Berlin, 2000.
[2] Vrij A 1979 *J. Chem. Phys.* **71** 3267.
[3] Beurten van P and Vrij A 1981 *J. Chem. Phys.* **74** 2744.
[4] Sharma R V and Sharma K C 1977 *Physica A* **89** 213.
[5] Dhont J K G 1996 *An introduction to dynamics of colloids* (Amsterdam: Elsevier).
[6] Kruif de C G, Briels W J, May R P and Vrij A 1988 *Langmuir* **4** 668.
[7] Petukhov A V *personal communication*.
[8] Rosensweig R E 1985 *Ferrohydrodynamics* (Cambridge: Cambridge University Press).
[9] Scholten P 1983 *J. Magn. Magn. Mater.* **39** 99.
[10] Hansen J P and Mc Donald I R 1986 *Theory of simple liquids* second ed. (Suffolk: St Edmundsbury Pres Limited).
[11] *Small Angle X-ray Scattering*; Glatter O and Kratky O, Eds.; Academic Press Inc.: London, 1982.
[12] Gazeau F, Dubois E, Bacri J C, Boue F, Cebers A and Perzynski R 2002 *Phys. Rev. E* **65** 031403.
[13] Bauer-Grosse E and Le Caër G 1987 *Philosophical Magazine B* **56** 485.

Appendix

SAXS-measurements on dispersions of PIB-coated iron particles

1. Introduction

This appendix describes SAXS-measurements on a series (A-E) of dispersions of PIB-coated iron particles. The measurements showed that the total relative intensity of the scattering patterns was not always reliable. For this reason, the data analysis (background subtraction and scaling to concentration) was problematic. In addition, the q-ranges in the measurements were narrow, so that only a small part of the curves was available. Since for each sample a very limited amount of concentrations was measured, it was also difficult to obtain clear information from the structure factors. Due to the reasons described above, no quantitative information could be deduced from the measurements. However, some clear qualitative results could be obtained and are presented here.

2. Experimental

SAXS-measurements were performed on a series of iron dispersions of PIB-coated particles differing in average particle radii (dispersions are coded A to E, ordered with

increasing particle size). The synthesis and characterization of the dispersions by various techniques is described in chapter 3. For general experimental methods of the SAXS measurements and analysis of the data is referred to section 2 of this chapter. Samples were all prepared from the stock dispersions (particle size and concentration are indicated in tables 3 and 4) by dilution with solvent (decalin) or concentration by evaporation of the solvent under vacuum atmosphere. Measurements were performed on samples of different concentrations (from 3-4 to 1/30 times the stock concentration) in zero field and in magnetic fields up to 100 mT (occasionally up to 1.5 T). Both non-oxidized samples and samples that were exposed to air for a few days were measured. Because samples were obtained in several measuring sessions, the used wavelength of the X-rays and the sample-detector distances varied, resulting in different q-ranges (0.05-1.35 nm^{-1}, 0.07-1.65 nm^{-1}, 0.04-1.21 nm^{-1} and 0.15-2.9 nm^{-1}).

Table 3. Size of the PIB-coated iron particles.

Code	a_{TEM}[1](nm)	R_g[2] (nm)	a_G[3] (nm)	a_P[4] (nm)	$R_{g,OX}$[2] (nm)	$a_{P,OX}$[4] (nm)	a_M[5] (nm)
A	2.1 ± 0.3	1.7 ± 0.03	2.2 ± 0.04	-	2.2 ± 0.04	2.7 ± 0.6	1.3
B	6.0 ± 0.74	4.1 ± 0.4	5.3 ± 0.5	4.6 ± 0.3	4.6 ± 0.4	5.5 ± 0.6	4.1
C	6.6 ± 1.1	4.7 ± 0.2	6.0 ± 0.3	5.4 ± 0.3	7.0 ± 1.8	6.4 ± 0.5	5.1
D	6.9 ± 1.0	6.8 ± 1.8	8.8 ± 2.4	5.4 ± 0.9	8.2 ± 2.9	6.5 ± 0.9	6.0
E	8.2 ± 1.5	7.4 ± 1.6	9.5 ± 2.1	5.9 ± 0.8	8.7 ± 3.1	7.6 ± 1.5	-

[1]Particle radius measured from TEM-micrographs. [2]Radius of gyration as determined from Guinier curves. [3]Guinier radius as determined from radius of gyration, not corrected for polydispersity. [4]Porod radius as determined from minima in Porod plot. [5]Magnetic radius determined from magnetization curves. Note that the uncertainty in radii obtained from SAXS is due to the measurement method and does not reflect the polydispersity of the sample.

Table 4. Particle concentration in stock dispersions of PIB-coated iron particles

Code	Fe amount (Mass fraction)[1]	$Conc._{AGM}$ (particles/l)[2]	ϕ_{EA}[3]	ϕ_{AGM}[4]	$\phi_{theoretical}$[5]
A	0.004	$1.7 * 10^{19}$	0.00059	0.00066	0.00070
B	0.038	$8.0 * 10^{18}$	0.0049	0.0072	0.0057
C	0.061	$8.2 * 10^{18}$	0.0079	0.0099	0.0098
D	0.108	-	0.015	-	0.018
E	0.219	-	0.027	-	0.029

[1]Amount of iron in dispersion from elemental analysis (gFe/g dispersion). [2]Particle concentration determined from AGM measurements using the values for M_s, μ and sample volume. [3]Iron volume fractions using results from elemental analysis and a density for $Fe_{0.75}C_{0.25}$ of 7.58 g/cm^3 [13] . [4]Iron volume fractions using results from column 3 and the TEM-radius. [5]Theoretical iron volume fraction using the amount of $Fe(CO)_5$ used in the synthesis and a density for $Fe_{0.75}C_{0.25}$ of 7.58 g/cm^3 [13].

3. Results and Discussion

Guinier and Porod radii of the different samples, obtained from scattering curves of dilute samples of both oxidized and non-oxidized particles (table 3), are described and discussed in chapter 3. It appeared that the scattering curves of dilute samples of non-oxidized particles could not be fitted properly with a form factor for polydisperse homogeneous spheres (equations (1) and (2)). Most likely, this is due to the fact that the shape of PIB-coated iron particles deviates from that of a perfect sphere, as can also be seen in TEM- and cryo-TEM pictures of the dispersions (chapters 3 and 6). Indeed, the scattering curves of oleic-acid-coated particles could be fitted reasonably well with the form factor in equations (1) and (2) due to the more spherical shape of these particles (see figure 3). The curves of dispersions D and E showed the presence of structure and a steep increase at very low scattering angles, indicating aggregation of the particles, even at dilute concentrations. This is in agreement with results from cryo-TEM (chapter 6) and magnetic susceptibility measurements (chapter 7), which showed the presence of large (anisotropic) chains in dispersions D and E. Of course, fitting of such curves with a form factor of single non-interacting spheres would not be meaningful.

Comparison of the curves of oxidized dispersions to those of non-oxidized dispersions always showed a shift of the minima in the form factor to lower q-values, which was earlier also found for oleic-acid-coated particles (section 3.1) and was explained by increase of the particle size upon oxidation. The effect was observed for all PIB-samples, although for dispersion A, it was only seen from the measurements performed three months after their synthesis, and not anymore from the measurements performed one year after the synthesis. As is also discussed in chapter 3, the particles A most likely are completely oxidized in this period. This is confirmed by the fact that the radius of gyration in this time has increased from 1.7 nm to 2.2 nm (equal to the value found for the oxidized particles). For none of the samples, a quantitative estimation could be made of the shift of the minima upon oxidation, since the q-range was too small (the first minimum was only partly seen) and the minima very shallow (due to non-sphericity of the particles). The scattering curves of all oxidized dispersions showed an increase of scattering at low q-values, pointing to aggregation due to oxidation. This effect was most clear for dispersions D and E. Presumably, this aggregation is caused by a decrease of the surfactant grafting density, due to increase of the particle size upon oxidation.

All samples were influenced by a magnetic field, except for dispersion A (because these particles were completely transformed into a non-magnetic oxide). For samples B, C, D, and E, the scattering patterns integrated parallel to the field showed a first minimum in the form factor at a lower q-value than for the scattering pattern integrated perpendicular to the field. A similar effect was found for the largest oleic-acid-coated particles (OA3, see section 3.3) and can be explained by shape anisotropy of the particles; for particles that are not completely spherical, the magnetic moments are preferably aligned in the direction of the

longer axis due to shape anisotropy, resulting in a particle that is effectively larger in the field direction upon alignment of the dipoles with this field. A quantitative determination of the shift was difficult due to the small q-range, but for one sample (B (stock), in a field of 1.5 T) a very rough estimate of 20 % shift of the first minimum could be made. This value is somewhat higher than was estimated for OA3 (5-10 % shift for the stock dispersion in a field of 1.5 T), which is expected, since the shape of PIB-coated particles is less spherical than of oleic-acid-coated particles. Contrary to samples B and C, where no significant other (structural) effects of the field were observed, the radially integrated scattering curves of samples D and E measured in a field (compared to the curves in zero field) showed an increase of the scattering at very small q, most likely due to the formation of field-induced aggregates. This behaviour is confirmed by cryo-TEM measurements (chapter 6), where in the presence of a magnetic field, enormous anisotropic aggregates aligned with the field were observed, whereas only much smaller randomly oriented chains were found in zero field.

4. Conclusions

- PIB-coated iron particles are less spherical than oleic-acid-coated particles, and their scattering curves cannot be properly fitted to a form factor for polydisperse homogeneous spheres.
- In dispersions of large particles (D and E), aggregates are present (also in dilute dispersions), consistent with cryo-TEM (chapter 6) and dynamic susceptibility measurements (chapter 7).
- Oxidation of particles causes the particle radius to increase.
- Particles A oxidized completely in a period of one year, despite careful measures to exclude oxygen.
- Larger particles (B, C, D, E) align in a magnetic field, causing the minima in the scattering form factor to shift to lower q-values in the field direction.
- Structural changes due to magnetic fields are only observed in the scattering patterns of particles D and E, in agreement with cryo-TEM results (chapter 6).

6 Direct observation of dipolar chains in ferrofluids in zero-field using cryogenic electron microscopy

Abstract

The particle structure of ferrofluids is studied *in situ*, by cryogenic electron microscopy, on vitrified films of iron and magnetite dispersions. By means of synthesis of iron colloids with controlled particle size and different types of surfactant, dipolar particle interactions can be varied over a broad range, which significantly influences the ferrofluid particle structure. Our experiments on iron dispersions (in contrast to magnetite dispersions) for the first time demonstrate, in ferrofluids in zero field, a transition with increasing particle size from separate particles to linear chains of particles [1]. These chains, already predicted theoretically by de Gennes and Pincus [2], very much resemble the fluctuating chains found in simulations of dipolar fluids [3,4]. Decreasing the range of steric repulsion between particles by employing a thinner surfactant layer is found to change particle structures as well. The dipolar nature of the aggregation is confirmed by alignment of existing chains and individual particles in the field direction upon vitrification of dispersions in a saturating magnetic field. Frequency-dependent susceptibility measurements indicate that particle structures in truly three-dimensional ferrofluids are qualitatively similar to those in liquid films.

This chapter was earlier published as a paper in the special issue on magnetic colloids of the Journal of Physics: Condensed Matter [38]. To preserve the structure of this paper, we chose to present it here in its original shape. Consequently, some textual parts and tables from other chapters are present in this chapter as well.

1. Introduction

Ferrofluids (dispersions of magnetic colloids) behave as magnetizable liquids (figure 1) and are applied e.g. as rotary shaft seals [5] or magnetic carriers for drugs [6]. In addition, ferrofluids are of interest as a model system for dipolar fluids in general, since they consist of freely rotating permanent dipoles in a non-magnetic matrix, which can be studied relatively easily because of their large size in comparison to molecular dipoles. How dipole-dipole interactions influence particle structure and phase behaviour in ferrofluids is a fascinating question, which has been a subject of research for decades already [2,7,8]. In 1970, de Gennes and Pincus [2] predicted a van der Waals-like phase diagram and the presence of chainlike structures in ferrofluids in zero field. Since then, many theories [9,10] and simulations [3,11] have been published relating to the subject, which remains a matter of debate [7,8]. Despite various studies [12,13,14,15], direct experimental proof for the existence of particle chains is lacking. Conclusive evidence is difficult to obtain from indirect techniques; e.g. scattering patterns from ferrofluids in zero field are isotropic and extracting the shape and distribution of aggregates, if any, from measured intensity profiles is far from straightforward. Using conventional Transmission Electron Microscopy (TEM), original particle structures may be severely distorted due to drying effects, giving no direct information about particle arrangement in the fluid state. In addition, most commonly studied ferrofluids consist of magnetite particles (Fe_3O_4), where dipole-dipole interactions are relatively weak [8,16], making it questionable whether significant chain formation in zero field occurs in these dispersions anyway.

Figure 1. An example of iron dispersions, synthesized by thermal decomposition of $Fe(CO)_5$ in decalin in the presence of modified polyisobutene (PIB) following reference [18] and always stored under nitrogen atmosphere. Average particle radii were varied by changing the $Fe(CO)_5$/PIB ratio. The dispersion exhibits the equilibrium shape in a field gradient typical for a stable ferrofluid [16].

Cryogenic Transmission Electron Microscopy (cryo-TEM) images of vitrified liquid films were obtained via low-dose TEM. A fast temperature quench of films of dispersions vitrifies the solvent, arresting thermal diffusion of colloids on the timescale of vitrification. This enables one to study particle structures in a ferrofluid *in situ*. Because dipole-dipole interactions are very sensitive to particle dipole moments and interparticle distances, ferrofluid microstructures are expected to be influenced significantly by particle radii, particle concentrations and the thickness of their surfactant layer. We therefore synthesized iron dispersions for our study, following a method by which particle sizes can be controlled over a broad size range (with a narrow size distribution) and, in addition, particles can be stabilized by different surfactants (see chapter 3 and [17,18]). These dispersions were studied by Cryo-TEM to systematically investigate particle structures in ferrofluids for two different surfactant layers as a function of particle size. In addition, we studied conventional oleic-acid-coated magnetite dispersions. To verify the dominance of dipolar forces in our dispersions, some iron samples were also vitrified in a saturating magnetic field. Because cryo-TEM studies thin films of dispersions, which should be considered as quasi-two-dimensional, particle structures of the same dispersions in the bulk were studied by frequency-dependent susceptibility measurements for comparison. This chapter is organized as follows: in section 2 the theory and equations relevant for the various measuring techniques are explained. Section 3 describes the experimental methods of the synthesis and characterization of our ferrofluids, as well as of cryo-electron microscopy and susceptibility measurements. Results are presented and discussed in section 4.

2. Theoretical background

2.1. Ferrofluids

Ferrofluids consist of monodomain magnetic colloids, which can be considered as point dipoles with a magnetic moment $\mu = (4\pi/3)a_M^3 m_s$, a_M being the particle radius of the magnetic core and m_s the saturation magnetization of the particle material ($1.7*10^6$ and $0.48*10^6$ Am^{-1} for bulk iron and magnetite respectively [16]). In a dispersion in zero field, all magnetic moments are oriented randomly due to thermal motion of particles resulting in a net magnetic moment M of the sample of zero. A magnetic field aligns particle dipoles in the field direction, inducing a magnetic moment in the sample. For dilute ferrofluids, M as a function of the magnetic field strength H is given by the Langevin equation [16]:

$$M(H) = M_s \left(\coth\left(\frac{\mu_0 \mu H}{kT} \right) - \frac{kT}{\mu_0 \mu H} \right) \qquad (1)$$

where M_s is the saturation magnetization of the sample, reached upon complete alignment of all particles in the field direction. For low fields, equation (1) can be approximated by:

$$M(H) \approx M_s\left(\frac{\mu_0 \mu H}{3kT}\right) \qquad \text{for } \mu_0\mu H << kT \tag{2}$$

M_s and the initial susceptibility $\chi_i = (\partial M/\partial H)_{H=0}$ can be determined experimentally from the magnetization curve, from which the mean magnetic particle radius a_M (assuming a spherical shape) is calculated, using:

$$a_M^3 = \frac{\chi_i}{M_s}\left(\frac{9kT}{4\pi\mu_0 m_s}\right) \tag{3}$$

Note that this radius only includes the magnetic part of the particle, which will be somewhat smaller than the physical particle radius, if particles contain a non-magnetic surface layer [16]. The magnetic interaction potential between two dipoles μ_i and μ_j depends on their magnitude and orientation and is given by

$$U_{d\text{-}d} = \frac{\mu_0}{4\pi}\left(\frac{\vec{\mu_i}\cdot\vec{\mu_j}}{r^3} - \frac{3\left(\vec{\mu_i}\cdot\vec{r}\right)\left(\vec{\mu_j}\cdot\vec{r}\right)}{r^5}\right) \tag{4}$$

where $\vec{r}$ connects the two dipoles. The attraction is maximal when particle dipoles are oriented head-to-tail and for monodisperse particles it is equal to:

$$U_{max} = -2\frac{\mu_0}{4\pi}\left(\frac{\mu^2}{r^3}\right) \qquad \left(\mu = \frac{4}{3}\pi a_M^3 m_s\right) \tag{5}$$

Note that U_{max} is proportional to a_M^6/σ^3 when particles are at the closest centre-to-centre distance $r = \sigma$. The surfactant layers of sterically stabilized particles, often modelled as hard spheres, cause a strong repulsive potential U_{rep}, where $U_{rep} = 0$ for $r > \sigma$ and $U_{rep} = \infty$ for $r \leq \sigma$. Here, the minimal interparticle distance is determined by their effective hard sphere diameter σ, consisting of twice the sum of the core radius a_{core} and the thickness of the surfactant layers t_s. A third contribution to the interaction potential between particles is the van der Waals attraction, given by the Hamaker formula for the London-van der Waals attractive interaction energy between spherical particles:

$$V_{VdW} = -\frac{A}{6}\left[\frac{2a_{core}^2}{r^2 - 4a_{core}^2} + \frac{2a_{core}^2}{r^2} + \ln\left(1 - \frac{4a_{core}^2}{r^2}\right)\right] \tag{6}$$

with A the Hamaker constant ($A \approx 10^{-19}$ J for iron and iron oxide [16]). For magnetic colloids, V_{VdW} is of the order of kT. Except for the fact that the van der Waals interaction is isotropic, whereas the magnetic interaction is anisotropic, another important difference is that the former is a function of a_{core}/r only, whereas the latter has a stronger particle volume dependence [19]. Thus, on increasing the particle size, the magnetic attraction will become relatively more important; for example, the magnetic attraction is estimated to be dominant for oleic-acid-coated maghemite particle radii larger than about 5 nm [19], while for smaller particles the van der Waals attraction is more important.

As the strength of the dipole-dipole interaction scales with a_M^6 (see equation (5)) and is inversely proportional to r^3, the ferrofluid microstructure is expected to be very sensitive to particle radii as well as the surfactant layer thickness. For a collection of dipoles, it is energetically favourable to form linear chains of dipoles. For example, the energy gain U_{d-c} to add one dipole to the end of an infinitely long chain is [20]:

$$U_{d-c} = U_{max} \sum_{n=1}^{\infty} \frac{1}{n^3} \approx (1.202) U_{max} \tag{7}$$

The attraction potential between two long chains of dipoles oriented head-to-tail at closest contact is even larger (approximately $1.64U_{max}$) [21].

The interaction potential between two chains of dipoles in the lateral direction (perpendicular to the chain axes) is analogous to the case of chains of particles in electrorheological fluids calculated by Halsey and Toor [22,23]. They found that the dominant interaction between two parallel chains of dipoles in a saturating magnetic field (for $l>>a$, with dipole spacing $2a$ at lateral distance l) is induced by fluctuations in their shape and has the same form as the van der Waals attraction between chains (which scales with l^{-5}) [23]. Although for electrorheological fluids the fluctuation-induced dipolar interaction between parallel chains is an order of magnitude larger than the van der Waals interaction, for ferrofluids they are of the same order due to the high Hamaker constants of iron and iron oxide. Still, the effect of the fluctuation coupling can be seen as an increase of the Hamaker constant. Only at small distance (of the order of a particle diameter) is the interaction potential between parallel chains determined by the discrete nature of the particle chain and this is attractive when chains are shifted half a particle diameter with respect to each other [23].

2.2. Small Angle X-Ray Scattering

The average scattered intensity I(q) of a suspension of identical spherical colloidal particles with number concentration c_p, particle volume V_p and electron density difference with the solvent $\Delta\rho^e$ is given by [24]:

$$I(q) \propto c_p (\Delta\rho^e)^2 V_p^2 F^2(q) S(q) \tag{8}$$

Here, q is the magnitude of the momentum transfer vector, $F^2(q)$ the form factor and S(q) the structure factor. For scattering curves of dilute suspensions the radius of gyration R_g can be obtained from the Guinier approximation for $q < 2/R_g$ [24]:

$$I(q) = I(q=0) \exp(-q^2 R_g^2 / 3) \tag{9}$$

For homogeneous spheres, the radius of gyration is related to the sphere radius a by:

$$R_g^2 = 3a^2 / 5 \tag{10}$$

For polydisperse systems, the particle radius as determined from the Guinier plot is an

overestimation of the average particle radius. For size distributions with a small standard deviation σ, the apparent radius derived from the scattering at low q can be corrected for polydispersity, according to [24]:

$$a_G = \langle a_G \rangle \left[1 + \frac{13}{2} \left(\frac{\sigma}{\langle a_G \rangle} \right)^2 \right] \tag{11}$$

Here, a_G is the apparent and $\langle a_G \rangle$ is the number average Guinier radius. Dividing the scattered intensities of a dispersion at a given volume fraction by those of a dilute dispersion gives the experimental static structure factor. The peak in the structure factor roughly corresponds to the distance of nearest approach between particles, given by Bragg's law:

$$d_c q_{max} = 2\pi \tag{12}$$

Here, q_{max} is the q-value at the maximum intensity and d_c is the centre-to-centre distance of nearest approach.

2.3. Susceptibility as a function of frequency

The frequency-dependent susceptibility of a ferrofluid can be measured using two concentric coils (having N loops) with length L much smaller than the coil radius R. An alternating current $I(\omega) = I_{ampl} \exp(i\omega t)$ generates an external alternating magnetic field $H(\omega)$ at the centre of such a coil [25]:

$$H(\omega) = NI(\omega)/2R \tag{13}$$

The magnetic induction $B(\omega)$ differs from $\mu_0 H(\omega)$ when a magnetic sample with susceptibility $\chi(\omega)$ is placed inside the coil [25]:

$$B(\omega) = \mu_0 H(\omega)\left(1 + \chi(\omega)\right) \tag{14}$$

Using two concentric coils (with N_1 and N_2 loops), with $I(\omega)$ flowing through the primary (outer) coil with radius R_1, $H(\omega)$ induces an AC voltage $V(\omega)$ in the secondary coil equal to $-\partial\phi/\partial t$ where $\phi = N_2 B(\omega) A$ with A the area of the coil [25]. This means that the susceptibility of a sample can be determined by measuring the induced voltage $V(\omega)$ in the secondary coil:

$$V(\omega) = -i\omega A(1 + \chi(\omega))N_2(\mu_0 N_1 / 2R_1) I_{ampl} \exp(i\omega t) \tag{15}$$

The complex relative magnetic susceptibility of a ferrofluid in low fields is given by [26]:

$$\chi(\omega) = \chi'(\omega) - i\chi''(\omega) \tag{16}$$

When a single relaxation time τ is involved, $\chi(\omega)$ is given by [27]:

$$\chi(\omega) = \chi_\infty + (\chi_0 - \chi_\infty)/(1 + i\omega\tau) \tag{17}$$

where χ_0 and χ_∞ are the magnetic susceptibilities in the low and the high frequency limit

respectively. The mobility of magnetic moments in a ferrofluid is determined by two relaxation mechanisms; the Néel mechanism associated with rotation of the magnetic moment within the particle (relaxation time τ_N) and the Brownian relaxation by thermal rotation of particles in the solvent (relaxation time τ_B) [26]:

$$\tau_B = \frac{4\pi\eta a_h^3}{kT} \tag{18}$$

$$\tau_N = f_0 \exp\left(\frac{K\frac{4\pi}{3}a_M^3}{kT} \right) \tag{19}$$

with η the viscosity of the solvent, f_0 the Larmor frequency (about 10^9 s^{-1}) and K the material dependent anisotropy constant. The characteristic relaxation time τ is given by [27]:

$$\tau = 1/\left(1/\tau_N + 1/\tau_B\right) \tag{20}$$

When the only relaxation mechanism involved is Brownian rotation ($\tau_N >> \tau_B$), the frequency ω_{max} at which χ'' reaches a maximum for monodisperse spherical particles with hydrodynamic radius a_h is [27]:

$$\omega_{max} = kT/4\pi\eta a_h^3 \tag{21}$$

3. Experimental

3.1. Materials and Methods

Ironpentacarbonyl (Fluka Chemika) was taken from new bottles. Decalin (Merck), oleic acid (Merck, extra pure) and modified polyisobutene (PIB) coded SAP 285, consisting of a mixture of 2 polymers (figure 2) in a mineral base oil (Shell Research Ltd., England), were used as supplied. The modification of polyisobutene is reported elsewhere [28]. According to the supplier, the molecular weight of the PIB is 2400 $gmol^{-1}$ and the polyisobutene/polyamine ratio is 2.0-2.5. To protect the iron particles against oxidation, all dispersions were always treated and stored under dried nitrogen atmosphere, using a glovebox with oxygen pressure lower than 12 ppm as measured by a M.Braun MB-OX-SE1 active oxygen probe.

3.2. Synthesis of iron and magnetite dispersions

Dispersions of oleic-acid-coated magnetite (Fe_3O_4) particles in toluene were synthesized by coprecipitation of Fe^{2+} and Fe^{3+} salts following reference [29] (see also chapter 2) and coded FFOl. Dispersions of monodisperse iron particles were synthesized by thermal decomposition of ironpentacarbonyl in decalin, in the presence of a stabilizing surfactant

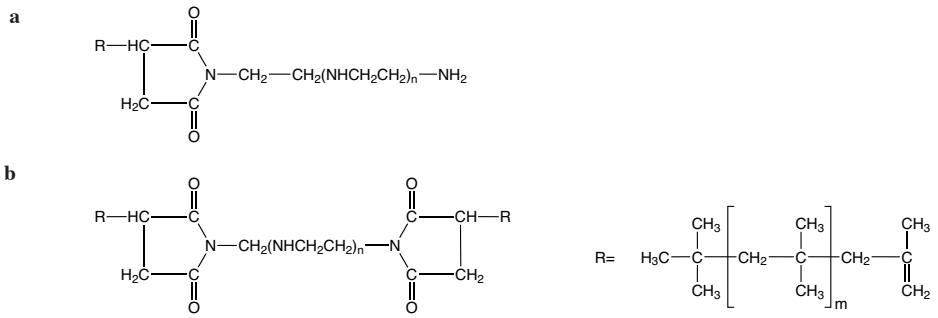

Figure 2. The structural formula of modified PIB (m = 41, n = 4). The used substance is 40-50 % of a 1:1 mixture of the compounds **a** and **b** in a mineral oil.

(PIB or oleic acid) following reference [18] (see also chapter 3). After addition of $Fe(CO)_5$ to a solution of SAP 285 in decalin, the mechanically stirred solution was refluxed under nitrogen atmosphere for 24 hours at 170°C, using an oil bath. The size of the colloidal particles was tuned by varying the $Fe(CO)_5$/surfactant ratio. The amounts of ironpentacarbonyl, decalin and surfactant used are presented in table 1.

Particles were synthesized with average radii in the range 2-10 nm. Dispersions of PIB-coated particles were coded A to E, alphabetically ordered with increasing size. To prepare particles with a large radius (dispersions D and E), extra ironpentacarbonyl was added to a dispersion of smaller particles (dispersion C) in portions of approximately 15 ml every few hours. Earlier experiments starting with a large amount of $Fe(CO)_5$ without seeds resulted in unstable dispersions. For this seeded growth the heating was stopped a few hours after the last portion had been added. Dispersions of oleic-acid-coated particles were coded OA3.

Table 1. Amounts of reactants used for synthesis of iron dispersions.

Dispersion code	$Fe(CO)_5$ (ml)	SAP 285 (g)	Oleic acid (g)	decalin (ml)
A	5	17.5	-	420
B	41	17.5	-	420
C	70	17.5	-	420
D	70+56	17.5	-	420
E	70+134	17.5	-	420
OA3	44	-	4	20

3.3. Characterization of iron and magnetite dispersions

On a Philips CM10H transmission electron microscope (TEM), micrographs were made of particles retained on grids coated with a Formvar film. The grids were placed in the vacuum of the sample holder of the microscope within three minutes after the opening of a glovebox under nitrogen atmosphere, in which grids were made by dipping them in a dilute

dispersion and letting them dry. Grids of dispersion FFOl were made in air. Particle size distributions were measured using IBAS, an interactive image analysis program. Small-Angle-X-Ray scattering experiments were performed at the DUBBLE (the Dutch-Belgian beamline) at the ESRF (Grenoble). The wavelength was fixed at 0.124 nm. The measurements were performed on dispersions A to E and OA3, sealed in round glass capillaries. The measured two-dimensional diffraction patterns were corrected for transmission, background radiation and detector response. All measured intensities are in arbitrary units and have only relative relevance. Particle radii were determined from the initial slope of Guinier curves of dilute samples, using equations (9) and (10). These values were corrected for polydispersity measured with TEM, using equation (11). Interparticle distances were determined from the structure factors of concentrated samples following equation (12).

Magnetization curves of dilute dispersions were measured at room temperature on an alternating gradient magnetometer (AGM) Micromag 2900 (Princeton Measurements Corporation) in small airtight glass cups, filled in a glovebox (except for the dispersion FFOl). Curves were fitted by the Langevin equation (1), from which M_s was determined. χ_i was determined from the slope of the curves at low magnetic fields (< 1000 Am^{-1}). Assuming a spherical particle shape, particle radii were calculated via equation (3), using the bulk values for m_s (see table 2). The number of particles n in a sample was determined from M_s, which is equal to $n\mu$. Knowing the sample volume, the particle concentration could be determined. This small volume of samples for AGM measurements (approximately 3 µl) was accurately determined by scaling of χ_i with the susceptibility measured on much larger known volumes of the same dispersions, using a Kappabridge KLY-3 susceptibility meter (Agico). For dispersions A to E and OA3, the content of iron was determined by elemental iron analysis of a known mass of dispersion from which the iron particles were extracted after flocculating them by addition of pentanol.

3.4. Cryo-TEM experiments

Most cryo-TEM work reported in the literature has been performed on aqueous samples [30], which are usually vitrified in liquid ethane. However, decalin and toluene were found to dissolve into ethane, making it impossible to produce glassy films in this way. We found that these solvents could readily be vitrified in liquid nitrogen, despite its lower cooling efficiency in comparison with liquid ethane [31]. Vitrified films were made from dispersions on grids coated with holey carbon film (R2/2, Quantifoil Micro Tools GmbH) using a vitrobot [32] in an oxygen-poor atmosphere (approximately 0.4 volume % O_2) to prevent particle oxidation. After placing a droplet of the dispersion onto the grid, a vitrobot automatically blotted the liquid with filter paper, producing a liquid film in the grid holes (diameter 2 µm) which was thin in the middle (of the order of a particle diameter) and thicker at the edges of the hole. Then the specimen was plunged into liquid nitrogen, which caused the solvent to glassify. In addition, samples C and D were vitrified in a magnetic field

after blotting by hand of a grid that was fixed between the poles of a strong magnet (1.6 Tesla). Vitrification was performed by plunging the grid, fixed between the magnet poles, into liquid nitrogen. In this case particles were exposed to air short enough (~ 40 seconds) to prevent formation of any observable oxidized layers around particle cores, which we usually observed for particles exposed to air for a few hours. Keeping samples in liquid nitrogen, they were placed into a cryo-holder which was mounted and examined in a Philips CM12H electron microscope at –170°C and 120kV. Photographs were taken from thin parts in carbon film holes with a Philips CM12 Transmission Electron Microscope at 120 kV using low-dose techniques. For dispersion D, vitrification in a magnetic field resulted in a film that was extremely susceptible to electron beam radiation damage. The film stability was increased considerably by the addition of small particles A. For comparison, the same mixture has also been vitrified without magnetic field, giving similar pictures to samples without particles A.

3.5. EELS-measurements

Energy Electron Loss Spectroscopy (EELS) [33] was performed on cryo-TEM grids of dispersions A and D on a Philips Tecnai 12 Biofilter Transmission Electron Microscope. The film thickness x of the vitrified films was determined by the relation between the intensity I_{un} of the zero-loss peak (corresponding to the electrons that do not interact with the vitrified film) and the total intensity I_0, given by [34]:

$$I_{un} = I_0 \exp\left(\frac{-\rho x}{(\rho x)_c}\right) \tag{22}$$

where $(\rho x)_c$ is the critical mass thickness (100 ± 10 nm g ml^{-1} for most solvents [34]) and ρ the density of the vitrified film (estimated as 0.9 gml^{-1} for decalin).

3.6. Image analysis

Cryogenic electron micrographs were analysed, using an image analysis program (AnalySIS). Because the particle concentration in a cryo-film can not be controlled very well experimentally and usually varies on different parts of the grid, the final concentration was determined by measuring the area that is occupied by iron cores on the micrographs. Division of this area by the total micrograph area results in a surface fraction of particles ϕ_s. The radial distribution function g(r) of particle positions was calculated using special software (IDL). Cluster sizes were determined by dilation of particles using IBAS, an interactive image analysis program. Particles were considered part of the same cluster when the shortest distance between particle edges was not larger than the mean core radius.

3.7. Susceptibility measurements

For all iron dispersions, susceptibility measurements were performed in a large frequency range (1-100000 Hz) on a home-built susceptibility meter (as described in chapter 7) that

measures the local susceptibility at a chosen height of a sample tube. The set-up consists of two concentric coils, one (the primary coil) connected to an AC supply and the other (secondary coil) to a lock-in amplifier as AC voltmeter. Samples were made in long glass tubes under nitrogen atmosphere. The susceptibility was determined from $V(\omega)$, which was measured while a sample was positioned in the coils, using equation (15). The signal of a reference sample (solvent) was subtracted from the signal of the ferrofluid. To check the stability of the dispersions, susceptibility measurements at a low frequency were performed as a function of height on all iron dispersions using the same set-up.

4. Results and Discussion

4.1. Synthesis and characterization of ferrofluids

Approximately 30 minutes after starting the synthesis of iron dispersions the yellow ironpentacarbonyl solution turns either brown (dispersion A) or black (for larger particles), due to formation of iron. Dispersions of particles with different average radii in the size range 2-10 nm with a polydispersity of 7-18 % can be synthesized, as described in chapter 3. The particles do not consist of pure iron, but also contain carbon. From Mössbauer spectroscopy measurements on dispersions C and E described and discussed elsewhere [35] (see also chapter 3), the particle composition is concluded to be $Fe_{0.75}C_{0.25}$. The same composition was also found by other authors [36] for oleic-acid-coated iron particles synthesized via the same method as we used. Therefore, it is a plausible assumption that particle cores in all iron dispersions described in this thesis consist of $Fe_{0.75}C_{0.25}$. Characterization results of all dispersions are summarized in table 2.

Sizes measured with different techniques correspond reasonably well with each other (table 2). However, radii measured with TEM presumably contain a relatively large uncertainty, since we found that radii measured on various electron microscopes differed up to 20%.

Particle radii determined from magnetization measurements are smaller than TEM radii, presumably because a non-magnetic layer is always present at magnetic particle surfaces and, moreover, we used the bulk value for m_s, which may not be the same for small particles. Since the interaction potential is very sensitive to particle size, the spread in particle radii in table 2 only allows a qualitative estimate of this potential. For dispersion E, magnetization curves could not be fitted with the Langevin function, due to hysteresis effects. As will be discussed later, a plausible reason for this behaviour is the presence of larger particle structures in the dispersion. From the interparticle spacing derived from the positions of the maximum in the static structure factor of SAXS scattering curves of dispersion C, a thickness of a polymer layer of 7.0±0.4 nm was determined. Susceptibility measurements show that particles oxidize fast (timescale of minutes) to a non-magnetic oxide on exposure of dispersions to air. Susceptibility measurements as a function of height confirm that all

dispersions in this study, which were always kept under nitrogen, are stable and do not phase separate.

Table 2. Characterization of iron and magnetite dispersions.

Code	a_{TEM}[1](nm)	a_{SAXS}[2] (nm) (a_{CORR}[3])(nm)	a_M[4] (nm)	μ_{AGM}[5] (*Am^2*10^{19})	Fe amount (mass fraction)[6]	Conc. (particles/l)[7]
A	2.1 ± 0.3	2.2 (1.9)	1.3	0.123	0.004	$1.7*10^{19}$
B	6.0 ± 0.7	5.3[8] (4.8)	4.1	4.149	0.038	$5.1*10^{18}$
C	6.6 ± 1.1	6.0 (5.1)	5.1	8.38	0.061	$8.2*10^{18}$
D	6.9 ± 1.0	8.8 (7.8)	6.0	13.19	0.108	-
E	8.2 ± 1.5	9.5 (8.0)	-	-	0.219	-
OA3	4.3 ± 0.3	3.9 (3.8)	3.3	2.29	0.257	$1.4*10^{20}$
FFOl	5.5 ± 2.5	-	5.1	3.24	-	-

[1]Particle radius measured from TEM-micrographs. [2]Particle radius determined from Guinier curves using equations (9) and (10). [3]Guinier radius corrected for polydispersity (from TEM) using equation (11). [4]Magnetic radius determined from magnetization curves (equation (3)). [5]Dipole moment $\mu = 4\pi a_M^3 m_s/3$ with bulk value for $Fe_{0.75}C_{0.25}$ ($m_s = 1.49*10^6$ Am^{-1} [37]) or Fe_3O_4 ($0.48*10^6$ Am^{-1} [16]). [6]Amount of iron in dispersion from elemental analysis (gFe/g dispersion). [7]Determined from magnetization measurements. This concentration could not be determined for dispersions D and E, since the susceptibility (necessary for calibration of the sample volume), is frequency-dependent in the range of operating frequencies of the magnetometer. [8]This value differs from the value of 4.88 as reported in [38], which was found to be incorrect.

4.2. Cryo-TEM experiments

In aqueous samples, film stability is based on a balance of attractive van der Waals forces between the air-liquid interfaces and electrostatic repulsions between charged surfactants organized at these interfaces [39]. Making stable glassy films of organic solvents is not trivial [30] and only a few reports have appeared [40]. We found that thin films of ferrofluids in organic solvents are surprisingly stable, despite the absence of charged surfactants, and that they could readily be vitrified in liquid nitrogen. Film thicknesses determined from EELS measurements varied considerably for different parts of the grid, but were of the order of a particle diameter. An illustrative example of variation of film thickness in a grid hole is shown in figure 3, where the thickness increases from the hole center (lower right corner), with only one layer of individual particles, to the edge of the gridhole (upper left corner), where particles are arranged into linear chains due to the high concentration and presumably are positioned in different layers.

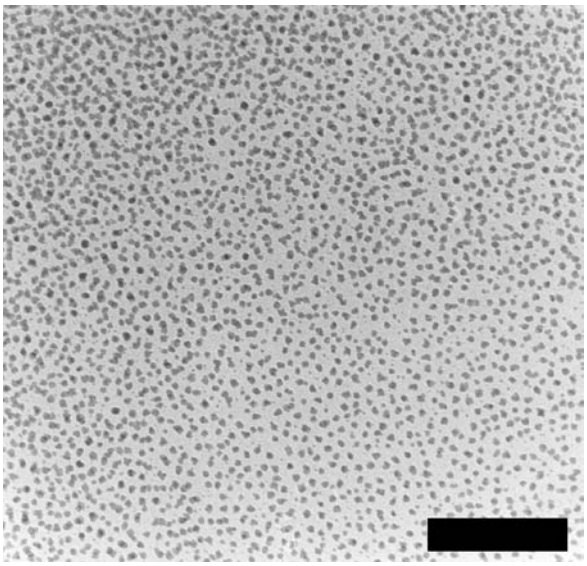

Figure 3. An example of a cryogenic electron micrograph of dispersion B with gradually increasing film thickness going from the lower right corner to the upper left corner. Aggregate sizes increase with concentration (see the text). The scale bar corresponds to 200 nm.

4.2.1. Influence of particle size

Figure 4 shows typical examples of cryo-TEM micrographs of a dilute ferrofluid of oleic-acid-coated magnetite particles in toluene (FFOl), where clusters of colloids are present with an isotropic shape, most probably caused by van der Waals attractions and weak magnetic attractions, which are both of the order of kT. Note that these micrographs are snapshots of the ferrofluid; since all dispersions described in this paper are stable (as found from sedimentation experiments and susceptibility measurements as a function of height), cluster formation is presumably reversible or permanent aggregates are small enough to sediment very slowly. Figure 5 shows cryo-TEM micrographs of dispersions A to E (i.e. dispersions of PIB-coated iron particles for increasing particle size). In contrast to the magnetite dispersions, where dipolar interactions appear to be too weak to form linear aggregates, in iron ferrofluids we clearly observe linear structures at zero field (figure 5d) as predicted by de Gennes and Pincus [2]. These randomly organized chains very much resemble the fluctuating chains found in simulations of dipolar fluids [3,11,4], see figure 6. As confirmed by simulations [11,7] chains do not aggregate to larger clusters, showing that chain-chain interactions are weak. The presence of many individual particles in figure 5d indicates that chains are dynamic and easily disrupted due to thermal motion. Despite the large number of single particles, the mean number of particles per cluster is 2.49 due to the presence of many larger clusters (see figure 7 for a histogram). However, for larger particles (figure 5e) cluster sizes increase considerably and almost no single particles are found, obviously an effect of much stronger dipole-dipole interactions. Smaller particles, magnetically interacting more

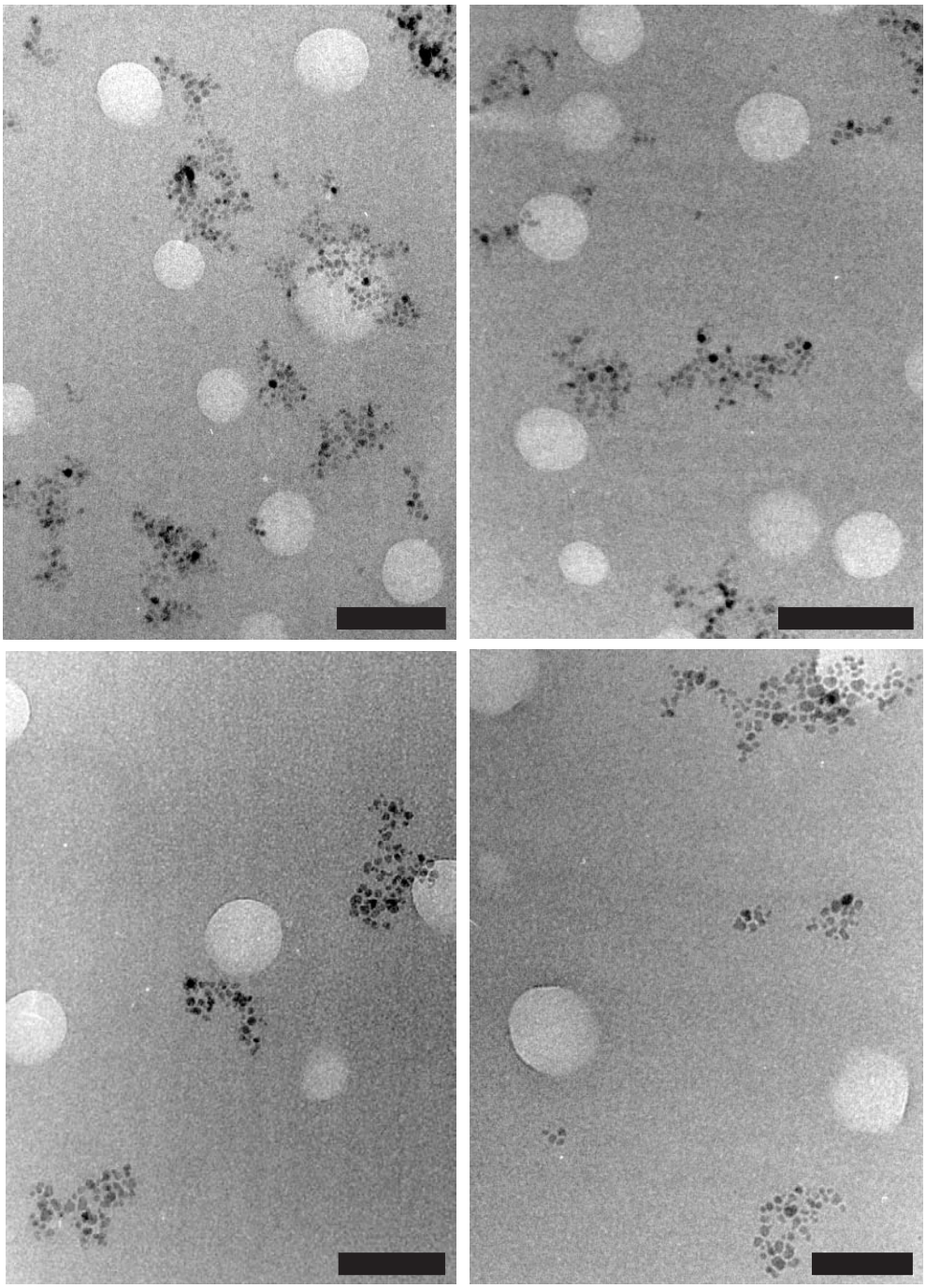

Figure 4. Typical cryogenic electron micrographs of a dispersion of magnetite particles in toluene (FFOl) glassified in liquid nitrogen. The scale bar corresponds to 200 nm. The large white objects are artefacts.

weakly, show an ordered configuration (see figures 5b,c), where particles stay separated, because isotropic steric repulsion between their thick surfactant layers is the dominant interaction. This is in contrast to the case for oleic-acid-coated magnetite particles, where van der Waals interactions cannot be neglected and isotropic clusters are present. For the

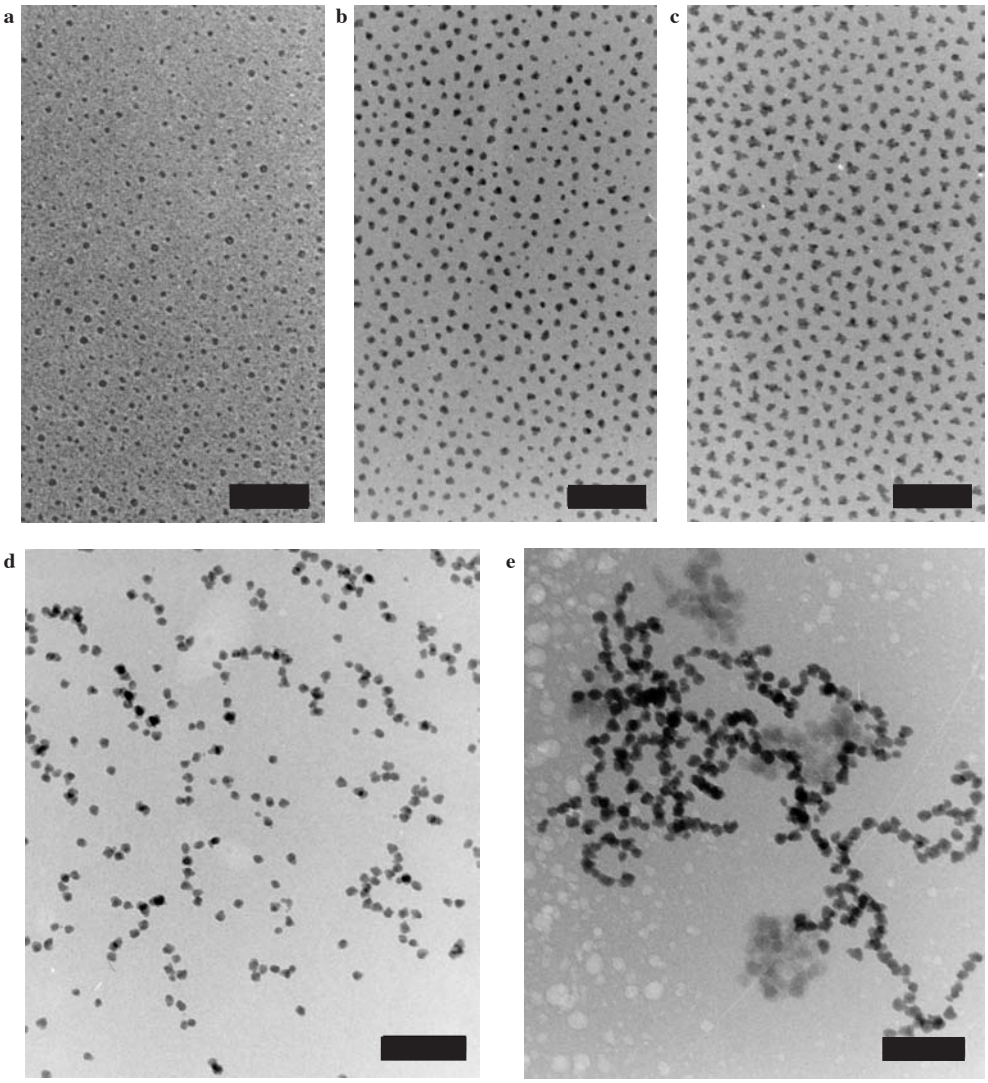

Figure 5. Typical cryogenic electron micrographs of dispersions of PIB-coated iron dispersions with increasing average particle radius, determined from separate TEM-measurements. **a**, 2.1 nm (referred to as particles A); **b**, 6.0 nm (particles B); **c**, 6.6 nm (particles C); **d**, 6.9 nm (particles D); **e**, 8.2 nm (particles E). The scaling bars correspond to 100 nm. In figure **e**, the white patches on the left and the three larger structures with poor contrast are artefacts.

ordered structure of dispersion B the particle concentration is so high that we expect the interparticle distance to be of the order of two particle surfactant layers t_s. Assuming this, t_s can be estimated from the average centre-centre distance between nearest-neighbour particles (which is determined as 24.8 ± 2.5 nm) by subtraction of the TEM core diameter (12.0 nm) and dividing by 2, giving a value of t_s = 6.4 nm, which corresponds very well with 7 nm, found from the first peak of the structure factor as measured by SAXS. These values are in agreement with the expected maximum thickness of the PIB-layer of 7-8 nm, assuming C-C bond lengths of 0.154 nm and bond angles of 110°. Note that for dispersion D and E particles within a cluster are much closer than would be expected from the thickness of the PIB-layer; for example, the distance between core edges of close particles in dispersion D are in the order of 3-4 nm. Here, dipolar interactions are large enough to compress the polymer layers. In addition, the surfactant layers of particles D and E might be somewhat thinner because the grafting density of PIB is lower (and therefore the polymer chains are less extended) in comparison with that of smaller PIB-coated particles, due to the different method of synthesis (particles D and E are grown from seed particles C without adding extra PIB). From figure 5 it is clear that the particle structure in ferrofluids is very sensitive to particle size, as expected from the scaling of dipolar interactions with a_M^6/σ^3 for particles at contact (equation (5)). It must be noted however, that cryo-TEM images thin films of dispersions (thickness of the order of one particle diameter), which ought to be considered as two-dimensional. Nevertheless, the presence of anisotropic structures is not limited to thin films; as will be discussed later, susceptibility measurements on the same dispersions show that larger structures are also present in three-dimensional ferrofluids.

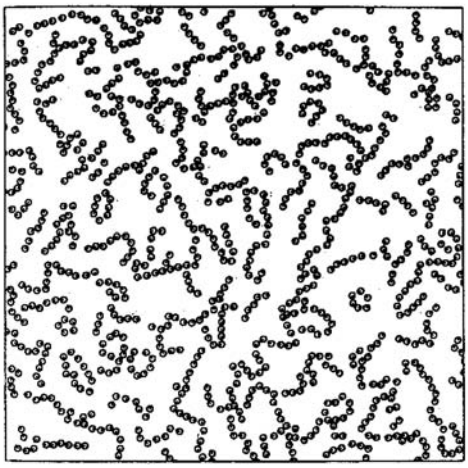

Figure 6. A snapshot of a two-dimensional Monte Carlo simulation on cobalt particles of 15 nm diameter with a surfactant layer of 2 nm (Chantrell [4])

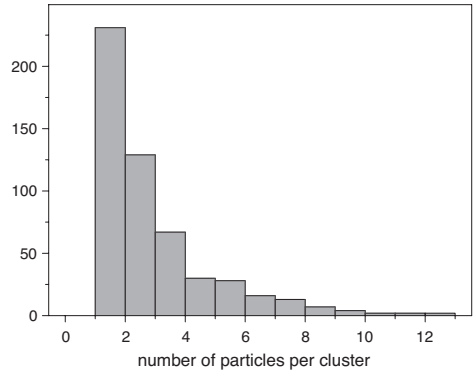

Figure 7. The distribution of cluster size, as determined from a series of cryo-TEM micrographs of dispersion D. Particles were assumed to be part of the same cluster if the surface-to-surface distance between neighbouring particles was smaller than the mean particle radius. The mean number of particles per cluster is 2.49.

Dried samples, required for conventional TEM, show significantly different ordering of particles in comparison with cryo-TEM of vitrified films of dispersions, as can be seen in figure 8, where some TEM micrographs are presented. While cryo-TEM micrographs are reproducible for a given dispersion, conventional TEM pictures show large differences between various pictures of the same dispersion (compare 8a and b). In addition, drying of grids clearly induces cluster formation, as the clusters in figure 8 are much larger than in the same dispersions in figure 5.

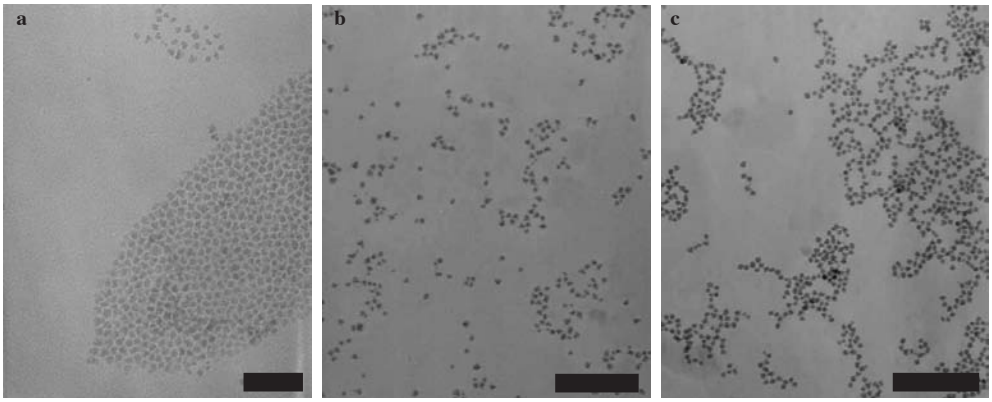

Figure 8. Conventional TEM pictures of dried samples of **a**,**b**, dispersion C; **c**, dispersion D. The scale bars correspond to 100 nm (figure a) and 200 nm (figure b,c). Particle structures are significantly different from structures in cryo-TEM micrographs of the same dispersions (compare with figure 5c,d) and not reproducible (compare figure 8a,b).

4.2.2. Influence of surfactant layer

We studied two dispersions with comparable iron core size, but different thickness of their surfactant layers (dispersion OA3 (a_{TEM} = 4.3 nm, oleic-acid-coated) and dispersion B (a_{TEM} = 6.0 nm, PIB-coated)), to investigate the effect of the range of steric repulsion between particles. The dipole-dipole interactions between two particles in a head-to-tail configuration at minimum distance (i.e. including the core diameter and two surfactant layers) can be calculated using equation (5) with the experimental value for μ from table 1 and r = 2*(a_{core}+t_s). However, values for particle sizes measured with different techniques are not equal and consequently give different interaction energies. The thickness of the oleic acid layer was not determined, but a thickness of 1-2 nm is usually assumed (see also chapters 4 and 5). Using different values for r, U_{max} ranges from 0.48 kT (a_{core}= 6.0 nm, t_s=7.0 nm) to 1.22 kT* (a_{core}= 4.8 nm, t_s=4.7 nm) and from 1.3 kT (a_{core}= 4.3 nm, t_s=2.0 nm) to 3.1 kT (a_{core}=3.7 nm, t_s=1.0 nm) for dispersion B and OA3 respectively. Despite the large spread in U_{max}, these values show that due to the smaller surfactant layer, dipole-dipole interactions are larger for particles OA3 than for particles B. Typical examples of the two dispersions for a comparable surface fraction of iron cores (ϕ_s = 0.14 and 0.13 respectively) are shown in figures 9a and 9b, which indeed are different. Although particles from dispersion OA3 seem to form loose linear structures, we are not sure whether they are resulting from dipolar interactions, since particle distances are rather large. In contrast, figure 9b (dispersion B) shows separate particles with strong ordering. The corresponding radial distribution functions of the particle positions from figures 9a (dispersion OA3) and 9b (dispersion B) are also presented in figure 9. While for dispersion OA3 g(r) is approximately 1 for all values of r (no order), for dispersion B at least two clear peaks are seen, indicating an ordered structure with dominant interparticle distances of 25.2 nm and 49 nm (corresponding to the peak maxima). Presumably in figure 9b the surface fraction of particles (including cores and thick surfactant layers) is so large that steric repulsion forces are dominant and no chain formation can occur because particles are too tightly packed. However, for lower concentrations of particles B also (figure 9c), no clear chain formation is found, indicating that dipolar interactions are indeed rather small. Although dipolar attractions are calculated to be higher for dispersion OA3, and cryo-TEM micrographs show clear difference with dispersion B, the interactions seem to be too small to result in the presence of very distinct linear chains, as are seen for dispersion D (figure 5d).

4.2.3. Influence of particle material

Although for dispersions OA3 (figure 9a) and FFOl (figure 4) the dipolar interactions are estimated to be in the same range (1.3-3.1 kT and 1.5 kT-2.8 kT (for (a_{core}=5.5 nm, t_s=2.0 nm) and (a_{core}=5.1 nm, t_s=1.0 nm) respectively), there is a large difference in particle

* This value differs from the value of 1.39 kT as reported in [38], which was calculated from an incorrect Guinier radius (table 2).

structure between clearly isotropic clusters for magnetite particles and the presence of only a few anisotropic clusters which seem to be induced by dipolar interactions for dispersion OA3. It must be noted that an accurate estimate of particle interactions is very hard for small magnetic colloids with thin surfactant layers; in particular, the van der Waals interaction is extremely sensitive to interparticle distance near contact, resulting in a large uncertainty in the interaction potential. That the polydispersity (which is found to enhance aggregation [41]) and particle shape differ in the two dispersions makes quantitative predictions even more complicated. However, the cryo-TEM results show that dominant interactions in the magnetite dispersion FFOl are clearly isotropic (van der Waals) attractions, whereas they probably are dipolar in the iron dispersion OA3.

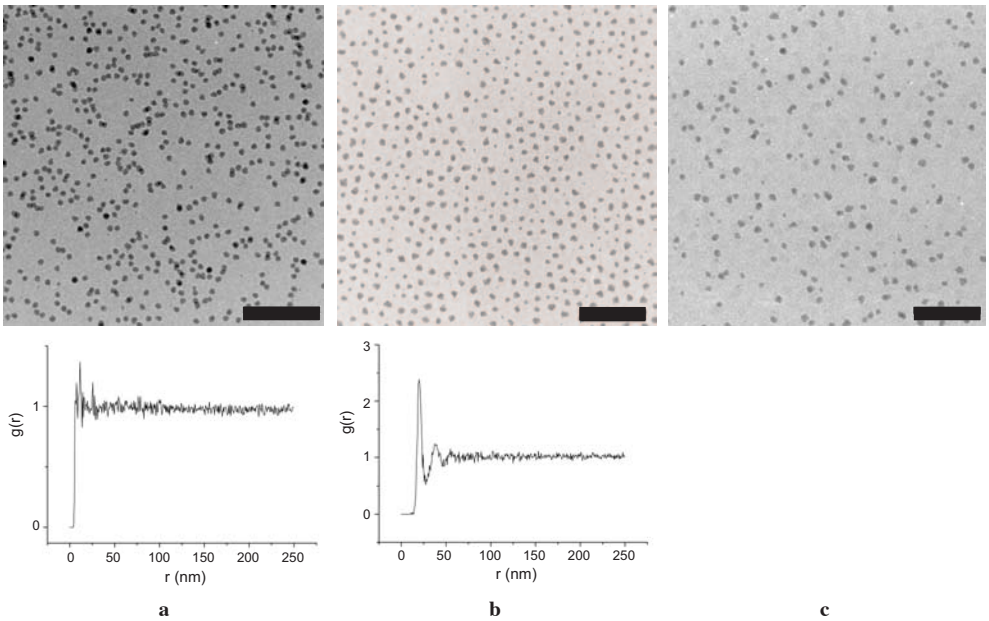

Figure 9. Examples of cryogenic electron micrographs of dispersions of iron particles coated with different surfactants, glassified in liquid nitrogen. **a**, Dispersion OA3 (Oleic-acid-coated, a_{core}(TEM)=4.9 nm, ϕ_s = 0.14); **b**, Dispersion B (PIB-coated, a_{core}(TEM) = 6.0 nm, ϕ_s = 0.13); **c**, Dispersion B (ϕ_s = 0.05). The scale bars correspond to 100 nm.

4.2.4. Influence of magnetic field

If the linear structures as found in dispersion D (figure 5d) are due to dominating dipolar attractions, they should align in a magnetic field. Indeed, figure 10 shows that the randomly oriented chains that exist in zero field (figure 10a), are all aligned in the direction of the saturating magnetic field (1.6 Tesla, figure 10b). Aggregates are much longer, presumably because orientation of all dipoles in one direction increases the mean dipole-dipole attraction between particles or particle chains. In addition, shape fluctuations in parallel

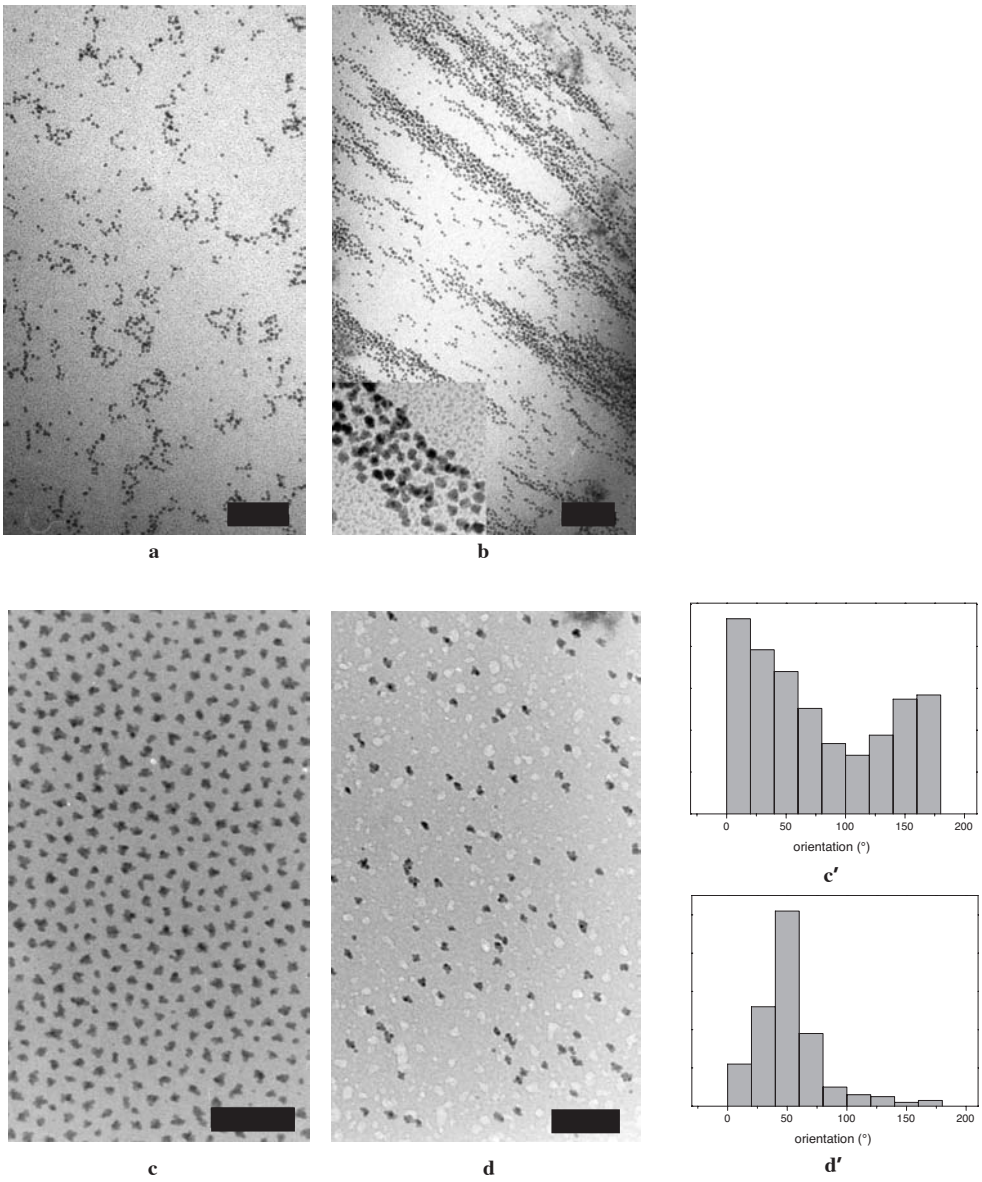

Figure 10. Examples of cryogenic electron micrographs made from dispersions D (mixed with dispersions A, with iron volume fractions of particles D and particles A of 0.0006 and 0.0004 respectively) and dispersions C. **a**, Dispersion D in zero field; **b**, Dispersion D in a saturating magnetic field. The insert is an enlargement (2.5 times) of a part of the complete picture. The scaling bars correspond to 200 nm. Chains, already existing in zero field, align in the magnetic field. **c**, Dispersion C in zero field. **d**, Dispersion C in a saturating magnetic field. The scaling bars correspond to 100 nm. Individual particles align in the field direction. Histograms (**c′**, **d′**), presenting the orientation distribution of the longest particle axes, show that particles C are oriented randomly in zero field, while the orientation is peaked in a saturating magnetic field.

chains give rise to chain-chain interaction perpendicular to the field direction, causing the formation of thick sheets of particles due to lateral aggregation. It is observed that films of particles D are stable without a magnetic field but only marginally stable with a large magnetic field, which suggests that the presence of homogeneously distributed particles is necessary to stabilize the films. When big clusters of particles D are formed, leaving large areas without any particles, the addition of the much less magnetic particles A leads to stabilization by ensuring that particles remain distributed throughout the film. Aggregates similar to those as in figure 10b are found in magnetorheological and electrorheological fluids [42,43] and dispersions of non-magnetic particles in ferrofluids [44,45]. These cases, however, involve induced dipoles that lose their magnetic moments on turning off the magnetic field, whereas in our dispersions permanent dipoles already form linear aggregates in zero field. It appears also that individual particles that magnetically interact too weakly to form clusters (dispersion C) do respond to high magnetic fields. Because our iron particles are not completely spherical, their magnetic moments may be preferentially oriented along the longer particle axis, due to magnetic shape anisotropy. Indeed, upon application of a saturating magnetic field ($\mu_0\mu H/kT \approx 328$, figure 10d), the C particles orient in the direction of the magnetic field, resulting in an image where longer particle axes mostly point in the same direction (see the histograms in figure 10c,d). Although in this case magnetic interparticle interactions will be larger than in zero field, they remain too weak to cause magnetic-field-induced aggregation.

4.2.5. Susceptibility measurements

The frequency-dependent susceptibility curves for dispersions B, C, D and E are presented in figure 11. For dispersion A, the susceptibility was too low to be measured accurately. For dispersions B and C in figures 11 (a) and (b) respectively, a maximum in the susceptibility (equation (21)) is expected at a frequency corresponding to single-particle rotation (28 and 24 kHz for a hydrodynamic particle radius a_h of 11.9 nm (a_{core} = 5.3, t_s =7.0) and 13 nm (a_{core} = 6.0, t_s = 7.0) respectively). For particles B, the susceptibility maximum is at a higher frequency than the measuring range, presumably because the dipole moments rotate inside the particles (Néel relaxation). For particles C, the maximum found is of the order of magnitude of the theoretical value, although somewhat lower than expected (4000 Hz), probably because these particles are not completely spherical (see figure 5c), which will increase the Brownian rotation time. However, for particles D (figure 11c), a maximum in the susceptibility is found at approximately 150 Hz, much lower than expected for single particles. For dispersion E (figure 11d) a maximum is not even reached at a frequency of 1 Hz. These results clearly indicate that much larger structures must be present in dispersions D and E, in agreement with what was found from cryo-TEM. Most probably, this is also the reason for hysteresis in the magnetization curves of dispersion E, because the lower-frequency limit of the AGM is 100 Hz, which is too high for relaxation of the large particle structures present. For dispersion OA3, where the

susceptibility maximum for single Brownian particles is expected at 208 kHz (and the onset of the imaginary susceptibility at a lower frequency), no imaginary contribution is found. Probably, these particles perform Néel relaxation. The absence of an imaginary susceptibility confirms that these particles interact only very weakly; the structures seen on cryo-micrographs for these dispersions, indeed looking very loose in contrast to those for dispersions D and E, are reversible on a timescale of the measuring frequency (up to 100 kHz). Although we cannot give a decisive answer about the exact particle morphologies, we conclude that cryo-TEM presents at least a qualitative correct picture for fluids in three dimensions.

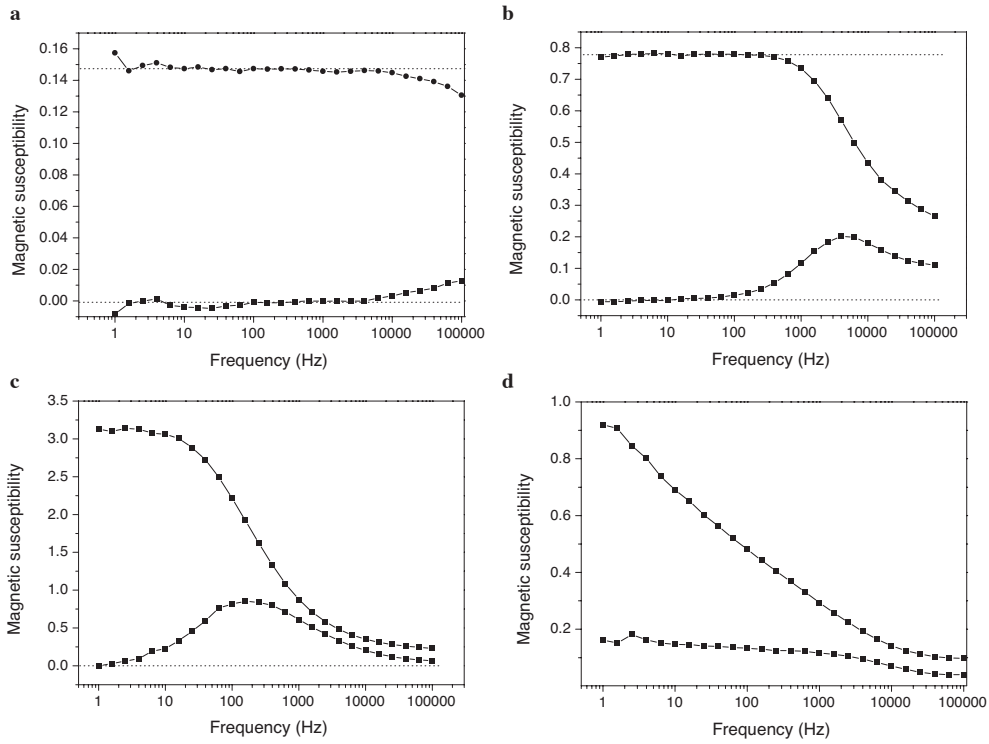

Figure 11. Curves of the real (upper curve) and imaginary susceptibility (lower curve) as a function of frequency. **a**, dispersion B; **b**, dispersion C; **c**, dispersion D; **d**, dispersion E.

4.2.6. Comparison with theory and simulations

As in many simulations [3,7,4], we do not find signs of phase separation in our ferrofluids. However, supporting several theories and simulations [2,9,11,7], our results experimentally demonstrate the presence of linear structures in ferrofluids in zero field for large enough dipoles. Our results qualitatively agree with simulations in two and three dimensions, where fluctuating chains are found, that thermally dissociate and recombine again. Although in

some simulations ring-like structures are found [46], we did not see any in our samples. Almost no quantitative results are known for simulations on ferrofluids in two dimensions, but our results can be compared to theories and simulations in three dimensions. Here, the onset of chain formation roughly starts at a dimensionless reduced dipole moment μ^* (defined as $(\mu_0\mu^2/4\pi kT\sigma^3)^{1/2}$ with μ_0 the permeability of free space and σ the hard sphere diameter) of 2-2.5 with an average chain length varying from 1.36 to 10.25 particles for a concentration ρ^* (defined as $N\sigma^3/V$ with N/V the number of particles per volume) of 0.3 [7]. This value is similar to our experimental results, where for iron particles in dispersion D chain formation starts with a value of 2.4 for μ^* (with $\mu = 13.2*10^{-19}$ Am^2 and σ = 25 nm (a_{core}=6.9 nm, t_s= 6 nm)) and a mean cluster size of 2.49 for a 'two-dimensional' concentration ρ_s^* (defined as $N\sigma^2/A$ with N/A the number of particles per unit of surface) of 0.4.

5. Conclusions

We have exploited the possibility to synthesize dispersions of monodisperse iron particles by thermal decomposition of $Fe(CO)_5$, for which the size and the type of polymeric stabilization layer can be controlled. Larger particles can be grown from seed particles by adding extra $Fe(CO)_5$. We have shown that cryo-TEM is a valuable technique for studying (magnetic) dispersions: particles can be directly imaged *in situ*, giving a realistic view of how particles are organized in a liquid film of the dispersion. Frequency-dependent susceptibility measurements indicate that particle structures in zero field in three-dimensional ferrofluids resemble those in liquid films.

Our experiments for the first time directly visualize the presence of linear clusters in ferrofluids in zero field. Ferrofluid structures appear to be very sensitive to particle size; upon systematically increasing particle size, we find an abrupt transition from separate particles to randomly oriented linear aggregates and even branched networks. These results qualitatively agree with simulations results [3,11,4]. The linear structures we find are indeed dipolar, as is confirmed by their response to high magnetic fields; existing chains at zero field align and grow larger in the field direction as well as perpendicular to that due to lateral attraction. Individual non-aggregated iron particles appear to be magnetically anisotropic due to their particle shape, and align their dipoles with a magnetic field.

For oleic-acid-coated particles a quantitative estimate of interactions between particles is difficult due to their thin surfactant layer, and Van der Waals interactions cannot be ignored. However, PIB-coated iron particles, where the polymer layer masks the Van der Waals attraction and dipolar interactions are adjustable, may well be the experimental equivalent of dipolar spheres in computer simulations [7].

Acknowledgements

Paul Bomans and Peter Frederik from the Electron Microscopy department of the faculty of Medicine, University of Maastricht, are greatly acknowledged for their help with cryo-TEM and for valuable discussions. Dispersion FFOl was synthesized by Dr. Bica (University Politehnica in Timişoara, Romania). Liesbeth Donselaar is thanked for performing cryo-TEM on the magnetite dispersions. Marc Storms and Felix de Haas from the FEI company are thanked for performing the EELS-measurements. The autocorrelation functions were calculated by Roel Dullens. Maarten Terlou is thanked for his help with the image analysis and Ben Erné and Thido Arts for their help with the susceptibility measurements. Financial support was granted by the Dutch Technology Foundation (STW) with financial aid from the Council for Chemical Science of the Netherlands Organization for Scientific Research (CW/NWO).

References

[1] Butter K, Bomans P H, Frederik P M, Vroege G J and Philipse A P 2003 *Nature Materials* **2** 88.
[2] de Gennes P G and Pincus, P A 1970 *Phys. Kondens. Materie* **11** 189.
[3] Weis J J 1998 *Mol. Phys.* **93** 361.
[4] Chantrell R W, Bradbury A, Popplewell J and Charles S W 1982 *J. Appl. Phys.* **53** 2742.
[5] Berkovski B and Bashtovoy V 1996 *Magnetic fluids and applications handbook* (New York: Begel House Inc.).
[6] Lubbe A S, Alexiou C and Bergemann C 2001 *J. Surgical Research* **95** 200.
[7] Teixeira P I C, Tavares J M and Telo da Gama M M 2000 *J. Phys.: Condens. Matter* **12** R411.
[8] Cabuil V 2000 *Current Opinion in Colloid & Interface Science* **5** 44.
[9] Osipov M A, Teixeira P I C and Telo da Gama M M 1996 *Phys. Rev. E.* **54** 2597.
[10] Tlusty T and Safran S A 2000 *Science* **290** 1328.
[11] Tavares J M, Weis J J and Telo da Gama M M 1999 *Phys. Rev. E.* **59** 4388.
[12] Shen L, Stachowiak A, Fateen S K, Laibinis P E and Hatton T A 2001 *Langmuir* **17** 288.
[13] Donselaar L N, Frederik P M, Bomans P H, Buining P A, Humbel B M and Philipse A P 1999 *J. Magn. Magn. Mater.* **201** 58.
[14] Cebula D J, Charles S W and Popplewell J 1983 *J. Physique* **44**.
[15] Gazeau F, Dubois E, Bacri J C, Boue F, Cebers A and Perzynski R 2002 *Phys. Rev. E* **65** 031403.
[16] Rosensweig R E 1985 *Ferrohydrodynamics* (Cambridge: Cambridge University Press).
[17] Griffiths C H, O'Horo M P and Smith T W 1979 *J. Appl. Phys.* **50** 7108.
[18] Pathmamanoharan C, Zuiverloon N L and Philipse A P 2000 *Progr. Colloid Polym. Sci.* **115** 141.
[19] Scholten P 1992 in *Studies of Magnetic Properties of Fine Particles and their Relevance to Materials Science*; Dormann J L and Fiorani D Ed. Elsevier Science Publishers B.V.
[20] Lavender H B, Iyer K A and Singer S J 1994 *J. Chem. Phys.* **101** 7856.
[21] Philipse A P and Maas D 2002 *Langmuir* **18** (25) 9977.
[22] Halsey T C and Toor W 1990 *J. Stat. Phys.* **61** 1257.
[23] Toor W R 1993 *J. Colloid Interface Sci.* **156** 335.
[24] Dhont J K G 1996 *An introduction to dynamics of colloids* (Amsterdam: Elsevier).
[25] Jiles D 1995 *Introduction to Magnetism and Magnetic Materials* (London: Chapman & Hall).
[26] Charles S W 1988 *Chem. Eng. Comm.* **67** 145.
[27] Fannin P C, Scaife B K P and Charles S W 1986 *J. Phys. E.* **19** 238.
[28] De Hek B and Vrij A 1981 *J. Colloid Interface Sci.* **79**.

[29] Bica D 1995 *Romanian Reports in Physics* **47** 256.
[30] Talmon Y 1996 *Ber. Bunsenges. Phys. Chem.* **100** 364.
[31] Steinbrecht R A and Zierold K 1987 *Cryo techniques in biological electron microscopy* (Berlin Heidelberg: Springer Verlag).
[32] Frederik P M, Bomans P H H, Laeven P F J and Nijpels F J T Device for preparing specimens for a cryo-electron microscope. *Netherlands Industrial Property Office (RO/NL)*, 2002.
[33] Reimer L 1989 *Transmission Electron Microscopy: Physics of Image Formation and Microanalysis* Second Edition ed.(Heidelberg: Springer Verlag).
[34] Carlemalm E, Colliex C and Kellenberger E 1985 *Advances in Electronics and Electron Physics* **63** 269.
[35] Goossens A, de Jongh L J, Butter K, Philipse A P, Crajé M W J and van der Kraan A M 2002 *Hyperfine Interactions* **141/142** 381.
[36] Hanson M, Johansson C, Pedersen M S and Morup S 1995 *J. Phys.: Condens. Matter* **7** 9269.
[37] Bauer-Grosse E and Le Caër G 1987 *Philosophical Magazine B* **56** 485.
[38] Butter K, Bomans P H, Frederik P M, Vroege G J and Philipse A P 2003 *J. Phys.: Condens. Matter* **15** S1451.
[39] Frederik P M, Stuart M C A, Schrijvers A H G J and Bomans P H H 1989 *Scanning Microscopy* **supplement 3** 277.
[40] Oostergetel G T, Esselink F J and Hadziioannou G 1995 *Langmuir* **11** 3721.
[41] Bradbury A, Menear S and Chantrell R W 1986 *J. Magn. Magn. Mater.* **54-57** 745.
[42] Gast A P and Zukoski C F 1989 *Adv. Coll. Int. Sci.* **30** 153.
[43] Halsey T C 1992 *Science* **258** 761.
[44] Skjeltorp A T 1983 *Phys. Rev. Lett.* **51** 2306.
[45] de Gans B J, Blom C, Philipse A P and Mellema J 1999 *Phys. Rev. E.* **60** 4518.
[46] Tavares J M, Weis J J and Telo da Gama M M 2002 *Phys. Rev. E* **65** 061201.

7 Rotational diffusion in iron ferrofluids

Abstract

The dynamic magnetic susceptibility of relatively monodisperse iron ferrofluids was measured from 1 Hz to 100 kHz for different sizes of the iron particles (all with a 7 nm thick organic surface layer, dispersed in decalin). In the case of particles with an iron core of 6 nm radius, the orientation of the magnetic dipole moment thermally rotated inside the particles (Néel rotation). In the case of particles with a slightly larger iron core, the orientation of the magnetic dipole moment was blocked inside the particles but could still change by rotational diffusion of the particles themselves (Brownian rotation). With even larger particles (above 7 nm iron core radius), aggregates were formed: the rotational diffusion rate was lower than that of single particles by more than one order of magnitude. This sudden appearance of aggregates above a certain size of the iron particles agrees with previous observations in two dimensions, by cryogenic transmission electron microscopy (cryo-TEM) of ultra-thin ferrofluid films. Here it is found that the threshold for aggregation is practically the same in three dimensions. Moreover, the rotational diffusion rate of the aggregates is seen to increase upon dilution, which suggests that the aggregate size results from a dynamic equilibrium.

Chapter 7 is based on the paper: Erné, B.H., Butter, K., Kuipers, B.W.M., Vroege, G.J., Rotational diffusion in Iron Ferrofluids, *Langmuir*, in press (intended volume 19(21)).

1. Introduction

Ferrofluids are colloidal dispersions of magnetic nanoparticles with a single magnetic domain [1-3]. They are used in several commercial applications [4,5] and as model systems in fundamental work on dipolar fluids [6-8]. When the magnetic interaction between particles is sufficiently strong, they form aggregates. In a previous study [9-11] (see also chapter 6), anisotropic aggregation was observed as a function of the particle size using a series of iron ferrofluids. The aggregates were imaged using cryogenic electron microscopy (cryo-TEM). Here, the same iron ferrofluids are investigated by measuring the dynamic magnetic susceptibility, giving new information about the rotational diffusion of single particles and aggregates.

The series of ferrofluids consists of relatively monodisperse metallic iron particles (10 to 15 % polydispersity) with a 7 nm thick organic surface layer, dispersed in the solvent decalin. The low polydispersity is important for the interpretation because the magnetic interaction energy between two monodomain particles is extremely sensitive to the particle size (see Theory section). When ferrofluid samples were prepared for cryo-TEM in the previous study [9-11] (see chapter 6), they were cooled down so rapidly that the solvent vitrified and magnetic particle positions remained unchanged. Films of dispersions could therefore be studied *in situ*. Figure 1 summarizes those results (except for ferrofluid A, which had even smaller particles than ferrofluid B and was only weakly magnetic). No aggregates are observed for the ferrofluids with the smallest particles (B and C). The slightly larger D particles show chain-like aggregates of a few particles, and the ferrofluid with the largest particles (E) shows larger aggregates with branched chains.

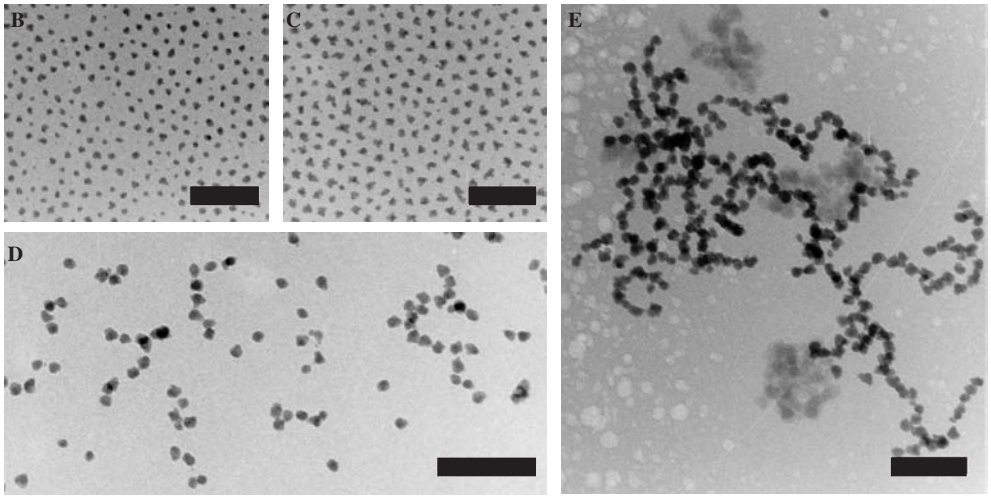

Figure 1. Cryo-TEM pictures of ferrofluids consisting of metallic iron particles with a 7 nm thick organic surface layer dispersed in decalin [9-11]. The radius of the iron core gradually increases from ferrofluid B (6 nm) to ferrofluid E (8 nm). The scale bars are 100 nm.

Compared to scattering techniques, which yield results in reciprocal space and whose interpretation is model-dependent, cryo-TEM has the advantage of giving a direct image of the ferrofluid structure, without the strong drying effects obtained with conventional TEM. Nevertheless, aggregates seen by cryo-TEM are not necessarily the same as in bulk ferrofluid. During sample preparation, before vitrification, a thin film of ferrofluid is made which is not much thicker than the magnetic particles themselves. Any aggregates seen by cryo-TEM are therefore two-dimensional, whereas aggregates in bulk ferrofluid can be branched in three dimensions. The magnetic susceptibility spectra in this chapter are complementary to the cryo-TEM results because they probe aggregates as they occur in bulk ferrofluid. Moreover, the magnetic susceptibility measurements are easily performed as a function of concentration, in contrast to cryo-TEM, for which the two-dimensional concentration is difficult to control.

The frequency dependence of the magnetic susceptibility tells how fast the magnetic dipole moments in a ferrofluid reach a new steady-state average orientation when a magnetic field is applied [12]. In the measurements of the present work, the applied magnetic field is so weak that reorientation occurs by thermal motion. One possible mechanism is that the magnetic dipole moment rapidly rotates inside the particles (Néel rotation, Figure 2a). Otherwise, if the orientation of the magnetic dipole is locked within the particles, entire particles or aggregates must rotate (respectively Figure 2b and Figure 2c). The Brownian rotation rate of single spheres is a well-known function of the particle radius and the solvent viscosity (see Theory section), whereas the Brownian rotation of an aggregate is much slower and should depend on the size, shape, and flexibility of the aggregate. Determining the frequency up to which the magnetization of a ferrofluid can be modulated using an alternating magnetic field is a way to characterize the magnetic particles or aggregates.

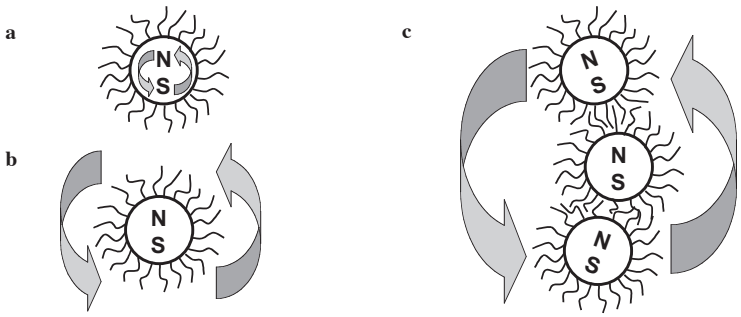

Figure 2. Schematic illustration of mechanisms which lead to a change in orientation of the magnetic dipole moments of ferrofluid particles: **a**, Néel rotation of the magnetic moment inside a particle, **b**, Brownian rotation of a single particle, and **c**, Brownian rotation of an aggregate. The magnetic poles are indicated by "N" and "S".

The following section recalls general theory about the magnetization of ferrofluids in a constant or alternating external magnetic field. The Experimental section refers to the

synthesis and characterization of the ferrofluids and describes the dynamic magnetic susceptibility setup. This is followed by the results and a separate discussion.

2. Theory

The magnetic properties of ferrofluids are introduced, with emphasis on the dynamic magnetic susceptibility. A more complete presentation of this technique was authored by Fannin [12], and general reviews of the properties of magnetic fluids can be found in References [1-3].

Since each magnetic particle in the ferrofluid has a single magnetic domain, the magnetic dipole moment μ of a particle is given by its volume times the saturation magnetization per unit volume, m_s. Assuming that the particles are spherical with a magnetic radius a_M, μ is given by

$$\mu = \frac{4}{3}\pi a_M^3 m_s \tag{1}$$

In other ferrofluids, the magnetic radius a_M was observed to be somewhat smaller than the physical radius a_{core} of the sphere of magnetic material, an effect which was ascribed to the pinning of spins near the surface as a result of interaction with surfactant molecules [3]. The interaction energy U between two particles depends on the magnitude and orientations of the dipole moments $\vec{\mu}_1$ and $\vec{\mu}_2$ and the separation vector $\vec{r}$ (with amplitude r) between the centers of the particles:

$$\frac{\mu_0}{4\pi}\left(\frac{\vec{\mu}_1\cdot\vec{\mu}_2}{r^3} - \frac{3(\vec{\mu}_1\cdot\vec{r})(\vec{\mu}_2\cdot\vec{r})}{r^5}\right) \tag{2}$$

where μ_0 is the permeability of vacuum. The attraction is maximal in the head-to-tail orientation, and assuming that all the particles are alike, it is given by

$$U_{max} = \frac{-\mu_0}{2\pi}\left(\frac{\mu^2}{(2a)^3}\right) \tag{3}$$

where a is the physical radius of the particles, including the surfactant layer, and 2a is the closest distance at which the particles can approach each other. Note that, due to equation (1), this scales with a_M^6/a^3. Aggregation is expected when $-U_{max}$ is above $\approx 2k_BT$, where k_BT is the thermal energy [13-16]. In Figure 3, equation (3) was used to calculate $-U_{max}/k_BT$, using the saturation magnetization of our carbon-containing iron material (see experimental) and assuming a difference of 1.5 nm between a_{core} and a_M and an organic surface layer of 7.0 nm ($a-a_{core}$).

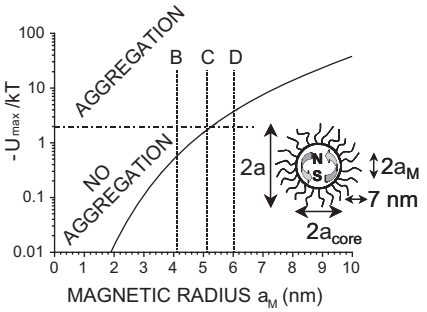

Figure 3. Theoretical calculation of the maximum interaction energy $-U_{max}/k_BT$ between two iron particles with a 7 nm thick organic surface layer and a magnetic radius a_M 1.5 nm smaller than the iron core radius a_{core}, plotted as a function of a_M (equation 3). For ferrofluids B, C, and D, the experimental magnetic radii are indicated. The inset illustrates different types of radii used to describe the particles in the text.

2.1. Magnetization in a constant magnetic field

In zero external magnetic field, the orientations of the magnetic dipoles are isotropically distributed in all directions, resulting in zero magnetization of the ferrofluid. When a magnetic field is applied, alignment of the magnetic dipoles is favored in the same direction as the magnetic field, because the particles are (super)paramagnetic. The interaction energy of a dipole of magnetic moment μ aligned with a magnetic field H equals $\mu_0\mu H$. The average degree of alignment of the magnetic dipoles depends on the ratio of $\mu_0\mu H$ to k_BT, since thermal motion tends to destroy the alignment. For noninteracting monodisperse particles, the average magnetization M of the ferrofluid as a function of the external magnetic field is given by the Langevin equation,

$$M = M_s\left[\coth\frac{\mu_0\mu H}{k_BT} - \frac{k_BT}{\mu_0\mu H}\right] \tag{4}$$

where M_s is the saturation magnetization and it is assumed that all particles have the same magnetic dipole moment μ. This equation accounts for the general shape of the magnetization curve.

In the low-magnetic-field limit, magnetization is linear with the external magnetic field, and the proportionality factor is called the magnetic susceptibility χ:

$$M = \chi H \tag{5}$$

According to equation (4), the steady-state value χ_0 of the magnetic susceptibility in the low-magnetic-field limit is given by:

$$\chi_0 = \mu_0\mu M_s / 3k_BT \tag{6}$$

In the high-magnetic-field limit, all magnetic dipoles point in the same direction and the magnetization of the ferrofluid is given by

$$M_s = N\mu \tag{7}$$

where N is the number of particles per unit volume.

The measurement of a magnetization curve allows the determination of the ratio of χ_0 to

M_s, from which the magnetic dipole moment μ can be calculated (equation 6). In the case of separate spherical particles, the magnetic radius can then be calculated using equation (1). For an aggregate, the magnetic dipole moment depends on the number of magnetic particles as well as on their spatial positions, orientations, and sizes.

2.2. Magnetization in an alternating magnetic field

When the external magnetic field H is changed, a new steady-state magnetization is not reached right away, because reorientation of the magnetic dipole moments takes time. In the low-field limit, the rate at which the magnetization M goes toward the steady state magnetization $\chi_0 H$ can be assumed to be proportional to the difference between the two:

$$\frac{dM}{dt} = -\omega_{char}(M - \chi_0 H) \tag{8}$$

where t is time and ω_{char} is the rate constant in s^{-1}, i.e., it is a characteristic frequency. One way to study the reorientation rate is by applying a weak alternating magnetic field,

$$\widetilde{H} = H_0 \exp(i\omega t) \tag{9}$$

where H_0 is the amplitude of the magnetic field modulation ("weak" means $\mu_0 \mu H_0 << k_B T$), $i = \sqrt{-1}$, and ω is the radial frequency in s^{-1} (2π times the frequency in Hz). The alternating magnetic field induces a harmonic change in the magnetization, $\widetilde{M}$, so that equation (8) can be rewritten as:

$$i\omega\widetilde{M} = -\omega_{char}(\widetilde{M} - \chi_0 \widetilde{H}) \tag{10}$$

Solving for $\widetilde{M}$ leads to

$$\widetilde{M} = \left[\omega_{char}/(\omega_{char} + i\omega)\right]\ \chi_0\ \widetilde{H} \tag{11}$$

The dynamic magnetic susceptibility can now be defined as the ratio of $\widetilde{M}$ to $\widetilde{H}$:

$$\chi(\omega) = \widetilde{M}/\widetilde{H} = \left[\omega_{char}/(\omega_{char} + i\omega)\right]\chi_0 \tag{12}$$

This can be split into a *real* (in-phase) part χ' and an *imaginary* (out-of-phase) part χ'':

$$\chi(\omega) = \chi'(\omega) - i\chi''(\omega) \tag{13}$$

$$\chi'(\omega) = \left[\omega_{char}^2/(\omega_{char}^2 + \omega^2)\right]\chi_0 \tag{14a}$$

$$\chi''(\omega) = \left[\omega\,\omega_{char}^2/(\omega_{char}^2 + \omega^2)\right]\chi_0 \tag{14b}$$

In the low-frequency limit, when $\omega << \omega_{char}$, the alternating magnetic susceptibility has a value which corresponds to the initial slope χ_0 of the steady-state magnetization curve. In the high-frequency limit, when $\omega >> \omega_{char}$, the orientations of the magnetic dipole moments cannot keep up with the alternating magnetic field, and the dynamic magnetic susceptibility is zero. The imaginary component is maximal at $\omega = \omega_{char}$.

When the magnetic dipole moment is free to move within the particles (Néel rotation), the characteristic frequency is given by

$$\omega_N = 2\pi f_0 \exp\left[-\frac{KV}{k_B T}\right] \tag{15}$$

where f_0 is in the 10^7 to 10^{12} Hz range [12,17] and is often assumed to be of the order of 10^9 Hz [2,3], K is a material- and shape-dependent anisotropy constant, and V is the magnetic domain volume, i.e., $(4/3)\pi a_M^3$ for a spherical domain.

When the magnetic dipole moment has a fixed orientation within the particles, a change in the orientation of the magnetic dipole moment requires rotation of the entire particle or aggregate. For single spherical particles, the characteristic frequency of Brownian rotational diffusion is given by [12]

$$\omega_B = 2D_r = k_B T/(4\pi\eta a_h^3) \tag{16}$$

where D_r is the rotational diffusion coefficient, η is the viscosity of the solvent, and a_h is the hydrodynamic radius of the particle. The latter can be slightly larger than the physical radius a because of a layer of solvent which moves along with the particle.

Characteristic frequencies for Néel and Brownian rotation of single particles are calculated as a function of the radius in Figure 4. The characteristic frequency of the rotational diffusion of aggregates is a subject of the Discussion section. In principle, both the Néel and Brownian mechanisms can occur simultaneously for the same particles, so that

$$\omega_{char} = \omega_N + \omega_B \tag{17}$$

When the two mechanisms occur on different time scales, the fastest determines the characteristic frequency. Due to the strong dependence of ω_N on a_M, the rotation of a chosen particle is likely to be determined by only one of the two mechanisms (Figure 4). In ferrofluids C-E, most of the particles show Brownian rotation and a smaller part shows Néel rotation at much higher frequencies, beyond our experimental range. If two populations of particles had characteristic frequencies of 1 kHz and 10 MHz, respectively, a spectrum as in

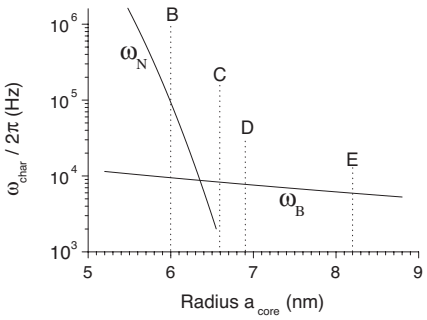

Figure 4. Theoretical calculation of the Néel rotation frequency ω_N (equation 15) and the Brownian rotation frequency ω_B of single particles as a function of the iron core radius a_{core} (equation 16, $\eta = 2.5 \times 10^{-3}$ kg m^{-1} s^{-1}). The particles are assumed to be spherical, with $a_h = a_{core} + 7.0$ nm and $a_{core} = a_M + 1.5$ nm. The calculation of ω_N is based on $f_0 = 10^9$ Hz and K=100 kJ m^{-3}, chosen to reproduce the observed dominance of the Néel or the Brownian mechanism for ferrofluids B-E (see discussion). The experimental iron core radii from TEM are indicated.

Figure 5 would be obtained. At 100 kHz (the upper frequency limit of our experiments), the imaginary component of $\chi(\omega)$ is almost zero, in contrast to the real component, since this is in the low-frequency limit of the 10 MHz particles.

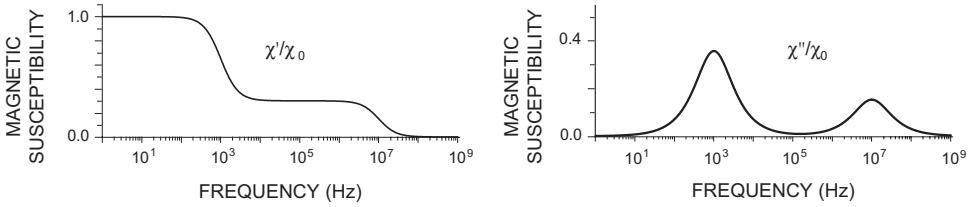

Figure 5. Theoretical calculation of the dynamic magnetic susceptibility as a function of frequency (real and imaginary components) for a ferrofluid with two populations of particles, with characteristic frequencies of 1 kHz and 10 MHz, respectively (equations 13 and 14).

In experimental ferrofluids, a distribution of the size of the particles and/or aggregates leads to a distribution of the characteristic frequency. Figure 6 shows the effect of a log-normal distribution of the characteristic frequency:

$$W = \exp\left\{-\left[\log_{10}(\omega_{char}) - \log_{10}(\omega_0)\right]^2 / \left[2\sigma^2\right]\right\} \tag{18}$$

where W gives the relative contribution of particles with a characteristic frequency ω_{char} to the susceptibility spectrum, ω_0 is the average characteristic frequency, and σ is the standard deviation. When σ increases, the inflection point of the real component of $\chi(\omega)$ and the maximum of the imaginary component remain at the same frequency. However, the transition from the low- to the high-frequency limit is spread out across a wider frequency range. Moreover, the maximum of the bell-shaped curve of the imaginary component is relatively lower.

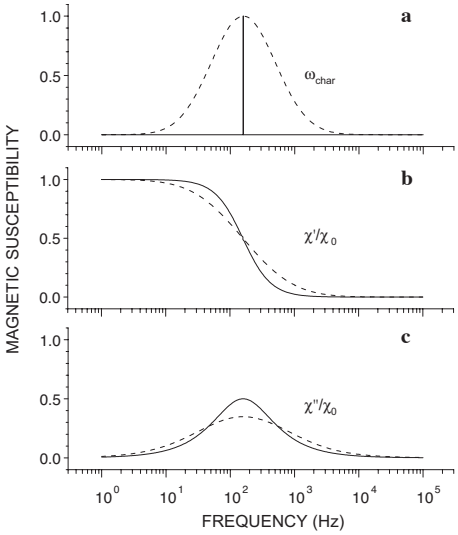

Figure 6. Effect of **a**, a log-normal distribution of the characteristic frequency on the frequency dependence of **b**, the real and **c**, the imaginary component of the dynamic magnetic susceptibility. The curves were calculated using equations 14 and 18 ($\omega_0 = 1000\ s^{-1}$, full curve: $\sigma = 0$, dotted curve: $\sigma = 0.5$).

3. Experimental

The synthesis and characterization of the iron ferrofluids are also described in Chapter 3 [9-11]. In brief, iron particles coated with modified polyisobutene [18] (2400 g mol^{-1}) were obtained by thermal decomposition of iron carbonyl in a solution of polyisobutene in decalin, in a similar way as described by Pathmamanoharan et al [18]. The ferrofluids were characterized using different techniques, including TEM (Figure 1) and Small Angle X-ray Scattering (SAXS). From these measurements, it was deduced that the organic layer at the surface of the iron particles was 6 to 7 nm thick and that the radii of the iron cores were as listed in Table 1. Different iron core radii are obtained by TEM (a_{TEM}) and by SAXS (a_{SAXS}, obtained from Guinier fits) [9-11], partly because the two techniques give different types of weighed averages. Mössbauer spectroscopy revealed the presence of carbon in the iron cores according to the stoichiometry of $Fe_{0.75}C_{0.25}$ [19] (see also chapter 3). The saturation magnetization of this material is 1.49×10^6 A m^{-1} [20], slightly lower than that of pure iron [21] (1.71×10^6 A m^{-1}). The concentrations in Table 1 were determined by elemental analysis.

Table 1. Iron core radii and concentrations of the ferrofluids [9-11].

ferrofluid	iron core radius (nm)		concentration (mass fraction Fe)
	a_{TEM}	a_{SAXS}	
B	6.0 ± 0.8	5.3	0.038
C	6.6 ± 1.4	6.0	0.061
D	6.9 ± 1.0	8.8	0.108
E	8.2 ± 1.5	9.5	0.219

The dynamic magnetic susceptibility was measured at room temperature (20 °C) across the 1 to 10^5 Hz range using a homebuilt setup with mutually inducting coils schematized in Figure 7. An alternating current $\tilde{I}$ with an amplitude of 10 mA was passed through two sets of identical primary coils (coils 1-4) in Helmholtz configuration connected in series (diameter d_1 = 57.5 mm, $N_1 = 2 \times 110$ turns per coil, height difference z = 30 mm between coils 1 and 2 and between coils 3 and 4). This generated homogeneous alternating magnetic fields and produced alternating voltages in two identical secondary coils (5 and 6, diameter d_2 = 10.0 mm, N_2 = 220 turns per coil) positioned halfway between the primary coils. A lock-in amplifier measured amplitude and phase of the difference in alternating voltage between the two secondary coils (coils 5 and 6), which is proportional to the susceptibility of the ferrofluid sample placed inside secondary coil 5 (secondary coil 6 was kept empty). The ferrofluid was contained in a hermetically sealed glass tube with an internal diameter d_3 of 5.0 mm. The AC voltage difference $\tilde{V}_{56}$ was corrected for the weak signal of a glass tube filled with solvent. The magnetic susceptibility of the ferrofluid was calculated using

the following equation

$$\chi = \frac{i\tilde{V}_{56}}{\tilde{I}} \frac{2(d_1^2 + z^2)^{3/2}}{f\mu_0 \pi^2 d_1^2 d_3^2 N_1 N_2} \tag{19}$$

where f is the frequency in Hz.

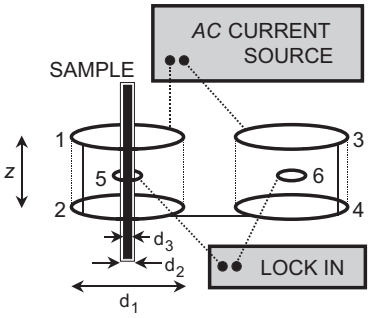

Figure 7. Schematic illustration of the dynamic magnetic susceptibility setup.

Magnetic susceptibilities determined in this way were in quantitative agreement with a Kappabridge KLY-3 susceptibility meter (Agico) at its operating frequency of 875 Hz. The reliability of the latter equipment itself was verified by measuring the diamagnetic susceptibility of various solvents, which were in agreement with the literature [21]. The phase of the dynamic susceptibility measured with the homebuilt setup was verified using a magnetite ferrofluid with a negligible imaginary component of the dynamic magnetic susceptibility in the frequency range of our experiments.

The interaction energy $\mu_0 \mu H$ of the alternating magnetic field (30 A m^{-1} amplitude) with the iron particles used was of the order of 10^{-2} $k_B T$. On this basis, it is assumed that the forces exerted on the particles and aggregates were negligible and did not alter the systems. This assumption is supported by the observation that spectra measured at 10 or 100 times lower amplitude were the same, except for a lower signal-to-noise ratio. The height of the glass tube containing the ferrofluid could be varied with respect to the coils. Height-resolved susceptibility measurements performed in this way indicated that the ferrofluids were stable at least over a period of several months. The frequency-dependent measurements which are presented were performed at a single height, halfway the column of ferrofluid, which was 10 cm high.

Magnetization curves were measured at room temperature using a Micromag 2900 Alternating Gradient Magnetometer (Princeton Measurements Corporation). Samples of about 3 μL were contained in airtight glass cups, filled in a glovebox. This equipment uses a piezo-electric element to measure the motion of the sample due to a weak alternating magnetic field (amplitude: 700 A m^{-1}) superimposed on the much stronger static magnetic

field whose value was scanned from -1.2×10^6 A m^{-1} to $+1.2 \times 10^6$ A m^{-1} at a rate of 6×10^4 A m^{-1} s^{-1}. The frequency of the alternating magnetic field was in the 100-1000 Hz range and corresponded to the mechanical resonance frequency, approximately 250 Hz.

4. Results

Frequency-dependent magnetic susceptibility measurements of iron ferrofluids B-E are presented in Figure 8. For comparison, measurements performed after dilution by a factor of 10 are also shown (except for B, for which the shape of the spectrum remained the same upon dilution but the amplitude decreased by more than the expected factor of 10, presumably due to oxidation of iron by residual oxygen in the decalin used for dilution). In ferrofluids B-D, the low-frequency limit is reached (frequency-independent real component, zero imaginary component), in contrast to ferrofluid E. In none of the systems the high frequency limit ($\chi = 0$) is reached. The measurements on C-E correspond to the situation simulated in Figure 5, with at least two populations of particles with different average characteristic frequencies, one of which in excess of 100 kHz.

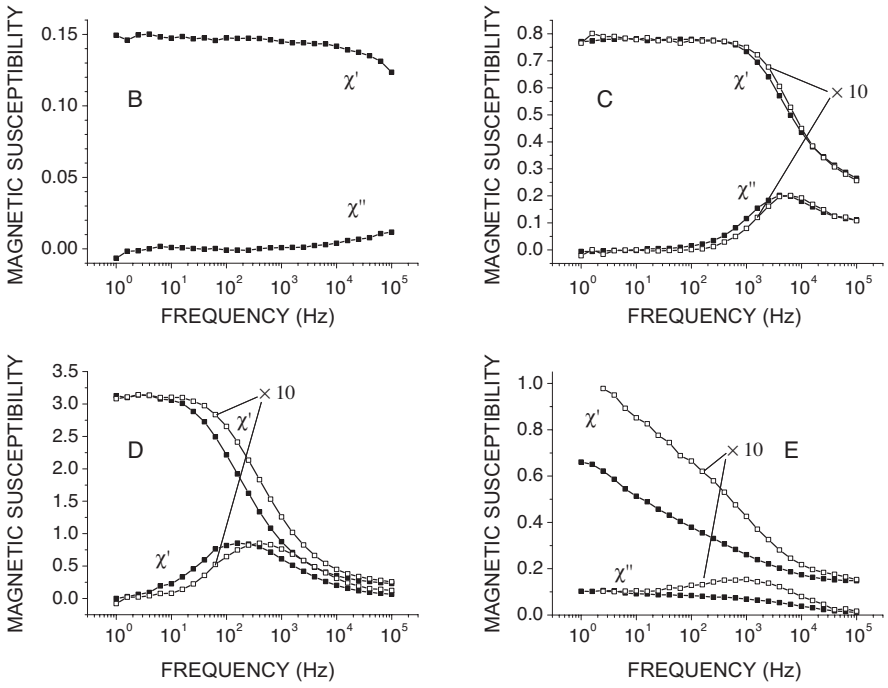

Figure 8. Frequency dependence of the real (χ') and imaginary (χ'') components of the magnetic susceptibility of ferrofluids B-E. Measurements performed after dilution by a factor of 10 have been rescaled by multiplying the data by a factor of 10 ("×10"). The lines are fits of the data (see Table 2).

The measurements have been fitted using a single log-normal distribution of the characteristic frequency (equation 18) and a frequency-independent offset of χ' due to particles with a characteristic frequency well above 100 kHz. For the diluted E ferrofluid, a second log-normal distribution was also used to fit the measurements. The values of the fit parameters are given in Table 2. For ferrofluid B, the characteristic frequency is above 100 kHz, outside the measurement range. For ferrofluid C, the characteristic frequency is 5.5 kHz and remains about the same after dilution, even by a factor of 100 (not shown). For ferrofluid D, the characteristic frequency is 220 Hz before dilution and 470 Hz after dilution. Dilution by a factor of 100 increases the characteristic frequency further (not shown). The measurements on ferrofluid E correspond to a very wide distribution of the characteristic frequency. Before dilution, the data can be fit using a log-normal distribution around an average characteristic frequency lower than 1 Hz, with a standard deviation of a few logarithmic units. After dilution, there are two populations of particles, one similar to the distribution before dilution and another with a characteristic frequency of about 1.5 kHz.

Table 2. Values of parameters ω_0 and σ used to fit the measurements in Figure 8 according equations 14 and 18. Ferrofluids C, D, and E also contain particles with an average characteristic frequency ($\omega_0/2\pi$) above 10^6 Hz.

ferrofluid	$\omega_0 / 2\pi$ (Hz)	σ
B	$\sim 3 \times 10^6$	~1.3
C	5500	0.4
C diluted 10×	5900	0.5
D	220	0.6
D diluted 10×	470	0.6
E	0.05	4.2
E diluted 10×	0.003	3.3
	1500	0.7

Magnetization curves of ferrofluids B-E were measured to determine the magnetic radius from the initial slope and the saturation magnetization (equations 1,6,7). As an example, Figure 9 shows the curve for ferrofluid D. No hysteresis was observed between the forward and backward scans of the magnetic field, except for ferrofluid E. For the latter system, no steady-state magnetization curve could be obtained: the hysteresis loop depended on the magnetic-field-scan history of the sample. This is in line with the slow dynamics of ferrofluid E revealed in Figure 8. For ferrofluids B, C, and D, magnetic radii of 4.1 nm, 5.1 nm, and 6.0 nm were determined, respectively. As expected (see Theory), the magnetic radii are somewhat smaller than the iron core radii from TEM (Table 1). However, for ferrofluid D, the calculated radius does not directly correspond to single particles, because aggregates are present (Figure 1) and the frequency of the magnetic probe of the magnetometer (250 Hz) is above the frequency range where the slope of the magnetization curve corresponds to the low-frequency limit of the magnetic susceptibility (which is below

about 10 Hz for ferrofluid D, see Figure 8).

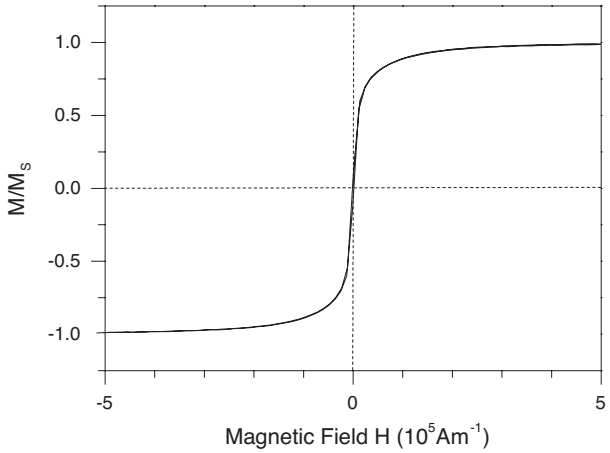

Figure 9. Magnetization M of ferrofluid D (scaled to the saturation magnetization M_s) as a function of the external magnetic field H determined using a weak alternating magnetic probe field at 250 Hz (no hysteresis between forward and backward scans).

5. Discussion

The results are discussed separately for each member of the series of iron ferrofluids, starting with the system with the smallest magnetic particles.

Ferrofluid B

The characteristic frequency for thermal rotation of the magnetic dipole moment in ferrofluid B is well above 100 kHz (Figure 8 and Table 2). Considering the physical radius of the particles (from TEM), 6 nm iron plus 7 nm organic surface layer, this frequency is too high to correspond to the Brownian rotational diffusion of single particles which would have led to a characteristic frequency of about 10 kHz (Figure 4). It must therefore be caused by Néel rotation of the magnetic dipole moment inside the particles.

When the particles are just slightly larger than in ferrofluid B, Néel rotation of the magnetic dipole moment inside the particles no longer is faster than Brownian rotation of the particles in the solvent. It was already seen in the theory section that the characteristic frequency for Néel rotation is given by

$$\omega_N = 2\pi f_0 \exp\left[-\frac{KV}{k_B T}\right] \tag{15}$$

In Figure 4, the observed threshold above which Brownian rotation becomes the dominant

mechanism could be reproduced by assuming that $f_0 = 10^9$ Hz and K = 100 kJ m^{-3}. Although that value of f_0 has often also been assumed in the past [2,3], there are measurements on iron which indicate that a better value for f_0 is 10^{12} Hz [17], in which case the anisotropy constant K of our particles would be about 175 kJ m^{-3}. From either estimate, the magnetic anisotropy of our particles is one order of magnitude larger than the bulk magnetocrystalline anisotropy of iron (≈ 12 kJ m^{-3}) [22]. The reason is probably that in single domain particles, the magnetocrystalline anisotropy is not the main contribution: other terms such as the surface anisotropy are more important [17].

Ferrofluid C

For most particles in ferrofluid C, the characteristic frequency for thermal rotation is about 5.5 kHz (Figure 8 and Table 2). Considering the radius of the particles, 6.6 nm iron (from TEM) plus 7 nm organic surface layer, this frequency is of the order expected for the Brownian rotational diffusion of single particles (Figure 4). This indicates that the Brownian rotation of the particles is uncorrelated, in agreement with the absence of aggregates seen by cryo-TEM (Figure 1). For the same reason, the characteristic frequency does not change when the ferrofluid is diluted, and the slope of the magnetization curve corresponds to the magnetic moment of single particles ($\mu = 8.4 \times 10^{-19}$ A m^2).

Using equation (16), the log-normal characteristic frequency distribution can be converted into a hydrodynamic radius distribution, leading to Figure 10. The hydrodynamic radius of 16 ± 6 nm is slightly larger than the physical radius of about 14 nm (iron core radius a_{TEM} = 6.6 ± 1.4 nm, organic layer thickness 6 to 7 nm). In principle, the hydrodynamic radius can include a solvent layer and is affected by particle roughness and nonsphericity. The larger standard deviation than that of the iron core radius can be due to a distribution of the surface layer thickness and of the particle shape.

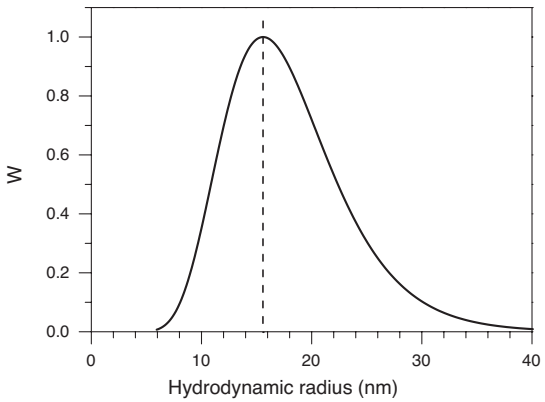

Figure 10. Hydrodynamic radius (a_h) distribution calculated from the characteristic frequency distribution of ferrofluid C (Table 2) using equation 16 ($\eta = 2.5 \times 10^{-3}$ kg m^{-1} s^{-1}). The vertical dotted line indicates the average radius.

Part of the particles in ferrofluid C appears to have a characteristic frequency above 100 kHz, indicating Néel rotation as in ferrofluid B. These are the smallest C particles, although they do not have to be much smaller than the average C particle, since the transition from Néel to Brownian rotation as function of particle size is quite abrupt (Figure 4).

Ferrofluid D

In ferrofluid D, a minor part of the magnetic dipoles has a thermal rotation frequency above 100 kHz and the major part has a broad distribution of the characteristic frequency around 220 Hz. Néel rotation occurs for the particles with a characteristic frequency above 100 kHz. However, the 220 Hz characteristic frequency of most particles is well below that for the Brownian rotation of single particles (about 5.9 kHz, Figure 4) and must correspond to the rotational diffusion of aggregates. These observations agree with cryo-TEM, which shows a population of single particles and a population of particles present in aggregates of a few particles.

In principle, there is insufficient information to deduce the number N of particles per aggregate from the characteristic rotation frequency. The Brownian rotation rate should depend on the size, shape, and rigidity of the individual particles and of the aggregates which they form. Nevertheless, a rough estimate will now be made of how the characteristic frequency depends on N, to illustrate how much the rotational diffusion can slow down even when relatively small aggregates are formed. The estimate is based on the formula of Tiroda et al [23-25] for the rotational diffusion coefficient of spherocylinders with an aspect ratio $L/d \geq 2$, where L is the rod length and d is the cross-sectional diameter. By dividing that expression by equation (16) for the Brownian rotation of a single spherical particle, and by interpreting the length-to-thickness ratio of the spherocylinder as a measure for N, the following relation is obtained ($N \geq 2$):

$$\omega_{chain} / \omega_{single} \approx \frac{3}{N^3}(\ln N - 0.662 + 0.917N^{-1} - 0.050N^{-2}) \qquad (20)$$

where ω_{chain} is the characteristic frequency for the rotational diffusion of a chain of N particles and ω_{single} is the characteristic frequency for a single particle. The ratio $\omega_{chain}/\omega_{single}$ calculated using equation (20) is plotted as a function of N in Figure 11. It can be seen that the formation of aggregates of 4 particles is sufficient to decrease the rotational diffusion rate by a factor of 25 compared to the rotational diffusion rate of single particles. The factor of 25 corresponds to the ratio $\omega_{chain}/\omega_{single}$ for ferrofluid D (before dilution), whose aggregates indeed contain about 4 particles. According to cryo-TEM, the average number of particles per aggregate is 3.6 if single particles are left out of the average.

Upon dilution, the characteristic frequency goes up, which indicates that the size of the aggregates goes down (Figure 8 and Table 2). This suggests that the size of the aggregates is determined by a dynamic equilibrium. If single magnetic particles can reversibly join an aggregate or leave it, the size of the aggregates results from the competition between both

processes, and it is possible to have a small steady-state number of particles per aggregate. The lower the concentration of single particles, the more the dynamic equilibrium shifts toward small aggregates. If aggregation were irreversible, aggregates would only be able to grow in size and would not shrink upon dilution.

According to equation (3), the maximum magnetic attraction energy of two particles in ferrofluid D is of the order of 3 k_BT, assuming a rigid organic surface layer of 7 nm and a difference of 1.5 nm between a_{core} (from TEM) and a_M. This agrees with results by other authors, who found aggregation starting at an attraction energy of 2 to 2.5 k_BT [13-16]. In an aggregate, the distance between two particles is likely to be somewhat closer due to flexibility of the organic surface layer, leading to an even higher attraction energy. In ferrofluid C, the maximum attraction between two particles is about 1.6 k_BT (Figure 3), which apparently is insufficient for the formation of aggregates.

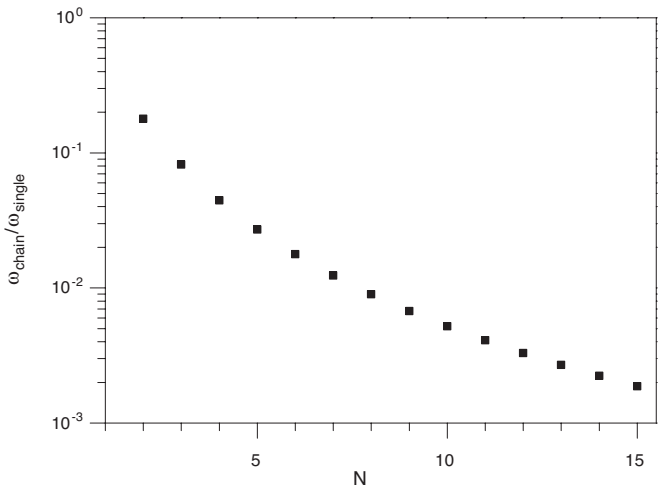

Figure 11. Ratio of the rotational diffusion frequency ω_{chain} of a chain of N particles to the rotational diffusion frequency ω_{single} of a single particle according to equation (20).

Ferrofluid E

As in ferrofluid D, a minor part of the particles in ferrofluid E exhibits Néel rotation of the magnetic moment and the major part of the particles is in aggregates. Judging from the much lower characteristic frequencies in ferrofluid E (Figure 8 and Table 2), the aggregates are much larger than in ferrofluid D. This is in agreement with cryo-TEM (Figure 1).

Upon dilution, a second population of particles appears with a characteristic frequency of about 1.5 kHz. This frequency is too low to correspond to the rotation of single particles. According to equation (20), it is probably due to aggregates of two particles. If the size of the aggregates results from a dynamic equilibrium, a smooth distribution of the aggregate size would be expected, instead of two separate populations. In that respect, the behavior of ferrofluid E appears to differ from ferrofluid D. To elucidate this, a more detailed study of

the concentration dependence of aggregation in both ferrofluids would be needed.

6. Conclusions

The dynamic susceptibility spectrum of a ferrofluid is sensitive to the presence of aggregates. The ferrofluids for which aggregates were observed by cryo-TEM, ferrofluids D and E (Figure 1), have much slower rotational diffusion rates than expected for single particles (Figure 8). The number of particles in the aggregates is difficult to estimate on the basis of the rotational diffusion rate, because it also depends on the shape and flexibility of the aggregates. Nevertheless, the increase in the rotational diffusion rate upon dilution indicates that the size of the aggregates decreases. This suggests that the size of the aggregates results from a dynamic equilibrium, at least in ferrofluid D.

The ferrofluids without any aggregates according to cryo-TEM, ferrofluids B and C, have much higher rotational diffusion rates. From the rotational diffusion rate of the C particles, the hydrodynamic radius of the particles could be calculated. In ferrofluid B, the magnetic moment rotated inside the particles, so that no information could be obtained about rotational diffusion of the particles. The threshold size above which Brownian rotation is faster than Néel rotation suggests that Néel rotation is relatively slow in our particles, probably due to surface anisotropy.

The presence and size of aggregates is very sensitive to particle size. The parallels between the cryo-TEM and the dynamic susceptibility measurements indicate that when aggregates occur in the two-dimensional geometry of cryo-TEM, they also occur in the three-dimensional geometry of the susceptibility measurements. The apparent explanation is that the interaction energy required for aggregation is practically the same in two and in three dimensions. The combination of cryo-TEM with dynamic magnetic susceptibility measurements appears to be a powerful approach to study aggregation in model (monodisperse) magnetic fluids. Cryo-TEM gives direct images of aggregates, although only in two dimensions and without a good control of the concentration. Frequency-resolved magnetic susceptibility measurements are at least in qualitative agreement with cryo-TEM, and they make it possible to study three-dimensional aggregation as a function of concentration.

Acknowledgements

Ben Erné is greatly thanked for his help with the susceptibility measurements and their analysis. We thank Mircea Raşa for helpful discussions, Thido Arts for writing software and for performing preliminary measurements, and Bonny Kuipers and Cees Rietveld for helping to construct the experimental setup.

References

[1] Rosensweig R E 1982 *Scientific American* **247** 124.

[2] Rosensweig R E 1985 *Ferrohydrodynamics* (Cambridge: Cambridge University Press).

[3] Charles S W 1992 in *Studies of magnetic properties of fine particles and their relevance to materials science*; Dormann J L and Fiorani D, Ed.; Amsterdam: North-Holland; pp 267.

[4] Berkovski B and Bashtovoy V 1996 *Magnetic fluids and applications handbook* (New York: Begel House Inc.).

[5] Raj K and Moskowitz R 1990 *J. Magn. Magn. Mater.* **85** 233.

[6] Cabuil V 2000 *Current Opinion in Colloid & Interface Science* **5** 44.

[7] Teixeira P I C, Tavares J M and Telo da Gama M M 2000 *J. Phys.: Condens. Matter* **12** R411.

[8] Charles S W 1988 *Chem. Eng. Comm.* **67** 145.

[9] Butter K, Bomans P H, Frederik P M, Vroege G J and Philipse A P 2003 *Nature Materials* **2** 88.

[10] Butter K, Philipse A P and Vroege G J 2002 *J. Magn. Magn. Mater.* **252** 1.

[11] Butter K, Bomans P H, Frederik P M, Vroege G J and Philipse A P 2003 *J. Phys.: Condens. Matter* **15** S1451.

[12] Fannin P C 1998 *Adv. Chem. Phys.* **104** 181.

[13] de Gennes P G and Pincus P A 1970 *Phys. Kondens. Materie* **11** 189.

[14] Weis J J 1998 *Mol. Phys.* **93** 361.

[15] Tavares J M, Weis J J and Telo da Gama M M 1999 *Phys. Rev. E.* **59** 4388.

[16] Chantrell R W, Bradbury A, Popplewell J and Charles S W 1982 *J. Appl. Phys.* **53** 2742.

[17] Gang X, Liou S H, Levy A, Taylor S N and Chien C L 1986 *Phys. Rev. B* **34** 7573.

[18] Pathmamanoharan C, Zuiverloon N L and Philipse A P 2000 *Progr. Colloid Polym. Sci.* **115** 141.

[19] Goossens A, de Jongh L J, Butter K, Philipse A P, Crajé M W J and van der Kraan A M 2002 *Hyperfine Interactions* **141/142** 381.

[20] Bauer-Grosse Eand Le Caër G 1987 *Philosophical Magazine B* **56** 485.

[21] Weast R C 1987 *CRC Handbook of Chemistry and Physics* (Boca Raton: CRC Press).

[22] Jiles D 1995 *Introduction to Magnetism and Magnetic Materials* (London: Chapman & Hall).

[23] Tirado M M and Garcia de la Torre J 1979 *J. Chem. Phys.* **71** 2581.

[24] Tirado M M and Garcia de la Torre J 1980 *J. Chem. Phys.* **73** 1986.

[25] Garcia de la Torre J, López Martinez M C and Tirado M M 1984 *Biopolymers* **23** 611.

Appendix

Coating of iron particles to prevent their oxidation

1. Introduction

In our dispersions of magnetic iron particles, the colloids rapidly oxidise to a non-magnetic oxide on exposure to air (measurable on a timescale of minutes) due to their large surface-to-volume ratio. This property is very impractical for applications and fundamental studies on the dispersions, since the particles should always stay under nitrogen atmosphere to maintain their magnetic properties. We attempted to coat our particles with various layers, to prevent their oxidation. First, we tried to coat iron particles by a silica layer, using a method for the synthesis of a micro-emulsion of small silica particles [1] in cyclohexane in the presence of iron particles, which would probably act as nuclei for the silica formation. In addition, attempts were made to coat iron particles with a metallic layer, by reduction of salts of gold and silver, following an experiment performed by Paulus et al [2,3]. Another method we explored was the coating with chrome by thermal decomposition of chrome carbonyl (similar to thermal decomposition of iron carbonyl, the synthesis method of our particles) in the presence of iron particles. Finally, attempts were made to synthesize iron particles coated with octadecylmercaptane (ODM), since on ultrasonification of a dispersion of PIB-coated iron particles to which a small amount of ODM was added, the oxidation velocity was earlier found to decrease significantly [4], probably due to changes on the particle surface. Unfortunately, none of the above described experiments resulted in a significant, reproducible decrease of oxidation of our iron particles. This appendix documents the various experiments, which may also be useful for future studies.

2. Experimental

For sample codes of iron dispersions used for coating is referred to chapter 3. All coating reactions were performed in a glovebox under nitrogen atmosphere, to prevent the particles from oxidation. Particles were characterized by Transmission Electron Microscopy (Philips CM10H TEM) of Formvar-coated grids, that were dipped into dilute dispersions and left to dry. The oxidation behaviour was studied by means of susceptibility measurements (using a Kappabridge KLY-3 susceptibility meter, Agico) in time during exposure of the dispersions to air, always using a reference sample of the same concentration of (uncoated) iron particles in the same solvent.

2.1. Coating of iron particles with silica

We followed the method of Osseo-Asare and Arriagada [1] for the synthesis of a micro-emulsion of silica particles in cyclohexane, using the same amounts, but the surfactant Igepal (polyoxyethylene nonylphenyl ether) was dissolved (0.2 M) in an iron dispersion in decalin (C) diluted with cyclohexane instead of in pure cyclohexane. After addition of 30 µl of TES, another 0.5 ml was added the next day. TEM-micrographs showed that the iron

particles were indeed encapsulated in a (presumably) silica layer, but the shape of these composite particles was not so well-defined (figure 1). Susceptibility measurements did not show a significant difference in oxidation behaviour compared to uncoated particles. Presumably, silica is porous enough for oxygen to diffuse through the shell.

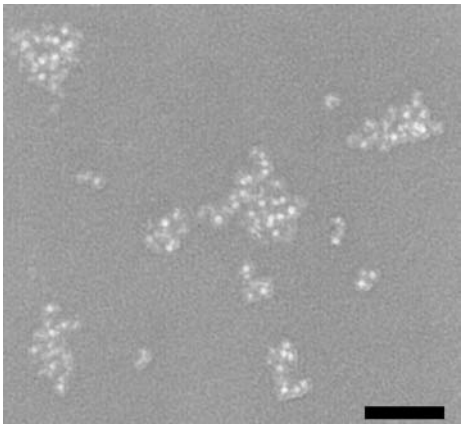

Figure 1. TEM-micrograph of iron particles (cores with larger intensity) encapsulated in silica shells. The scale bar corresponds to 100 nm.

2.2 Coating of iron particles with gold or silver

Earlier experiments of Paulus [2,3] made use of the reduction of $AuCl_3$ by iron particles in toluene, to allegedly obtain a layer of gold around the iron particles. However, we were unable to reproduce these results. In our experiments, $HAuCl_4$ (0.125 g) was added to an iron dispersion in decalin (0.5 ml FeE), or a dispersion (0.5 ml FeC) diluted 10 times with toluene. In addition, we tried to use DMF as a reducing agent adding $HAuCl_4$ to an iron dispersion diluted with toluene and DMF. All dispersions showed an immediate change of colour from black to brownish upon addition of the gold salt. Instead of the formation of a metallic layer on the iron particles, all experiments described above resulted in the formation of large particles (~30-100 nm radius), presumably consisting of gold, which were found in between the iron particles on TEM micrographs and were partly aggregated. Also following the method of Paulus, adding $AuCl_3$ instead of $HauCl_4$ to a dispersion of iron diluted with toluene resulted in the formation of separate gold particles. To check the possibility of the presence of a small oxygen-excluding gold layer, invisible on TEM micrographs, the oxidation behaviour was studied by susceptibility measurements in time, but these showed no significant difference between particles treated with gold salts and non-coated particles. An experiment adding $AgNO_3$ instead of a gold salt to a dilute iron dispersion in decalin was not studied by TEM, but did also not result in any change in the oxidation behaviour of particles.

2.3. Coating of iron particles with chrome

$Cr(CO)_6$ (s) (0.82 g, in principle enough to form a layer of about 1 nm on the colloids) was added to a dispersion of iron particles (10 ml FeB diluted 6 times) in decalin, which was refluxed for 24 hours at 180 °C under nitrogen atmosphere to thermally decompose the carbonyl compound to chrome. TEM micrographs did not show a significant difference with the uncoated sample. However, the oxidation was found to be much slower than before the treatment with $Cr(CO)_6$ (see figure 2). It was not clear if indeed a metallic chrome layer formed on the particle surfaces caused the decrease of oxidation. Although the susceptibility experiments could be reproduced for this particular sample, we were not able to reproduce the result for other similarly coated samples.

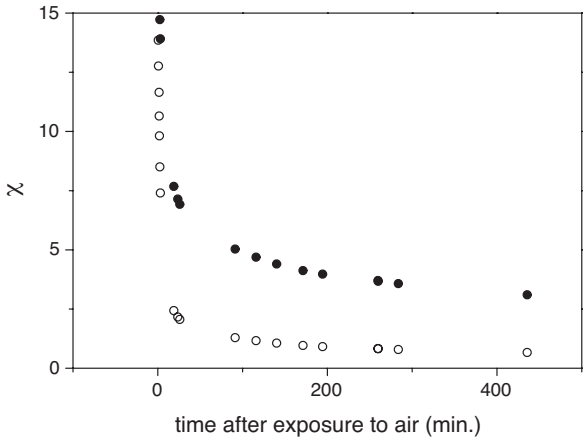

Figure 2. Decrease of susceptibility in time after exposure of dispersion FeB treated with $Cr(CO)_6$ (●) compared to non-treated FeB (○).

2.4. Coating of iron with octadecylmercaptane (ODT)

We attempted to synthesize iron particles using ODT as a surfactant instead of PIB. The same method and (relative) amounts were used as for the synthesis of dispersion C (see chapter 3, 60 ml decalin, 10 ml $Fe(CO)_5$, 0.13 g (0.45 mmol) ODT). Since in this case large aggregates of iron particles were formed, that sedimented to the bottom, leaving a clear supernatant, an additional sample was prepared using a much larger amount of ODT (0.39 g, 1.4 mmol). However, a similar result of aggregated iron particles was obtained. Finally, we tried to exchange PIB for ODT by adding 0.5 ml or 3 ml of a solution of ODT in decalin (8.3×10^{-4} M) to 3 ml of dispersion C at room temperature and ultrasonicating for 60 minutes. It was unclear whether the exchange had taken place, but in any case no effect was found on the oxidation behaviour of these particles.

References

[1] Osseo-Asare K and Arriagada F J 1990 *Colloids and Surfaces* **50** 321.

[2] Paulus P M 2000 *Nanometer-sized Metal Particles studied by Mössbauer Effect Spectroscopy and Magnetic Probes*, thesis Leiden University.

[3] Paulus P M, Bönneman H, A.M. K v d, Luis F, Sinzig J and Jongh de L J 1999 *Eur. Phys. J. D* **9** 501.

[4] Ewijk van G A *personal communication*.

Summary

This thesis describes a study on two connecting research subjects concerning ferrofluids, i.e. the synthesis and use of catalytic magnetic colloids and the microstructural behaviour of ferrofluids in general. An interesting application of ferrofluids (dispersions of magnetic colloids) would be their use in catalysis; catalysts attached to the surface of small magnetic particles could in principle be separated magnetically for recycling after their application as catalyst, combining the advantages of homogeneous catalysis (high efficiency due to the relatively large available surface) and heterogeneous catalysis (easy recycling). A feasibility study of this principle is described in **chapter 2**. Various kinds of magnetic colloids were synthesized and coated with catalytic Pd-complexes, which were shown to be active in aldol condensation reactions. Grafting of the particles is indeed found to be possible, although resulting in instable dispersions. Further study is required to obtain stable catalytic colloids, which will improve their catalysis efficiency. High Gradient Magnetic Separation (HGMS) is a well-known magnetic separation technique, mostly used for separation of large, micron-sized magnetic particles, e.g. from waste water. We were able to separate much smaller single magnetic colloidal particles by HGMS, when their dipole moments were sufficiently large.

Out of fundamental interest, but also for a better understanding of applications of ferrofluids (e.g. as described above), the structural behaviour of ferrofluids in general was

studied and is presented in **chapters 3-7** of this thesis. Since the 1970s and until today a lot of theoretical work and simulations on the physical behaviour and interparticle structure of dipolar fluids has been performed, showing interesting but often contradictory results on which a full consensus still has not been reached. Numerous experimental studies on ferrofluids as model system for dipolar fluids have been performed, mostly on magnetite dispersions containing relatively weakly magnetic particles with limited size control and large polydispersity. In this thesis we describe a systematic and extensive study on the physical and structural properties of ferrofluids, in which dipolar and isotropic interparticle forces are varied. For this research we used iron dispersions in an organic solvent, synthesized by thermal decomposition of ironpentacarbonyl. Iron dispersions appeared to be a very suitable model system for dipolar fluids, since they are relatively monodisperse and their particle size and surfactant layer can be varied in a broad range, resulting in controllable dipolar and Van der Waals interactions between particles. In addition, iron has a large saturation magnetization resulting in relatively large dipole moments of the colloids. The preparation and characterization of iron dispersions with different average particle sizes is described in **chapter 3**. Particles were coated with two different surfactant layers (i.e. oleic acid, 1-2 nm thickness, or modified polyisobutene, 5-7 nm thickness). The synthesis resulted in black stable dispersions of mono-domain magnetic colloids with low polydispersity (7-18 %), consisting of an amorphous $Fe_{0.75}C_{0.25}$ alloy. Particle radii could be controlled in the 2-10 nm range by varying the amount of reactants. Extensive characterization with various techniques gave particle sizes that agree well with each other. Oleic-acid-coated particles were found to be more spherical and less polydisperse than PIB-coated particles, but the latter ones could be prepared in a broader size range. SANS and SAXS measurements on one specific dilute dispersion of oleic-acid-coated particles (described in **chapter 4**) were used to study the composition of single particles and revealed that our particles are mono-domain dipolar spherical particles, with a lognormal size distribution of the iron cores, surrounded by a surfactant shell, which is partially penetrated by solvent. Upon oxidation, an oxide layer forms on the particle surface, consisting of a disordered non-magnetic ironoxide, but a magnetic core remains present, even after one year.

The structural behaviour of ferrofluids was investigated using Small Angle Scattering techniques, Cryogenic Electron Microscopy and Dynamic Susceptibility measurements, giving a rather complete picture of the physical behaviour of ferrofluids. Our ferrofluids are stable and do not phase separate, as found from susceptibility measurements. The interparticle structure strongly depends on the particle size (related to the dipole moment). SAXS measurements on oleic-acid-coated colloids (**chapter 5**) indicated that concentrated dispersions of small particles consist of single non-interacting dipolar hard spheres, while dispersions of only slightly larger particles contain a significant contribution of dipolar attractions. Cryogenic electron microscopy (cryo-TEM) was used to study vitrified liquid films of dispersions, giving *in-situ* information about the interparticle structures. Cryo-TEM

on dispersions of PIB-coated particles (**chapter 6**), where Van der Waals attractions are screened by the thick surfactant layer, demonstrated an abrupt transition with increasing particle size (corresponding to increasing dipolar attraction) from separate particles to linear chains or large networks. These chains, already predicted theoretically by de Gennes and Pincus in 1970, very much resemble the fluctuating chains found in simulations of dipolar fluids. Although the cryo-TEM technique studies ferrofluids in 2 dimensions, the behaviour described above was confirmed by dynamic susceptibility measurements on the bulk dispersions (**chapter 7**); while for small particles the orientation of the magnetic moment changed by thermal rotation inside the particles (Néel rotation) or for slightly larger particles by rotational diffusion of the single particles themselves (Brownian rotation), an enormous increase of relaxation times was found upon increasing the particle radii, demonstrating the presence of large clusters. The rotational diffusion rate of these aggregates was found to increase upon dilution, suggesting that the aggregate size resulted from a dynamic equilibrium. The dipolar nature of the aggregation in zero field was confirmed by alignment of existing chains in the field direction upon vitrification of dispersions in a magnetic field (using cryo-TEM, **chapter 6**). For sufficiently large dipoles, also single magnetic particles were found to align in a magnetic field (SAXS-measurements (**chapter 5**) and cryo-TEM (**chapter 6**)) and in some cases showed a tendency to field-induced chain formation (SAXS, **chapter 5**). Our research, combining the results of various complementary techniques, reveal a rich structural behaviour of ferrofluids, depending on the exact dipolar and isotropic interparticle interactions present. Iron ferrofluids, where control of these properties is possible by varying their particle size and surfactant layers, are found to be very suitable model systems to study dipolar fluids.

Samenvatting

Samenvatting voor niet-vakgenoten

Inleiding

Het specialistische onderzoek dat is beschreven in dit proefschrift zal niet voor iedereen begrijpelijk zijn, zeker niet zonder achtergrond in de scheikunde of natuurkunde. Deze samenvatting is bedoeld voor iedereen, en hierin probeer ik uit te leggen waar ik me de afgelopen jaren eigenlijk mee heb beziggehouden.

De titel van dit proefschrift luidt: **Iron(oxide) ferrofluids; synthesis, structure and catalysis** (of in het Nederlands: **IJzer(oxide**) '**ferrofluids', synthese, structuur en katalyse**). Wat zijn **ferrofluids**? Om dit te begrijpen zal ik allereerst ingaan op de begrippen colloïden en dispersies. Colloïden zijn zeer kleine deeltjes (b.v. van metaal, silica (zand) of aluminiumoxide) met een grootte tussen ruwweg 1 nm (een miljoenste millimeter) en 1 µm (een duizendste millimeter). Een suspensie van colloïden in een vloeistof noemen we een dispersie. Dispersies zijn zeer alledaags, je kunt daarbij denken aan verf (pigmentdeeltjes in een organisch oplosmiddel, of tegenwoordig gelukkig ook vaak in water), melk (vetbolletjes in water), of bloed (cellen in plasma). Het 'dispergeren' van colloïden in een oplosmiddel lukt vaak niet zomaar. De colloïdale deeltjes trekken elkaar namelijk aan (door de zogenaamde Van der Waals-attractie), zoals eigenlijk alle atomen en moleculen dat doen. Wanneer je de colloïden zonder meer in een vloeistof brengt zullen ze steeds grotere klonten vormen die onder invloed van de zwaartekracht naar de bodem zakken. Een voorbeeld van het samenklonteren (aggregeren) van colloïden is zure melk, waarbij alle vetbolletjes op de bodem van het glas belanden (figuur 1).

Figuur 1. Voorbeeld van een stabiele dispersie (verse melk, vetbolletjes in water) en een instabiele dispersie (bedorven melk), waarin een doorzichtige vloeistof te zien is boven de samengeklonterde vetbolletjes onderin het glas.

Er zijn dus voorzorgsmaatregelen nodig om dit klonteren tegen te gaan. Vaak gebeurt dit door het maken van geladen colloïden, die elkaar afstoten en daardoor gedispergeerd blijven in het oplosmiddel. Een andere methode is het aanbrengen van lange 'haren' (surfactants) op het deeltjesoppervlak (figuur 2). Deze surfactants zitten aan één zijde vast aan het deeltjesoppervlak, maar de andere kant is graag in contact met het oplosmiddel. Omdat de surfactants niet in elkaar kunnen doordringen, gaan ze het klonteren van de deeltjes tegen en zorgen ze voor een stabiele dispersie.

Natuurlijk werkt er ook op losse deeltjes een zwaartekracht die ze naar beneden zal trekken. Echter, deze worden steeds weer 'opgeschud' doordat oplosmiddelmoleculen (die veel kleiner zijn dan de deeltjes) van alle kanten tegen ze aan botsen. Omdat de

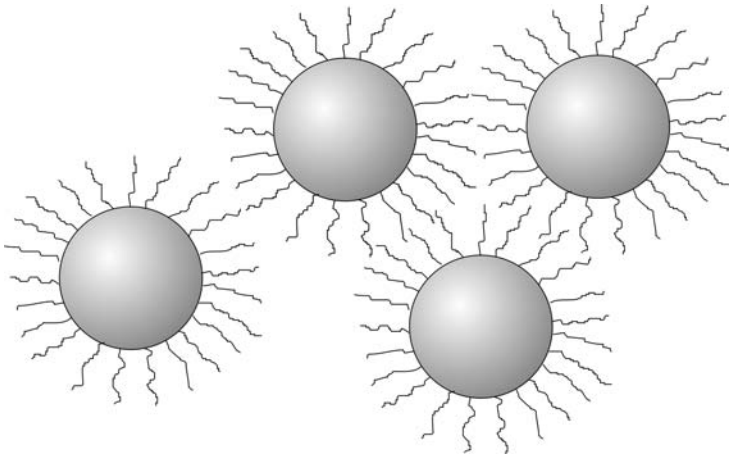

Figuur 2. Op het oppervlak van colloïden zijn vaak lange haren (surfactants) aangebracht. Omdat deze haren niet in elkaar kunnen doordringen, wordt het klonteren van de deeltjes tegengegaan. De minimale afstand tussen deeltjes wordt bepaald door de dikte van de surfactantlagen.

oplosmiddelmoleculen op willekeurige plaatsen tegen de deeltjes aanbotsen, is de beweging van de colloïden heel grillig. De deeltjes maken hierbij zowel translatie- als rotatiebewegingen. Dit effect werd voor het eerst waargenomen in 1827 door Robert Brown in suspensies van stuifmeelkorrels in water en wordt daarom Brownse beweging genoemd. Vanwege hun eigenschappen worden colloïdale dispersies vaak gezien als modelsysteem voor moleculaire systemen; net als colloïden in een oplosmiddel zijn moleculen ook continu thermisch in beweging en ondervinden ook zij Van der Waals attracties.

Ferrofluids zijn dispersies die magnetische colloïden bevatten. Deze deeltjes zijn te vergelijken met piepkleine magneetjes met elk afzonderlijk een noordpool (N) en zuidpool (Z) (en heten daarom dipolen). De deeltjes in ferrofluids zijn ongeveer 1-20 nm groot. Meestal zijn de deeltjes van ijzer of ijzeroxide, vandaar de naam ferrofluids. Een ferrofluid is een zwarte vloeistof omdat alle licht dat erop valt geabsorbeerd wordt door de colloïden. Behalve de Van der Waals-attracties en afstotende (repulsieve) krachten, bestaat er tussen deze deeltjes ook een magnetische (dipolaire) wisselwerking, waardoor deeltjes elkaar kunnen aantrekken of afstoten (afhankelijk van de oriëntatie). Als de deeltjes kop-staart liggen (NZ-NZ) trekken ze elkaar het sterkste aan, andersom stoten ze elkaar het meeste af. Door de Brownse beweging zijn de deeltjes in een ferrofluid willekeurig georiënteerd (de dipolen hebben alle een verschillende richting). Echter, in een magneetveld zullen ze gaan draaien in de richting van het aangelegde veld. De mate waarin de deeltjes uitgericht zijn, hangt af van de sterkte van het veld; als het veld sterk genoeg is, zullen uiteindelijk alle dipolen dezelfde kant op staan. De deeltjes trekken elkaar dan ook harder aan omdat ze kop-staart liggen. Als het veld wordt uitgeschakeld, zullen de deeltjes door de thermische beweging weer terugdraaien en wordt weer een willekeurige oriëntatie verkregen. Behalve dat de dipolaire krachten tussen deeltjes richtingafhankelijk zijn en de Van der Waals attractie niet, is het ook zo dat de dipolaire wisselwerking op langere onderlinge afstand 'voelbaar' is; we zeggen dat dipolaire interacties een 'langere dracht' hebben dan Van der Waals interacties.

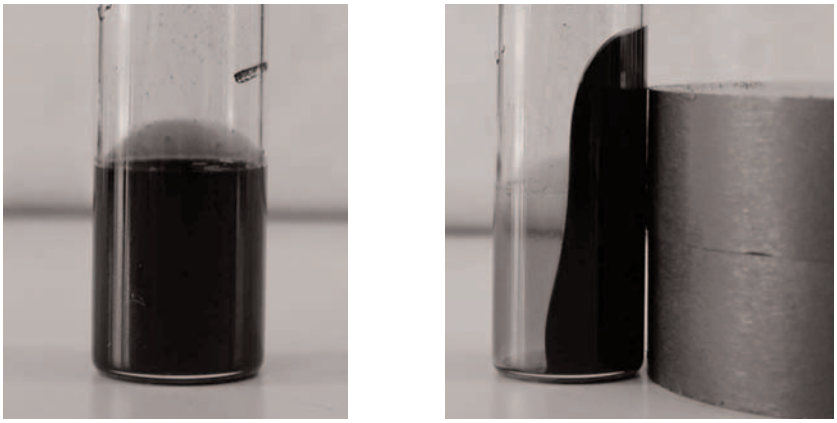

Figuur 3. Voorbeeld van een ferrofluid zonder magneetveld (links) en in een magneetveld (rechts).

Een grappige eigenschap van ferrofluids is dat ze worden aangetrokken door een magneet (dit is al te zien met een kleine handmagneet), maar toch hun vloeibare karakter behouden (zie figuur 3). Veel toepassingen van ferrofluids zijn gebaseerd op deze eigenschap. Zo worden ze o.a. gebruikt in luidsprekers, die bestaan uit een cylindrische spoel in een cylindrische permanente magneet met een kleine ruimte ertussen waarin de spoel kan bewegen. De warmte die hierbij ontwikkeld wordt kan gemakkelijker afgevoerd worden als in de tussenruimte een koelvloeistof zit. Een normale vloeistof zou eruit lopen, maar een ferrofluid wordt vastgehouden door het toch al aanwezige magneetveld. Ferrofluids worden ook gebruikt als magnetische inkt, b.v. in printers waarbij de deeltjes door magneetvelden op de goede plek op het papier worden aangebracht of voor het 'magnetisch' lezen van getallen en cijfers (b.v. op cheques).

Dit proefschrift

Het onderzoek dat is beschreven in dit proefschrift (**IJzeroxide 'ferrofluids': synthese, structuur en katalyse**) is tweeledig. Ten eerste heb ik mij beziggehouden met een specifieke potentiële toepassing van ferrofluids, namelijk het gebruik als katalysator (**katalyse**). Het tweede deel van het proefschrift gaat over de microscopische structuur van een ferrofluid (**synthese en structuur**).

Katalyse

Een katalysator is een stof die een (chemische) reactie versnelt, zonder daarbij verbruikt te worden; na de reactie kan de katalysator opnieuw gebruikt worden. In de industrie wordt veel gebruik gemaakt van katalysatoren, omdat zo veel tijd en energie bespaard wordt bij het maken van chemische verbindingen. Een lastig punt is het terugwinnen van de gebruikte katalysator (die na gebruik nog steeds in het reactiemengsel zit, maar voor hergebruik gescheiden moet worden van het product).

In mijn onderzoek heb ik dispersies van magnetische ijzeroxidedeeltjes met een straal van ongeveer 10 nm gemaakt, en geprobeerd katalysatoren aan te brengen op het deeltjesoppervlak. Het idee achter deze 'magnetische katalytische deeltjes' is dat ze als katalysator op zouden kunnen treden in een chemische reactie en daarna relatief eenvoudig gescheiden zouden kunnen worden met een magneet. Voor een zo hoog mogelijk rendement van de katalysator moeten de magnetische deeltjes zo klein mogelijk zijn, omdat dan het totale beschikbare oppervlak om katalysatoren aan te hechten groot is. Echter, de magnetische scheiding wordt steeds moeilijker voor kleinere deeltjes, omdat daarvoor steeds hogere magneetvelden nodig zijn. **Hoofdstuk 2** beschrijft deze studie van katalytische magnetische deeltjes en hun scheiding. Het is inderdaad gelukt om magnetische colloïden te voorzien van een laagje van katalysatoren. Een ongewenst neveneffect was wel dat de colloïden daardoor samenklonterden en uitzakten, waardoor er oppervlak verloren ging. Om te testen of het in principe mogelijk was om afzonderlijke deeltjes af te scheiden uit een reactiemengsel heb ik experimenten gedaan met de zogenaamde 'High Gradient

Magnetic Separation'-techniek. Dit is een techniek die vaak gebruikt wordt om veel grotere magnetische deeltjes van een vloeistof te scheiden en maakt gebruik van een kolom vol gemagnetiseerde draden, waar magnetische deeltjes aan vast blijven plakken bij langsstromen van de vloeistof. Als het magneetveld wordt uitgezet, komen de deeltjes weer los. Uit het onderzoek bleek dat het ook mogelijk is om veel kleinere deeltjes, zoals in de ferrofluids, te scheiden met deze techniek. Echter, voor de allerkleinste deeltjes (kleiner dan 3 nm) was de aantrekkingskracht van de draden niet groot genoeg en vond geen scheiding plaats.

Synthese en Structuur

Een interessante vraag is hoe zo'n ferrofluid er nu op microscopisch niveau uitziet. Dat kan b.v. belangrijk zijn om toepassingen te begrijpen en te ontwikkelen, maar ook om algemene kennis te vergaren over het gedrag van dipolen. Ferrofluids worden vaak gezien als een modelsysteem voor dipolaire moleculen (bv. water, waarvan alle moleculen kleine dipolen zijn), maar colloïden zijn veel groter en daardoor makkelijker te bestuderen. De overige inhoud van het proefschrift (**hoofdstuk 3 t/m 7**) gaat over een studie naar de microscopische eigenschappen van ferrofluids (**synthese en structuur**). Hoe zien de deeltjes er precies uit? Wat is de invloed van de magnetische wisselwerking? Blijven de deeltjes los of vormen ze ketentjes danwel ringetjes van deeltjes? Wat is de invloed van de deeltjesgrootte? Wat gebeurt er in een magnetisch veld? Dit zijn vragen waar al veel onderzoek naar gedaan is, maar waarop het antwoord nog steeds niet geheel duidelijk is. In 1970 voorspelden de wetenschappers De Gennes en Pincus al de aanwezigheid van ketentjes van deeltjes in ferrofluids zonder aangelegd veld, maar experimenten konden niet echt uitsluitsel geven. De magnetische krachten tussen deeltjes nemen toe met hun grootte (evenredig met het volume) en hangen ook af van de afstand tussen deeltjes (hoe dichter bij elkaar, hoe groter de aantrekkingskracht). Het zou daarom interessant zijn om dispersies met verschillende deeltjesgrootten te bekijken. De minimale afstand waarop deeltjes elkaar kunnen naderen wordt bepaald door de dikte van de surfactantlagen die niet in elkaar door kunnen dringen (fig 2).

Voor dit onderzoek heb ik een serie van dispersies gemaakt van metallische ijzerdeeltjes van verschillende grootte. Deze kunnen worden gemaakt door een vloeibare verbinding (ijzercarbonyl) te verhitten (170 ºC). De verbinding ontleedt dan in ijzer en koolmonoxide. Wanneer meteen een surfactant 'meeverwarmd' wordt, ontstaan stabiele ijzerdispersies doordat de surfactant de nieuw gevormde ijzerdeeltjes omhult, en zo verhindert dat ze aan elkaar plakken. Het voordeel van ijzerdeeltjes is dat ze sterker magnetisch zijn dan deeltjes van ijzeroxide en dat ze gemaakt kunnen worden in verschillende grootten. Bovendien zijn de deeltjes binnen één dispersie niet zo heel verschillend van grootte (lage polydispersiteit), iets wat voor ijzeroxidedeeltjes wel het geval is. Met monodisperse deeltjes kan de invloed van de grootte beter bestudeerd worden. De deeltjes waren in mijn geval gedispergeerd in een organisch oplosmiddel (decaline) en gestabiliseerd met een surfactantlaag (oliezuur of

gemodificeerd polyisobuteen). Een nadeel van ijzer is wel dat de deeltjes oxideren (roesten) in lucht en daarna niet langer magnetisch zijn. Daarom zijn de synthese en alle experimenten in 100 % stikstof uitgevoerd (80 % van lucht bestaat uit stikstof). De synthese van deze ijzerdispersies staat beschreven in **hoofdstuk 3**. De grootte van de deeltjes werd onder meer bepaald met een elektronenmicroscoop en door magnetische metingen. De kleinste deeltjes hadden een straal van ongeveer 2 nm, de grootste van 8 nm.

In hoofdstuk **4 en 5** zijn verstrooiingsmetingen aan een ijzerdispersie beschreven. Bij lichtverstrooiing wordt een lichtbundel door een buisje met dispersie gestuurd en aan de achterkant weer opgevangen op een detector. In het monster wordt het licht door de deeltjes afgebogen (verstrooid). Uit de precieze afbuiging van het licht kan nu informatie verkregen worden over de grootte, samenstelling en onderlinge ordening van de deeltjes. In mijn geval gebruikte ik geen zichtbaar licht, maar röntgenstraling en neutronen (een neutron is één van de bouwstenen van een atoom), omdat gewoon licht geabsorbeerd wordt door de zwarte vloeistof. Er bleek dat onze deeltjes inderdaad bestaan uit een magnetische kern omringd door een minder compacte surfactantlaag. Terwijl kleine deeltjes elkaar nauwelijks beïnvloedden, bleek dat iets grotere deeltjes elkaar duidelijk aantrokken. In dit laatste geval was niet helemaal duidelijk of deze aantrekking het gevolg was van dipolaire wisselwerkingen of Van der Waals-attracties.

Door een dikkere surfactantlaag op de colloïden aan te brengen, waardoor de minimale afstand tussen de deeltjes groter werd, kon het effect van de Van der Waals attractie (met korte dracht) grotendeels uitgeschakeld worden. Deze deeltjes werden bekeken met een speciaal soort microscoop, waarbij in plaats van licht elektronen worden gebruikt (elektronenmicroscoop). Normaal gesproken worden ingedroogde monsters bekeken. Echter, dit geeft alleen informatie over de deeltjes zelf en niet over de structurering ervan in de vloeistof. Om nu de deeltjes in hun 'natuurlijke' omgeving (dus in het oplosmiddel) te bekijken, heb ik een speciaal soort elektronenmicroscopie toegepast, te weten cryo-elektronenmicroscopie (cryo-TEM). Hierbij wordt een dun laagje ferrofluid zeer snel ingevroren. Dit invriezen gaat zo snel dat de dipooltjes als het ware geen tijd meer hebben om te bewegen. Daarna wordt dit ingevroren plakje ferrofluid microscopisch gefotografeerd. Zo kon ik de ijzerdeeltjes in de ferrofluid bekijken zoals ze zich in de vloeistof gedragen. Dit wordt beschreven in **hoofdstuk 6**.

Er bleek dat kleine deeltjes allemaal apart van elkaar liggen, terwijl grotere deeltjes inderdaad kleine ketentjes van deeltjes vormen (figuur 4). In de figuur is te zien dat de ketentjes allemaal willekeurig georiënteerd zijn (er is immers geen magneetveld aanwezig). Dat de deeltjes ketentjes vormen en geen *ronde* clusters (groepen van deeltjes), komt doordat de vorming van de clusters veroorzaakt wordt door de dipolaire wisselwerking (deeltjes gaan kop-staart liggen) en niet door de Van der Waals-attractie (waarbij andere deeltjes in alle richtingen even hard zouden worden aangetrokken). Nog grotere deeltjes vormen uitgebreide netwerken van deeltjes (figuur 4). We moeten wel bedenken dat de foto's momentopnames zijn van de ferrofluids. De ketentjes die we zien zijn 'dynamisch',

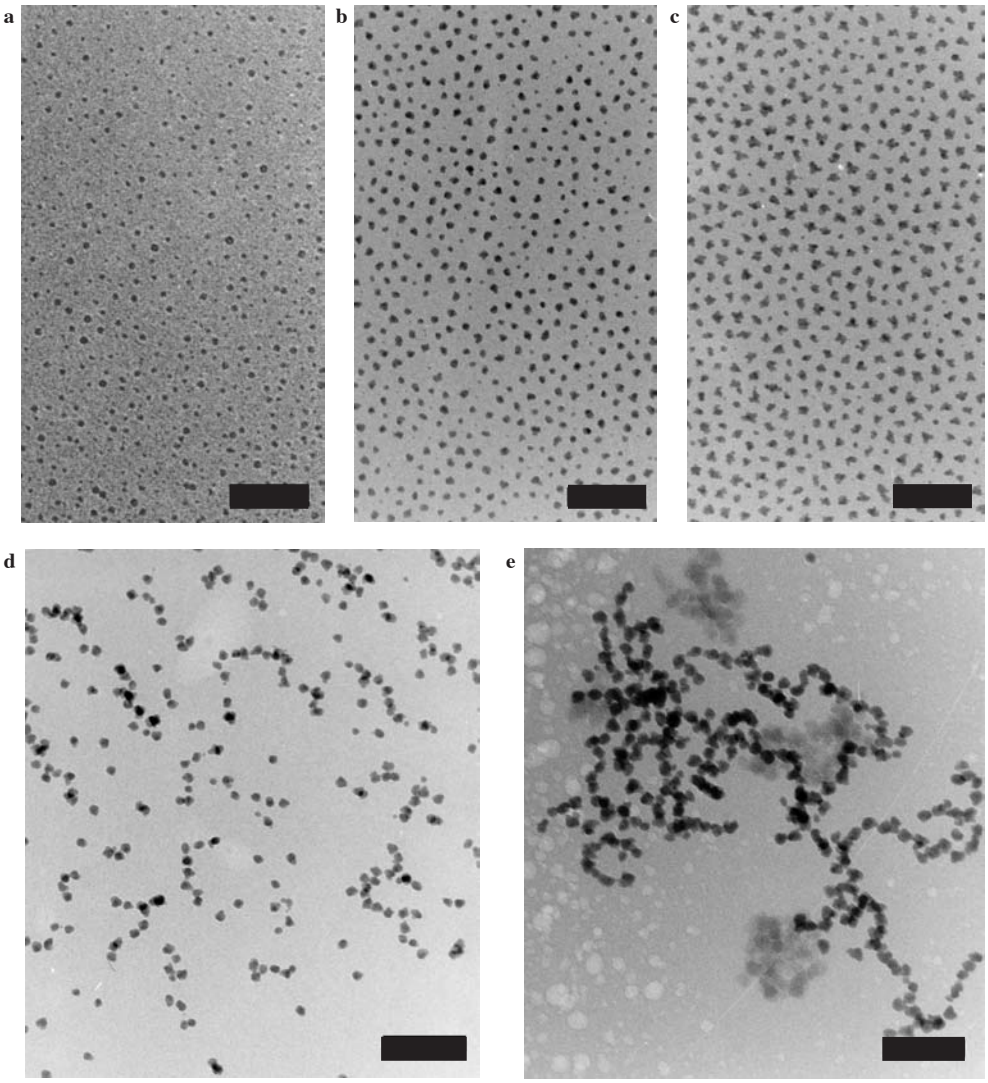

Figuur 4. Voorbeeld van cryo-TEM foto's van ijzerdispersies. De gemiddelde deeltjesgrootte loopt op van figuur **a** naar figuur **e** (van 2-8 nm straal). Terwijl kleine deeltjes allemaal los liggen (figuur **a-c**), vormen grotere deeltjes ketentjes (figuur **d**) of netwerken (figuur **e**).

dat wil zeggen dat ze zich steeds herorganiseren (deeltjes laten los van een keten, anderen haken aan). Daardoor blijft de dispersie toch stabiel (de ketentjes zakken niet naar de bodem).

Het bleek ook mogelijk te zijn de ferrofluids in te vriezen in een magneetveld. Zoals te zien in figuur 5, levert dit een geheel ander beeld op. De kleine, willekeurig georiënteerde

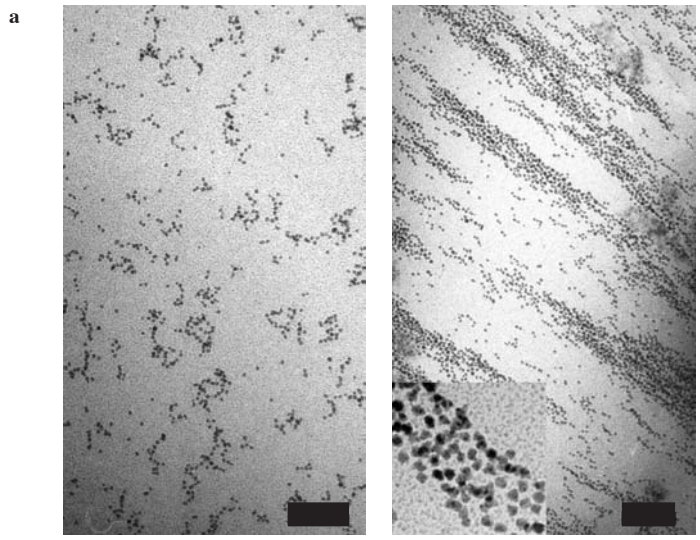

Figuur 5. Voorbeeld van een ijzerdispersie (als in figuur 4d) **a**, zonder veld, **b**, ingevroren in een magneetveld.

ketentjes die al aanwezig zijn zonder magneetveld (figuur 5a) worden in een veld alle uitgericht in de veldrichting (figuur 5b). Ook blijken ze veel grotere clusters te vormen dan zonder veld. De reden hiervoor is dat flexibele parallelle ketens van magnetische deeltjes elkaar ook aantrekken in de richting loodrecht op de ketens.

Zoals boven beschreven, bestudeert de cryo-TEM techniek een dun laagje (twee dimensies) van een ferrofluid en dit zou zeker invloed kunnen hebben op het gedrag van de deeltjes. Daarom is ter vergelijking een andere techniek gebruikt: dynamische susceptibiliteitsmetingen, beschreven in hoofdstuk 7. Hierbij wordt een zeer klein magneetveld aangelegd op een buisje met dispersie (zo klein dat het geen invloed zal hebben op de ordening van de colloïden) waardoor de deeltjes zich een beetje draaien in de richting van het veld. Nu wordt gemeten hoelang de deeltjes erover doen terug te draaien (relaxeren) na uitschakeling van het veld. Er bleek dat in de dispersies met kleine deeltjes deze relaxatietijd heel kort is, terwijl die zeer veel langer is voor iets grotere deeltjes. Dit kan verklaard worden door de vorming van ketentjes en netwerken in de betreffende dispersies. Grotere structuren zullen namelijk veel trager ronddraaien dan kleine enkele deeltjes. Uit beide technieken bleek dus dat deeltjes vanaf een bepaalde grootte ketentjes vormen. Verrassend genoeg is deze grens in een dunne film (cryo-TEM, twee dimensies) ongeveer hetzelfde als in de gehele ferrofluid (susceptibiliteitsmetingen, drie dimensies).

De toegepaste combinatie van technieken en de gebruikte ijzerdispersies blijkt heel succesvol in het bestuderen van ferrofluids. Dit maakt het ons mogelijk een blik te werpen in het binnenste van deze fascinerende magnetische vloeistoffen.

Dankwoord

Een promotieonderzoek doe je gelukkig niet alleen. Anders dan de voorkant van dit boekje (met slechts één naam) doet vermoeden, hebben vele anderen buiten mijzelf ook bijgedragen tot de totstandkoming ervan. Dit is de plek om al die mensen te bedanken.

Hierbij wil ik graag beginnen met mijn dagelijks begeleider en copromotor Gert-Jan. Hoewel je niet vanaf het begin bij het onderzoek betrokken was, ben ik enorm blij jou als begeleider te hebben gehad. In al die jaren heb ik veel van je geleerd, zowel inhoudelijk als op het gebied van het opschrijven van onderzoek. Bedankt ook voor de gezellige tripjes naar Grenoble en Berlijn, waar we prachtige metingen hebben gedaan en waarvan de analyse niet altijd eenvoudig was, en jouw hulp daarbij onmisbaar. Behalve in het onderzoek kunnen we het ook op persoonlijk vlak prima vinden en dat heb ik erg leuk gevonden. Bedankt voor alles!

Mijn promotor, Albert Philipse, wil ik graag bedanken voor zijn enthousiasme en het initiëren van dit onderzoek. Albert, dankzij jou heb ik een grote mate van vrijheid gekregen om die dingen in het onderzoek te doen, die ik zelf leuk vond. Als ik een idee had werd dit altijd met veel enthousiasme ontvangen en als ik een leuk (of minder leuk) experiment had gedaan liep je onmiddellijk mee het lab in om het te bekijken en te bediscussiëren. Je bent altijd erg goed geweest in het leggen van contacten met collega-onderzoekers, hetgeen voor mij niet onbelangrijk was (zie o.a. hoofdstuk 2 en 6).

Behalve mijn ‘officiële begeleiders’ zijn er anderen geweest die zeer veel hebben bijgedragen aan het onderzoek. Andrei, het was fantastisch zoals jij letterlijk altijd tijd had voor mijn vragen en moeilijkheden wat betreft verstrooiing (ik had bijna het idee dat ik je ’s nachts uit bed kon bellen). Ik heb zelden zo’n enthousiast wetenschapper meegemaakt.

Verder ben ik grote dank verschuldigd aan Paul Bomans en Peter Frederik van de Universiteit van Maastricht. Paul, een betere 'cursus' voor het gebruik van de cryo-microscoop had ik me niet kunnen wensen, maar behalve dat was je ook werkelijk geïnteresseerd in de resultaten en dacht je enthousiast mee. Zonder jouw kennis en hulp was het nooit gelukt! Peter, bedankt voor alle nuttige discussies en je aanstekelijke enthousiasme. Jij legt je er niet bij neer als iets niet meteen lukt. Beiden zijn jullie op een goede manier ongeduldig: jullie wachten niet tot een werkplaats een perfect apparaat heeft gemaakt, maar struinen gewoon wat rond op het lab en fabriceren iets van satéprikkers en piepschuim. Bedankt voor de leuke tijd in Maastricht, ik heb het heel erg naar m'n zin gehad. Ralph, bedankt voor het afdrukken van de honderden foto's!

Ben, dankjewel voor de fijne samenwerking tijdens de metingen voor hoofdstuk 7. Je bent ontzettend grondig en volhardend en samen hebben we prachtige metingen gedaan. Bedankt ook voor je heldere uitleg als ik weer iets niet begreep. In het opschrijven van de metingen was je zo goed en precies, dat ik me er absoluut geen zorgen over hoefde te maken. Je was een fijne collega! Katarina, bedankt voor jouw grote bijdrage aan hoofdstuk 3, ik vond ons bezoekje aan Grenoble heel gezellig en de samenwerking ook. Nilesh, van jou heb ik veel geleerd op het gebied van de organische chemie en ik vond het erg plezierig om samen op het lab bezig te zijn. Wij hebben het werk dat al door Chris was opgestart (bedankt Chris!) goed kunnen uitbouwen, leidend tot hoofdstuk 2. Ook wil ik hier Bert Klein-Gebbink bedanken: je stond altijd klaar om dingen uit te leggen en metingen te doen in de periode 'tussen Chris en Nilesh in', maar ook daarna.

Bei Armin Hoell, Albrecht Wiedenmann und Martin Kammel möchte ich mich für die Möglichkeit bedanken, die SANS-Experimente am BENSC durchzuführen. Ihr seid wirklich Experten auf diesem Gebiet und wir haben sehr angenehme und ergebnisreiche Tage in Berlin verbracht. Vielen Dank für alle Hilfe, auch während des zweiten Besuchs (zur Analyse der Daten) und danach!

Veel metingen uit mijn proefschrift heb ik niet zelf verricht en zouden niet gebeurd zijn zonder de bereidwilligheid en kennis van anderen. Hierbij wil ik Marjan Verluijs-Helder, Helen de Waard, Hans Meeldijk, Pim van Maurik, Henk Pluijgers, Joop van der Maas, Ad Mens, Marc Storms en Felix de Haas bedanken voor al hun inspanningen. Dit geldt ook voor de collega's uit Delft, Leiden en Eindhoven (Anton Goossens, Menno Crajé, Adri van der Kraan, Peter Paulus en Kees Flipse): we komen uit heel andere vakgebieden en dat vergde veel overleg om elkaar 'onze' dingen duidelijk te maken. Bedankt voor de Mössbauer-metingen en de interpretatie. Ook het team van de DUBBLE was altijd bereid tot hulp tijdens metingen, het aanpassen van de apparatuur en het oplossen van problemen. Bedankt Igor, Dirk, Ruud en Wim.

Binnen de faculteit staat een heel leger mensen klaar om onderzoekers zo goed mogelijk te helpen en daar ben ik zeer dankbaar voor. Alle collega's van de glasblazerij en werkplaats, jullie hebben de meest fantastische en onmogelijke dingen voor me gefabriceerd, maar waren ook altijd bereid om 'gewoon' weer eens een serie Schlenkvaatjes te maken. Ingrid,

Jan en Aloys: bedankt voor alle posters, scans en natuurlijk niet te vergeten de lay-out van dit proefschrift (het is toch kunst wat jullie maken!).

Nico Boots van STW en alle leden van de gebruikerscommissie, dank jullie wel voor de input op de vergaderingen. Het is goed om elk halfjaar weer gedwongen te worden alles op een rijtje te zetten voor een presentatie en rapport. 'Mijn' studenten Vasco, Jolke en Diederik wil ik eveneens bedanken voor hun bijdragen, jullie hebben niet alleen meegeholpen aan het onderzoek, maar mij ook veel geleerd over het begeleiden van anderen.

Het Van 't Hoff laboratorium is het 'land van de vele mogelijkheden'. Congres- en werkbezoeken zijn vrijwel altijd mogelijk, net als de aanschaf van apparatuur, chemicaliën en wat je je verder nog maar zou wensen voor het onderzoek. Ook de ondersteuning is prima en wordt met veel enthousiasme gedaan. Bonny, je hebt geweldig geholpen met het bouwen en gebruiken van alle apparatuur en het meedenken met het onderzoek. Ook wil ik hierbij Mieke, Marina, Carel, Cees, Haran (voor alle hulp bij de syntheses), Chantal (o.a. prachtige foto's en mooie magnetietdeeltjes!) en Dominique bedanken voor hun inzet.

Straks zal ik het Van 't Hoff lab erg gaan missen en dat is niet voor niets. Ik geloof niet dat er een gezelliger vakgroep is binnen onze faculteit dan FCC. Hierbij wil ik alle collega's en ex-collega's bedanken voor de haast huiselijke sfeer. Bedankt ook voor alle labuitjes, squashtoernooien, fietstochten en andere leuke dingen. Bedankt N701 (waar ik altijd kon binnenlopen voor een praatje of voor gezeur over computerproblemen), Henk (voor je belangstelling voor het onderzoek, Sinterklaas en het aanvoelen van het 'groepsgevoel' (af en toe moesten er volgens jou nodig weer eens pannenkoeken worden gegeten)), Yannick (voor je niet-stuk-te-krijgen humeur en belangstelling) en Natalie (voor geklets en synthese-tips). Bedankt ook aan iedereen die met me meeging naar de sessies in Grenoble: Katarina, Mohammed, Remco, Gerard, Gert-Jan en Andrei, het waren leuke dagen (en nachten).

Ik heb het erg naar m'n zin gehad op N709. Dankjewel Tjerk (ik miste je echt toen je weg was!), Judith (voor je gezellige gebabbel), Mircea (de Nederlandse lessen zijn nu bijna voorbij) en Gerard. Gerard, jij kunt wel een soort 'rode draad' door mijn promotietijd genoemd worden, als (ex-)collega, kamergenoot, huisgenoot en goede vriend. Het is dan ook niet meer dan logisch dat je straks mijn paranimf zult zijn.

Bianca, Stefan en Michel, jullie hebben mij begeleid tijdens mijn eerste (en iets latere) stappen als onderzoeker en hebben dat fantastisch gedaan. Door jullie heb ik gekozen voor dit promotieonderzoek. Bianca, je bent zo enthousiast en wist dat ook heel goed op mij over te brengen. Als ik het onderzoek even niet meer zag zitten, was een gesprek met jou de oplossing! Stefan, ik ben weliswaar niet de kant van jouw vakgebied opgegaan, maar heb toch een hele leuke tijd gehad bij Gecondenseerde Materie. Michel, jij hebt me ontzettend veel geleerd en me er volledig van overtuigd dat colloïdchemie leuk is. Bedankt voor je heldere uitleg en aanstekelijke interesse.

Veel verder terug waren meneer Teunissen, meneer Maat en mevrouw Klein-Entink degenen die me hebben gebracht tot de keuze voor een studie scheikunde. Ik heb het geluk dat ik 3 heel goede scheikundedocenten heb gehad, allen even enthousiast en didactisch

vaardig. Dank jullie wel, ik hoop dat jullie het leuk vinden om mijn boekje te lezen!

Hoewel je op sommige momenten anders zou denken, is het promotieonderzoek gelukkig niet het enige waaruit mijn leven de afgelopen jaren bestond. Hierbij wil ik dan ook alle vrienden en vriendinnen van harte bedanken voor de leuke dingen die gelukkig niets met chemie en onderzoek te maken hadden. Ik hoop dat onze vriendschap nog lang zal voortduren. Bedankt Regje (al 13 jaar!), Steven, Alrik (ik hoop nog veel lullige keukenhulpjes van je te krijgen), Timmo, Yannick, Martijn en Albine. Carolien, wij kennen elkaar nu ook alweer bijna 12 jaar en je bent een echte zielsverwant. Niet geheel toevallig misschien, dat ook jij scheikunde hebt gestudeerd en bent gepromoveerd. Je was me steeds een stapje voor en dat was handig, kon ik bij jou informatie inwinnen. Ik vind het erg leuk dat ook jij mijn paranimf wilt zijn. Koert, Mario, Sjors, Arno, Ageeth, Gijsje, Ingrid, Victor en Myrthe, wij zijn de studie samen begonnen. Bedankt voor alle etentjes en andere gezellige samenkomsten. Het blijft bijzonder hoe wij in al die jaren veranderd, maar soms ook met elkaar 'meegegroeid' zijn (soms ook niet, maar dat stoort ons niet, we kunnen het nog steeds uitstekend met elkaar vinden). Ook de 'club van Mathijs' (Jorg, Martin, Marjolein en Arie) wil ik hierbij bedanken voor de squashpartijen, barbecue-, gourmet-, bowl- en video (slaap)avonden. Cees en Nel, bedankt voor de vele bezoekjes, fietstochten en gezelligheid.

Tijdens mijn gehele promotietijd was ik met plezier lid van de Utrechtse Reddingsbrigade. Ik heb erg genoten van de maandagse zwemavonden (met bijbehorend kantinebezoek), de bewakingen, oefeningen, wedstrijden, JEC-activiteiten, redactievergaderingen, etentjes, verjaardagen, weekendjes weg en van alles wat ik nu nog vergeten ben. Beste Maartje, Carla, Roland, Hester, Ernst, Ko, Dilejan, Jaqueline, Hilga, Peter Peltzer, Marion, Irene, Ria, Peter Jellema, Bas, Wouter, Martin, Ko, Femke, David, Ceciel en alle anderen: dank jullie wel voor de leuke tijd. We moeten maar zien of ik nog lang in Utrecht woon, maar hoe dan ook kom ik nog heel vaak langs!

Jeroen, bedankt voor al je interesse. Ook als je eigenlijk veel belangrijker zaken aan je hoofd had, bleef je altijd aan je grote zus denken! Lieve pap en mam, dank jullie wel dat jullie mij altijd gestimuleerd hebben, vertrouwen in mij hadden en achter mijn keuzes stonden. Jullie zijn nog altijd een heel vertrouwde en fijne basis om naar terug te keren. Bedankt ook voor het lezen van de 'samenvatting voor niet-vakgenoten'. Pap, we hebben zelfs inhoudelijk nog heel wat gediscussieerd over dit proefschrift, dat was altijd erg leuk. Het zijn heel moeilijke tijden, maar ik ben ontzettend dankbaar dat je mijn promotietijd tot het einde toe hebt kunnen meemaken.

Mathijs, jij bent wel met recht mijn rots in de branding. Jouw gelijkmatige humeur en vertrouwen in mij zorgden voor een wel zeer stabiel thuisfront. Als ik het eens niet zag zitten, maakte jij alles goed. Ook was jij het die steeds met de juiste raad kwam als ik door de bomen het bos niet meer zag. Zeker het laatste jaar heb je heel wat moeten doorstaan. Gelukkig hield je in de gaten dat we genoeg leuke dingen deden naast het werk. Dankjewel voor alles. Nu gaan we samen verder!

CV
Curriculum Vitae

De schrijfster van dit proefschrift werd geboren op 13 juni 1975 te Heemskerk (Noord-Holland). Zij behaalde in 1993 het VWO-diploma aan het Bonhoeffer College te Castricum. In hetzelfde jaar begon zij aan de studie Scheikunde aan de Universiteit Utrecht. In augustus 1994 legde zij het propedeutisch examen af en in augustus 1998 behaalde ze het doctoraal examen met als hoofdvak fysische chemie en colloïdchemie en als bijvak gecondenseerde materie van halfgeleiders. Eveneens werd een extra stage uitgevoerd op het gebied van de colloïdchemie bij het natuurkundig laboratorium van Philips, te Eindhoven. In oktober 1998 trad zij in dienst van de stichting STW (Stichting Toegepaste Wetenschappen) als Onderzoeker in Opleiding. Het promotieonderzoek beschreven in dit proefschrift werd verricht op het van 't Hoff Laboratorium voor fysische chemie en colloïdchemie onder begeleiding van prof. dr. A. P. Philipse en dr. G. J. Vroege. Een deel van dit onderzoek werd verricht bij de vakgroep Pathologie (afdeling Electronenmicroscopie) van de faculteit Geneeskunde aan de Universiteit van Maastricht.

Publications

Publications

This thesis is based on the following papers:

Butter K, Kassapidou K, Vroege G J, Philipse A P, Preparation and properties of colloidal iron dispersions.
in preparation (Chapter 3)

Butter K, Wiedenmann A, Hoell A, Petukhov A V, Vroege G J, Small angle neutron and X-ray scattering of dispersions of oleic-acid-coated iron particles.
in preparation (Chapter 4)

Butter K, Petukhov A V, Vroege G J, Small angle X-ray scattering of iron dispersions: influence of concentration and magnetic field.
in preparation (Chapter 5)

Butter K, Bomans P H, Frederik P M, Vroege G J, Philipse A P, Direct observation of dipolar chains in ferrofluids in zero-field using cryogenic electron microscopy, *J. Phys.: Condens. Matter.* 2003 **15 (15)** S1451.
(Chapter 6)

Erné B, Butter K, Vroege G J, Rotational diffusion in ferrofluids, *Langmuir*.
in press, intended volume **19 (21)** (Chapter 7)

Other papers by the author:

Kooij E S, Butter K, Kelly J J, Hole injection at the silicon aqeous electrolyte interface: A possible mechanism for chemiluminescence from porous silicon, *J. Electrochem. Soc*. 1998 **145 (4)** 1232.

Kooij E S, Butter K, Kelly J J, Silicon Etching in HNO_3/HF solution: Charge balance for the oxidation reaction, *Electrochem. Solid St.* 1999 **2 (4)** 178.

Butter K, Philipse A P, Vroege G J, Synthesis and properties of iron ferrofluids, *J. Magn. Magn. Mater.* 2002 **252** 1.

Goossens A, de Jongh L J, Butter K, Philipse A P, Crajé M W J, van der Kraan A M, Monodisperse magnetic iron colloids grafted with polyisobutene: A model system for Fischer Tropsch catalysts ?, *Hyperfine Interact*. 2002 **141 (1-4)** 381.

Butter K, Bomans P H H, Frederik P M, Vroege G J, Philipse A P, Direct observation of dipolar chains in iron ferrofluids by cryogenic electron microscopy, *Nature Materials* 2003 **2 (2)** 88.